Blast Testing and Modelling of Composite Structures

Giversen, Søren

Publication date:
2014

Document Version
Publisher's PDF, also known as Version of record

Blast Testing and Modelling of Composite Structures

PhD Thesis

$$(EIv'')'' = q - \rho A\ddot{v}$$

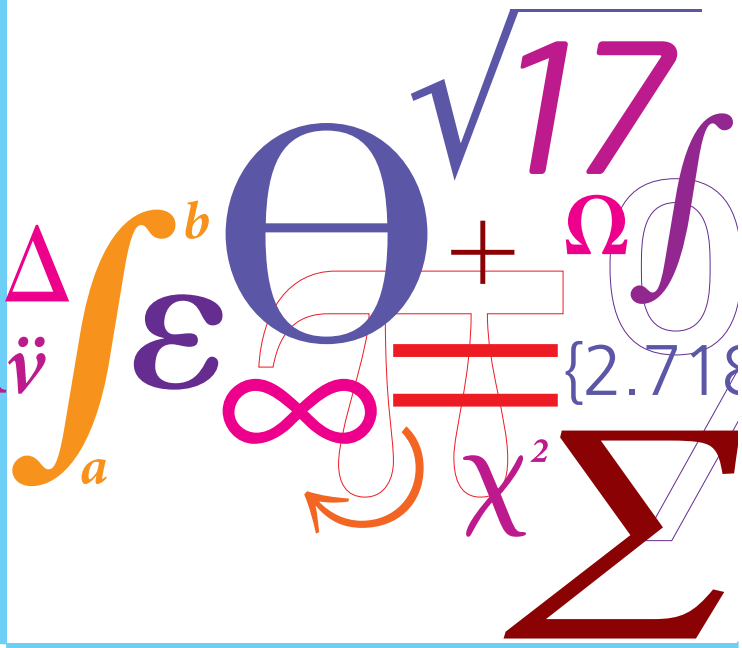

Søren Giversen
DCAMM Special Report No. S167
March 2014

DTU Mekanik
Institut for Mekanisk Teknologi

Blast Testing and Modelling of Composite Structures

Søren Giversen

March 2014

DTU Mechanical Engineering
Department of Mechanical Engineering
The Technical University of Denmark

Published in Denmark by
Technical University of Denmark

Department of Mechanical Engineering
Lightweight Structures Group
Technical University of Denmark
Nils Koppels Allé, Building 403
DK-2800 Kgs. Lyngby
Denmark

http://www.mek.dtu.dk/
Tel: (+45) 45 25 19 60
Fax: (+45) 45 93 14 75
E-mail: info@mek.dtu.dk

Publication Reference Data
Giversen, S.
Blast Testing and Modelling of
Composite Structures
Ph.D.Thesis
Technical University of Denmark, Mechanical Engineering
March 2014
Keywords; blast testing,modelling,LS-DYNA composite,sandwich,DIC,High-Speed Imaging,PVC foam

Success consists of going from failure to failure without loss of enthusiasm.

WINSTON CHURCHILL

Preface

This thesis is submitted as a partial fulfilment of the requirements for the Danish Ph.D.degree. The work has been performed in the Structural Light Weights Group, Department of Mechanical Engineering, the Technical University of Denmark, during the period of August 2010 to March 2014. The project was supervised by Associate Professor Christian Berggreen and co-supervised by Director Benjamin Riisgaard, Force Protection & Survivability at TenCate Active Protection, and Professor Brian Hayman, Oslo University.

The study was part of an overall project, RESIST, which involved the participation of the Danish Army, Falck Schmidt Defence Systems, COMFIL® and DTU Risø Campus.

Special thanks is given to Benjamin Riisgaard for his inspiring effort in the work with the experimental blast tests which could not have been done without his assistance and for many cherfull moments during the project. Also thanks for the support and good discussions regarding how to solve specific issues in LS-DYNA. Thanks are also given to my colleague and friend Rasmus Eriksen for many valuable discussions over the years and for being an inspiration in the daily work. Many thanks are also given to Professor Brian Hayman for taking time to participate in meetings and contribute with ideas for the solution of specific challenges met. The help has been much appreciated. Finally thanks to my supervisor for supporting the work through the entire project.

In a 5 month period from October 2012 to March 2013 the studies were carried out at Imperial College London. I would like to thanks Professor John Dear for letting me be a part of his research group during the month and for making my stay at Imperial College a memorable time.

Finally I would like to give my most devoted thanks to my wonderful girlfriend Tina; for your support, your encouragement when needed and for just making me happy.

. . . and for those I probably have forgotten, but whose help has been much appreciated;

THANK YOU

Abstract

The motivation for this work is based on a desire for finding light weight alternatives to high strength steel as the material to use for armouring in military vehicles. With the use of high strength steel, an increase in the level of armouring has a significant impact on the vehicle weight, affecting for example the manoeuvrability and top speed negatively, which ultimately affects the safety of the personal in the vehicle. Strong and light materials, such as fibre reinforced composites, could therefore act as substitutes for the high strength steel, and minimize the impact on the vehicle weight or actually reduce the weight. Before such materials can be brought into use, their performance against blast loading need to be evaluated. This can be done through the use of small scale blast testing. The overall objectives of this thesis have therefore been to establish and validate an experimental facility, usable for performing small scale blast test on laminate and sandwich panels, and to set-up a numerical framework for modelling the test panel response when impacted by a blast load.

The test set-up was designed such that the panel response could be measured by use of high-speed DIC (Digital Image Correlation). A test series, using Eglas/Epoxy laminates and sandwich panels, with Eglas/Epoxy skins and foam core, was conducted, to evaluate the functionality of the designed test set-up, and to gain insight into the response of the panels, when impacted by a blast load. The test set-up proved functional and provided consistent data of the panel response. The tests reviled that the sandwich panels did not provide a decrease in panel deflection compared with the monolithic laminates, which was expected due to their higher flexural rigidity. This was found to be because membrane effects became the controlling parameter for the panel deflection, activated by the large deflection of the panels relative to their thicknesses. The tests on the sandwich panels showed that no compression of the core had taken place, an effect that was thought could be utilized for absorbing energy from the blast pressure, but which had to be rejected. A comparison between E-glas/Epoxy and S-glas/Phenol laminates, with a quarto-axial (QA) and plain weave (PW) fibre layup respectively, showed that the S-glas/Phenol system could, as a minimum, withstand the load from an explosive charge 50% larger than the E-glas/Epoxy laminate could, without rupturing, indicating that the PW layup has attractive properties for absorbing energy from a blast load.

To model the blast tests the numerical solver LS-DYNA was used. The blast load was modelled using two approaches; (i) with *LOAD_BLAST_ENHANCED model in LS-DYNA, which applies a pressure distribution on a selected surfaces and has been based on experimental pressure measurement data, and (ii) with a designed 3 step numerical load model, where the blast pressure and FSI (Fluid Structure Interaction) between the pressure wave and modelled panel is modelled numerically. The tested laminates and sandwich panels was modelled using material models available in LS-DYNA.

Comparison between modelled and tested panel response from a 25g charge detonated 100mm from the panel surface, showed the modelled panel response to be 19% lower than the

test data. This difference could be argued to originate from test set-up uncertainties, but also due to inconsistencies between model and test pressure. It was attempted to design a test set-up to measure the blast pressure, but the variation in the measured pressure data was too large to be used for comparison with the modelled pressure. In a future work this set-up should be improved such that the modelled pressure can be validated.

For tests performed with a 250g charge load comparisons with model data showed poor agreement. This was found to be due to improper design of the modelled laminate panels, where the layer interface delamination was not represented physically, but was taken into consideration through failure parameters in the used laminate model. To improve the observed behaviour the layer interface should be modelled, by using a cohesive zone approach, based on fracture resistance data for the layer interfaces.

By comparing model and test data for the blast testing performed on the sandwich panels, it was found that in the models the foam core was compressed, a behaviour opposite what was identified from the test results. The models showed that the foam was compressed with a strain rate, several orders of magnitude larger than the strain rate used in the material testing performed to obtain data for describing the strain rate sensitivity of the foam. Extrapolating the rate behaviour to such large strain rate might therefore not be valid, and the material testing should be extended to include tests at higher strain rates. Other reasons for the inconsistency are believed to be due to improper representation of the laminate interfaces and the skin core interface.

Abstrakt

Baggrunden for dette projekt er basseret på et behov for at finde letvægtsalternativer til højstyrkestål som beskyttelses materiale i militære køretøjer. Ved brug af højstyrkestål vil en forøgelse af armeringsniveauet have signifikant indvirkning på køretøjets vægt, som for eksempel vil påvirke køreegenskaberne og top hastigheden i negativ retning, hvilket i sidste ende vil kunne formindske sikkerheden for personerne i køretøjet. Stærke og lette materialer, såsom fiberforstærkede kompositter, kunne derfor blive brugt som alternativer til højstyrkestålet og derved minimere vægt forøgelsen eller direkte reducere køretøjets vægt. Før sådanne materialer kan blive taget i anvendelse, skal deres egenskaber i forhold til en sprængningspåvirkning evalueres. Dette kan blive opnået ved brug af små-skala sprængningstest. De overordnede formål med dette projekt har derfor været at etablere og validere en test opstilling, som kan anvendes til at gennemføre skalerede sprængningstest på monolitiske fiberkompositplader og sandwichpaneler, samt at opbygge numeriske modeller til at modellere responset fra sprængningspåvirkede kompositpaneler.

Forsøgsopstillingen blev designet således at pladeudbøjningen kunne måles ved brug af højhastigheds DIC (Digital Image Correlation). Der blev gennemført en testserie på E-glas/Epoxy laminater og sandwich paneler, med E-glas/Epoxy skind og skum kerne, for at evaluere funktionaliteten af den designede forsøgsopstilling, og for at opnå indsigt i hvordan disse paneltyper reagerer når de bliver påvirket af en trykpåvirkning fra en eksplosion. Testene bekræftede brugbarheden af forsøgsopstillingen, som leverede konsistente målinger af panelernes udbøjning. Testene viste at sandwich panelerne ikke havde en mindre udbøjning end de monolitiske laminater, hvilket ellers var ventet på grund af sandwichpanelernes højere bøjningsstivhed. Dette skyldtes at membraneffekter blev den styrende parameter for udbøjningen, aktiveret af de store udbøjninger af pladerne i forhold til deres tykkelse. Testene på sandwich panelerne viste også at skumkernen ikke blev trykket sammen under testen. En effekt som var tænkt ville kunne udnyttes til at tage energi ud af sprængningsbelastningen, men som blev afkræftet via testene. I en sammenligning mellem E-glas/Epoxy og S-glas/Phenol laminater, med henholdsvis et Quarto-Axialt (QA) og et Plain-Weave (PW) fiberoplæg blev det vist at S-glas/Phenol systemet, som minimum, kunne modstå trykket fra en 50

Den numeriske kode LS-DYNA blev brugt til at modellere sprængningstestene. To forskellige tilgange blev brugt til at modellere eksplosionstrykket; (i) via *LOAD_BLAST_ENHANCED modellen i LS-DYNA, som påfører en trykfordeling på en udvalgt overflade, og som er basseret på eksperimentelle trykmålinger, og (ii) via en designet 3 trins numerisk last model, hvor eksplosionstrykket og FSI (Fluid Structure Interaction) mellem trykbølgen og de modellerede paneler bliver modelleret numerisk. De monolitiske laminater og sandwich panelerne blev modelleret via de tilgængelige materialemodeller i LS-DYNA.

Ved sammenligning mellem modelleret og målt panel udbøjning, forårsaget af en 25g ladning detoneret 100mm fra paneloverfladen, var den modellerede udbøjning 19% lavere. Der kunne

argumenteres for at forskellen kunne bunde i opstillingsusikkerheder, men også fra forskelle mellem det modellerede tryk og det reelle tryk i testene. Det blev forsøgt at designe en forsøgsopstilling til måling af tryk fra en eksplosion, men variationerne i de målte data var for store til at en valid sammenligning med model data kunne gennemføres. I et fremtidigt arbejde bør denne forsøgsopstilling valideres således at valide trykmålinger kan gennemføres til brug ved sammenligning med model data.

For test foretaget med en 250g ladning viste en sammenligning mellem test og model data dårlig overensstemmelse. Dette blev vurderet til at skyldes et forsimplet design af de modellerede test paneler, hvor interfacet mellem de forskellige fiberlag ikke blev modelleret fysisk, men blev taget i betragtning via fejlparametre i den anvendte laminat model. For at forbedre dette skal laminatmodeldesignet ændres således at fiberlag interfacet medtages i modellen og for eksempel repræsenteres via en kohæsiv model, som bruger brudmekaniske data for fiberlag interfacene.

For sandwichpanelerne viste en sammenligning mellem test og model data, at skumkernen i modellen blev trykket sammen, hvilket var i modsætning til hvad der blev observeret i testene. Modellerne viste at skummet blev presset sammen med en tøjningsrate, som var flere størrelsesordner højere enden de tøjningsrater, som blev brugt i materialetestning af skummet for at opnå data til at beskrive skummets tøjningsratefølsomhed. Ekstrapolering af tøjningrate dataene til de tøjninger, som er observeret i modellerne er muligvis ikke valid, hvilket bør afklares eksperimentelt. Andre årsager til kompressionen af kernen i modellen kan være den forsimplede repræsentation af laminaterne i sandwich skindene eller manglende repræsentation af skind-kerne interfacet.

Contents

Chapter 1

Introduction

The increasing use of Improvised Explosive Devices (IED) against military vehicles in war zones has become a severe threat to military personnel. The latest Iraq War and the Afghan War have emphasised the need for protection and survivability when operating in asymmetric theatres. The Iraqi insurgents showed how simple means could inflict high losses against high-tech modern armies. Likewise, the Taliban and other armed groups in Afghanistan have adopted similar strategies by using IEDs as one of their main weapons. The use of sophisticated detonating devices makes it possible for insurgents to bring the IED to detonation, causing a worst-case scenario for the vehicle undercarriage.

These threats have led to the need for a higher degree of vehicle armouring. Traditionally high strength steel was used as armour on military vehicles. However, modern military vehicles

Figure 1.1: Military vehicle exposed to a mine blast

must balance the need for protection against mobility and payload capacity. Increasing the armouring by using high strength steel will results in an overall increase in vehicle mass, which will negatively impact the functionality of the vehicle through:

- Reduced crew carrying capacity
- Reduced ammunition carrying capacity
- Reduced manoeuvrability
- Increased fuel consumption

Therefore, there is a need to identify and test alternative materials that are lighter than steel, but provide the same or better protection. Such alternative materials could include advanced composite materials [1]. Composites are known to possess higher stiffness and strength to weight ratios compared to steel, and it is therefore envisioned that such materials can offer improved blast protection performance. Before new types of lightweight armour are used on vehicles in operation, the performance of the armour must be tested and compared with existing armour to evaluate whether the new alternative is better than the old. This is typically done by full-scale blast testing of a vehicle that has the new armour mounted. Full-scale blast testing is both costly and time consuming, especially given the many variables that can be changed in the lay-up of composite materials. It is therefore highly desirable to find a way that enables the evaluation of the performance of candidate materials and structures, without the need to carry out a full scale blast test on them. This can be done using small scale blast tests, where the performance of the candidate materials are tested at small scale, after which only the best performing candidate materials are tested at full-scale. The use of small scale blast tests is much more cost effective and less time consuming than full scale blast tests.

In the literature several examples exist where small scale blast testing has been used to investigate the structural response of different types of materials and structural designs. Examples span from blast tests on steel plate and steel sandwich structures [2, 3], to tests on different kinds of laminates and fibre metal laminate structures [4, 5], and tests on various sandwich designs [6, 7], all describing the advantages and disadvantages of the tested structures. Recently the use of Carbon Fibre Reinforced Polymers (CFRP) for blast protection has been investigated in the European CAFV project [1]. Still, this project, did not recommend a better alternative to commercial armour steel products. However, it was concluded that composite materials have the potential to be used in blast protection and further research should be performed. Common for all of these studies are that they required special blast testing facilities, as these tests cannot be conducted in a standard laboratory. There is a desire to be able to perform such tests in Denmark and so establish an experimental foundation that can support the development and research into the use of composite structures for blast protection. This desire is the driving force behind the present project.

An alternative approach to evaluate candidate materials for lightweight armour is to use a numerical tool, such as FEA (Finite Element Analysis). Here, using mathematical models, the blast and material responses are evaluated. The advantage of FEA is that it does not require physical testing of candidate materials, which makes it a highly cost effective alternative to traditional physical testing. The disadvantage is that results from FEA are not more accurate than the models used to describe for example the explosives and materials that are modelled. Such models are generally heavily dependent on material parameter input, which has to be

found through material testing. Therefore, using FEA requires a material testing program to be established in order that the materials to be modelled can be properly described.

The present Ph.D. project will therefore focus on both experimental blast testing and on using FEA to set up models that can be used in the analysis of blast loading on composite panels.

1.1 Project Objectives

Two overall objectives have been defined for the present Ph.D. project;

1. Design and verify an experimental facility that can be used to conduct small scale blast testing on composite panels while monitoring their response with high-speed cameras allowing DIC to be performed on the recorded images, such that the panel deflection and deformation can be analysed

2. Establish a numerical framework that can be used to model the blast load on a tested panel such that the response of the panel to the applied blast load can be modelled, using the experimentally measured panel response from the blast tests as basis for validation.

The establishment of the blast facility will involve the following tasks;

- Design the experimental set-up to be used
- Introduce the high-speed cameras in the set-up and verify that DIC can be performed on test panels and provide valid data for analysis
- Perform a series of blast tests on designed monolithic and sandwich composite panels, to test the stability of the designed set-up, and to test if valid data can be generated from tests on different panel types.
- Test the set-up in extreme conditions, for example, when a hole is blown through the thickness of a test panel

To establish the numerical frame work the numerical solver LS-DYNA will be used. The work will involve the following steps;

- Becoming familiar with LS-DYNA and its ability to model blast and laminated structures
- Design a numerical model for modelling blast on structures based on Fluid Structure Interaction (FSI)
- Investigate the capability of the available laminate material models in LS-DYNA,
- Compare model and test results for selected blast test set-ups

1.2 Report Outline

To cover the described objectives the thesis has been divided into chapters with the following content:

In Chapter 2 a general overview will be given to the field of blast, and the primary parameters that describe a characteristic blast wave will be presented. The concept of geometrical scaling will be introduced to show how a limited number of blast measurements can provide the foundation for predicting parameters for a wide range of blast load scenarios. In addition the interaction between blast wave and structures will be described highlighting some of the effects that develops due to this interaction.

In Chapter 3 an introduction to LS-DYNA will be given together with the possibilities that exist in LS-DYNA to model blast loads on structures. In addition a description of the different models needed to set up a blast load scenario will be given. This is followed by an overview of the models available in LS-DYNA for modelling laminated and foam structures, and a walk through of the models used for this purpose will be given.

In Chapter 4 a description of the designed experimental blast test set-up will be given. Here details of a designed blast box to hold the test panels and of the functionality of the installed high-speed DIC system will be outlined. The chapter ends with a description of the steps involved in performing a blast test.

In Chapter 5 a detailed description of the results of the performed blast test is given. A comparison of the performance between monolithic laminates and sandwich panels will be shown. This comparison indicates that there were no significant advantages in using sandwich panels over monolithic laminates. This will be followed by the results from a test series performed on a single panel receiving multiple blast load impacts, where a characteristic change in the response of the panel was identified, a change that could be related to the onset of internal failure development. Finally a comparison between the performances of two monolithic laminates is made, where one laminate was constructed from quarto axial fabric layers and the other from plain weave (PW) layers. This comparison shows a significantly better performance for the PW laminate type.

In Chapter 6 a presentation of material tests performed on the two foam types used as core materials in the designed sandwich panels will be given. The tests are primarily performed to generate input to numerical models to model the sandwich panels during a blast load. First, the chapter will give an introduction to foam as a material and then a comparison of the two foam types will be made. This will be followed by the results from the quasi-static and dynamic material testing, which compare the behaviour of the two foams. Finally the rate dependent response of the foams will be analysed and a simple model for to describe the rate behaviour will be introduced.

In Chapter 7 comparisons between modelled and tested panel responses from the performed blast tests will be given. First it will be shown how LS-DYNA is used to numerically model the blast wave and also how it is brought into contact with the modelled panel by use of Fluid Structure Interaction (FSI) modelling. Then comparisons between model and experimental test

data for blast on a monolithic laminate panel loaded by a charge sizes of 25g is presented. This is followed by a discussion on how to model a layered laminate, using the available material models. Included in the discussion are the challenges that still remain to obtain a correct response of the modelled laminate. Finally, comparisons between modelled and tested responses from blast loading on the sandwich panels are shown, where challenges still remain in getting the foam to respond correctly in the model.

Chapter 8 contains a summary of the overall conclusions that can be drawn from the performed work and gives recommendations for future work.

Chapter 2

Behind the Blast

An explosion is a phenomenon resulting from a sudden release of energy [8], where the exact source can be anything from gunpowder, wheat flour dust in a grain elevator to a pressurized steam boiler or an uncontrolled nuclear transformation. The energy release must be sudden and very rapid, such that a local accumulation of energy can take place. The accumulated energy is then suddenly spread to the surroundings where a blast wave is generated when the surrounding air is rapidly pushed back. The blast wave expands and impacts with any obstacles it passes on its way, where energy from the blast wave is transferred to the impacted structure and a structural response takes place. The shape, speed and duration of the blast wave depend on the type of explosive used and the shape of the explosive charge before detonation. A perfect spherically shaped charge will generate a blast wave that spreads spherically from the detonation point.

In this work, a PETN (Pentaerythritol tetranitrate) based Plastic Bonded Explosive (PBX), where the explosive is mixed with a binder, such as polystyrene or polyester, to make the explosive formable is used. The PBX used here is a mixture with an 85% PETN content and has the designation PETN(85/15). This type of explosive is a *detonating explosive* or *High Explosive (HE)*, a name that relates to the rate at which the explosive decomposes. In an HE, the activation energy for the explosive reaction to occur requires a shock pressure force acting on the explosive material[8]. This means that HE cannot be brought to reaction by igniting it but requires that a shock pressure front is sent through it. HE therefore needs to be activated by use of a detonator[1], that will generate a shock wave which is sent through the HE charge and brings it to detonation.

2.1 Blast Theory

The generated blast wave expands in the surrounding atmosphere, and the pressure in the blast wave measured at a stationary point some distance from the detonation point has the theoretical shape illustrated in figure 2.1, from which several parameters, characteristic for a blast pressure front, can be identified. The first is the arrival time t_a which is the time it takes

[1] A small devise used to trigger the HE charge. It is placed in the HE charge and then activated, e.g. by a voltage, igniting a small primary charge in the detonator, which then activates a base charge, that generates the shock front needed to activate the HE charge

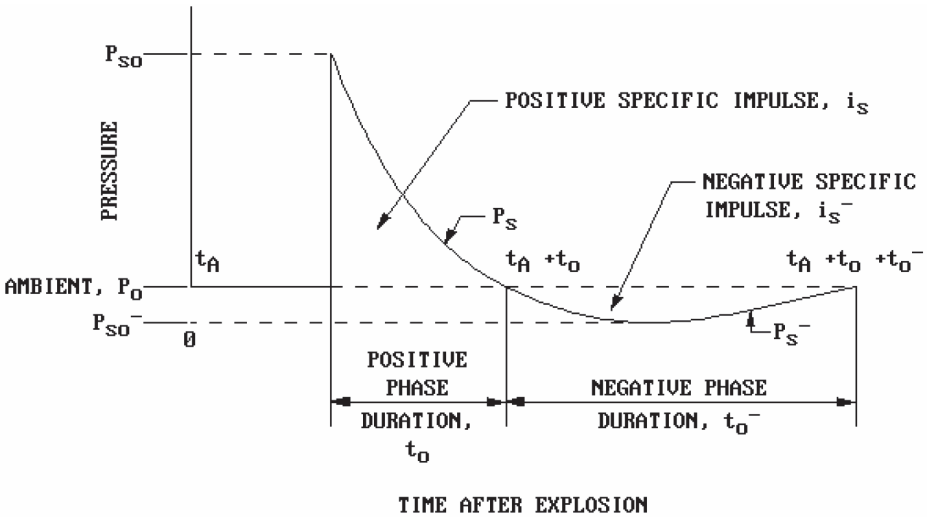

Figure 2.1: Development of pressure over time for a free air explosion [9]

the blast wave front to travel from the detonation point to the measuring point. When the blast wave reaches the specific reference point, an instantaneous increase from ambient pressure P_0 to the *peak overpressure* P_{so}, also known as the *side-on* or *incident* pressure, which is the pressure in the undisturbed pressure wave, will be observed. After passage of the peak overpressure the blast wave pressure steadily decays until the pressure has drops to the ambient pressure, which marks the end of the *positive phase*, where the blast pressure i higher than ambient pressure. The time it takes the pressure to drop form P_{so} to P_0 is known as the duration time t_d. From here the pressure drops below ambient pressure, known as the *negative phase*, until the ambient pressure is again stabilized. In most blast studies the negative phase is ignored [10], because the impulse generated in the negative phase in most cases is much smaller than that of the positive phase, and therefore leads to very little damage [11]. As illustrated in figure 2.2 this is especially seen to be true for blasts at low scaled distances which is relevant for the present work where scaled distances will be in the approximate range of $0.16 - -0.34 m/kg^{1/3}$

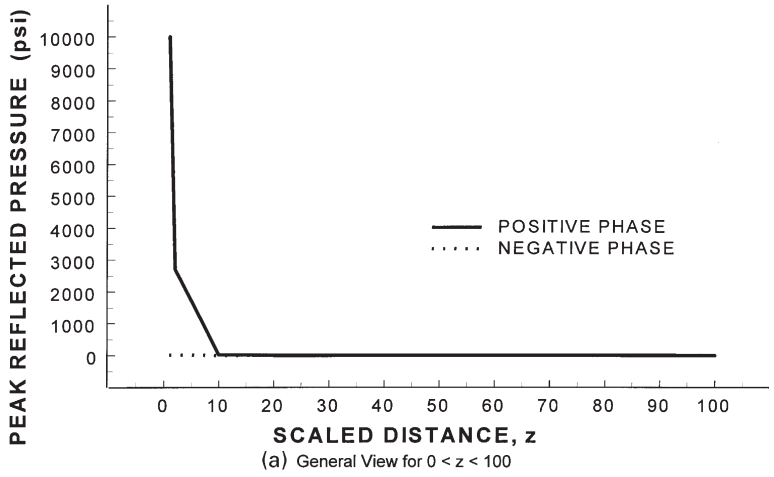

Figure 2.2: Level of positive and negative pressure phase as function of scaled distance [11]

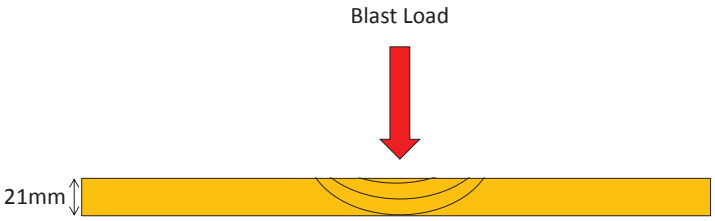

Figure 2.3: 1D pressure wave travelling through the thickness of a composite panel

Even though the pressure level in the negative phase is low, then for composite panels it might still be able to inflict damage due to the weak through thickness properties of the laminates. But by comparing the duration time of the positive pressure phase with the time it takes a stress wave to travel through the thickness of a panel, illustrated in figure 2.3, it can be justified that the negative pressure phase can be ignored

For simplicity the stress wave is treated as 1D for which the wave speed can be calculated by use of 2.1.

$$\nu = sqrt\frac{E}{\rho} \tag{2.1}$$

Using the plate thickness of the tested panels (21mm), the time it takes the stress wave to travel from the frontside to the backside of the panel can be found. In the blast experiments performed a distance from charge to target (the Stand Off Distance) of 100mm is used, and the smallest and largest charge sizes used are 25g and 250g respectively. Using emperical formulas for calculating blast parameters (presented in Chapter), the duration of the positive pressure phase for the two extremity points can be calculated.

$$\begin{aligned} t_{wave} &= 7.5\mu s \\ \text{25g@100mm} \rightarrow \quad t_0 &= 126\mu s \\ \text{250g@100mm} \rightarrow \quad t_0 &= 126\mu s \end{aligned}$$

As can be seen from the calculated t_{wave} and the two t_0 the generated stress wave will have time to reflect several times before the positive phase is ended. The incoming compressive stress wave will therefore have been reflected from the panel backside as a tensile wave. Since the stress level in the positive phase is much larger than in the negative phase, as illustrated in figure 2.3, any damage inflicted duo to tensile loads will therefore have occurred in the positive pressure phase supporting the general accept of ignoring the negative pressure phase.

A typical example where the negative phase cannot be ignored is in a nuclear blast, where the negative pressure can lead to further damage on structures already affected from the positive phase duration. Looking only at the positive phase in figure 2.1 the pressure in the blast wave can be described by the Friedlander formulation [9, 10], shown in equation (2.2)

$$P(t) = P_{so}\left(1 - \frac{t - t_a}{t_d}\right)\exp\left(-\alpha\frac{t - t_a}{t_d}\right) \tag{2.2}$$

and the impulse can be calculated from [10]

$$J_s = \int_{t_a}^{t_d} P(t)dt = P_{so}t_a\left[\frac{1}{\alpha} - \frac{1}{\alpha^2}\left(1 - \exp\left(-\alpha\right)\right)\right] \tag{2.3}$$

The blast wave pressure and impulse during the positive duration is thus completely described by t_a, t_d, P_{so}. The parameter α is the *wave form parameter* that affects the shape of the decay in figure 2.1, which can be found by simultaneously solving equation (2.2) and (2.3).

2.1.1 Scaling of Blast Parameters

The magnitude of the incident pressure P_{so}, the arrival time t_a and duration time t_d depend on the amount of explosive used and the distance at which the blast parameters are measured. This means that two charges of different explosive mass measured at different distances can result in the same P_{so}. This principle is used to construct a dimensionless scaling parameter that can be used to predict blast parameters for blast set-ups that have the same value of the scaled parameter. When scaling spherical blast waves, a commonly used method is the Hopkinson or *cube root* scaling law which states that; '*self-similar blast waves are produced at identical scaled distances when two explosive charges of similar geometries and explosive, but different weight, are detonated in the same atmosphere*' [12]. When using this scaling law the scaled parameters are

$$Z = \frac{X}{W^{1/3)}}, \quad \tau^* = \frac{\tau}{W^{1/3}}, \quad J^* = \frac{J}{W^{1/3}} \tag{2.4}$$

where Z is the scaled distance, τ^* is the scaled time and J^* is the scaled impulse for a blast with a SOD (Stand-Off Distance) R, an arrival or duration time τ and an impulse J, generated by a charge with mass W. The scaling laws imply that quantities with dimensions of *pressure* and *velocity* for the same Z are unchanged through scaling, because the charge radius is proportional to the cubic root of the charge mass. So for the same Z two charge sizes generate the same P_{so} at the stand-off distances used for the two set-ups. For the scaled time τ^* and impulse J^* the same is not valid since time and impulse is not proportional to the cubic root of charge mass. To get the real time and impulse values for the scaled set-up the scaled τ^* and J^* has to be multiplied by $W^{1/3}$ [12, 13].

The scaling relations can be used to generalize measured blast load parameters from a limited number of tests such that they can be used to predict blast load parameters for a wide range of geometrically similar charge weight and SOD configurations. This principle is one of the fundamental principles for the ∗LOAD_BLAST function in LS-DYNA, which will be described later.

2.1.2 Reflected Pressure and Impulse

The peak pressure in the undisturbed pressure wave is P_{so}. If the blast wave impinges with the surface of an object the blast wave is reflected but also locally reinforced at the object surface. This reinforcement is due to compression and damming up of the air in the blast wave at the surface of the structure, caused by the air particles coming to an abrupt halt before their movement is reversed. This creates a pressure build up which increases the incident pressure to what is known as the *peak reflected pressure* P_r, which is the pressure experienced by the structural surface. The magnitude of the reflected pressure depends on the orientation of the normal of the impinged surface with respect to the direction of travel of the blast wave. If the shock wave impinges the surface oriented such that a line describing the path of travel of the blast wave is parallel with the normal to the surface, then the point of initial contact will experience the maximum possible reflected pressure. This kind of reflection is known as the *normal reflected pressure*. As the angle between the direction of blast wave travel and the

surface normal increases the reflected pressure decreases and reaches its minimum value at an angle of 90°, where $P_r = P_{so}$. For a rigid surface the theoretical peak reflected pressure is $8P_{so}$ [8], but higher reflected pressures can be generated depending on the venting conditions around the impacted surface.

The response of the reflected pressure over time at a specific point on the impinged surface has a shape similar to that of the incident pressure, shown in figure 2.1. Expression (2.2) can thus also be used to calculate the pressure over time for the reflected pressure, since it is governed by the same time scales as the incident pressure. The *reflected impulse* can be determined by use of expression (2.3) with P_{so} replaced by P_r.

2.1.3 Blast Effects on Structures

Upon impact with a structure, the blast wave generates both a shock effect in the structure and a dynamic response of the structure, where the first effect is controlled by the peak reflected pressure P_r and the second is controlled by the reflected impulse J_r, transferred to the structure from the blast wave. Compared with the reflected pressure, the reflected impulse can be understood as the *push* on the structure, whereas the reflected pressure is the initial shock that the structure experiences.

When the blast wave impinges the structure P_r is instantaneously built up and a compressive stress wave is generated and starts to travel through the structure. If the structure is a flat panel impinged normal to its surface, the stress wave will travel through the thickness of the panel and if the generated compressive stresses are large enough, they can cause damage in the panel. In a laminate the fibres could be damaged by the compressive stress, and in a foam core sandwich the core could start to crush, and thereby weaken the panel before the panel has started to respond to the applied impulse. When the stress wave reaches a free surface it is reflected as a tensile stress wave, which travels back through the thickness of the panel. The tensile wave can lead to further damage e.g. spalling, which is seen in steel panels impacted by a blast load. For laminates, a failure type that can be initiated by the tensile wave is delamination between adjacent fibre layers, since the tensile wave can generate a mode I crack opening type.

Impulse is the change in momentum, so as the impulse increases on the panel, a velocity is build up and the panel starts to deflect.

$$\mathbf{J} = \int_{t_1}^{t_2} \mathbf{F} dt = \Delta \mathbf{p} = m\mathbf{v_2} - m\mathbf{v_1}$$

Depending on the localization of the blast load, the velocity build-up can take place over the entire panel, in case of a planar blast wave impacting the panel, or the deflection can be built up from the centre of the panel, in case of a localized spherical blast wave impacting in the panel centre, where after the deflection is built up over the remaining part of the panel. The impulse is a measure of the energy transferred to the structure and is highly influential on the amount of deflection created [1]. The rate at which the impulse is built up is also of importance, as it will control the strain rate experienced by the panel. The rate of change in impulse is primarily controlled by the duration time t_d and the wave for parameter α.

When the blast wave impinges a structure, the phenomenon known as *Mach Stem* can develop and is illustrated in figure 2.4. The phenomenon happens when the angle of incident exceeds 45°[14], and is caused by the reflected pressure wave catching up with the incident wave. The two wave intersect at what is known as the *triple point*, and the merging of the two waves form a single outward travelling wave as illustrated in the figure. The merging of the

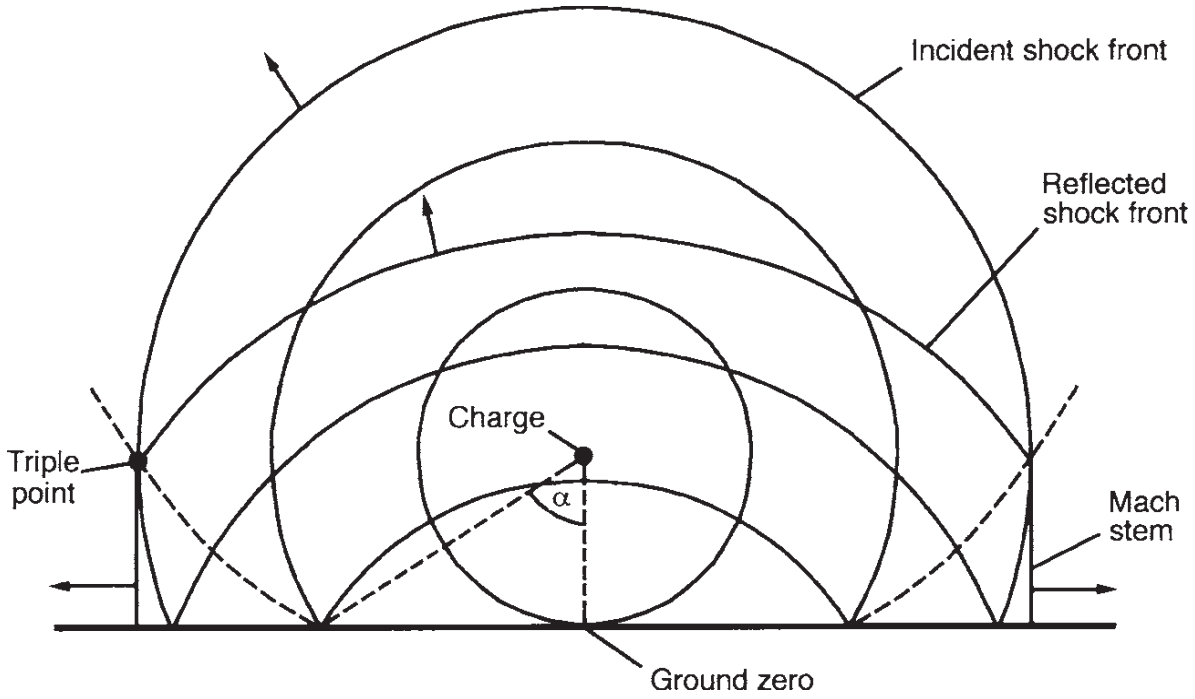

Figure 2.4: Mach stem creation by merging of the reflected and incident pressure waves [14]

two waves creates a new wave with a pressure higher than the single reflected pressure wave, and can thus contribute to an increase in the impulse transferred to the structure. In the blast tests performed, the SOD used is 100mm and the exposed panel area is 500×500mm. Incident angles larger than 45°will therefore be present and the Mach Stem effect can develop.

Equations (2.2) and (2.3) do not take into account the effect of the Mach Stem. They can only be used to predict the pressure at a point. Another issue which the two equations also do not account for is reflections from other nearby surfaces or structural edges hindering the high pressure from moving away from the impacted surface. These effects can prolong the duration of the blast pressure applied to the structure, and thus increase the impulse delivered to the structure, which can lead to a more severe structural response of the impacted object.

Chapter 3

Modelling of Blast

As seen from section 2.1, the blast wave generated from the detonation of an explosive charge is characterized by a peak pressure and an impulse, which impose different effects on an impinged structure. Simple analytical expressions exist to describe the pressure and impulse of the blast wave, which can be used as a foundation to analyse the response of blast loaded structures. However the interaction between the blast wave and the object can lead to effects such as Mach Stem and reflections from edges, which are not properly described by the simple analytical equations. One approach to overcome this challenge is to use FEA to analyse a blast problem, where effects such as reflections can be accounted for, for example through fluid structure interaction. Many finite element codes exist, that are capable of modelling the blast pressure from an explosive, for example LS-DYNA and Abaqus. In this work LS-DYNA was used to investigate the possibilities of modelling blast scenarios similar to the set-up used in the performed blast tests.

LS-DYNA, developed by Livermore Software Technology Corporation (LSTC), is a general-purpose finite element code which can be used to analyse large deformations, static and dynamic responses of structures including structures coupled to fluids. The main solution methodology is based on explicit time integration. An implicit solver is currently available with somewhat limited capabilities including structural analysis and heat transfer [15]. LS-DYNA is not limited to any particular type of modelling and any of LS-DYNA's features can be combined to model a wide range of physical events. Because of its generality and its ability to work with fluid structure interaction, LS-DYNA is well suited for use in modelling blast impacts on structures. Its ability to model blast incidents has also been reported in a number of different articles [1, 10, 16, 17]. In addition, LS-DYNA holds a large material library that comes with the code, where several alternatives exist for modelling for example laminated structures.

3.1 Finite Element Analysis

Using FEA, the problem is defined within a numerical domain as illustrated in figure 3.1. The numerical domain is divided into a large number of elements connected through element nodes. For each material type represented in the numerical domain, relevant constitutive laws cover the physical behaviour and at material interfaces, structural boundaries and at the geometrical boundaries of the domain, proper conditions are defined to represent physical behaviour. The

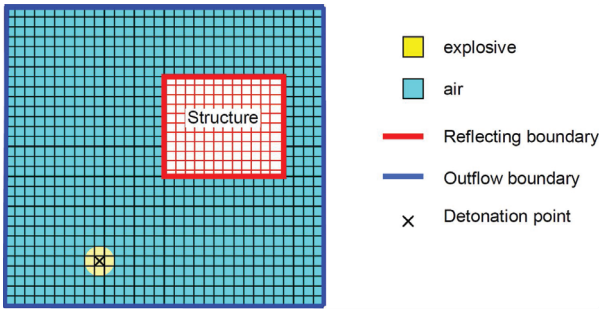

Figure 3.1: Illustration of air blast defined with in a numerical domain

defined problem is then solved using the LS-DYNA solver, after which the modelled structural response can be analysed in a suitable post-processor, for example LS-PrePost. Unless the modelled problem is linear, the solution needs to be processed over several time steps, whose size is problem dependent. Figure 3.2 illustrates the solution procedure used in each solution cycle by LS-DYNA. The nodal acceleration, velocity and displacement used in each solution is calculated from the equation of motion [15]

$$\mathbf{M}\ddot{\mathbf{u}} + \mathbf{C}\dot{\mathbf{u}} + \mathbf{K}(\mathbf{u})\mathbf{u} = \mathbf{p}_{ext} \tag{3.1}$$

where $\mathbf{M}$, $\mathbf{C}$ and $\mathbf{K}$ are the mass, damping and stiffness matrices respectively, and $\mathbf{u}$ and $\mathbf{p}$ are the displacement and force vectors respectively. For a linear problem the stiffness matrix $\mathbf{K}$ is constant and analytical solution methods to 3.1 exists. For non-linear problems simple analytical solutions do not exist and equation 3.1 is instead solved by use of *direct integration* [18].

3.1.1 Time Integration

Direct integration refers to calculation of the response history using step-by-step integration in time, and the term *direct* indicates that, prior to integration, no transformation of the equations to a different form is carried out as done for example in a modal analysis. Direct integration methods calculate conditions at time step $n + 1$ for the numerical domain by use of (3.1), a

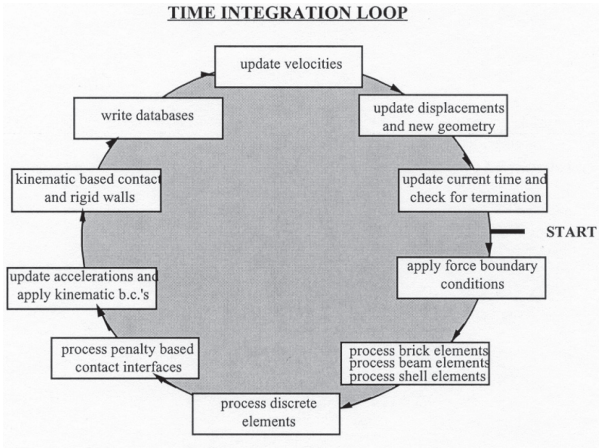

Figure 3.2: Time integration loop used in LS-DYNA

difference expression and known conditions at one or more preceding time steps [18]. Generally two types of algorithms for direct integration are used; an *explicit* algorithm with difference expressions of the form

$$\mathbf{u}_{n+1} = f\left(\mathbf{u}_n, \dot{\mathbf{u}}_n, \ddot{\mathbf{u}}_n, \mathbf{u}_{n-1} \dots\right) \tag{3.2}$$

and an *implicit* algorithm with the following general form

$$\mathbf{u}_{n+1} = f\left(\dot{\mathbf{u}}_{n+}, \ddot{\mathbf{u}}_{n+1}, \mathbf{u}_n, \dot{\mathbf{u}}_n, \ddot{\mathbf{u}}_n \dots\right) \tag{3.3}$$

The main difference between the two methods is that the explicit method only contains information for times steps $\leq n$, whereas the implicit algorithm also uses data for the step $n+1$. The two methods have some distinctive differences. The explicit method is only conditionally stable, meaning that the time step must be below some critical value. This means that with this method many time steps are needed to solve a problem, but for the explicit method the coefficient matrix for $\mathbf{u}_{n+1}$ in (3.2) can be made diagonal such that the system can be solved computationally cheap [18]. For the implicit method there is no restrictions on the time step, but in contrast to the explicit method the coefficient matrix for $\mathbf{u}_{n+1}$ cannot be made diagonal, which means that a system of simultaneous equations must be solved [18]. The low cost per time step combined with the small time step to avoid instability makes the explicit suited for *wave propagation* problems such as blast loading, where the time duration is very short and high frequencies dominate the structural response, requiring a small time increment for proper modelling of the structural response. Implicit methods are more suited for *structural dynamics* problems, where the time duration is over several seconds and the structural frequency response is dominated by the lower modes [18].

3.2 Time Integration in LS-DYNA

In LS-DYNA it is possible to choose between an implicit and explicit solver. But as described above the explicit solver is preferred in case of blast modelling, where the structural response is very short and of high-frequency. The direct integration method used in LS-DYNA for explicit analysis is the*Half-Step Central Difference* method [19], a variation of the classical central difference method shown in appendix D. In the following a recapitulation of the formulation of the Half-Step Central Difference method used in LS-DYNA is given based on the procedures in [18, 19].

Figure 3.3 illustrates the principle behind the Half-Step Central Difference method used in LS-DYNA, which is formulated in actual geometry (xyz) rather than being based on nodal displacements u. Using the Half-Step Central Difference method, the velocity and accelerations can be written as

$$\dot{\mathbf{x}}_{n+\frac{1}{2}} = \frac{1}{\Delta t_{n+\frac{1}{2}}}\left(\mathbf{x}_{n+1} - \mathbf{x}_n\right) \tag{3.4}$$

$$\begin{aligned}\ddot{\mathbf{x}}_n &= \frac{1}{\Delta t_n}\left(\dot{\mathbf{x}}_{n+\frac{1}{2}} - \dot{\mathbf{x}}_{n-\frac{1}{2}}\right) \\ &= \frac{1}{\Delta t_n^2}\mathbf{x}_{n+1} - 2\mathbf{x}_n + \mathbf{x}_n - 1\end{aligned} \tag{3.5}$$

which can be combined to give an expression for the position of x_{n+1}

$$\mathbf{x}_{n+1} = \mathbf{x}_n + \Delta t \dot{\mathbf{x}}_{n-\frac{1}{2}} + \Delta t^2 \ddot{\mathbf{x}}_n \tag{3.6}$$

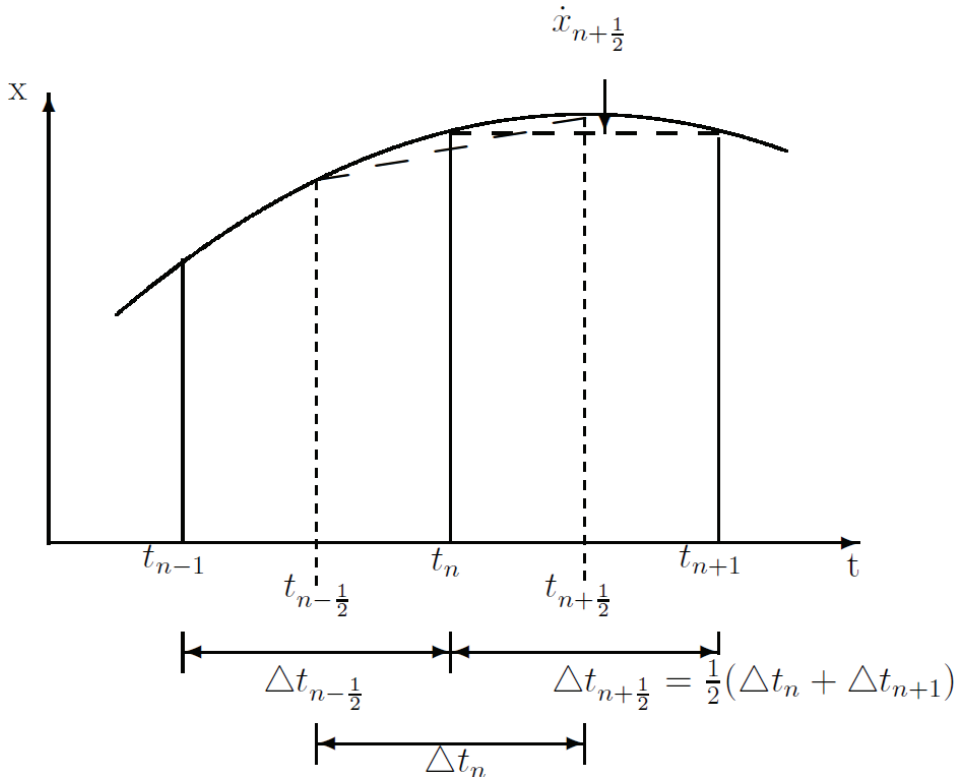

Figure 3.3: Illustration of the Half-Step Central Difference method used in LS-DYNA [19]

At time t_n equation 3.1 will yield

$$\mathbf{M}\ddot{\mathbf{x}}_n + \mathbf{C}\ddot{\mathbf{x}}_n + \mathbf{K}_n\mathbf{x}_n = \mathbf{p}_{n_{ext}} \tag{3.7}$$

In (3.7) the acceleration can be replaced by use of (3.6), but an expression for $\dot{x}_n$ is missing. To come around this LS-DYNA assumes that

$$\mathbf{C}\dot{\mathbf{x}}_{n-\frac{1}{2}} \approx \mathbf{C}\dot{\mathbf{x}}_n$$

Using this x_{n+1} can be found from

$$\frac{1}{\Delta t^2}\mathbf{M}\mathbf{x}_{n+1} = \mathbf{p}_{ext} - \mathbf{K}_n\mathbf{x}_n + \frac{1}{\Delta t^2}\mathbf{M}\left(\mathbf{x}_n + \Delta t\dot{\mathbf{x}}_{n-\frac{1}{2}}\right) - \mathbf{C}\dot{\mathbf{x}}_{n-\frac{1}{2}} \tag{3.8}$$

which only depends on data for time steps $\leq n$, and by use of x_{n+1} the velocity and acceleration in (3.4) and (3.5) can be calculated. Compared with the classical central difference method (see appendix D), only the mass matrix $\mathbf{M}$ is present on the left hand side in (3.8), and since the mass matrix is diagonal, due to lumped masses, $\mathbf{x}_{n+1}$ is easily solved without the problems of requiring a diagonal damping matrix as needed for the classical central difference method.

As mentioned earlier, the explicit integration method is conditionally stable, which puts a requirement on the times step Δt not being larger than some critical $\Delta t_{cr_{int}}$. If the time step exceeds the critical value the calculations *blow up* resulting in an overflow error. In LS-DYNA the critical time step is based on the methods of the classical central difference method for a

linear system, where the critical time step, for a problem with constant time step, is given by

$$\Delta t_{cr\_int} = \frac{2}{\omega_{max}} \qquad \text{,for the undamped case}$$
$$\Delta t_{cr\_int} = \frac{2}{\omega_{max}} \left(\sqrt{1+\xi^2} - \xi \right) \qquad \text{,for the damped case}$$

where ω_{max} is the maximum Eigen-frequency of the system. For varying time step sizes the critical time step is given by

$$\Delta t^2_{cr\_int_n} = \frac{4\delta_i}{\omega_i^2} \quad \text{with} \quad \delta_i = \frac{\Delta t_i}{\Delta t_{i-1}} \quad 0 \leq \delta_i \leq 1 \tag{3.9}$$

Δt_{cr_int} is bounded by the largest natural frequency of the structure, which in turn is bounded by the highest frequency of any individual element in the finite element mesh [15].

In LS-DYNA the time step is also limited by the element size. Instability occurs if any deformation mode in the model has a period that is less than $\pi \times \Delta t$. The time step must therefore divide the period of the highest mode by at least π. In general a single element mode represents the highest mode [19]. In this work only solid elements will be used and for these element types the critical times step Δt_{cr_ele} is given by

$$\Delta t_{cr\_ele} = \frac{L_e}{\left[Q + (Q^2 + c^2)^{1/2} \right]} \quad \text{with} \quad Q = \begin{cases} C_1 c + C_0 L_e \mid \dot{\varepsilon}_{kk} \mid & \text{for } \dot{\varepsilon}_{kk} < 0 \\ 0 & \text{for } \dot{\varepsilon}_{kk} \geq 0 \end{cases} \tag{3.10}$$

where C_0 and C_1 are bulk viscosity coefficients. L_e is the characteristic element length, which for an 8-node solid element, is given by $\upsilon_e / A_{e_{max}}$, with υ_e being the element volume and $A_{e_{max}}$ the area of the largest element side. The final parameter in (3.10) c is the adiabatic sound speed given by

$$c = \left[\frac{4G}{3\rho_0} + \frac{\partial p}{\partial \rho} \Big)_E + \frac{pV^2}{\rho_0} \frac{\partial p}{\partial E} \Big)_\rho \right]^{1/2} \tag{3.11}$$

As seen, the critical time step size based on the elements, depends on the element dimensions, and therefore decreases if elements for example are compressed. It also depends on the material sound speed in the element, which depends on the density and change in pressure in the material. This becomes of significance for example in a purely Eulerian formulation, where the mesh is stationary and the material *flow* through the elements, where the amount and speed of material flow influences the density and pressure of the material, in the element, and therefore the time step to use. Such formulation is used in the blast modelling described later.

There are thus performed two time step controls in LS-DYNA. One based on the element condition, and one based on the integration scheme. The lowest of the critical values controls the time step size Δt. In LS-DYNA Δt is set to $0.9\Delta t_{crit}$ by default. If high-explosives are used it is recommended to lower the value to $0.67\Delta t_{crit}$.

The shown integration procedure also helps to understand the time integration loop shown in figure 3.2 on page 14. After the boundary conditions has been applied, the elements are processed, where expression (3.8) is solved and the new displacements found. From these the strains and strain rates are calculated after which the stresses are determined from the constitutive laws in the material models used. Penalty based contact interfaces (if any are defined) is then checked for nodal penetration, which indicates contact between two surfaces,

and proper contact algorithms are applied. Then the accelerations are updated and used for control of kinematic based contact definitions. After this, velocities and displacements are updated together with the geometry. Finally, the time is updated and checked for termination. If termination is not reached the processes is repeated by stepping one more step forward in time, using the updated time step size.

3.3 Modelling of a Blast Problem

Several methods can be used to model the load developed from the detonation of an explosive material. Using LS-DYNA A at least three different approaches are possible [16]

- Empirical
- Uncoupled
- Fully Coupled

Here focus is put on the first and last approach.

3.3.1 Empirical Approach

Using this approach only the structure exposed to the blast is modelled. The load is applied directly to the structure using idealized pressure-time curves from developed empirical models. A number of different empirical models exist (ConWep, BlastX, SHOCK, TACOM) [20, 21], that can predict the pressure developed from a given blast charge. The empirical models are essentially based on correlation with experimental data and the different models are limited by the extent of the underlying data.

ConWep (Conventional Weapons and Effects Program) is a DOS based computer program used to calculate the effect off conventional weapons [22]. To apply blast loads on structures, equations, developed by Kingery and Bulmash [23], to predict air blast parameters such as reflected pressure P_r and incident pressure P_{so}, from spherical air bursts and from hemispherical surface bursts have been implemented into ConWep. The equations are based on data from explosion tests using charges with weights from 1kg to 400,000kg, where the pressure, arrival time, duration time and other blast parameters were measured. The experimental data have been represented by using curve fitting with high order polynomials, which have been constructed such that they describe the primary blast parameters, described in section 2.1, as function of the scaled distance and thus are capable of covering a large number of blast test set-ups. The ConWep load equations are widely accepted as engineering predictions to determine free-field pressure and loads on structures. The model cannot account for shadowing objects and is not able to account for the effect of a buried mine in terms of localization and particulate effects.

TACOM (Tank Automotive Command), developed by Westine et al. [24] can predict the impulse from a buried mine applied to a plate at a given distance from the mine. The model is based on a series of tests conducted to measure the impulse at various locations above a mine explosion. From the data a model were developed that accounts for the effect of burial depth, charge size, target height, impact angle and soil density. A disadvantage is that the model was developed on the use of small charge sizes and it might be questionable if it is possible to extrapolate the model to be used on larger charge sizes.

BlastX allows the user to choose between two blast load schemes. One, which uses the equations of Kingery and Bulmash, and one, which uses a tabular TNT model based on a series of one dimensional Computational Fluid Dynamics (CFD) calculations. Contrary to ConWep, BlastX is capable of calculating negative pressure and impulse, corresponding to the negative phase of a blast.

SHOCK is a blast load analysis program, which will calculate the impulse and pressure on either all or part of the blasted surface, which can be bounded by 1 to 4 reflecting surfaces, from the incident blast wave and from the waves reflecting off of each adjacent surface [25].

Among the listed empirical models, ConWep is the most recognised. A comparison performed in [21] between ConWep, BlastX and SHOCK found that the ConWep model was in best overall agreement with experimental data.

The ConWep model has been implemented into LS-DYNA by Randers-Perhson and Bannister [26], who have extracted the blast-loading algorithms from ConWep. These have been collected into the ∗LOAD_BLAST (or ∗LOAD_BLAST_ENHANCED) model in LS-DYNA. To account for the angle of incident the following expression is used to calculate the pressure at a point impacted by a peak reflected P_r or peak incident pressure P_{so} with an angle *theta* between the direction of travel of the impacting pressure wave and the surface normal [26]

$$P = P_r \cos^2(\theta) + P_{so}(1 - \cos(\theta))^2 \tag{3.12}$$

The implementation of ConWep into LS-DYNA allows users of LS-DYNA to model blast on a structure using the empirical blast equations constructed by Kingery and Bulmash. This requires only the blast loaded structure to be modelled in a numerical mesh, together with information about the charge size, position of the charge, stand-off distance and definition of the surface area on which the load is to be applied. From these inputs the scaled distance Z is calculated, from which the blast parameters can be found in the blast loading algorithms, which will provide a pressure-time distribution on the target. The upper and lower limit for the scaled distances that can be used in the ∗LOAD_BLAST model is $0.147\text{m/kg}^{-1/3} < \text{Z} < 40$ $\text{m/kg}^{-1/3}$, which is the limit of the scaled distance in the underlying experimental data from the Kingery and Bulmash equations.

The blast curves from Kingery and Bulmash are based on measurements from TNT based charges. The blast parameters in the ∗LOAD_BLAST model in LS-DYNA therefore use TNT as the reference explosive type. If other types of explosives are wanted to be used their mass must be represented in TNT *equivalent weight*. This is done by use of a scalar conversion factor which is multiplied by the weight of the used explosive type to convert it to equivalent TNT weight. The conversion factor can be estimated in several ways. It can be based on the relation between peak pressure values, generated impulse, detonation velocities etc. [27, 28]. In the LS-DYNA user-manual [27] the suggested conversion is based on the detonation velocities

$$M_{eq-\text{TNT}} = M_{explosive} \frac{D^2_{explosive}}{D^2_{\text{TNT}}} \tag{3.13}$$

where $M_{explosive}$ is the mass of the explosive used and $M_{eq-\text{TNT}}$ is the calculated equivalent TNT mass to use in ∗LOAD_BLAST. D is the detonation velocities of the used explosive and TNT, which has the standard value $6930\frac{\text{m}}{\text{s}}$. As discussed in [28]s one explosive type may have several equivalent weight factors depending on which blast parameter of the used explosive that is to be scaled. The conversion factor to achieve the same peak pressure is most likely not the same as the factor to be used for getting the same impulse. The scaling parameter might also

be dependent on the stand-off distance used, such that the parameter used for a specific mass of explosive at for example a stand-off distance of 100mm is different from the scaling factor needed for the same explosive mass at for example 500mm [28]. The scaling factors often found in the literature do normally not state the specific set-up used, when they were determined. Knowing what scale factor to use is thus not simple to determine as it can be set-up specific and also depend on the specific blast parameter against which the comparison is to be made.

The advantage of the empirical approach is that it is computationally very fast since only the target structure is modelled. The disadvantage is that no interaction effects of target and pressure wave can be accounted for. Another disadvantage of the ∗LOAD_BLAST function in LS-DYNA is that it only works for spherical air blasts and hemispherical surface blasts with no reflection from impacted surfaces. This makes the model less suited for modelling blasts in a semi confined space, where the confining walls will prevent out flow and generate reflections of the impacting blast waves and thus build up a quasi-static pressure that will substantially prolong the blast loading.

3.3.2 Fully Coupled Euler Lagrange Approach

Using this approach the entire problem is modelled from the beginning and solved as a whole. The set-up could be similar to that illustrated in figure 3.1, but in contrast to the empirical approach, where only the structure is modelled numerically, the air and explosive charge is now also modelled numerically. When running the model, the detonation is simulated and the explosion generates a pressure wave that expands through the modelled air, and when it reaches the structure an interaction with the pressure wave and the structure will be modelled. The advantage of this approach, compared with the empirical approach, is that reflections and Mach Stem effects can be accounted for. The clear disadvantage is that the approach is significantly more time consuming due to the much more extensive calculations needed and the larger size of the numerical domain.

Modelling of the structural part is done with elements using a Lagrangian formulation, where the mesh moves with the material. The air around the structure, the blast wave and the detonation products are fluids, and are not represented well by a Lagrangian formulation. Instead an ALE element formulation is used for these materials. In LS-DYNA the ALE formulation consists of a Lagrangian time step followed by a *remap* or *advection* step, where the mesh is either restored to its original shape and position, or to a remapped shape controlled by smoothing algorithms or rigid body motion and scaling of the mesh [15, 27]. This procedure is referred to as the *operator split technique* [29]. In the ALE mesh the material *flows* through the elements, meaning that an element can hold more than one material at a time. To account for the interface between the materials in a single element, material interface reconstruction algorithms, using the gradient of the nodal volume fraction field, are used.

To get the pressure in the generated blast wave transferred to the structural part, a Fluid Structure Interaction (FSI) model is used. In LS-DYNA FSI is simulated using a coupling algorithm through the keyword ∗CONSTRAINED_LAGRANGE_IN_SOLID. The FSI couples the fluid to the surface of the deformable structure. The blast pressure in the air can then be transferred to the structure surface, which then reacts to the applied pressure. In LS-DYNA two coupling techniques can be used; Constrained-based and Penalty-based. The constraint-based formulation is an algorithm that alters the velocities of the nodes implicitly and forces them to follow each other. The method attempts to conserve momentum, but not energy. The penalty-based formulation, however, applies nodal forces explicitly by tracking the relative

motion of a given point. The method conserves energy [30]. In the present study the penalty based approach is used. The coupling algorithm ensures that the fluid flows around and not through the structure. Flow through the structure is prevented by the application of a penalty force. As soon as a fluid particle penetrates the surface of the Lagrangian structure, a penalty force is applied to both the fluid particle and the structure node to prevent penetration. The applied force is proportional to the size of the penetration [15]. Penetration of the fluid through the structure is referred to a *leakage*. Leakage is mainly caused by too few *coupling points* and/or a too course Lagrangian mesh. The FSI coupling occurs at structural nodes and at coupling points defined for each Lagrangian surface segment. To prevent leakage similar mesh sizes should be used for the ALE and Lagrange surface mesh. The Lagrange elements should not be larger than the ALE elements. If similar mesh sizes are used 1–3 couplings points should be adequate. Too many coupling points can lead to instability. In addition using too high penalty forces in the coupling algorithm can lead to instability or very small time steps. Mesh refinement is the most effective tool to avoid leakage.

In LS-DYNA the explosive is modelled with the ∗MAT_HIGH_EXPLOSIVE_BURN material model taking input regarding the explosive density, detonation velocity and the Chapman-Jouget pressure. This model controls the detonation of the explosive material. The model gives a fraction F of the explosive material in an element that has detonated. In the initialization phase, a lighting time is computed for each element, initially making up the explosive, by dividing the distance from the detonation point to the centre of the element, with the detonation velocity [31]. The detonation point is controlled with the keyword ∗INITIAL_DETONATION where the detonation point is defined through an xyz coordinate point.

The blast pressure generated from the detonated explosive material is modelled through an Equation Of State (EOS) that relates the energy released from an explosive to the pressure developed. An EOS model that can represent the pressure developed from a detonated charge is therefore appointed to the material representing the explosive. A widely used EOS for explosive materials is the Jones-Wilkins-Lee (JWL) equation [12, 30, 32, 33]

$$P_{\text{EOS}} = A\left(1 - \frac{\omega}{R_1 V}\right)e^{-R_1 V} + B\left(1 - \frac{\omega}{R_2 V}\right)e^{-R_2 V} + \frac{\omega E}{V} \tag{3.14}$$

where P_{EOS} is the calculated blast pressure, E is the *detonation energy per unit volume* and A, B, R_1, R_2 and ω are material constants related to the explosive used. In LS-DYNA the JWL EOS is accessed through the keyword ∗EOS_JWL. To account for the fraction of explosive material that has detonated the calculated pressure from the EOS is multiplied with the fraction number F from the ∗MAT_HIGH_EXPLOSIVE_BURN, such that the actual explosive pressure P_{exp} can be found

$$P_{exp} = F P_{\text{EOS}}((V, E) \tag{3.15}$$

When the detonation has occurred the expansion of the blast wave into the surrounding air has to be modelled. This also requires an EOS to describe the pressure in the air. An often used EOS for this purpose is the ideal gas law (Gamma Law) [12, 30, 33] on the form

$$P = (\gamma - 1)\frac{\rho}{\rho_0}E \tag{3.16}$$

where ρ_0 and ρ are the initial and current densities of air, E is the internal energy per unit reference volume and γ is the ratio of specific heats $\gamma = \frac{c_p}{c_v}$. In LS-DYNA the ideal gas law can be accessed by use of the keyword ∗EOS_LINEAR_ POLYNOMIAL.

3.4 Material Modelling

As presented in the introduction to this report, both monolithic composite panels and sandwich panels will be tested in the established blast test facility. As part of establishing a numerical frame work for modelling the response of such panels, when exposed to a blast load, material models that can represent the type of materials used in the tested panels are needed. LS-DYNA contains a large material model library, which has several models for modelling both laminate and foam materials. In this project focus has been on using the available models in LS-DYNA, as opposed to writing new models. The available laminate and foam models have therefore been screened to find the models that best represent the used materials.

3.4.1 Laminate Models

In LS-DYNA a wide selection of material models already exists for modelling laminated structures. Generally all of these are based on the *Classical Lamination Theory* (CLT) and the main difference between the models is how they handle failure of the composite, where some models use a simple maximum stress/strain based criteria, other use combined stress/strain criteria, and one model uses a damage mechanics approach, where the elastic moduli are gradually reduced until complete damage has developed. Table 3.1 shows the laminate models available in LS-DYNA indicating which element types that the models can be used with, if they can be used to model failure and if strain rate effects can be included in the models.

Because the blast loading on the panels induces stresses in the thickness direction of the panels it was decided to look for models that can be used with solid elements, where it is possible to analyse the effect of the initial stress wave going through the thickness of the panel. Of the remaining models it was decided to use *MAT_ORTHOTROPIC_ELASTIC, which

Table 3.1: Laminate models available in LS-DYNA

LS-DYNA model name	#	Element type[a]	Failure[b]	Rate[c]
*MAT_ORTHOTROPIC_ELASTIC	002	So/Sh	✗	✗
*MAT_COMPOSITE_DAMAGE	022	So/Sh	✓	✗
*MAT_ENHANCED_COMPOSITE_DAMAGE	054/055	Sh	✓	✗
*MAT_LAMINATED_COMPOSITE_FABRIC	058	Sh/T-Sh	✓	✗
*MAT_COMPOSITE_FAILURE_OPTION_MODEL	059	So/Sh	✓	✗
*MAT_COMPOSITE_LAYUP	116	Sh	✗	✗
*MAT_COMPOSITE_MATRIX	117	Sh	✗	✗
*MAT_COMPOSITE_DIRECT	118	Sh	✗	✗
*MAT_RATE_SENSITIVE_COMPOSITE_FABRIC	158	Sh/T-Sh	✓	✓
*MAT_COMPOSITE_MSC	161	So	✓	✓
*MAT_COMPOSITE_DMG_MSC	162	So	✓	✓

[a] Element type that can be used with the material model; So = Solid Elements, Sh = Shell Elements, T-Sh = Thick Shell Elements.
[b] Indication of the model can represent failure.
[c] Indication of the model can include rate effects.

is an orthotropic elastic model, that can for comparisons with tests performed at low blast charges where no or very limited damage has developed in the tested panels. For modelling test cases where failure develop in the panels, it was decided to use *MAT_COMPOSITE_DMG_MSC. The primary reason for choosing this model is the possibility to include strain rate effects, a possibility which none of the other models usable with solid elements offer, and because it can model failure. Secondly *MAT_COMPOSITE_DMG_MSC is based on damage mechanics where progressive failure in the different material directions can be modelled as opposed to the other models which model failure as an instantaneous event, where the stress is immediately reduced to zero.

MAT_ORTHOTROPIC_ELASTIC

*MAT_ORTHOTROPIC_ELASTIC models an orthotropic material by taking the elastic moduli, shear moduli and the Poison ratios defining an orthotropic material as input. For this model the stress is based on the second Piola-Kirchhiff stress S to the Green-St. Venant strain E by [15]

$$S = T^t C T E \tag{3.17}$$

where T is a transformation matrix and C the compliance matrix

$$C = \begin{bmatrix} \frac{1}{E_{11}} & -\frac{\nu_{21}}{E_{22}} & -\frac{\nu_{31}}{E_{33}} & & & \\ -\frac{\nu_{12}}{E_{11}} & \frac{1}{E_{22}} & -\frac{\nu_{32}}{E_{33}} & & & \\ -\frac{\nu_{13}}{E_{11}} & -\frac{\nu_{23}}{E_{22}} & \frac{1}{E_{33}} & & & \\ & & & \frac{1}{G_{12}} & & \\ & & & & \frac{1}{G_{23}} & \\ & & & & & \frac{1}{G_{31}} \end{bmatrix}$$

After updating the stress, S is transformed to the Cauchy stress before the stress is stored in the output data files.

MAT_ORTHOTROPIC_DMG_MSC

*MAT_COMPOSITE_DMG_MSC has been developed by Material Science Corporation (MSC) and requires a special license to run in LS-DYNA. The model is an elastic model and can be used to predict the progressive failure of composite materials [34]. Failure models have been established such that they can simulate fibre failure, matrix damage and delamination behaviour under opening, closure and sliding of failure surfaces. The failure criterion uses stress and elastic material components to predict failure. The model can be set either to model a unidirectional layup or a layup made from woven fabrics. Separate failure criteria exist for each of these layup types. Table 3.2 shows the material input needed for this model, together with the parameters for controlling rate and damage effects. In [34] a description of the material test to obtain the material parameters can be found.

The failure criteria in *MAT_COMPOSITE_DMG_MSC have been based on the 3-dimensional failure criteria for unidirectional fibre composites established by Hashin [35]. There, a piecewise smooth failure surface is developed, capable of representing different failure criteria for fibre and matrix failure in tension or compression. In *MAT_ORTHOTROPIC_DMG_MSC the failure criteria from [35] are generalized to also include the effect of highly constrained pressure on

Table 3.2: Material parameter input for *MAT_COMPOSITE_DMG_MSC

Variable	Description
Material properties	
RO	Mass density
$E_{a,b,c}$	Young's modulus for the longitudinal, transverse and through thickness direction
$PR_{ba,ca,cb}$	Poisson's ratio
$G_{ab,bc,ca}$	Shear moduli
$S_{aC,aT}$	Longitudinal tensile and compressive strength
$S_{bT,bC}$	Transverse tensile and compressive strength
S_{cT}	Through thickness tensile strength
S_{fc}	Through thickness crush strength
S_{fc}	Fibre mode shear strength
S_{ab^*,bc^*,ca^*}	Fibre mode shear strength
Rate parameters	
$CRATE_1$	Coefficient C_1 for strain rate dependent strength properties
$CRATE_2$	Coefficient C_2 for strain rate dependent axial moduli
$CRATE_3$	Coefficient C_3 for strain rate dependent shear moduli
$CRATE_4$	Coefficient C_4 for strain rate dependent through thickness moduli
Damage parameters	
AM_1	Coefficient m_1 for strain softening property for fibre damage in direction a
AM_2	Coefficient m_2 for strain softening property for transverse compressive matrix failure mode in direction b
AM_3	Coefficient m_3 for strain softening property for fibre crush and punch shear damage
AM_4	Coefficient m_4 for strain softening property for matrix failure and delamination damage

composite failure [34]. For the two layup types that the model can represent it divides the failure types into the following groups

- Tension-Shear fibre mode
- Compression fibre mode
- Crush mode
- Transverse compressive matrix mode
- Perpendicular matrix mode
- Parallel matrix mode (Delamination)

For each group a specific failure criterion is used to predict failure. The failure criteria are of the form shown in (3.18), which is the expression for the *tension-shear fibre mode* failure

$$\left(\frac{\langle \sigma_a \rangle}{S_{At}}\right)^2 + \left(\frac{\tau_{ab}^2 + \tau_{ca}^2}{S_{fs}^2}\right) - r_1^2 = 0 \tag{3.18}$$

where $\langle\ \rangle$ are Macaulay brackets and r_1 is the damage threshold value for these failure criteria, which have the initial value of 1 and are updated as damage accumulates. The damage threshold values thus provide an initial bound for the elastic region of the material. Each failure criterion holds a damage threshold value r_j that accounts for the amount of damage developed for that specific failure criteria. In appendix C the expressions for the remaining failure criteria can be found.

In material model ∗MAT_ORTHOTROPIC_DMG_MSC failure is expressed by a degradation of the elastic moduli parameters, an approach that is in contrast to failure formulation in all other laminate models in LS-DYNA. To enable this the method established by Matzenmiller [36] has been adopted, where a damage parameter ϖ is introduced and incorporated in to the compliance matrix

$$S = \begin{bmatrix} \frac{1}{(1-\varpi_1)E_a} & -\frac{\nu_{ba}}{E_b} & -\frac{\nu_{ca}}{E_c} & & & \\ -\frac{\nu_{ab}}{E_a} & \frac{1}{(1-\varpi_2)E_b} & -\frac{\nu_{cb}}{E_c} & & & \\ -\frac{\nu_{ac}}{E_a} & -\frac{\nu_{bc}}{E_b} & \frac{1}{(1-\varpi_3)E_c} & & & \\ & & & \frac{1}{(1-\varpi_4)G_{ab}} & & \\ & & & & \frac{1}{(1-\varpi_5)G_{bc}} & \\ & & & & & \frac{1}{(1-\varpi_6)G_{ca}} \end{bmatrix}$$

The damage variables ϖ are related to the damage threshold values r_j through [34]

$$\varpi_i = 1 - \exp\left(\frac{1}{m_j}\left(1 - r_j^{m_j}\right)\right), \rightarrow r_j \geq 1 \tag{3.19}$$

where j refers to a specific failure mode and m_j refers to the softening parameters for that specific damage mode. Initially the damage variable is zero since r_j is initially 1. When the damage thresholds exceed 1, damage starts to develop and the damage variables attain a value larger than one. The increased value of the damage threshold r_j now provides a new bound for

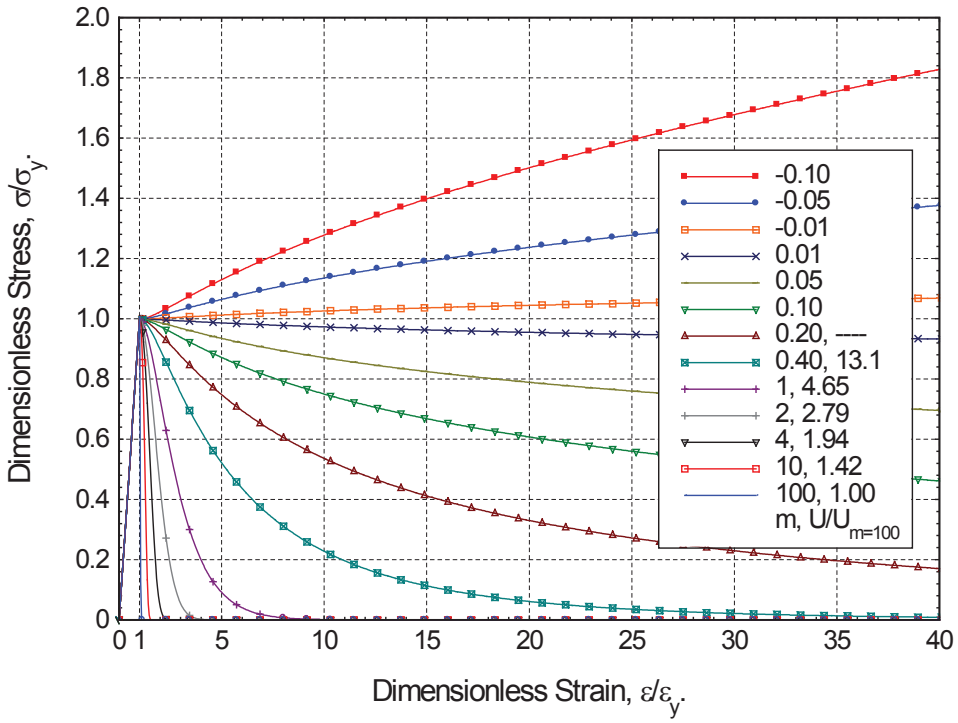

Figure 3.4: Effect of the softening parameters on the stress-strain response of a laminate modelled with ∗MAT_ORTHOTROPIC_DMG_MSC [34]

the elastic region inside which the linear elastic stress-strain response is governed by the now reduced compliance matrix. The damage variables grow from $0 \ldots 1$ but to avoid instabilities, that would arise by setting $\varpi = 0$, a limit is set for the damage parameters. This is done in the input deck through the parameter OMGMX. The effect of the softening parameters is illustrated in figure 3.4, where it can be seen that values less than 1 lead to a hardening behaviour of the laminate at the initiation of failure, whereas values greater than 1 lead to a softening effect. To have a brittle fracture response values larger than 10 should be used.

In the model a coupling is made between specific failure modes and the reduction of the elastic moduli, which is illustrated in figure 3.5. The coupling is made through a coupling matrix q_{ij} which, for the illustrated case, will have $i = 1, \ldots, 6; j = 1, \ldots, 6$. To calculate the combined effect of the failure modes on the damage parameters, ϖ_i, q_{ij} is multiplied onto equation (3.19). The coupling for the model, when set to model a plain weave laminate, can be found in appendix C.2.

Rate effects on the strength and moduli parameters are included in the model through a logarithmic function of the form

$$\frac{X_{rt}}{X_0} = 1 + C_n \ln\left(\frac{\dot{\bar{\varepsilon}}}{\dot{\bar{\varepsilon}}_0}\right) \tag{3.20}$$

where X_{rt} is the property of the parameter in question, at an average strain rate of $\dot{\bar{\varepsilon}}$, and X_0 is the parameter property at a reference strain rate $\dot{\bar{\varepsilon}}_0$, which is internally set to 1s^{-1}. This has the effect that the time unit in ∗MAT_ORTHOTROPIC_DMG_MSC has to be in seconds, which is important to note before choosing a unit set for the model. The rate sensitivity C_n is

UD DAMAGE TYPES		FIBER DAMAGE MODES			MATRIX DAMAGE MODES		
UD DAMAGE MODES		MODE 1u j = 1	MODE 2u j = 2	MODE 3u j = 3	MODE 4u j = 4	MODE 5u j = 5	MODE 6u j = 6
MODULI	q_{ij}^{U}						
E_a		1	1	1	0	0	0
E_b		0	0	1	1	1	0
E_c		0	0	1	0	0	1
G_{ab}		1	1	1	1	1	0
G_{bc}		0	0	1	1	1	1
G_{ca}		1	1	1	0	0	1

Figure 3.5: Illustration of which failure modes that affects the reduction of a specific elastic moduli for the version of the material model, modelling laminates with a unidirectional fibre layup [34]

controlled through the CRATE_n parameters in table 3.2. As can be seen from the table, the same rate parameter is used to describe the rate sensitivity for all the strength parameters, which might not correspond to what is seen in material testing. For the moduli the in-plane, through thickness and shear moduli have separate parameters for the rate sensitivity.

The relevance of the model can be understood by studying the correlation between model predictions and experimental data as done in [37]. Here it was seen that the logarithmic form of the model was effective in predicting the strain rate dependency observed for the strength values of the tested composite material. In addition the experimental observations in [37] also showed that the stiffness parameters did not depend on the applied strain rate. Since the model uses different rate parameters, CRATE_n, for modelling the rate effect of strength and stiffness parameters this effect can also be properly described by the model. By setting the CRATE_n related to the stiffness parameters to 0 and setting the rate parameters related to the strength parameters to the values identified in [37] only the strength parameters will depend on the applied strain rate. The opportunity to individually control the rate effect is thus a powerful property of the present material model. Regarding the rate dependency, the model only accounts for rate effects for strain rates larger than the reference strain rate. This means that the X_0 value in (3.20) is the reference value used for all strain rates $\dot{\bar{\varepsilon}}_0 \leq 1\text{s}^{-1}$, and is the value defined as the initial E and S property in the model input deck. The material described by the material model is thus one where rate effects does not have an impact for strain rates $\dot{\bar{\varepsilon}}_0 \leq 1\text{s}^{-1}$, a behaviour which is supported by observations made during the material tests performed in [37].

3.4.2 Foam Models

In LS-DYNA a foam material is typically characterized as a material that can support large compressive strains with no or limited Poisson effects. In figure 6.1 on page 68 a typical stress-strain curve for a rigid foam is shown. Such stress strain curves are not easy to represent by a single constitutive law, which is why for most of the foam models in LS-DYNA the stress-strain relations are described by in-putted stress-strain curves obtained from material testing.

From the material testing performed on the foams, see chapter 6, it was identified that the foam types were transverse-isotropic; that rate effects had a significant impact on the stress-strain response; and that the compaction of the foam took place with very limited Poisson effects. When the load was removed after compression the foam retained its compressed shape, which is characteristic of a crushable foam, in contrast to elastic foams which revert to their original shape after load removal, as seen for example for foams used in cushions. Based on these observations the foam model selected from the LS-DYNA material library should be able to describe a foam which:

- is crushable
- is transverse isotropic
- has no Poisson effects during crushing
- includes strain rate effects

Table 3.3 shows the foam models in LS-DYNA that are able to represent a crushable foam. Of these only two can represent a non-isotropic foam. From these, *MAT_HONEYCOMB was chosen to represent the foam.

Table 3.3: Foam models available in LS-DYNA that can be used to model a crushable foam

Model name	#	Formulation[a]	Poisson	Rate[b]
*MAT_HONEYCOMB	026	Ortho	✗	✓
*MAT_CLOSED_CELL_FOAM	053	Iso	✓[†]	✗
*MAT_CRUSHABLE_FOAM	063	Iso	✓	✗
*MAT_TRANSVERSELY_ISOTROPIC_CRUSHABLE_FOAM	142	T-Iso	✗	✓
*MAT_MODIFIED_CRUSHABLE_FOAM	163	Iso	✗	✓

[a] Formulation of the constitutive law of the material; Iso = Isotropic, T-Iso = Transverse Isotropic; Ortho = Orthotropic
[b] Indication of the model can include rate effects.
[†] The Poisson effect in this model is due to air pressure in the cell structure which is accounted for in this model

MAT_HONEYCOMB

*MAT_HONEYCOMB can be used for modelling honeycomb or foam materials, where a nonlinear elasto-plastic behaviour can be defined separately for the normal and shear stresses, with each material direction considered fully uncoupled [31]. Before densification, the material behaviour is orthotropic with *no* Poisson effects. At densification, the material becomes elastic-perfectly

Table 3.4: Material parameter input for *MAT_HONEYCOMB

Variable[a]	Description
RO	Mass density
E	Young's modulus for compacted honeycomb material
PR	Poisson's ratio for compacted honeycomb material
SIGY	Yield stress for fully compacted honeycomb
VF	Relative volume at which the honeycomb is fully compacted
LC_{kl}[i]	Load curve for $\sigma - nm$ versus volumetric strain
LC_{sr}	Load curve for strain-rate effects defining the scale factor versus strain rate
E_{kkU}[ii]	Elastic modulus E_{nn} in uncompressed condition
G_{klU}[ii]	Shear modulus E_{nm} in uncompressed condition

[a] Name of variable used in LS-DYNA
[i] A stress strain curve is inputted for each material direction. $n, m = 1, \ldots, 3$
[ii] $n, m = 1, \ldots, 3$ $n \neq m$

plastic and Poisson effects are now included. In the input deck for the model, material parameters for the foam in uncompressed and compressed condition therefore have to be defined. Table3.4 shows the material parameter input needed for *MAT_HONEYCOMB.

In [15, 31] a description of the model can be found, which will be recapitulated in the following. Before densification, normal and shear stress in the elastic region is based on expressions according to

$$\begin{aligned} \sigma_{kk}^{n+1^{trial}} &= \sigma_{kk}^{n} + E_{kk}\Delta\varepsilon_{kk} \\ \sigma_{kl}^{n+1^{trial}} &= \sigma_{kl}^{n} + 2G_{kl}\Delta\varepsilon_{kl} \end{aligned} \tag{3.21}$$

for $k, l = 1, \ldots, 3$ and $k \neq l$. The elastic and shear moduli in (3.21) varies linearly with the relative volume of the material from the initial uncompressed value to the fully compacted value, and is calculated from expressions on the following form

$$\begin{aligned} E_{kk} &= E_{kkU} + \beta\left(E - E_{kkU}\right) \\ G_{kl} &= G_{klU} + \beta\left(G - G_{klU}\right) \end{aligned} \tag{3.22}$$

where $G = \frac{E}{2(1+\nu)}$ is the shear modulus of the fully densified material and β is given by

$$\beta = max\left[min\left(\frac{1-V}{1-VF}, 1\right), 0\right] \tag{3.23}$$

where V is the current relative volume of the material, which initially is 1. During unloading and reloading, the stress path will be based on the update moduli values. As indicated in (3.21), the calculated stresses are *trial* stresses because a check has to be made to determine if the calculated elastic stress exceeds the permissible stress determined by the in-putted load curves [31]

$$|\sigma^{n+1^{trial}}| > \lambda\sigma^{curve}(V) \tag{3.24}$$

then

$$\sigma^{n+1} = \sigma^{curve}(V)\frac{\lambda\sigma^{n+1^{trial}}}{|\lambda\sigma^{n+1^{trial}}|} \tag{3.25}$$

If the trial stress is found to exceed the value of the load curve, then the stress is set equal to the value in the load curve, as expressed in (3.25), and the correct sign is given to the stress since the load curve data all are positive. To account for strain rate, the stress is scaled by the parameter λ, which is a value taken from the $\mathrm{LC_{sr}}$ load curve, and if the curve is not defined then λ is set to unity.

After passage of the defined compaction strain, the material is described as elastic-perfectly plastic with deviatoric stress updates according to

$$s_{kl}^{n+1\ trial} = s_{kl}^{n} + 2G\Delta\varepsilon_{kl}^{dev\ \frac{n+1}{2}} \tag{3.26}$$

Again the calculated stress in (3.26) is a trial stress in the sense that before the stress can be updated, a comparison with the defined yield stress SIGY has to be made, and if the stress is found to exceed the yield stress, the trial stress is scaled back to the yield surface. When the deviatoric stress has been updated the Cauchy stress is finally obtained by

$$\sigma_{kl}^{n+1} = s_{kl}\ n + 1 - p^{n+1}\delta_{kl} \tag{3.27}$$

where

$$p^{n+1} = p^{n} - K\Delta\varepsilon_{kk}^{n+1/2}, \quad and \quad K = \frac{E}{3\,(1-2\nu)}$$

As can been seen from the review, the model always estimates trial stresses based on the updated elastic moduli. If the compaction strain has not been reached, the stresses are then checked for permissibility by comparing with load curve values, otherwise they are checked against the defined yield stress. At each check, a lookup in the in-putted load curve is performed, which is the primary limiting factor with respect to speed efficiency of this model.

Chapter 4

Blast Test Facility

One of the main tasks of this Ph.D.project has been to establish and verify an experimental facility that makes it possible to perform small-scale blast tests on designed test panels, and monitor the response of the tested panels using a high-speed imaging system. Using DIC software on the recorded images, the displacement of the tested panel and surface strains can be evaluated making an analysis of the panel response possible.

Due to the hazards involved when testing using high explosive, the proving ground could not be established on the university campus, but was instead build on a restricted military area named Pionergaarden, close to the university. Currently Pionergaarden houses the Danish EOD (Explosive Ordnance Disposal) company, but through time it has served different purposes. The main buildings on the site date back to the late 19th century where the area served as a farm. During the Second World War, the ground was expropriated by the German occupation and served as a radar installation, and during the Cold War an MM-23 Hawk surface-to-air missile system was deployed there to defend Copenhagen against low flying fighter air-planes. These installations were taken down in 2001.

The construction of the blast test facility began before the initiation of this project. Here the foundation for the blast site was laid, but the established set-up only allowed for non-monitored blast test to be performed, meaning that only post-test inspection of the tested specimen could give any information on the panel performance. This initial work was continued in this project. This involved first and foremost incorporating the high speed imaging system in the test set-up,

Figure 4.1: Pionergaarden through history

(a) (b)

Figure 4.2: Location of the blast test facility on Pionergaarden, marked by the red circle in (a), and the layout of the designed test site shown in (b)

such that monitored tests could be performed, but it also involved a redesign of the whole test set-up as the original set-up proved to be unfit for providing usable data during a blast test.

4.1 Blast Test Setup

The blast test facility is located in one of the old launch sites for the HAWK missile system as indicated on figure 4.2a. The set-up consists of two 20ft containers, positioned as shown in figure 4.2b, where the container marked *Blast Container* holds the actual test set-up and the other container serves as an office, workshop and shelter during testing. Around the blast container and at the side of the shelter container facing the blast container, ground protection mats have been placed to prevent fragments from escaping the test site and eventually causing fatal injury.

The focal point of the experimental facility is the set-up inside the blast container, and the main components are shown in figure 4.2b. The set-up consists of a high-speed imaging system, coupled with 3D-DIC software (ARAMIS from GOM); a blast box where the test panels are fixed; and a 10MHz data acquisition system for transient data recordings.

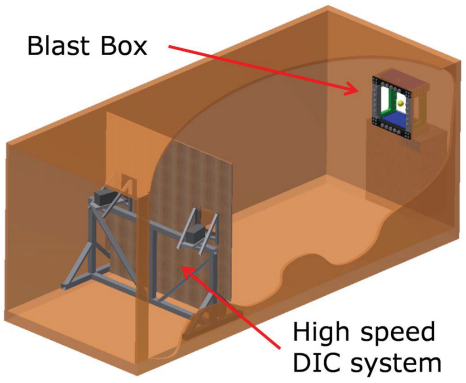

Figure 4.3: Setup inside the blast test container

4.1.1 The Blast Box

The blast box is positioned outside the container, in such a way that the test panel, mounted in the blast box, protrudes through a hole in the container wall to allow the camera system to monitor the panel during a test. The placement of the blast box prevents fire and smoke from entering the space in front of the cameras, such that a clear view of the test panel can be maintained during the entire test. Figure 4.4a and (b) show how the blast box looks from outside and inside the container in the situation where a panel has been mounted in the box ready to be tested.

The blast box consists of a box structure, constructed in ordinary construction steel, and a frame made from Impax Supreme steel from Uddeholm. The test panels are mounted between the box and the frame, where M30 10.9 bolts are used to mount the frame to the box through pre-fabricated holes in the test panels. The blast box is designed to perform tests on 700×700mm square panels with the central 500×500mm area exposed to the blast loading. The remaining area of the panel is clamped between the frame and the box to hold the test plate along all sides. The surfaces on the box and frame, pressing against the panel, have been milled into a pyramid shaped pattern to obtain a better grip in the clamped area of the test panels. As shown in figure4.4c the blast box is constructed of several steel parts that can be put together in different combinations such that tests can be performed under different venting conditions, mimicking for example the venting conditions below a vehicle or in a closed compartment. Some of the possible configurations are shown in figure 4.5a to (c) In all configurations, except the one in figure 4.5c the SOD can be changed from 0 up to 300mm which corresponds to the depth of the blast box. For the *surface explosion configuration*, figure 4.5c, the SOD is adjusted by distance plates placed between the bottom and the explosive charge, which currently allows for a minimum SOD of 100mm. Due to local restrictions the maximum charge size that can be used is 500g TNT (Trinitrotoluene).

The presented blast box is a redesign of one that was designed before the initiation of this project. Through a series of initial blast tests, the previous design was found to be inadequate for use in tests, primarily because the original design proved too weak for the planned tests, but also because the frame structure was poorly designed and the clamping area was not able to hold the panels in position. This lead to a redesign of the original blast box into the design

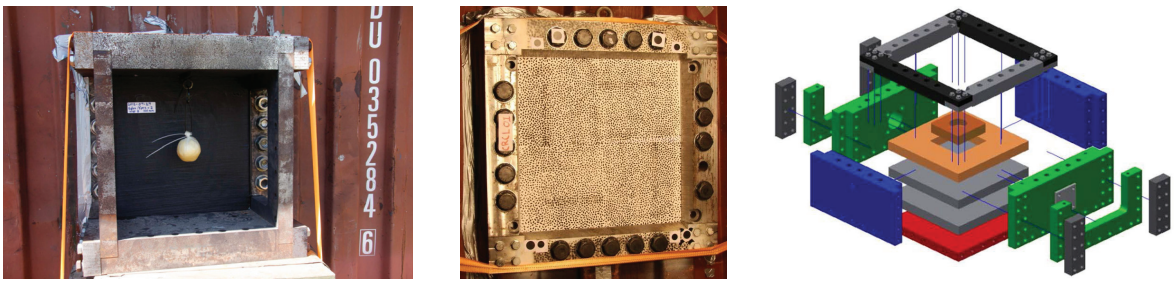

(a) (b) (c)

Figure 4.4: Illustrations of the blast box used for blast testing where; (a) shows the blast box from outside the container, (b) shows the blast box from inside the container, and (c) shows a model of the blast box illustrating the different parts making up the box

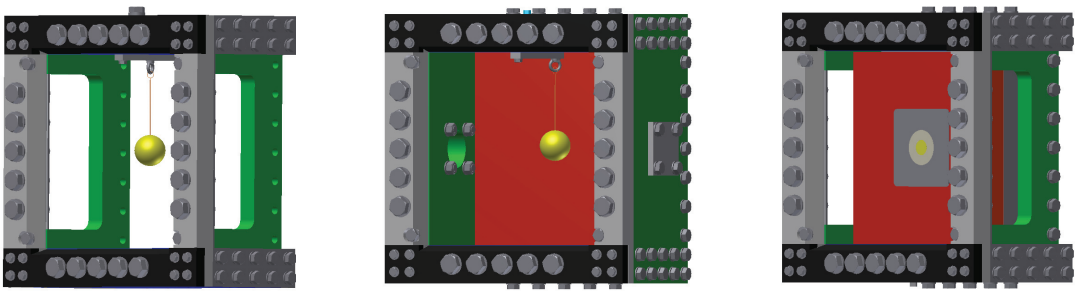

(a) (b) (c)

Figure 4.5: Examples of some of the different assembly configurations for the blast box where; (a) shows a configuration mimicking a free air blast set-up, (b) shows an example of a set-up imitating a blast in a closed environment, and (c) shows a configuration that simulates a surface explosion

presented here. The challenges with the original blast box and the changes made are described in appendix A.

Before a test the explosive is positioned in the desired location relative to the test panel. The explosive is formed to the wanted shape by hand. It is then wrapped in a plastic bag which is closed using a plastic cable tie, which also functions as an attachment point for cord, and attached to an adjustable hook at the top of the blast box. The vertical position of the explosive charge can then be adjusted by controlling the length of the cord and the horizontal distance to the panel is adjusted by moving the hook to the desired position. In all the presented tests the charge was positioned vertically opposite the centre point of the test panels. The horizontal distance is stated for the respective tests. In all tests spherical shaped charges were used.

4.1.2 High Speed Imaging System

To monitor and analyse the test panel deformation a high speed camera system in combination with DIC software is used. The use of high-speed imaging systems combined with DIC for blast loading experiments has proven to be a powerful tool for monitoring blast tests [38–41]. To be able to monitor the deflection of the tested panels, a stereo camera set-up is used with a relative camera angle of 25° as illustrated in figure 4.6 Two Photron APX-RS cameras are used

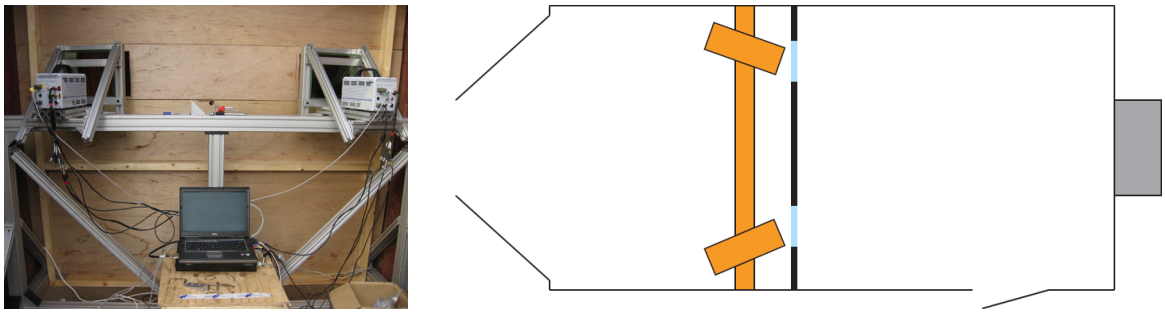

Figure 4.6: Camera set-up in blast container

Table 4.1: Photron APX-RS camera specifications

Full Resolution	1024 × 1024px (width × height)
Maximum frame rate	250.000fps
Maximum frame rate at full resolution	3000fps
Minimum shutter time	1µs
Sensor type	10 bit CMOS, grey scale
Pixel size	17µm
Physical sensor size	17.4 × 17.4mm

in a master/slave configuration. Table 4.1 shows data for these camera types. The cameras are positioned on a constructed aluminium rack where the two cameras are fixed to adjustable support plates. The position and angle of the support plates can be changed to achieve the desired relative camera position, and the distance from the cameras to the measuring target can be changed by moving the aluminium rack back and forth. Depending on the desired frame rate and resolution the required FOV (Field Of View) can thus be obtained by adjusting these physical parameters.

Speckle Pattern

The speckle pattern needed to perform the image correlation is applied by spraying black paint through small holes in a designed spray stencil positioned on top of test panel. In all test cases a dull white paint was first applied on the surface of the test panel to create a good contrast for the black speckles. The paint used for the speckles is standard spray can paint bought in a local DIY-retailer. The size of the speckles were designed in accordance with the guidelines given in [42], stating that the optimal size of the speckles is between 3 × 3 to 6 × 6px.

DIC Software

To perform the image correlation the software ARAMIS from the German company GOM is used. The software can work with cameras specifically designed for the GOM-systems but can also work with third-party cameras, as is the case here. The software provides a simple graphical user interface for both calibrating the system and to analyse the recorded test images. The calibration is performed by following a built-in calibration procedure in the ARAMIS software. To perform the calibration, a calibration cross, designed for a one megapixel system was acquired. The cross, which is shown in figure 4.7, is equipped with both coded and non-coded reference scale bars, which are recognized by the software during the calibration procedure. To perform a calibration of the system, 24 images of the cross in various positions are needed. The calibration process produces a number of parameters that provide information regarding the quality of the calibration. Of these parameters the *Calibration Deviation* is the most important. The ARAMIS manual [43] states that this parameter should be below 0.04, before the calibration can be accepted as valid. For all calibrations made in connection with the performed blast tests the calibration deviations were generally around 0.03. Ideally, the focus point of the cameras should be adjusted to the surface of the target to be measured. To get the best possible calibration the calibration cross should be positioned in the focus area. In the designed test set-up, it is not possible to position the calibration cross at the plane of the target because the blast box would need to be moved at each calibration process. The calibration cross is instead positioned

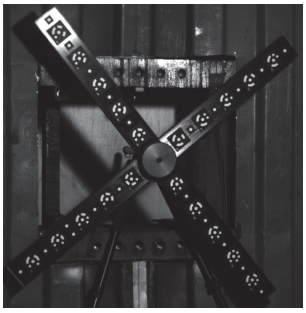

Figure 4.7: Calibration cross used in the calibration procedure of the cameras

a small distance in front of the target surface, as can be seen in figure 4.7, and focus is made to this position. This still results in a calibration of the system that can be used to measure the blast response of the test panels, because the process calibrates a volume around the calibration cross, which, for the present set-up, is approximately $1000 \times 1000 \times 1000$mm. The calibrated volume will thus enclose the test panel making the measurements possible.

Reference Markers

In the current test set-up the blast box is not secured to the support it rests on, making it possible to move the blast box during a test. If the blast box moves forward the movement will be superposed the movement of the panels and thus the movement that the DIC software calculates will be a combination of these two movements. To be able to track the box movement, black circular markers on white background are placed on the upper and lower part of the frame, see figure 4.8. These markers can be identified in ARAMIS as *reference markers* and can be used to make movement corrections of a measured area with respect to the position of these markers. This makes it possible to withdraw any rigid body movement of the blast box from the measured displacement, and then obtain the real panel deflection. For the movement correction to work ARAMIS needs to identify a minimum of 3 reference markers throughout the entire test

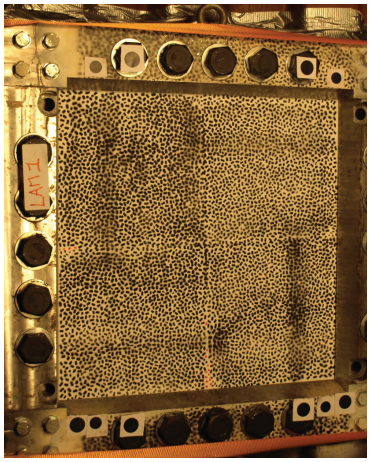

Figure 4.8: Illustration of reference markers placed on the blast box frame, used to keep track of the blast box movement during testing

and at least two of these markers should be on opposite frame parts. From these markers a reference plane is created and used to make the movement correction against. As can be seen from figure 4.8, more than 3 markers are put on the frame. This is because ARAMIS can lose track of individual reference markers during the test, for example due to dust or smoke covering some of the reference markers. Using more than 3 markers thus increases the probability of ending with a minimum of 3 markers.

Light

Because of the high frame rate used in the tests, artificial light is needed to illuminate the specimen such that the cameras can catch enough details on the test panel surface making it possible for ARAMIS to perform the image correlation without failure. Therefore a rack that holds nine 400W work lamps was built, as shown in figure 4.9. These types of lamps develop a great deal of heat when in use. The distance from the lamps to the test panels is approximately 2m, which reduces the thermal impact on the test panels. During test set-up and calibration, only one lamp is turned on. All nine lamps are only turned on immediately before the test is carried out to further minimize any heat effect. Since the lamps are turned away from the cameras, the cameras are not affected by the thermal radiation from the lamps, and the lamps therefore do not affect the calibration of the cameras.

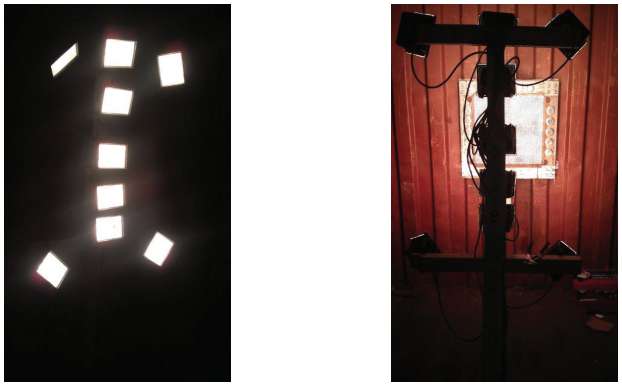

(a) Front **(b)** Back

Figure 4.9: Spot lights used to generate the necessary amount of illumination for the DIC procedure to work properly

4.1.3 Protective Measures

In the case of a through thickness rupture of a panel during a test dust, fire and smoke will enter the area inside the container. In addition, fragments from the panel will be spread out and due to the high acceleration, caused by the explosive reaction, these fragments will have very high velocities. Even though the fragments weigh very little, their high velocity means that they can cause significant damage to any equipment that they might impact with, which could be catastrophic if they hit the high-speed cameras. To reduce the risk of damaging the equipment, 55mm panzer glass positioned vertically in front of the cameras, as shown in figure 4.10, to prevent a fragment directly hitting them. In addition, a wooden covering is set-up to separate the area with all the electronic equipment (cameras, computer etc.), from the area where the

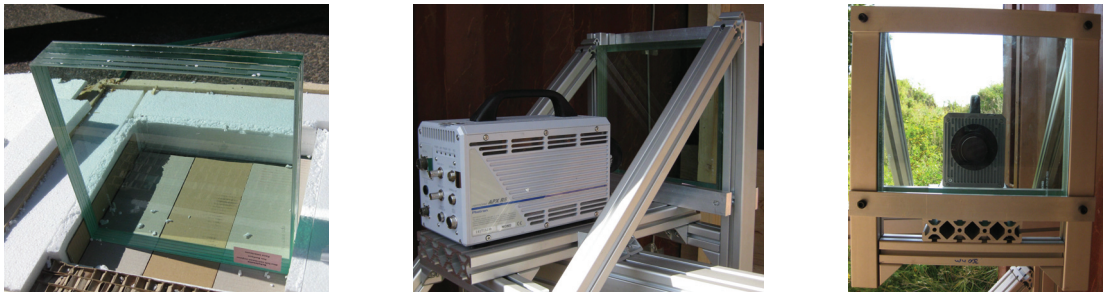

(a) (b) (c)

Figure 4.10: Panzer glass positioned in front of the high speed cameras to protect them from fragments in case of a hole is blown through the tested panel

test panel is located and, in case of a rupture, where all dust and fragments will be spread. The main purpose of the wooden covering is to protect the electronic equipment by reducing the amount of dust and fragments entering the area where it is located.

4.1.4 Camera Settings Used in the Blast Tests

The settings for the cameras and DIC software for all tests are shown in table 4.2;

Table 4.2: Camera and software settings during blast tests

Camera settings	
Resolution	512 × 512px (width × height)
Frame rate	10.000fps
Shutter time	1/frame rate
ARAMIS settings	
Facet size	15 × 15px
Step size	13 × 13px
Computation size[a]	3

[a] Number of facets along the edges of the square field used by ARAMIS to calculate the strain in the centre facet. The minimum computation size is 3. For further details see [43]

4.2 Blast Test Procedure

Preparing and carrying out a blast test in the established blast test facility includes a number of steps that have to be performed for each test. Figure 4.11 illustrates the steps that a single test includes, divided into pre- and post-test activities. After setting up the equipment the calibration is performed as described in section 4.1. Before each test a *Noise Test* is performed. This entails taking a small image series of the stationary plate; performing DIC analysis on it with ARAMIS; and then evaluating the strains and displacements. This test is performed for mainly two reasons; (i) to check that the speckle pattern on the panels is usable for

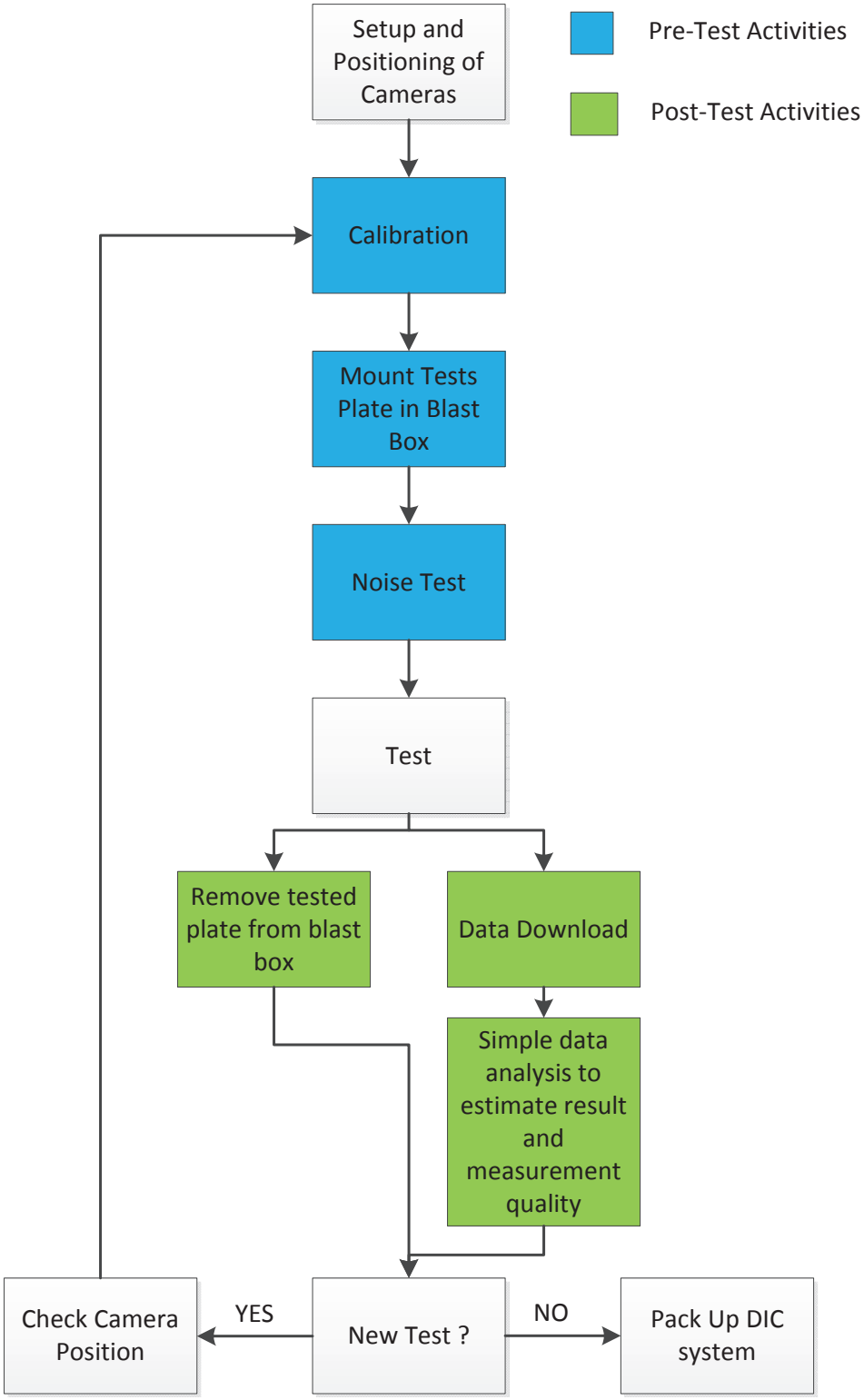

Figure 4.11: The steps involved in setting up and carrying out a blast test

DIC analysis, and (ii) to estimate the minimum level of displacement and strain that can be distinguished from the background noise. If the noise test is satisfactory the test panel is mounted in the blast box and the test performed, after which the post-test steps are carried out. During the noise test, it is important to verify that ARAMIS can identify the attached reference markers, as failure to do so means that movement correction for the blast box movement will not be possible. Figure 4.12 shows a panel mounted in the blast box, ready for testing. Along the edges of the blast box, gaffer tape has been used to seal off any openings to reduce the amount of dust and smoke that can enter the inside of the container due to the explosion. To reduce the movement of the blast box during the test, retaining straps has been stretched out along the top and bottom of the blast box frame.

One test takes roughly two hours to set up, execute and dismantle, and of this, the time used to record the actual panel response takes up less than 1‰. Because of the vibrations created from the detonation of the explosive the calibration of the cameras is lost during test. This happens even with the smallest explosive charges used (25g) and means that the common focus point of the cameras has to be re-checked and the system recalibrated after each test.

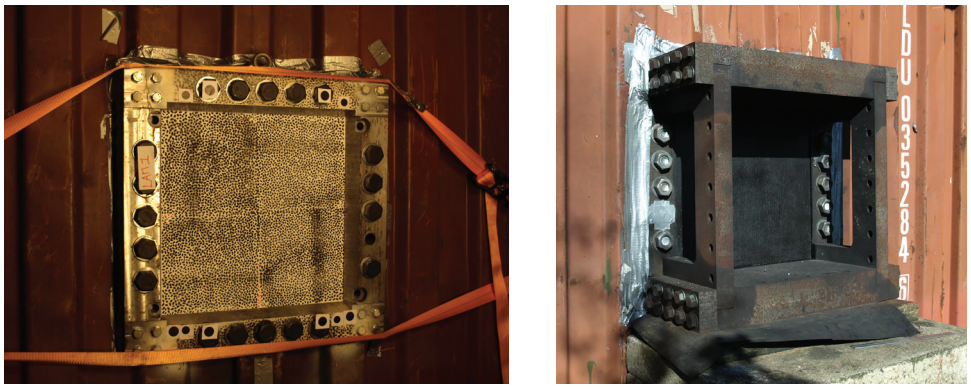

(a) **(b)**

Figure 4.12: Sealing of the openings around the edges of the blast box by use of gaffer tape, to minimize the amount of fire and smoke entering the area in front of the test panel which can disturb the DIC analysis

Chapter 5

Blast Testing

This chapter presents the results of the performed blast tests and the conclusions that can be drawn from them. Both monolithic laminates and sandwich panels of different configurations were tested under different blast conditions such that their performance over a broad spectrum could be evaluated. The blast tests were carried out at the blast test facility described in chapter 4. All tests were monitored by the calibrated high-speed camera system such that DIC analysis could be performed on the recorded images of the tested panels.

One of the purposes of the test was to validate if the designed test set-up could provide usable results for blast tested panels. In addition, the goal was also to compare the performance of the panel types tested to gain some insight on how composite panels behave during a blast impact such that a foundation for further development of composite panels, tailored to resist blast impact, could be established. Based on the designed panel configurations, the list below summarises the main goals of the performed tests. In the following these points will be treated for the test case relevant to them.

- Test the functionality of the blast test facility when used to test different panel types at different loading conditions.
- Compare the response of monolithic laminates and sandwich panels when exposed to a blast load.
- Test the influence of core type on the response of a sandwich panel when exposed to a blast load.
- Identify failure types developed in the different panels when impacted by a blast load.
- Test if it is possible, with the current high-speed cameras, to perform DIC analysis on a panel just before rupture, in the case of a test where through thickness fracture occurs.
- Investigate how panels perform during multiple blast impacts of increasing charge size.
- Generate data to be used for comparison with numerical models.

5.1 Test panels

Four different material systems were tested. Table 5.1 shows the technical details of the designed systems. Details of the fibre and matrix type can be found in appendix B. Except for the SGPH panels, the panels are produced by the partners in the RESIST project. For more elaborate fabrication details on these panels, see [44] and [45]. The SGPH panels are delivered by TenCate. The exact production details for these panels could not be obtained. E-glass/Epoxy as a material system was chosen because it is a well-known material system that is often used and was therefore regarded as a material system for which information could easily be found in the literature.

To test the blast performance of the materials presented in table 5.1, three different test scenarios were used:

(I) *Repeatability test*; where three panels of the same type were tested once each under the same test condition.

(II) *Multiple loading test*; where a single panel were tested several times with increasing blast loads.

(III) *Rupture test*; where the charge size and stand-off condition was chosen such that a hole were blown in the panels.

Table 5.2 shows the actual test conditions used for the three described test scenarios. As can

Table 5.1: Specifications for the panels used for blast testing

Panel Code	Panel Type	Material		Th [mm][a]	AW[kg/m^2][b]
CRBJ	Monolithic laminate	Eglas/Epoxy $[0, -45, 90, 45]_{30}$ $v_f = 0.56$		~ 21	~ 38.8
SGPH	Monolithic laminate	Sglas/Phenol $[0, 90]PW_{40}$ $v_f = 0.62$		~ 19.8	~ 39.8
		Skin	Core		
CRCK	Sandwich	Eglas/Epoxy $[0, -45, 90, 45]_{11}$ ~ 8.5mm $v_f = 0.45$	Divinycell H80[c] ~ 40mm	~ 57	~ 38.5
CRCL	Sandwich	Eglas/Epoxy $[0, -45, 90, 45]_{9}$ ~ 7.7mm $v_f = 0.45$	Divinycell H250[c] ~ 40mm	~ 55.5	~ 38.9

[a] Total thickness of panel
[b] Area weight of panel
[c] Cores material are manufactured by DIAB

Table 5.2: Blast test specifications used for the individual panels

Panel Code	Panel Number	Test Type	Hits[a]	Charge size[g]	SODmm
CRBJ	30–32	(I)	1	250	100
CRCK	1–3	(I)	1	250	100
CRCL	1–3	(I)	1	250	100
CRBJ	33	(II)	6	25 . . . 250	100
CRBJ	34	(III)	1	250	50
SGPH	3+9	(III)	1	250 + 375	50

[a] Number of blast impact the individual panels has received

be seen from the table, all panel types, except for the SGPH panels are tested for repeatability. This has been done to evaluate if identical panels behave similarly under identical loading conditions. For the multi load test case, (II), blast loads of 25g, 50g, 100g, 150g, 200g and 250g were used and the loads were applied in the stated order. This was carried out in order to test if the dynamic response of the panel would change at increased loadings. For the rupture tests the SOD was reduced to 50mm. This was done because earlier trial tests had revealed that a hole could not be blown in the panels using a charge size and SOD combination of 400g and 100mm. Keeping the SOD constant would thus dictate a larger charge mass, giving rise to two problems: *a*) the maximum charge size that can be used at the test facility is 500g and obtaining rupture at SOD = 100mm will most likely require a larger charge size than 500g, *b*) the functionality of the test set-up becomes increasingly unstable at charge size above 250g. This last limitation will be further discussed in section 5.3 on page 64. With the designed test layout the blast test set-up can be evaluated, and it also makes it possible to compare the performances of different composite structures when tested under the same conditions.

5.1.1 Boundary Conditions

To fixate the panels between the blast box and the frame holes has been cut by use of water cutting along the panel edges, as illustrated in figure 5.1a. The holes are positioned to match to holes on the frame and box and are made 3mm oversize in the diameter such that the screws used to mount the frame easily can go though the panel holes. The centre of the large Ø33 are 50mm from the panel edge. The panel edges are thus symmetrically constrained in the clamped region and held in position by the bolts and the friction between the frame and box surfaces. For the sandwich panels wooden supports has been placed along the clamped area, see figure 5.1b, to prevent the foam core from being crushed during tightening of the screws and thus preventing pre-damaging the panels. The wood support pieces was bonded to the foam core and then to each other.

5.2 Test Results

Figure 5.2 shows a typical output from ARAMIS, showing a contour plot of the deflection of CRBJ-30 at a single stage. When the recorded images are loaded into ARAMIS, a 3D coordinate system is created with the x-, y- and z-axis defined as shown in 5.2a. In the following, reference

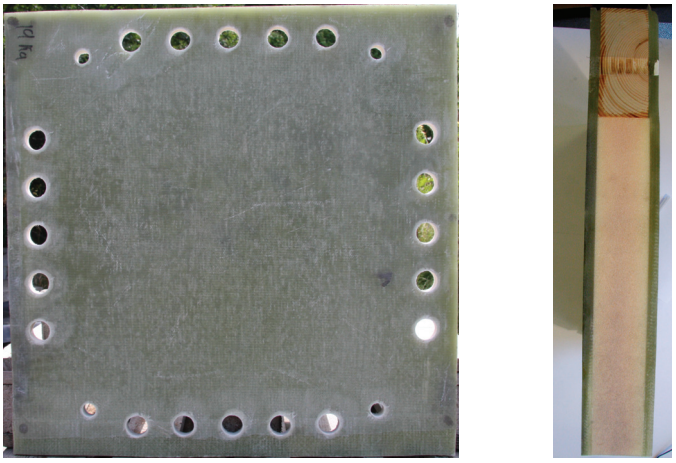

(a) (b)

Figure 5.1: Boundary conditions on the tested panels where; (a) shows the the 24 holes along panel edges, and (b) shows the wood supports put along the sandwich panels edges for preventing foam core compression during clamping of the panels

to panel deflection will always be in the z-direction, and strain will be in-plane major strain in the xy-plane. The displacement contour shown corresponds to the area marked on the panel in figure 5.2b. In ARAMIS terms this area is called the *masked area* and is the area used for analysis. This area is defined manually for all tests. As can be seen, the masking is not taken all the way to the edge. This has been chosen to avoid edge effect in the analysis, which can give spurious results.

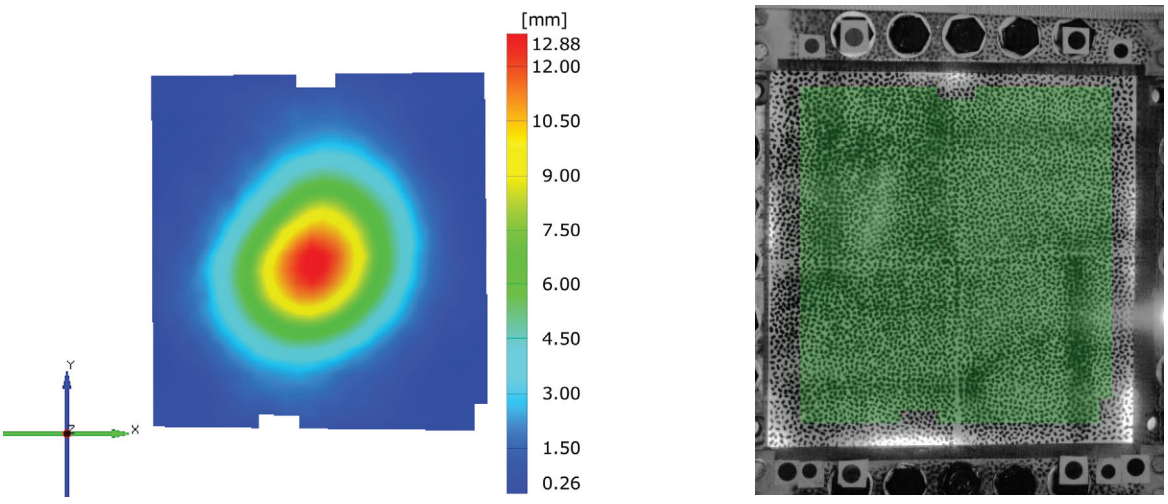

(a) (b)

Figure 5.2: Typical output from ARAMIS where; (a) shows a contour plot of the measured deflections with the coordinate system defined by ARAMIS shown, and (b) shows the selected area on the panel surface, called the masked area, on which the DIC analysis is performed

An important thing to note here is, that because of the way ARAMIS performs the analysis, it is not possible to obtain data at the exact edge location. In ARAMIS the masked area is divided into small rectangular areas called facets. The facets are then tracked from image to image by the underlying algorithms in ARAMIS and their centre point displacement is calculated. The actual displacement reported in ARAMIS is thus the displacement of the centre of these facets, which is why the exact displacement of an edge cannot be calculated. The strain is calculated by monitoring the relative movement of neighbouring facets. For further details see [43].

In all tests approximately 100 images, corresponding to 10ms of response time, usable for DIC analysis was recorded. After approximately 10ms the calibration of the cameras was lost due to the vibrations from the blast as described in chapter 4. The images recorded after the calibration loss can therefore not be used for DIC analysis, but can still be used for visual inspection of the panel response and thus still provide valuable information regarding the blast response of the tested panels.

After blast testing the condition in the clamped area was investigated visually. All panel types tested, except the panels tested under condition (III), did not show any visual signs that movement in the clamped area had occurred during testing. The holes along the panel edged was not deformed and on the panels surface the were no indications that the panel had been dragged along the frame and box surface. It was therefore concluded that in the test the panel boundary conditions had been very close to perfectly clamped edge conditions.

5.2.1 Movement Correction for Blast Box Movement

As described in section 4, the blast box is not restrained from movement during testing, resulting in rigid body movement of the blast box, which will be superposed the measured panel deflection. Using the DIC software, this can be adjusted for by monitoring reference points placed on the frame of the blast box, which was done for all tests. An example of a movement correction performed on CRBJ-30 is shown in figure 5.3. In this example four reference points

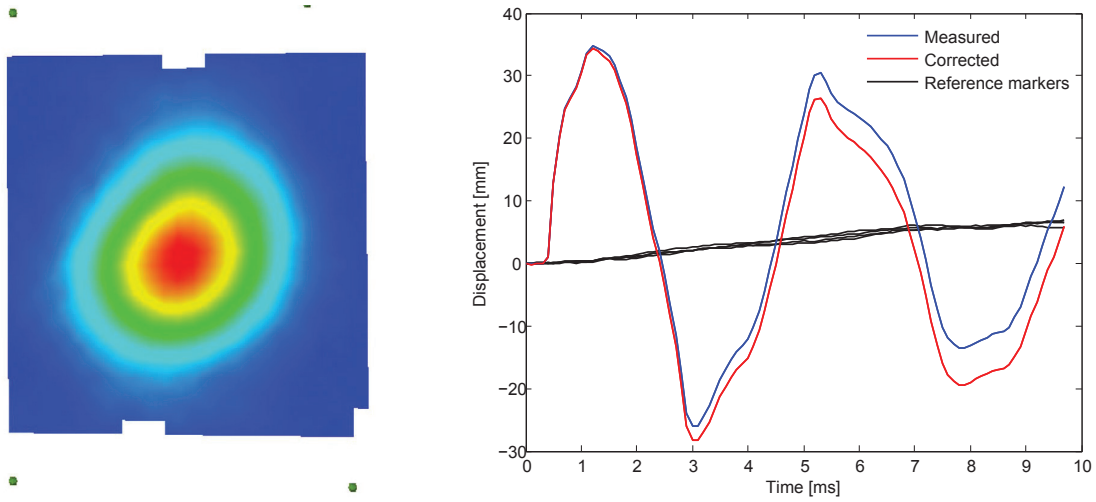

(a) (b)

Figure 5.3: Movement correction performed in ARAMIS where; (a) shows the identified reference points, and (b) shows the effect of the movement correction on the measured displacement

were identified through the entire test. In the first stage, all reference markers were identified (figure 4.8 on page 36 shows the attached reference markers), but ARAMIS was only able to identify the four shown in figure 5.3a at the final stage. This observation with loss of some of the reference markers was seen for all tests.

From figure 5.3b it can be seen that the difference between the measured and corrected displacement on the first peak is negligible, indicating that the blast box has not really started to move yet. In the presented example, the difference at the first peak is 0.3mm. Looking at the second peak, the difference is now clearly visible, which also fits well when looking at the lines describing the blast box movement. This means that the first part of the panel deformation can be measured correctly even though less than three reference points are tracked through the first 100 images, and no movement correction therefore can be performed. This is an important observation because at the first peak the largest deflection is observed and here the largest strains develop. If fracturing occurs it is therefore most likely that it would happen during this first part of the deflection. It is therefore possible to correctly measure the displacement before fracture even though a movement correction cannot be performed. In case the movement correction cannot be performed on a specific test then, as can be seen from figure 5.3b, the deviation will grow to several millimetres. In the presented example the final deviation is 6.4mm. To overcome this problem several approaches can be used. In ARAMIS *pixel points* can be defined manually on each image, which can then be used as a reference point to perform the movement correction. The problem with the pixel points is that they are very sensitive to their position, and since they have to be positioned manually, inaccuracies in their position are very likely to develop, which result in poor movement correction. Alternatively, an *average box movement* for a specific charge size and SOD combination can be defined from the measured box movement on the tests where the movement correction were successful. This *average box movement* can then be used to perform movement correction on a test, using a similar blast set-up, with insufficient reference point detection.

5.2.2 Repeatability Test

These tests were carried out with the following focus:

- Test the repeatability of the panel response when tested against identical loading conditions. This knowledge is important if modelling of the blast response is required since a model will always predict the same response.
- Test if sandwich panels offer any advantages in mitigating the blast load, compared with the monolithic laminates.
- Test if the sandwich core type has an effect on the response of the sandwich panels.

The data from the measurements will be presented in two ways: (i) by analysing data from the panel centre point over time, (ii) by analysing data at specific time steps from a section over the width of the panel. These two approaches will give important information on how the panel types react on the applied blast loading.

Centre Point Measurements

Figure 5.4 on the next page displays the measured centre deflection for the 3 panel types tested. For the CRBJ panels, only two of the tested panels provided usable strain measurements. This

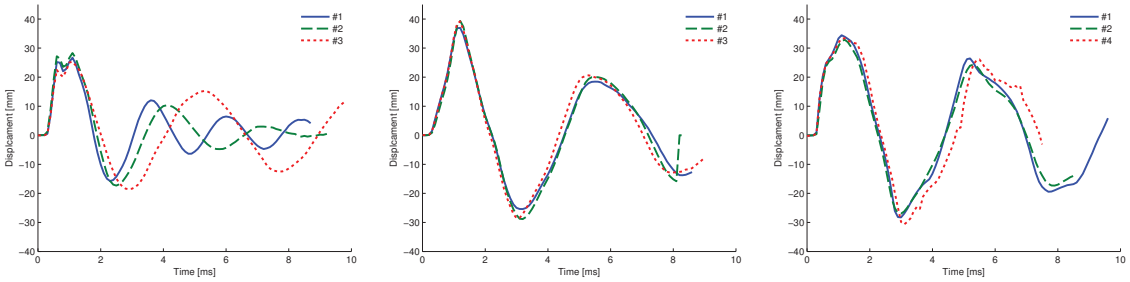

(a) CRCL 1-3 **(b)** CRCK 1-3 **(c)** CRBJ 30-32

Figure 5.4: Measured centre displacement for the 3 panel types tested

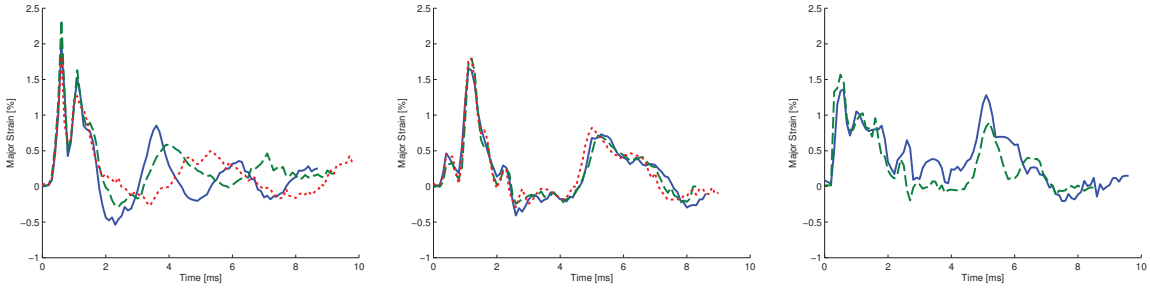

(a) CRCL 1-3 **(b)** CRCK 1-3 **(c)** CRBJ 30-32

Figure 5.5: Measured centre major strain for the 3 panel types tested

was because some of the paint applied to create the speckle pattern detached during the panel deflection thereby creating a lot of noise on the strain calculation. As can be seen, the CRCL panel has the lowest peak deflection and the CRCK panels have the largest peak deflection. For the same panels, the measured centre major strain is shown in figure 5.5. An interesting observation is that the largest strain is not seen for the panel with the largest deflection as one might expect. The largest strain is found on the CRCL sandwich panels with the H250 foam core, which is the panel type with the lowest deflection. The reason for this behaviour will be explained when analysing the sectional deflection of the panels. In table 5.3, the average maximum peak deflection for the three panel types is shown together with the average maximum major principle strain. For each measure the percentage difference with respect to the two other panel types is also shown.

For all panel types tested, the behaviour up to the first deflection peak shows good

Table 5.3: Maximum displacement and major strain of the curves from figure 5.4 and 5.5

Panel Code	$d_{\max_{avg}}$[mm]	%-dev[a] from $d_{\max_{avg}}$	$\sigma_{\max_{avg}}$ [%]	%-dev[a] in $\sigma_{\max_{avg}}$
CRCL	26.8	-30.4/-20.3	2.04	29.7/16.8
CRCK	38.5	43.8/14.7	1,75	-14.4/11.0
CRBJ	33.6	25.41/-12.8	1,57	-9.9/-22.8

[a] Deviation of the specific panel type relative to the two other panel types

repeatability. After the first peak, panel types CRCK and CRBJ continue to show good repeatability while a clear difference in the response is seen for the individual CRCL panels. The CRCL panel also shows a significantly different response over time. The response frequency of the CRCL panel is higher and the oscillation is damped out more rapidly. Comparing the CRBJ panels with the CRCL panels, a 20% reduction in the maximum deflection is seen for the CRCL panel. Comparing with the CRCK panel a 12.8% increase in deflection is seen with respect to the CRBJ panel. It was believed that the higher flexural rigidity of the sandwich panels would reduce the total panel deflection significantly, but the experiments showed that this was not the case. Even more surprisingly, the deflections of the CRCK sandwich panels are larger than that of the CRBJ panels. Looking at contour plots of the panel deflection, a possible explanation can be found by looking at the overall shape of the panel deformation. From figure 5.6 it can be seen that a square deformation shape is built up. This indicates that panel deflection has changed from a bending controlled problem to one that is controlled by membrane effect, where further bending becomes much harder since it is controlled by the in-plane panel stiffness. This effect is clearly visible on the CRCK and CRBJ panel, while the CRCL panel only shows a very small effect of this. This effect can explain why similar deflection is seen for the CRCL and CRBJ panels where the deflection of the CRBJ panel is restricted due to membrane effects. For the CRCK panels, membrane effects are also clearly visible in figure 5.6b. The large deflection of this type of panel must therefore be attributed to the weak core, H80, compared to H250 core type, which are in the CRCL panel. The weak H80 core can result in a significant shear contribution to the total deflection which can then explain the large difference between the CRCL and CRCK panels.

From ARAMIS the in-plane strain rates can also be calculated. Figure 5.7 shows the maximum strain rate for the tests on the 3 panel types. The in-plane strain rate regime is important, as material test data, valid in this regime, are needed for input in numerical models trying to replicate the test response. For all panel types the strain rate varies significantly from test to test. This might be due to inaccurate positioning of the explosive charge. As explained in chapter 4, the explosive charge is positioned manually with distances measured by a ruler. If the charge is positioned some distance over the geometrical centre of the panel, the peak strain rate experienced might be affected. The shape of the explosive charge might also have an effect since the shape has an effect on the shape of the generated blast waves. Since the charge is

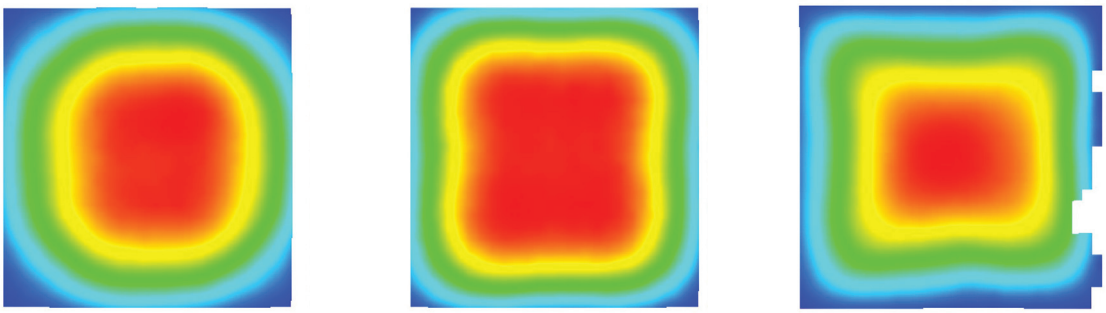

(a) CRCL **(b)** CRCK **(c)** CRBJ

Figure 5.6: Contour plots showing the square like deformation shape in the panels, indicating that membrane effects are controlling the deformation

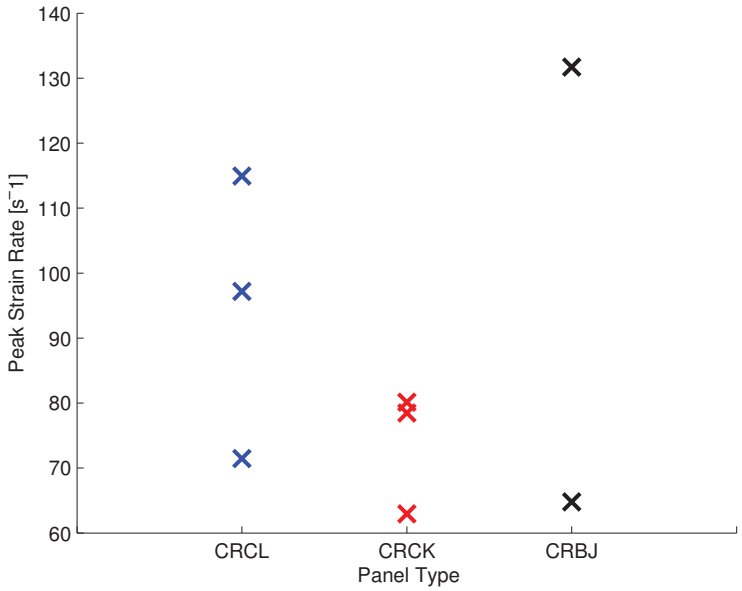

Figure 5.7: Measured maximum strain rate in the centre of the panels

formed by hand, deviation in shape must be expected from test to test.

Sectional Measurements

In table 5.3, it can be seen that the maximum strain is not found on the panel with the largest deflection. This can be explained from the shape that the panels obtain during the deflection, which is visualized by looking at the deflection along a section on the panel surface. In ARAMIS a sectional line can be created over which for example displacement data can be plotted for each time step. As illustrated in figure 5.8, for all tests a horizontal section line, which crosses through the geometrical centre of the panels, was created.

Figure 5.9 shows how the deformation of the panels are built up over time until the maximum deflection is reached. In the plots the green lines correspond to the maximum deflection. The red, blue and black coloured lines show the deflection at 0.2ms, 0.5ms and 0.7ms *before* the peak deflection is reached. The different line styles correspond to individual repetitions. In figure 5.10 the strain across the sectional line is shown in a similar fashion as that used in figure 5.9.

From figure 5.9 and 5.10 it can be seen why the largest strain is found on the CRCL panel, which had the lowest maximum deflection. Looking at figure 5.9a, it can be seen that after impact the panel almost immediately deflects to its maximum deflection in the centre, a response which is not seen for the two other panel types. This gives the panel a large curvature in the centre region, which gives rise to the high strains in this very first part of the panel deformation, see figure 5.10a. The two other panels types have a more gradual increase in the deflection but still show very different behaviour when compared to each other. The CRBJ panel also gets an initial high deflection in the centre, which also gives this panel the highest strains in the initial part of the deformation, as seen in figure 5.10c. After this the curvature decreases in the centre while it starts to increase towards the edge of the panel, as the deflection spreads across the panel. For the CRCK panels, shown in figure 5.9b, the deflection pattern is

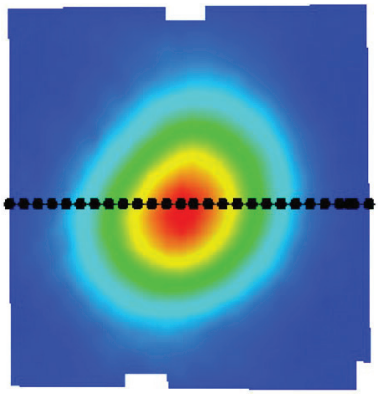

Figure 5.8: Position of section in ARAMIS along which displacement data are analysed

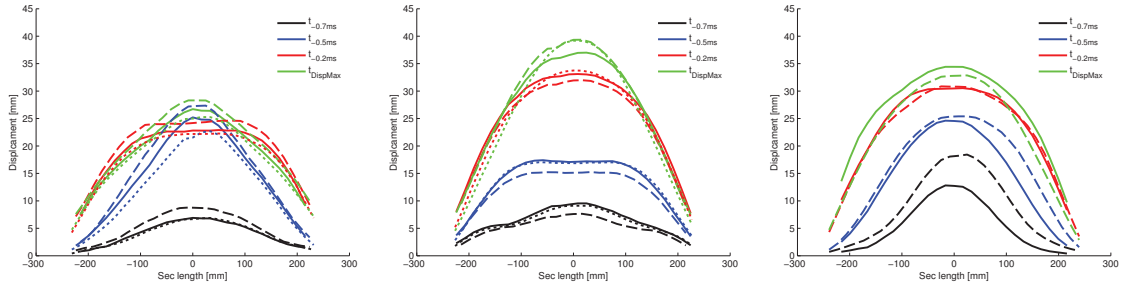

(a) CRCL 1-3 **(b)** CRCk 1-3 **(c)** CRBJ 30-32

Figure 5.9: Measured displacement along the horizontal section shown in 5.8. The line style types represents the individual test, and the different colouring corresponds to a specific time step, with the green line being the time step at maximum deflection, and the remaining colours being time steps before maximum deflection

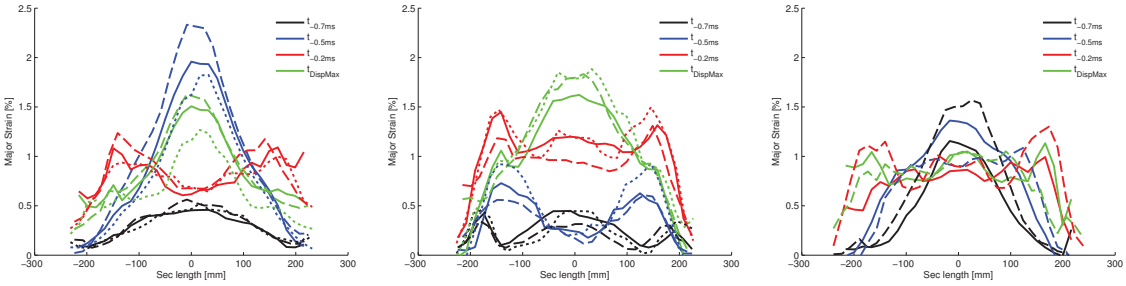

(a) CRCL 1-3 **(b)** CRCk 1-3 **(c)** CRBJ 30-32

Figure 5.10: Measured major principle strain along the horizontal section. For explanation of lines and colouring see figure 5.9

reversed when compared with the two other panels. Here, a small initial deflection is seen in the centre of the panel, but thereafter the deflection builds from the edges and inward over time. Comparing the two sandwich panels a very different deformation pattern is thus seen, as illustrated in figure 5.9. The only difference between the two sandwich configurations is the core type. The difference in deflection behaviour must therefore be attributed to the core properties in the two panels. Here the lower shear modulus of the H80 core could be one of the reasons for the observed difference.

Failure Identification

After testing, the panels used in the repeatability test were inspected to identify any internal damage that might have developed from the blast loading. This was done by cutting the panels, using water jet cutting, into four square pieces following straight line across the centre of the panel. In table 5.4 to 5.6 on pages 52–54 the identified failure types for the panel types are described. For the monolithic laminate, CRBJ-30–32, good consistency was found in the type and location of failure, which was identified as a large central delamination in the area around the centre of the panel cross-section. This location fits well with the location of the largest shear stresses that develop at the neutral axis during the panel bending. The observed delamination is not believed to be due to the initial pressure wave from the blast impact, which travels through the thickness of the panel. If that was the case, the delamination sites would have been more scattered and *not* localized in the centre region of the panel. The observed delamination is going from the panel centre all the way to the panel edges.

Looking at the sandwich panels the identified failure types are more inconsistent. Looking for example at the CRCL laminates with the H250 core, one sandwich panel shows no failure after the test whereas another shows both 45° and 90° core cracks and core skin debonding. The substantial difference seen in the failure extent for the CRCL panels may also help explain why the deflection over time, see figure 5.4, behaves less consistently than seen for the two other panel types. Differences in failure types and locations of the failure was also seen for the CRCK sandwich types, where one panel (#1) shows a central core–skin debonding, which is not seen in panel #2 and #3. Instead these panels show core cracking, which is not observed in panel #1. Regarding the observed core–skin debonding seen in CRCK-1, care should thus be taken regarding interpretation as this failure might have been initiated from the water jet cutting process. Use of water jet cutting to cut the material test specimens from an SGPH panel showed that the cutting process significantly affected the material and could generate internal delamination. For the CRCL panels, which showed core cracking (panel #2 and #3), the location of the 90° cracks are close to the central area of the panel indicating that these cracks are initiated from the initial high strains in this area, as seen in figure 5.10a. For the CRCK panels similar observations can be made for panels #2 and #3, where the location of the core cracking fits with the location of the high strain towards the edges, as seen in figure 5.10b.

One of the reasons for testing sandwich panels was to investigate whether the foam could act as an energy absorber through crushing, and thus mitigate some of the blast energy, and ultimately increase the survivability of a panel by increasing the explosive charge size needed to generate a hole in the panel. The potential usage of foam as an energy absorber in panels impacted by a blast load has been documented several places, for example in [7, 46, 47] and it has also been used for its energy absorbing capabilities in more commercial applications, for example in race track barriers to absorb energy during a crash [48]. In [49], full scale sandwich panels were tested against air blast loading. But here large explosive charges (30kg) were used

Table 5.4: Identified failure in the CRCL panels

Panel #1	Identified failure type
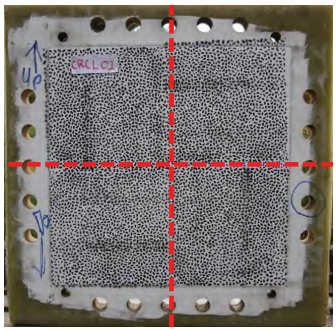	• No visual failure • No visual sign of core crushing
Panel #2	**Identified failure types**
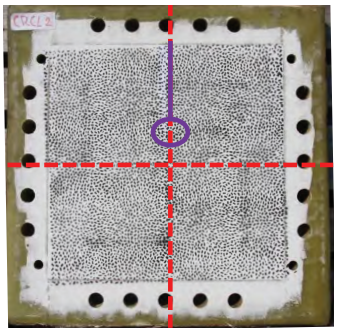	• Skin core debonding on blast side of panel along marked purple line • Core cracking located at purple circle • Indications that crack was initiated at interface between core and wood edge support • No visual core crush
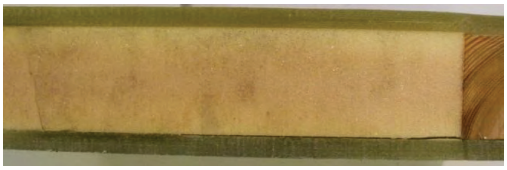	
Panel #3	**Identified failure types**
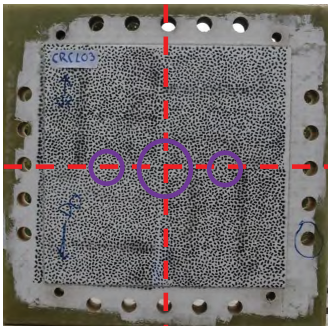	• Skin core debonding on both sides of core • On DIC side debonding is located around the panel centre • On the blast side the delamination extends from the edge and 2/3 into the panel • Core cracking at edge of centre circle and at the two small circles
 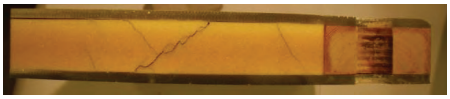	

Table 5.5: Identified failure in the CRCK panels

Panel #1	Identified failure types
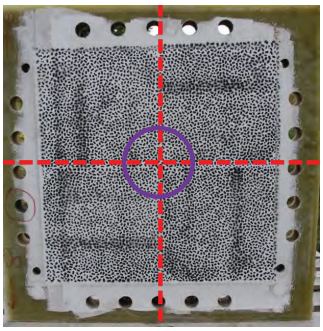	• Core skin debonding in centre region of panel • Delamination in skin on blast side. Visible in all cut sections • No visible core crushing 
Panel #2	**Identified failure type**
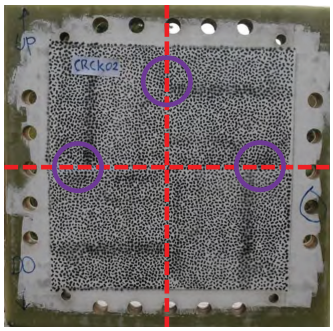	• Small degree of core crushing in centre region • Core cracking found in locations marked by circles 
Panel #3	**Identified failure type**
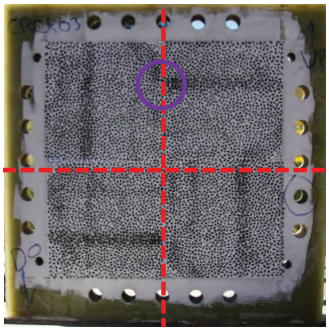	• Core cracking at location of circle • No visible core crushing 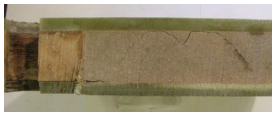

Table 5.6: Identified failure in the CRBJ30-32 panels

Panel #1	Identified failure type
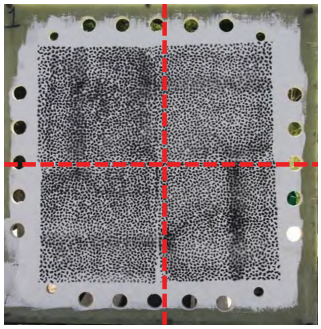	• Delamination halfway through the thickness. Delamination extends into all sections and all the way to where the panel was clamped • Multiple delamination sites extending from panel centre and towards the DIC side, corresponding to the panel side initially put into tension • Delaminations seem to be equally spaced 
Panel #2	**Identified failure type**
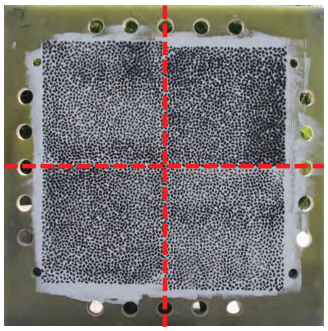	• Same delamination pattern as seen for CRBJ-30 • Single delamination found on the part of the panel initially put in compression • A surface defect was seen on this panel that could have given rise to the delamination on the compression side 
Panel #3	**Identified failure type**
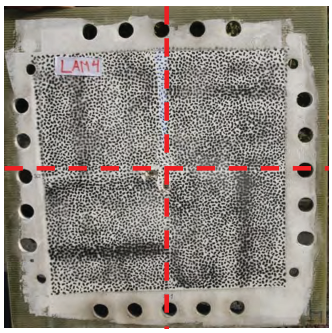	• Large delamination in the middle of the panel • Delaminations found 1/3 and 2/3 away from the middle towards the DIC side 

at a SOD of 8-14m. This gives a completely different load scenario, with much more evenly distributed pressure on the panel, compared with the much more localized initial loading that develops when testing at very short SOD, as used here in the present study. There was no mention of observed core crushing in [49], which might have been due to the evenly distributed loading. It can therefore not be concluded that no core crush develops in the case of localized blast loadings. Inspection of the cross-sections of both type of sandwich panels (CRBJ and CRCK) showed no sign of visual core crushing, indicating that *the foam core did not function as an energy absorber* in the tested blast scenarios. For the sandwich panel the energy seem to have been absorbed by core cracking and skin core debonding. This observation suggests that the idea of having a crushable core in sandwich structures with the purpose of absorbing energy through crushing must be reconsidered. The core types used are rigid foam types and a compression of the cores would therefore result in a permanent deformation. It therefore seems unlikely that the cores should have been crushed to a certain level and then stretched, by the skin movement, to their original height. If the cores had been crushed and stretched again, it would be visible in the cell structure of the foam (which is visible to the eye) as the cell walls fracture during the compression. Based on the observed results, it can thus be concluded that the sandwich panels do *not* offer any advantage over the monolithic laminates for the type of loading applied.

5.2.3 Multiple Blast Impact Test

To test how a laminate reacts when it is exposed to multiple blast impacts, the CRBJ-33 panel was tested at explosive charge sizes ranging from 25g up to 250g starting from the lowest charge load and increasing in steps to the highest load. For all the tests, a SOD of 100mm were used. Figure 5.11a shows the measured centre deflection of the tested panels for each of the charge sizes, and as expected the deflection increases with the charge size. Looking at the centre deflection response over time, it can be seen that for the 25g and 50g, tests the panel oscillates with approximately the same frequency. With the increase in charge size from 50g to 100g, a change in the oscillation frequency was detected. A frequency analysis was therefore conducted to see if looking at the panel response in the frequency domain could give further insight into the panel response. The frequency analysis was made by performing a FFT (Fast Fourier Transform) on the time-displacement data and identifying the dominating frequencies in the response. Figure 5.11b on the following page shows the identified dominating frequencies of the response. From there it can be seen that the frequencies group in to two levels. For charge loads of 25g and 50g the frequency is around 400Hz and for charge sizes from 100g to 250g the frequency is around 250Hz. There is thus a characteristic drop in response frequency of the panel when going from a 50g to 100g charge size. This drop in the frequency response could be due to failure that starts to develop internally in the panels, where for example an internal delamination could change the dynamic response of the panel.

In 5.11b the frequency response of the repetition tests performed on CRBJ-30–32 has also been plotted. These frequencies fall into the same range as the frequencies identified for the multi blast loading test case for charge sizes larger than 100g. Post-test panel inspection of panels CRBJ-30–32 revealed that internal failure in the form of delamination had developed, see figure 5.6. This supports the postulate above that the drop in the frequency is due to the build-up of internal failure. Why the frequencies identified in the multi blast impact test do not change when increasing the charge load above 100g is not yet clear. It could be that when the failure is first initiated at one location internally in the panel, the growth of failure

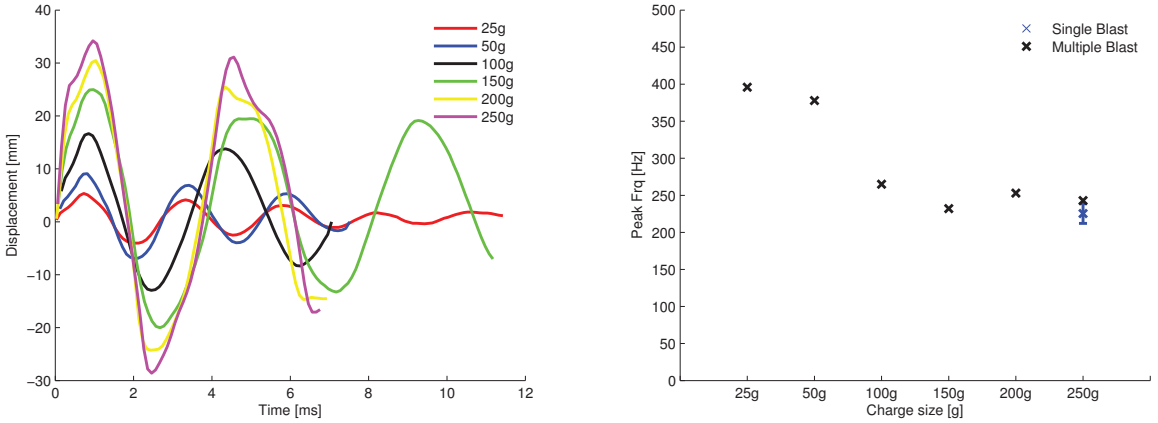

(a) Centre displacement

(b) Maximum frequency

Figure 5.11: Measured response of the CRBJ–33 panel where; (a) shows the measured centre displacement at the different blast loads used, and (b) shows the dominating frequency, found through an FFT analysis, of the panel response at each of the used blast load levels

will propagate from this location and therefore not result in further changes of the panels overall dynamic response. It has not been verified that the tests performed with charge sizes of 25g and 50g did not show any internal damage since the test panels were reused for the tests at the higher charge loads, and no other tests have been performed on the CRBJ panel types at 25g and 50g. For the SGPH panels, a test was performed, using a 50g charge, where the post-test inspection showed no internal damage, supporting the argument that no failure develops at these low charge sizes. In figure 5.12 the measured centre strain for the 25g and 50g test is shown. As shown, the peak strain for the 50g test is 0.68% which is below the measure strain limits of the material, see [50]. The low strain levels combined with the above-mentioned observations made on the inspected SGPH panels, provides solid indications that it *can* be assumed that the panels tested at 25 and 50g have not developed damage. This means that the frequency response of the panels can be used as an indicator of whether or not internal damage has occurred.

In 5.13 the measured centre deflection from CRBJ-33 tested at 250g has been plotted together with the deflection from the repetition tests performed on CRBJ-30–32. It can be seen that the initial deflection of CRBJ-33 follows well the deflection shape of the panels that received only one blast impact. As described, it is realistic to assume that the CRBJ-33 panel contained internal damage before it was tested at 250g. It was thus expected that a difference would have been seen in the response of CRBJ-33 compared with CRBJ-30–32, because the internal failure should reduce the flexural rigidity of the panel and thus give rise to a changed deflection pattern over time. Why a similar response is seen on the panels could be due to the internal delamination identified in panels CRBJ-30–32 that develops during the first deflection such that these panels, even though the panels have not been tested more than once, gets a response similar to the CRBJ-33. The difference in panel response seen after the first peak could then be attributed to the extent to which the delamination is more developed in the CRBJ-33 panel compared to the CRBJ-30–32 panels, since the damage in CRBJ-33 has developed over more blast impacts. As seen previously, the observed panel response indicated that membrane

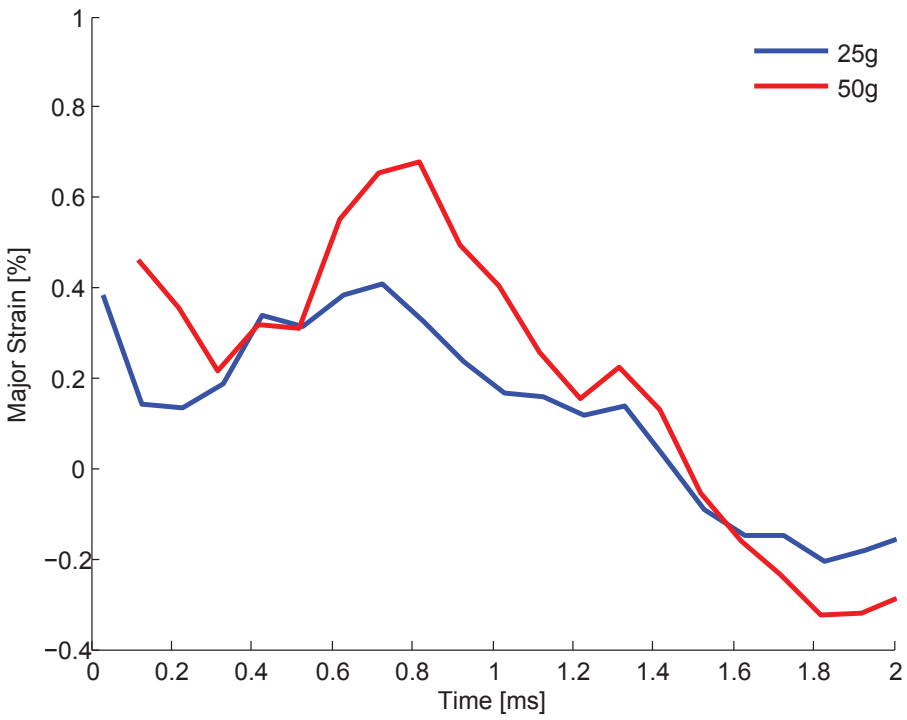

Figure 5.12: Measured strain in the centre of the CRBJ–33 panel tested with a 25 and 50g charge sizes

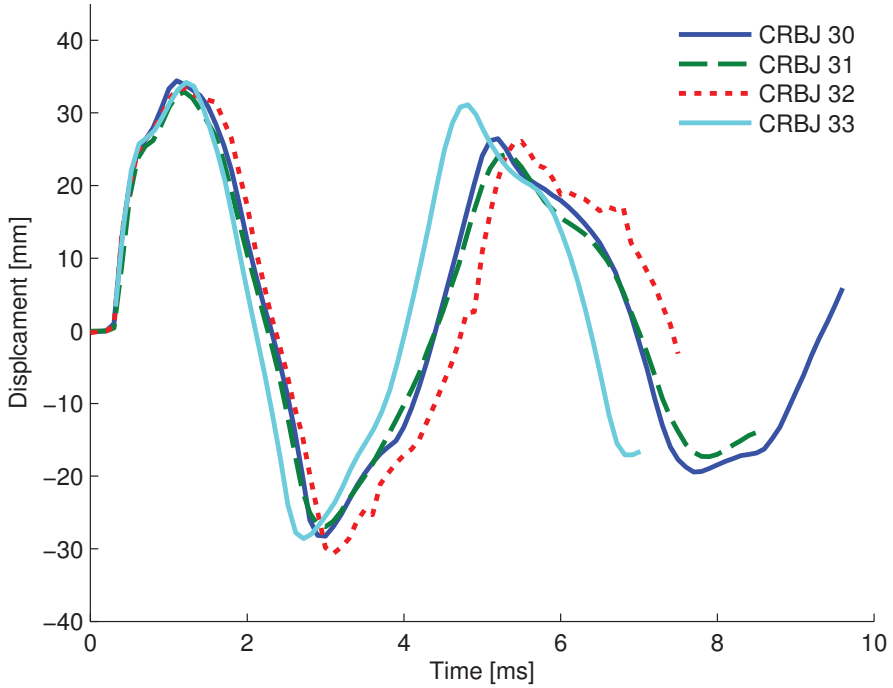

Figure 5.13: Measured centre displacement of the CRBJ30-32 and CRBJ-33 panels

effects at some point become governing for the panel response, where the in-plane properties control the further deflection of the panels. This could also explain the similar response seen for the CRBJ-30–32 and CRBJ-33 panels. If membrane effects are the dominating effects controlling the deflection, then the effect of internal damage in the form of delamination will be suppressed, because such failures will not influence the in-plane panel properties as significantly as they will affect the through thickness properties.

5.2.4 Rupture Test

The CRBJ and SGPH panel types were tested in a set-up to see if a hole could be blown in the panels. Experience from other tests had indicated that a hole could not be blown in the CRBJ panels using an SOD of 100mm. It was therefore decided to use an SOD of 50mm instead, where the blast loading becomes much more localized. These rupture tests were performed, firstly to see if it was possible to carry out a test where rupture could be obtained with the current blast test set-up, and secondly to determine if the available high-speed camera system can be used for analysis of the panel response just before rupture takes place. After the rupture has occurred it is not believed that the images can be used for analysis, since the speckle pattern will be lost and smoke, fire and fragments will disturb the images. Thirdly, and most importantly, the tests were conducted to compare the performance of the two panel types. Beside the difference in material properties, the main difference between the CRBJ and SGPH panels is that the SGPH panels are built from plain weave fabrics whereas the CRBJ panels are built from fabrics with a quarto-axial layup. The test could therefore give indications about the effect of the layup structure and its influence on the blast performance of the panels.

CRBJ-34 panel

Figure 5.14 shows a selection of the images from the rupture test, starting from the time where the charge is detonated (a) and then going 1ms forward. The figure shows both the raw images from one of the cameras (the image on the left side in the figure) and an image with the DIC data overlaid. In (b) the first image after the detonation of the explosive is shown. Here it can be seen that the speckle pattern in the central region of the panel has already been disturbed to a level where the DIC analysis fails, indicating that a hole has been punched almost through the panel. In (c) the disturbance has increased its area and from (d) and forward the hole is clearly visible.

From the DIC displacement overlays it can be seen that the DIC algorithm immediately loses track of the central part of the panel due to the severe disturbance of the speckle pattern. As this disturbed area grows, more and more of the speckle pattern is lost until the hole is fully developed and fragments cover the remaining part of the panel, as shown in (f). As can be seen, the information that can be retrieved from a DIC analysis in the case of panel rupture is very limited since the algorithm loses track of the speckle pattern after the first image. To obtain better information under such test conditions, cameras with a much higher frame rate are needed, such that more information can be retrieved in the time from the detonation of the explosive until the hole starts to develop, which takes place in a time frame smaller than 0.1ms. Looking closer at the few usable DIC images, it can be seen that the hole has fully developed before the deflection reaches the panel boundary, indicating that the hole is due to shear failure through the thickness of the panel, and not because of a tensile rupture of the fibres due to excessive bending of the panel. Figure 5.15 shows images of the panel after the test, showing

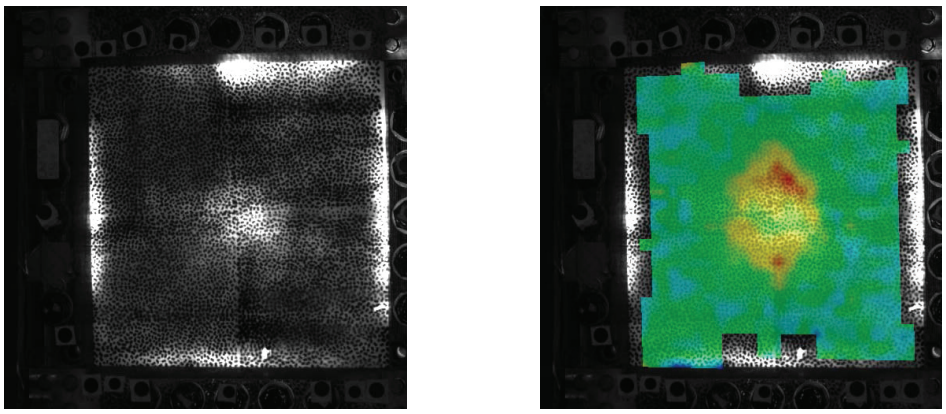

(a) t=0

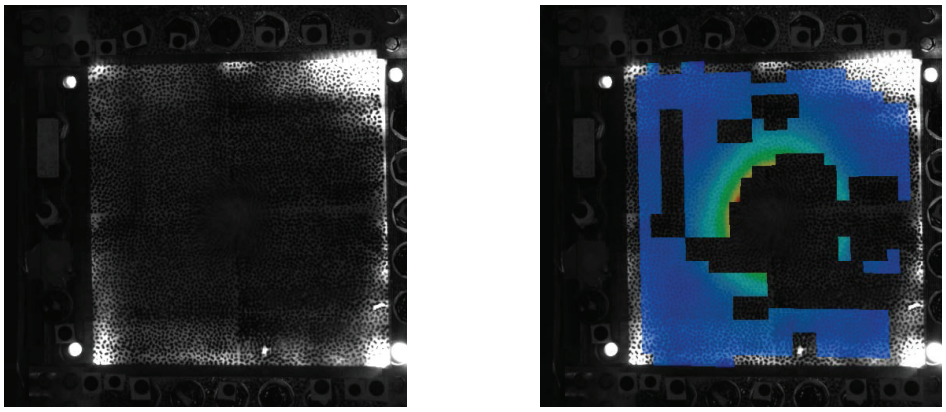

(b) t=0.1ms

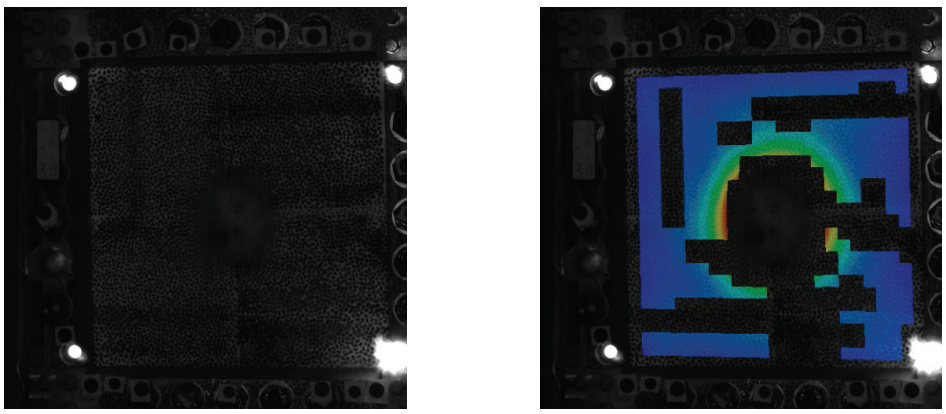

(c) t=0.2ms

Figure 5.14: Images from the high-speed cameras of the CRBJ-34 panel tested to rupture. Left images are raw images from the cameras and right images are with displacement overlay from ARAMIS

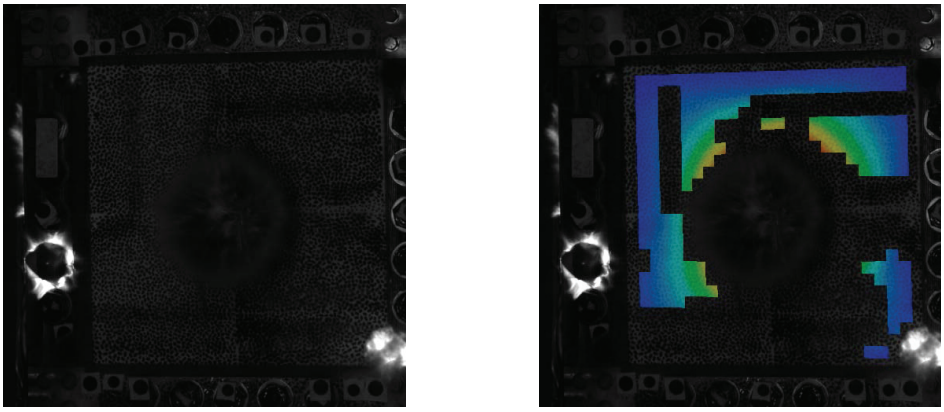

(d) t=0.4ms

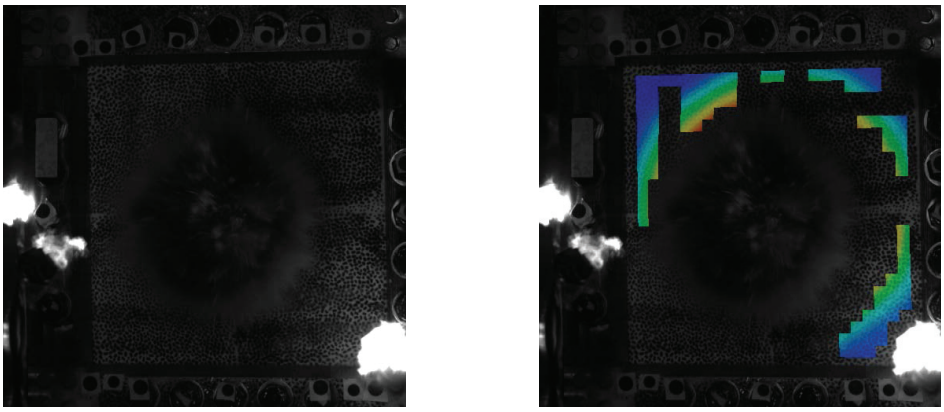

(e) t=0.7ms

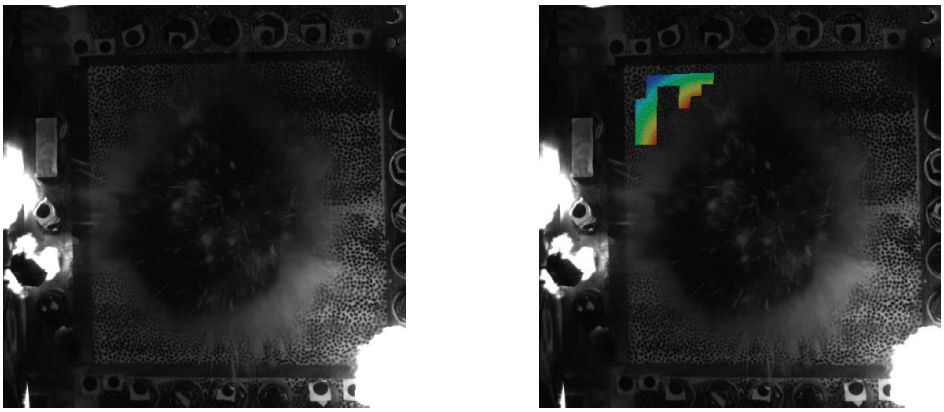

(f) t=1.0ms

Figure 5.14, continued

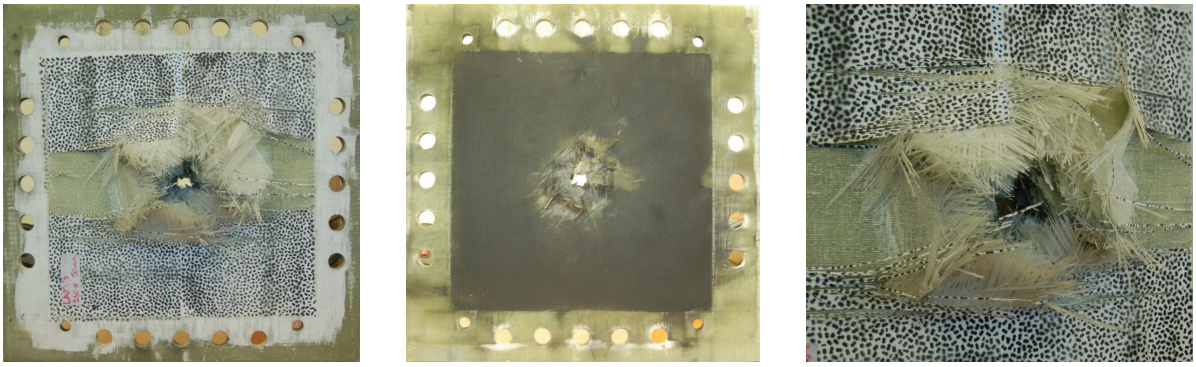

(a) Monitored side **(b)** Blast side **(c)** Monitored side, zoom

Figure 5.15: CRBJ-34 panel after rupture testing

that it is only the area of the panel close to the hole that has been affected, which further supports that the hole has been generated before a response has reached the boundaries of the panel.

SGPH panel

Contrary to the test on CRBJ-34, which resulted in rupture, the result of a similar test on SGPH-3 did not result in rupture. Figure 5.16 shows the measured deflection of this panel. Compared with the deflection patterns shown in figure 5.9, this deflection shape is very distinctive. After the initial peak deflection, an almost linear rebound over time is seen, after which the panel obtains a permanent deflection in the negative direction. This behaviour is believed to be due to the woven fabrics, where fibre interaction and failure creates some interlocking that prevents

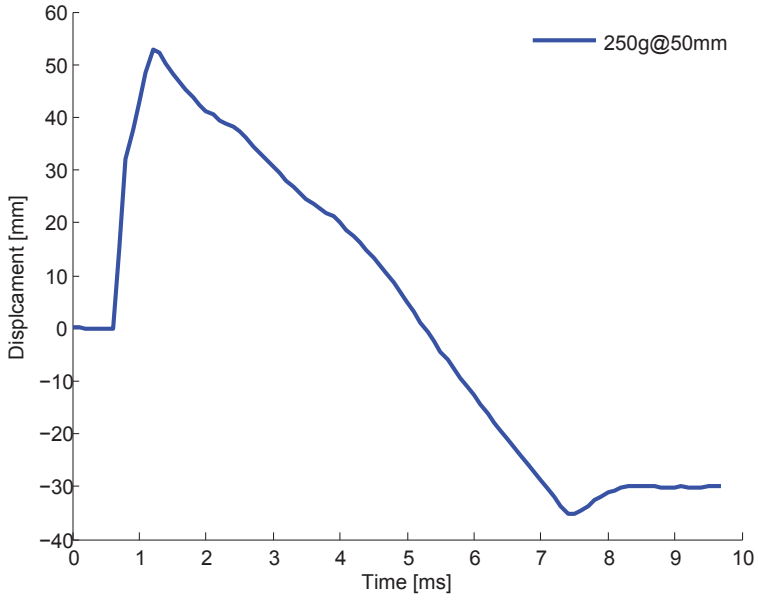

Figure 5.16: Displacement of the SGPH–3 panel tested with 250g at a SOD of 50mm

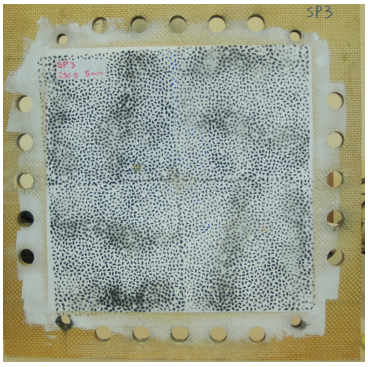

(a) Monitored side

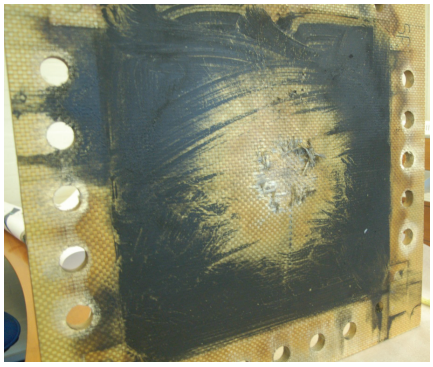

(b) Blast side

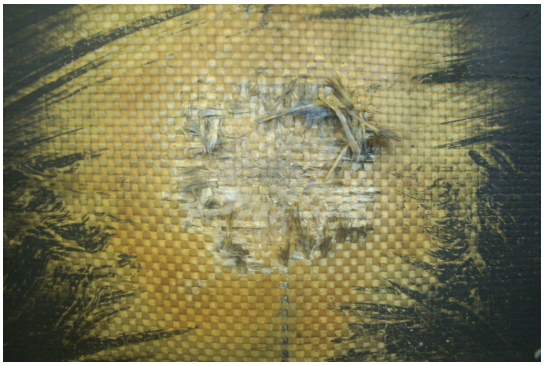

(c) Blast site center

Figure 5.17: Condition of SGPH–3 panel after rupture testing

the panel from bending back to its neutral position. None of the CRBJ panels tested showed any sign of permanent deformation and always ended up in the neutral position. Figure 5.17 shows images of the SGPH3 panel after testing, showing very little sign of damage on the front side of the panel. Looking at the blast side, a small amount of fibre damage is seen in the area where the blast load first impact. No indication of the panel being close to rupture is seen. Compared with the CRBJ34 panel, this panel shows much better resistance against hole rupture indicating that the weave structure is good in distributing and absorbing the blast load.

To further test the capability of the SGPH panels against hole rupture a second test was conducted on a new panel (SGPH-9) where the charge size was increased by 50% to 375g. This test was conducted without the cameras being calibrated. As shown in figure 5.18, the panel also survived this test, and as with the SGPH-3 panel, a permanent deflection in the negative z-direction was obtained. Looking at the front side of the SGPH-9 panel after testing, the panel surface looks a little more affected than was the case with the SGPH-3 panel. The surface has a wavy shape indicating that severe delamination has developed inside the panel. Looking at the blast side, the scenario is the same as seen for the SGPH-3 panel, just with a little more extensive fibre damage. However the state of the panel does not indicate that a hole rupture is about to develop.

The two tests on the SGPH panel showed some surprising results, which indicated that using a composite with woven fabric layers might have benefits over a non-woven quarto-axial

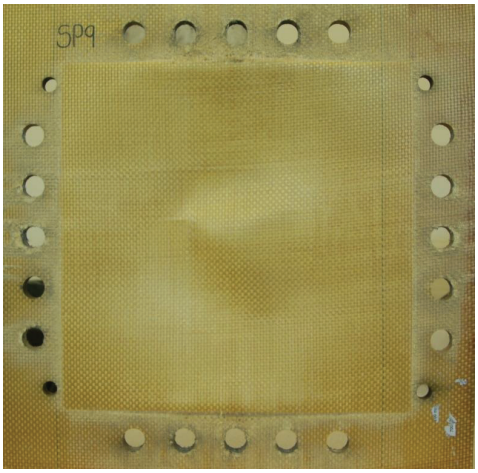

(a) Monitored side

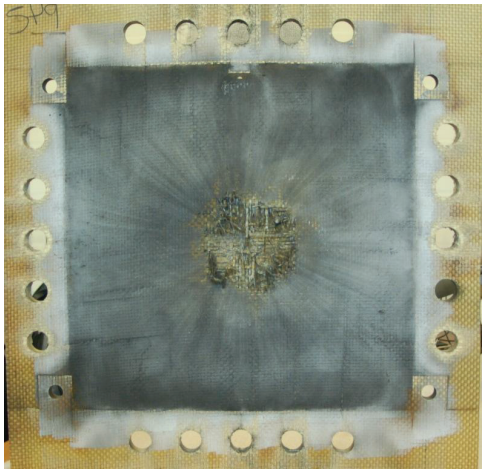

(b) Blast side

(c) Blast site center

Figure 5.18: Condition of the SGPH–9 panel after rupture testing

layup when it comes to mitigating a blast impact. The strength of the materials should be taken into consideration when comparing their behaviour against a blast impact. Table 5.7 compares to tensile and compressive strength of S-glass and Eglass fibres.

Comparing the weakest direction of the S-glas with the E-glas properties, as this direction will fail first, the S-glass is 18% stronger than E-glass i tension but 65% weaker in compression. The difference in the strength properties of the two fibre types therefore cannot solely explain the better performance of the S-glass panels. Considerable contribution to the S-glass performance could therefore be due to the woven layup used. To further verify weather the S-glass/Phenol panels are better than the E-glass/Epoxy panels tests should be performed where a woven

Table 5.7: Measured elastic properties of the two foam types

	σ_x^t [MPa]	σ_y^t [MPa]	σ_x^c [MPa]	σ_y^c [MPa]
S-glas	549	457	204	138
E-glas	387		398	

layup is used for the E-glass panels and also where a UD layup is used for the S-glass panels. Performing such testing would give more insight into if it is the woven layup that is favourable or if it is the S-glass/Phenol combination that is favourable.

5.3 Summary

As a result of the performed blast tests, the test set-up has been shown to be highly applicable for the purpose, and capable of providing data of consistently high quality. With the designed test set-up, blast tests ranging from very small charge sizes up to 250g have been performed and provided usable results for analysis of the panel blast response. In addition, it has also been shown that the set-up can be used to monitor a panel when tested to rupture. In its current state the test set-up performs best when charge sizes not larger than 250g are used. The main problem with exceeding this charge weight is that the blast box can move during the test, and the larger the charge load, the more movement is seen. Successful tests with charges sizes up to 400g have been performed, but when the charge sizes exceed 250g the movements become so severe that much work is needed to bring the blast box back in place again. In the worst case, the box would have to be disassembled before repositioning can take place. Some work is thus needed to find a feasible solution for holding the blast box more firmly in place during loading. This would significantly increase the functionality of the test site.

The DIC set-up has proven to be usable in analysing the blast response of the tested panels. The ability to analyse the deflection across a section over the panel surface has been especially useful in comparing the response of the three panel types tested. This kind of analysis would not be easy to perform using for example strain gauges as that would require many strain gauges mounted on the panel surface. This functionality clearly demonstrates the power of using full field measurement, like DIC, to analyse the response of panels when exposed to blast loading. For the rupture test case it was seen that the current high-speed cameras have too low a frame rate to provide enough data such that valid analysis of the panel response before a hole is created.

Through the post-test inspection of the water jet cut panels, it was possible to identify some of the failures that developed during the blast loading of the panels. For the monolithic laminates the failure development was relatively identical. The same thing was not observed for the sandwich panels where the CRCL panel type especially showed a large difference in the extent of the failure development. This variation in the failure of the sandwich panels is a significant challenge if modelling of blast loading on such panels is desired, since the model will always predict the same behaviour. If no clear failure limit can be predicted from tests, it will therefore be difficult to use a model approach to optimize the structure.

From the post-test inspections of the sandwich panels it was also revealed that no core compression had taken place for both core types. This suggests that the idea of using a foam core as an energy absorber in a sandwich panel exposed to a blast loading should be rejected. This, combined with the large deflection seen that made membrane effects the dominating factor for controlling the amount of deflection, indicates that there is no advantage in using sandwich structure over monolithic laminates for blast protection.

The performed rupture test showed that the composite panel made from plain weave woven fibre layers clearly outperformed the panel made from non-woven quarto axial fabrics. The woven fabric could withstand a charge size 50% larger than the non-woven laminate and still

show no sign of being close to rupture. This result indicates that the usage of woven fabrics in laminate for blast protection should be investigated further.

Chapter 6

Foam Testing

For the designed sandwich panels foam types Divinycell H80 and H250 from DIAB was used. If the blast response of the sandwich panels is to be modelled, knowledge of the mechanical properties of the foam is needed. A series of material tests has therefore been conducted on the foam types, where both the elastic and strength properties have been determined and the dynamic response of the foam has been investigated. In the blast testing the primary load will be through compression in the thickness direction of the foam. The focus of the tests has therefore been to identify the compressional stiffness of the foam and the stress-strain behaviour of the foam during compression in this direction. The non-measured material parameters will be sought in the literature.

The H-series foams are rigid closed cell foams based on a combination of cross linked polyurea and PVC [51], giving the foams the technical name IPN (Inter Penetrating Networks) foams. The foam is produced by introducing gas bubbles into a mould with the liquid polymer mixture, where the bubbles are allowed to grow to generate the cellular structure, after which the foam is solidified by for example cross linking [52]. The number and shape of the generated cells will determine the mechanical properties of the foam, and in general the larger the portion of the foam structure which consists of cells, the lighter the foam will be. The names of the two foams used refer to their density, indicating that the nominal density of H80 is 80kg/m^3 and the nominal density of H250 is 250kg/m^3. In appendix B.6 the material properties provided by the manufacture can be found. Looking at the data it can be seen that the lower the density (and thus a larger content of cells) the lower are the moduli and strength values. Intuitively this makes sense, sine the larger amount of cells gives a smaller amount of material to carry and applied load.

Figure 6.1 illustrates the typical shape of a stress-strain for foam under uni-axial compression. The stress-strain curve for foam is typically split into the three regions marked on the figure, each characterizing a specific deformation mechanism taking place in the foam. In the *elastic region*, elastic deformation takes place. If loading is removed in this region, the foam will return to its original shape. The *plateau region* covers the range over which the cells gradually collapses and are compressed in size. The plateau level can have an almost constant stress level or the stress can increase, depending on the specific foam type. When the cells are close to complete closure, the resistance to further deformation increases and a sharp increase in the stress will initiate, indicating the transition to the *densification region*, where the cells become completely

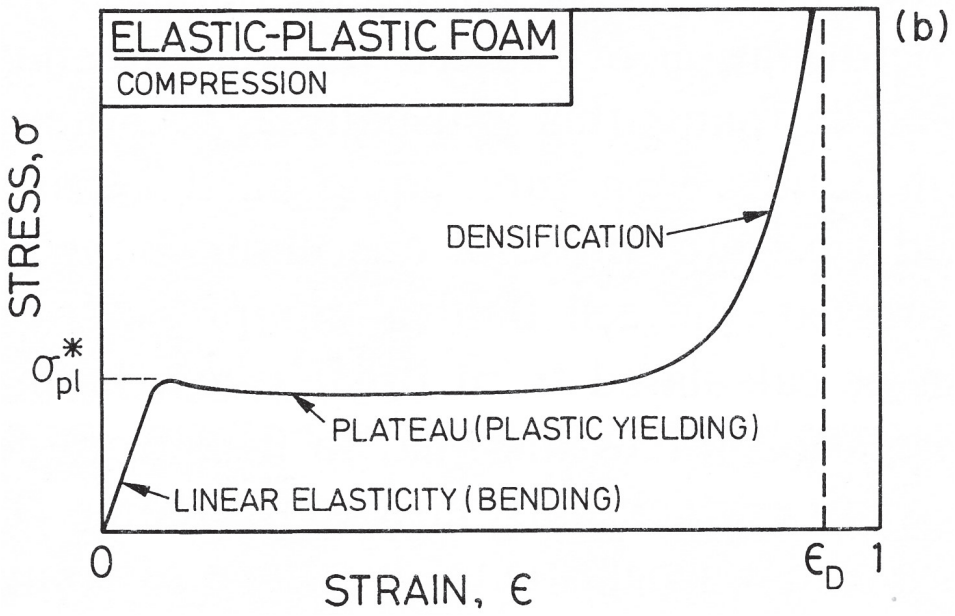

Figure 6.1: Typical shape of a stress strain curve for a rigid foam material [52]

compressed. Depending on the foam type, the foam will either return to its original shape or remain in a compressed shape if loading is removed. The types of foams used here are of the last type. The foam inside a cushion is an example of the reversible type. An important location on figure 6.1 is the transition point from the elastic region to the plateau region called the *plastic yield stress* or the *crush stress* σ_{cr}. This point indicates the stress level at which the cell walls start to collapse. For some foams a small drop in stress is seen after the passage of the crush stress level. The crush stress will be seen to play an important role in the determination of the foam's dependence on strain rate. Figure 6.1 also gives a good illustration of why foam is an interesting material to use to absorb energy. As illustrated by the figure, the material is able to support stresses under compression to a strain of almost one. Even though the stress level foams can resist before crushing initiates is relatively low, the strain energy the material can take up is significant. The same behaviour is not seen in for example tension, where the foam types used here are brittle and have little plastic deformation.

The production process of the foams results in a non-uniform cell size distribution in the thickness direction(or rise direction) of the foam, as can be visually confirmed just by looking at the foam specimens, as shown in figure 6.2. This effect is due to a change in the cell shape as illustrated in figure 6.3, which shows SEM (Scanning Electron Microscope) images of the microstructure at three locations through the thickness of the two foam types. Looking at the H250 foam it can be seen that in the centre of the foam the cells are elongated in the thickness direction. This effect diminishes when moving towards the surface of the foam when the cell shape becomes more circular and cells becomes smaller. The same effect can also be seen for the H80 foam type but here the tendency is less pronounced. As will be shown in the result section, this cell shape distribution has a significant impact on how the foam specimens behave during compression.

The elongated cell structure in the thickness direction is generated during the expansion process of the liquid foam when gas bubbles are blown through it. When formed in a mould,

(a) Divinycell H80 **(b)** Divinycell H250

Figure 6.2: Foam types used in the sandwich panels, where the effect of the non-uniform cell-size distribution can be noticed by the change in colouring through the thickness of the specimens

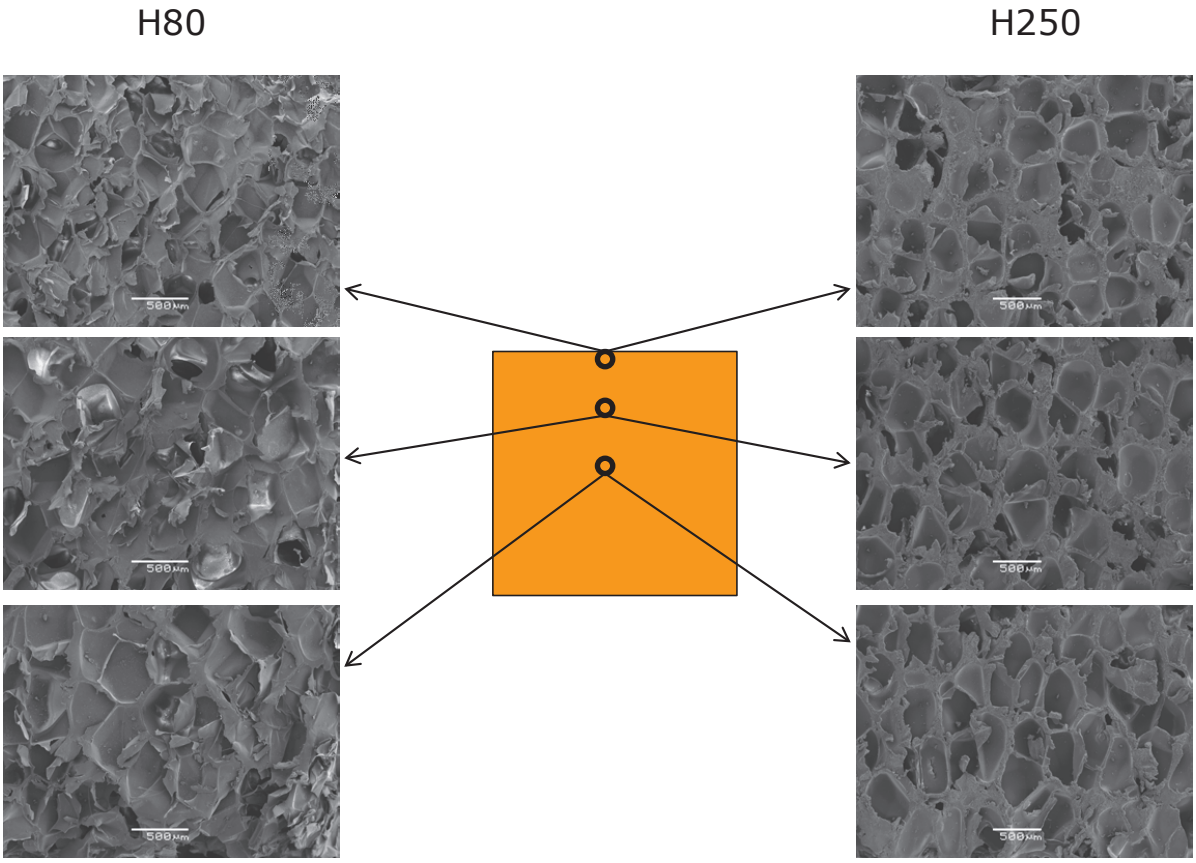

Figure 6.3: SEM images of the two foam types, at the marked locations through the thickness of the foam

the foam expands in the thickness (rise) direction where viscous forces will give rise to the elongated cell structure seen [52]. The same elongation is not found in the in-plane directions of the foam block. This difference in cell shape will lead to an anisotropic (transversely-isotropic) foam, an effect that has been reported in the literature [53–55], and according to [52] an *shape anisotropic factor* of 1.2 will make the foam almost twice as stiff in the rise direction compared with the two other directions.

6.1 Test Setup

The purpose of the characterization of the two foam types was:

- To estimate the in-plane and through thickness stiffness moduli and Poison ratios at quasi static-strain rate. From the data sheet in appendix B.6, it can be seen that there is a 14% difference between the nominal and minimum compressive moduli. The exact moduli will depend on the cell structure, which is hard to exactly replicate from one production batch to another.
- To measure the stress-strain relationship of the foam during compression.
- To estimate the foams dependency on strain rate, an effect which is not unfamiliar for polymeric foams [54, 56–58], by performing tests at elevated deformation speeds.

The quasi-static material test was conducted in corporation with two bachelor students, who performed the tests as part of their final project. The tests were performed in accordance with the specifications in ASTM standard D1621-10 and DS/EN ISO-844. For the high-speed tests an in-plane area below that specified in the standards were used, as the test machine employed could not otherwise deliver enough force to compress the foam specimens to the desired strain. This usage of a smaller surface area was considered not to affect the measured through thickness stress-strain behaviour as the in-plane cell structure is uniform compared with the through thickness cell structure as shown above.

For both test types the specimen deformation was monitored by cameras such that the specimen strain could be estimated through DIC by use of ARAMIS. To make this possible the monitored surface of the specimen was first painted with a dull white spray paint after which black speckle was applied by use of black spray paint. Both type of paints used was ordinary spray paint which can be obtained in a DIY-retailer.

6.1.1 Quasi-Static Material Tests

To estimate the elastic properties of the foams, cubical specimens with dimensions ($xyz = 60 \times 60 \times 40$) were tested. The set-up used is based on a test frame which holds a 50kN hydraulic actuator as shown in figure 6.4a. As shown in figure 6.4b, the specimens are positioned on a stationary compression plate in such a way that the cross-sectional surface prepared for DIC analysis can be monitored by the two cameras used. A secondary compression plate is attached to the movable piston, which is programmed to move with the desired speed under which the specimen is to be deformed. In the quasi-static tests, a deformation speed of 5.0×10^{-5}m/s is used, giving an average strain rate for the specimen of $1.24 \times 10^{-3}\text{s}^{-1}$. Table 6.1 shows the camera and ARAMIS settings used for the quasi-static measurements.

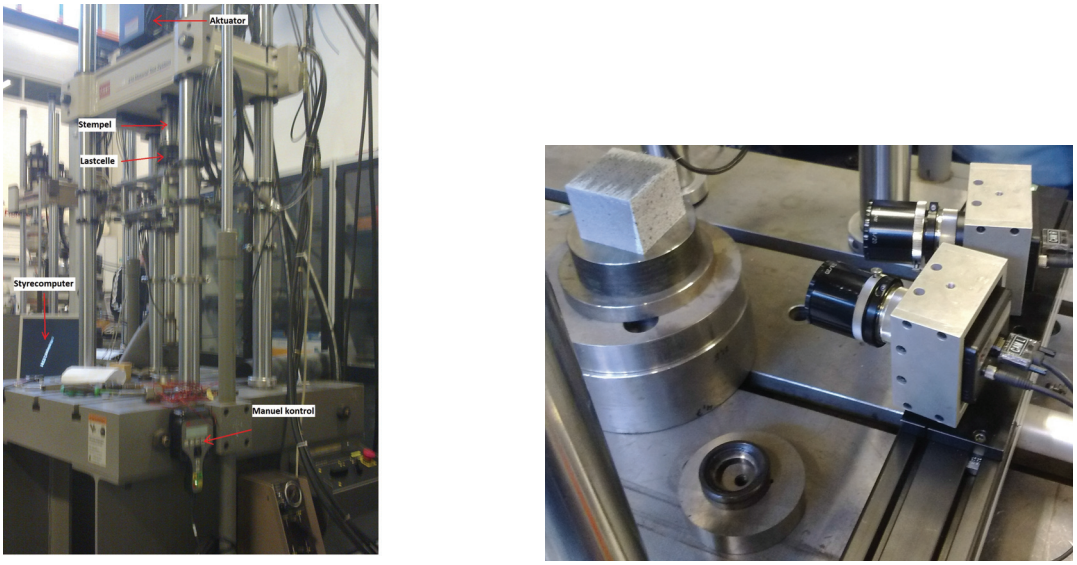

(a) (b)

Figure 6.4: Set-up used for the quasi-static foam tests

Table 6.1: Camera and ARAMIS settings used for the quasi-static foam tests

Camera settings	
Camera model	VDS Vosskühler
Resolution	2024×2024px
Frame rate	0.25fps
Shutter time	1/frame rate
ARAMIS settings	
Facet size	15×15px
Step size	13×13px
Computation size	3
Filtering	ARAMIS default

6.1.2 Dynamic Material Tests

To estimate the stress-strain behaviour of the foams and their dependence on deformation rate, cubical specimens with equal dimensions in all directions ($xyz = 40 \times 40 \times 40$mm), in addition to the quasi-static deformation speed, have been tested at three deformation speeds (4.0×10^{-4}m/s, 4.0×10^{-2}m/s, 0.4m/s) in the through-thickness direction. The applied test set-up, shown in 6.5, is based on a stiff test frame (capacity of 500kN) and a 50kN servo-hydraulic actuator capable of delivering a maximum piston speed of approximately 5 m/s. The specimens are positioned on the lower compression plate which is connected to the actuator piston. The piston is then accelerated to the specified velocity before the specimen reaches the stationary compression plate at the top, which is connected to the load cell. The specimen is subsequently compressed and deformed between the two compression plates. The high-speed

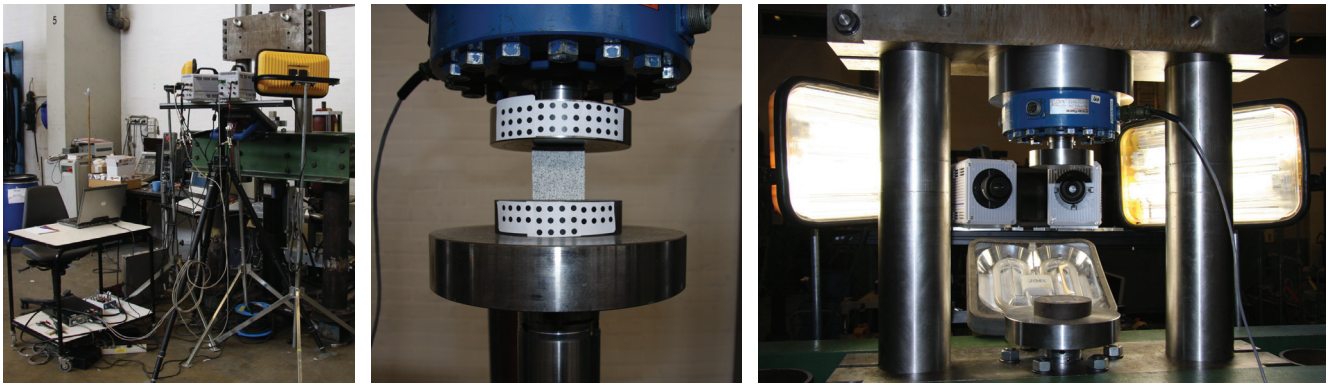

Figure 6.5: Set-up used for the dynamic compression tests of the foam materials

cameras are positioned such that, just before the specimens impact with the upper compression plate, the speckle-patterned surface will be in full view of the camera, making the DIC analysis possible. In addition to the speckle pattern on the specimen surface, the compression plates have been equipped with circular reference markers which can be identified by ARAMIS and used to perform additional analysis. Table 6.2 shows the camera and ARAMIS settings used for the dynamic compression tests.

Table 6.2: Camera and ARAMIS settings used for the dynamic foam tests

Camera settings	
Camera model	Photron APX-RS
Resolution[a]	
−0.01	1024 × 1024
−1	1024 × 1024
−10	768 × 768
Frame rate[a]	
−0.01	50
−1	500
−10	5000
Shutter time	1/frame rate
ARAMIS settings	
Facet size	15 × 15px
Step size	13 × 13px
Computation size[b]	3
Filtering	ARAMIS default

[a] Used resolution and frame rate for each target strain rate

[b] Number of facets along the edge in a quadratic area used to evaluate the strains

6.2 Elastic Properties of Divinycell H80 and H250 Foams

Table 6.3 shows the measured elastic properties for the two foam types. For each foam type five repetitions has been carried out. The elastic properties were based on the stress-strain values in the strain regime from 0 to 0.8% where a linear relation between the stress and strain existed. The stresses were calculated from the measured force divided by the surface area of the foam (60×60mm) onto which the load was applied. The strain is taken as the average strain over the area marked on the DIC contour plot shown in figure 6.6. From the area both the vertical and horizontal strain were measured. The area for measuring the strains has been placed in the centre of the specimen to avoid the influence of edge effect, which is seen for the through thickness strains in figure 6.6a, where there is a clear effect from the contact between the compression plates and the foam surface. Because of the cell structure of the foam, a completely uniform strain distribution cannot be achieved, as seen in figure 6.6b, where, for the marked area, the maximum strain is 0.47%, the minimum strain is 0.25% and the average is 0.35% with a standard deviation of 0.04%.

Table 6.3 shows the measured elastic properties for the two foam types tested and the 95% Confidence Interval. For both foams the through thickness moduli E_{th} was found to be approximately twice the value of the in-plane moduli E_{ip}, which fits well with the difference in the through thickness and in-plane cell structure of the foam, and also with the findings in other studies as mentioned above. Comparing the found E_{th} values with the values given in the data

Table 6.3: Measured elastic properties of the two foam types

	H80		H250	
	Average [MPa]	95% CI	Average[MPa]	95% CI
E_{th}	81.7	5.7	382.3	10.9
E_{ip}	40.7	6.6	192.9	9.2
ν_{zx}	0.35	0.022	0.36	0.012
ν_{xy}	0.37	0.013	0.38	0.014

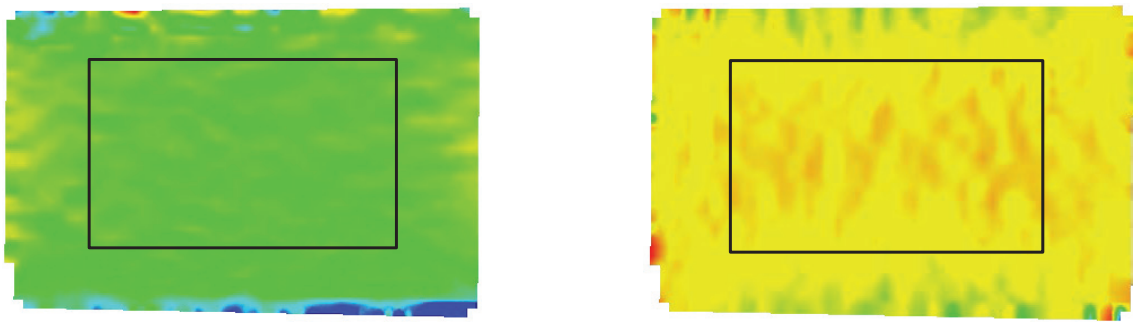

(a) Through thickness strains **(b)** Horizontal strain

Figure 6.6: DIC contour plots showing the area where the strains, for calculating the elastic foam properties, were taken.

Table 6.4: Difference between measured foam density and nominal values taken from the DIAB datasheet. The density is in kg/m^3

	Average	Nominal	%-dev
H80	74	80	8.1
H250	245	250	2.0

sheet from DIAB (see appendix B.6), then, for both foam types, the measured values are below the nominal values given in the data sheet, but above the guaranteed minimum values stated.

The difference between the nominal values and the measured values can be explained by a difference in the density between the data sheet material, and the tested material. Table 6.4 compares the calculated density of the tested foams and the nominal density of the data sheet foam. In both cases the density of the tested foam is less than the nominal density, indicating that the microstructure in the tested foam has a larger number of cells than the nominal foam. This also fits with the measured E_{th} being less than the nominal value, since the stiffness of the foam depends on its cell structure. The deviation between the measured and nominal moduli can be calculated to 10.2% for the H80 foam and 4.6% for the H250 foam. These deviations also fit with the deviations seen for the densities, which underline the close relationship between foam density, its cell structure, and the elastic moduli.

As seen from the test results a clear Poisson effect exists in the elastic regime. When shifting from the elastic to the crushing regime the Poisson effect vanishes. But as described section 3.4 the chosen material model does not include Poisson effects before densification is reached. This is in clear disagreement with experimental observations. But for the currently available material models in LS-DYNAfor modelling foam mateirals no model exists that can include Poisson effects in the initial elastic regime but not in the crushing regime. Either Poisson effects was included during the entire compression or not at all. It was therefore accepted to neglect the initial Poisson effects in the modelling as this only concerned in the very initial part of the entire foam compression. Including the Poisson effects in the entire compression would clearly lead to a more erroneous behaviour. To overcome this challenge would most likely require a reformulation of one of the existing foam material models in LS-DYNA, which was found to be out of the scoop of the present work.

In [54] Daniel and Cho reported elastic properties for H250 foam from DIAB. The reported values are shown in table 6.5. Good agreement between the measured values and the reported values in [54] was found for the in-plane moduli E_{ip}, ν_{12}, and ν_{13}, which has been calculated to 0.19 by used of the reciprocity equation

$$\frac{\nu_{xy}}{E_x} = \frac{\nu_{yx}}{E_y} \tag{6.1}$$

Table 6.5: Elastic properties for H250 foam type measured by Daniel & Cho [54]. The unit of E and G is MPa

E_{ip}	E_{th}	ν_{xy}	$\nu_{xz} = \nu_{yz}$	G_{xy}	$G_{xz} = G_{yz}$
201	322	0.33	0.20	85	110

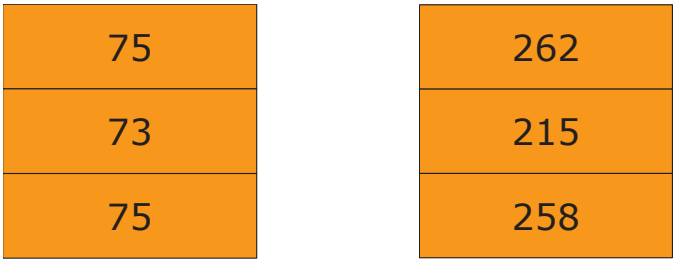

(a) Divinycell H80 **(b)** Divinycell H250

Figure 6.7: Measured density of three sections of the foam types, measured by slicing the foam into three pieces, illustrating the density distribution through the thickness of the foams. The shown densities are in kg/m^3

Looking at the E_{th} a much lower value is reported by Daniel and Cho. This difference can relate to differences in the test set-up. In [54], specimens with a smaller thickness than used here were tested. The specimens could therefore have another cell structure distribution, which could result in the low stiffness measured. Comparing the value from [54] with the DIAB data sheet value it is lower than the guaranteed minimum value and is actually closer to the nominal stiffness of H200 than H250. For the two measured foam types a study was performed to estimate the density distribution through the thickness of the foams, which must exist due to the difference in the microstructure through the thickness of the specimen, as shown in figure 6.3 on page 69. Here one specimen of each foam type were sliced into three pieces, as illustrated in figure 6.7, and for each slice the volume and weight was measured such that their approximate density could be estimated. The calculated density for each slice is shown in the figure and clearly shows that for the H250 specimen the centre part has a much lower density than the outer parts. For the H80 specimen a more even density distribution is seen. If for example the panel tested in [54] originates from an originally thicker H250 panel where the top and bottom surfaces have been cut away to obtain the desired thickness, resulting in a panel with a weaker cell structure than in the original H250 panel, then that could result in the low E_{th} reported.

6.3 Stress-Strain Behaviour of Divinycell H80 and H250 Foams

To measure the stress-strain response of the two foam materials under uniaxial compression, the test procedure outlined in section 6.1.2 was used. For each of the deformation speeds the specimen was deformed as much as the test machine was capable of, utilizing the specimen itself as a damper to prevent the two compression plates from impacting with each other. As for the test performed to measure the elastic properties of the foam types, five repetitions at each of the test velocities were performed. For these tests the stress was again calculated from the applied force divided by the surface area ($40 \times 40mm$) of the foam samples. The strain was based on the surface strains measured by the DIC system.

During the tests it was observed that the foam specimens did not deform uniformly, a behaviour that could be related back to the cell structure distribution described in the beginning of this chapter. This observed behaviour entailed that some considerations on how to measure the strain on the specimen had to be done before the stress-strain curves could be established.

Another issue that had to be dealt with was that at a strain of approximately 50% the speckle pattern on the specimen was so disturbed that the correlation algorithm in ARAMIS was no longer able to facet movement and thus not able to calculate the specimen strains.

6.3.1 Foam Deformation Behaviour

From the DIC analysis it was found that the deformation of the foam blocks was not homogeneous. After passage of the crush strength, σ_{cr}, the cell crushing started to develop in bands, a behaviour seen for both the H80 and H250 foam types. An example of such *collapse bands* is shown in figure 6.8. For all tests performed on the H250 foam the collapse bands always developed in a horizontal zone around the centre region of the specimen. For the H80 foam the collapse bands developed at more random locations through the cross-section of the specimen and the shape of the bands were not the same clear horizontal shape as seen for the H250 foam, but had different shapes for the individual tests. The location of the collapse band for the H250 specimen fits well with the observed cell structure and density distribution, showing that there is less material in the centre region to support the applied stresses. For the H80 the same clear cell size distribution was not identified which explains the more random location and shape of the formed collapse bands seen in these specimens. After the collapse bands had developed, all further straining grew from the collapse zone such that a large part of the specimen was almost unstrained a opposed to the part in the collapse zone which can be strained up to more than 50%.

Because of these collapse zones, measuring the strain of the specimen is not straight forward, as one part of the specimen experiences large strains, while other parts of the specimen experience almost no strain. Figure 6.9a shows the strain development over times for the H250 specimen for five different lines positioned as shown in figure 6.9b. As can be seen, there is a significant difference between the strain measured by only focussing on the central part of the specimen (Line-2) and over the whole specimen (Line-5). When Line-2 reaches its maximum strain (46.6%) the strain of Line-5 is 21.6%. For line 2-5 it can be seen that the maximum strain measured is approximately 50%. At this strain level the speckle pattern, necessary for the ARAMIS to calculate the strain, becomes so disturbed that ARAMIS no longer can recognise it and the calculations breaks down. Using the lines on the specimen, strain larger than 50% can thus not be measured. To overcome this problem, an additional line, Line-1, was created.

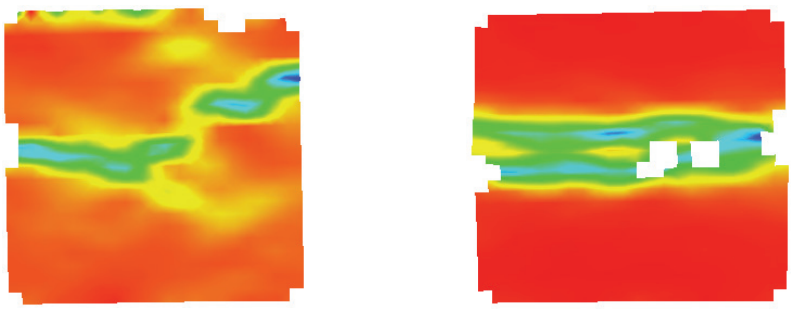

(a) H80 **(b)** H250

Figure 6.8: Example of the crush band formation developing when the cell structure in the foams starts to collapse

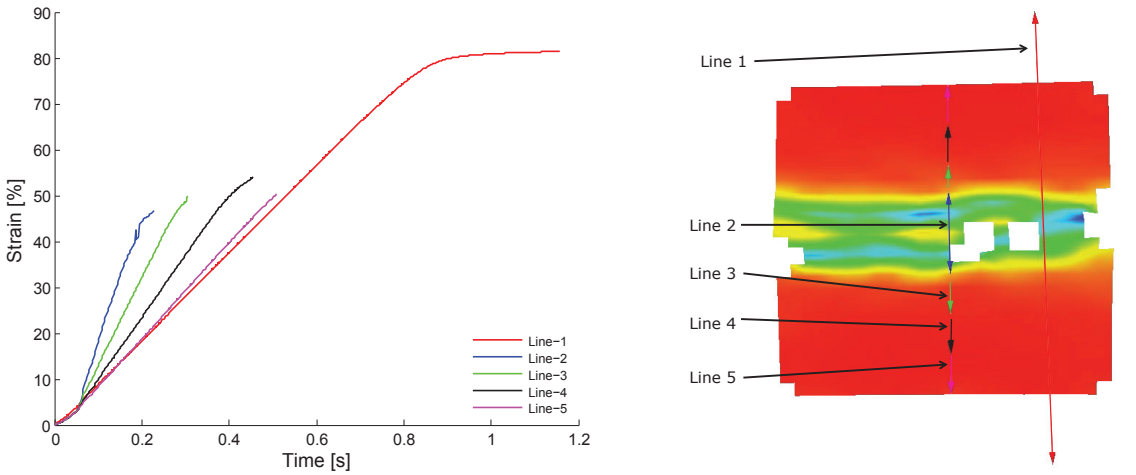

(a) (b)

Figure 6.9: Strain–time development measured along the five different lines shown in (b)

Line 1 in the figure represents the strain taken over a line between the reference points on the compression plates (shown in figure 6.5 on page 72). The strain of this line is evaluated with the specimen height as the reference length, as it is assumed that the strain is solely due to the straining of the foam specimen since the compression plates can be taken as rigid compared with the foam. Using Line-1 it is therefore possible to measure the strain of the specimen beyond 50%.

The difference in the strain development over time raises an issue with respect to the actual strain rate experienced by the specimen. Figure 6.10 shows the strain rate for each of the lines in figure 6.9, calculated by taking the point to point derivative and smooth the result with a 5-step moving average filter. As clearly shown, the line around the crush zone experience a significantly larger strain rate than, for example, the line closest to the specimen edges. As the foam starts to densify, the strain rate in the centre drops because the primary straining moves away from the centre area and to areas where the foam has not yet densified, and therefore is easier to deform. This mechanism continues through the thickness of the specimen, shown by the stepwise decrease in the strain rate for line 2-4. Due to the creation of the collapse zones there will therefore at no point of the compression, after the crush has initiated, be a constant strain rate through the thickness of the specimen.

For the given example the target strain rate was set to$1s^{-1}$. This was obtained by setting the speed of the piston to a constant velocity, knowing that the engineering strain rate relates to the velocity by

$$\dot{\varepsilon} = \frac{v}{h} \tag{6.2}$$

where v is the deformation velocity and h is the initial height of the specimen. As seen from figure 6.10 the target strain rate is naturally obtained for Line-1, since this line is based on points on the compression plate. Looking at Line-5 the strain rate here is also close to the target strain rate. A stress strain curve that has the target strain rate as a reference can therefore only be obtained by taking the strain over the whole specimen, as seen for Line-1 or Line-5. When the entire foam block has been compressed to the point of densification, the strain rate for Line-1 starts to drop as more and more force is needed for continued compression of the

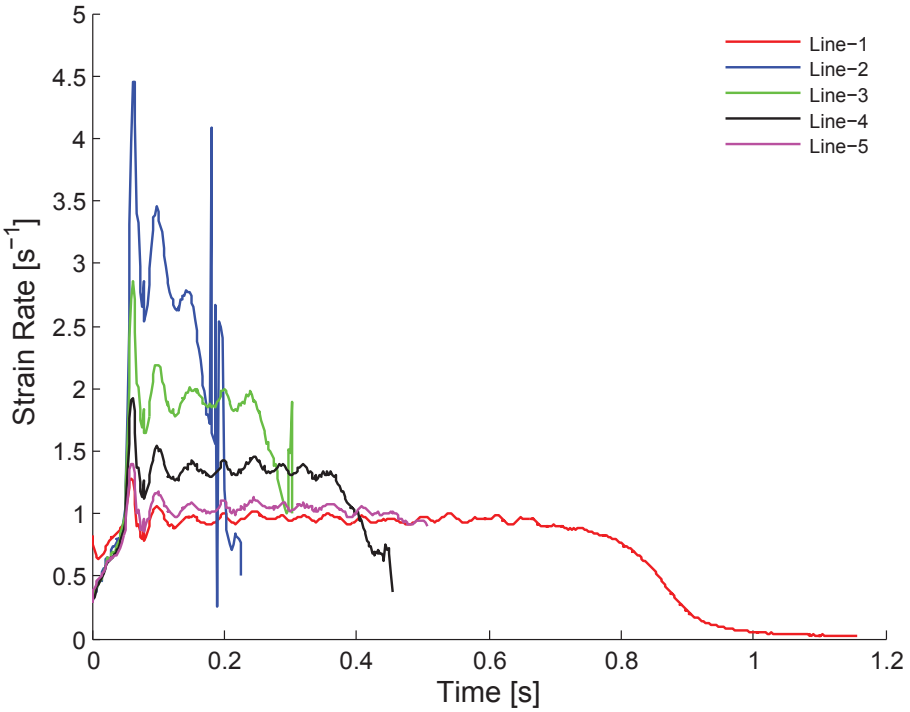

Figure 6.10: Strain rate for each of the measurements shown in figure 6.9a

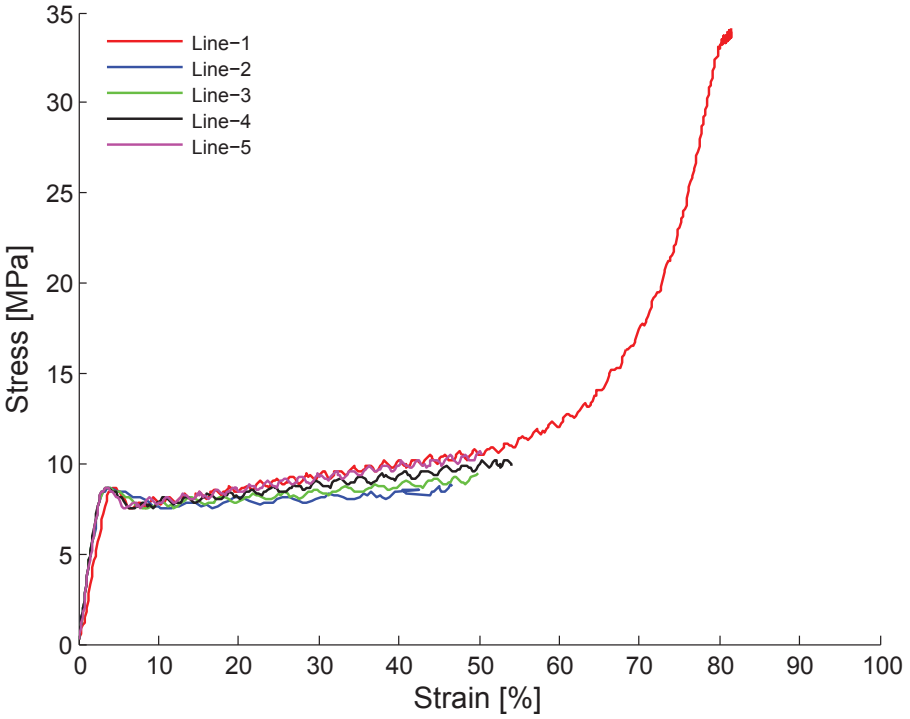

Figure 6.11: Stress strain curve based on each of the lines shown figure 6.9b

specimen. But due to lack in the machine response time and getting close to the maximum load capacity of the machine, the strain rate cannot be maintained for the last part of the compression. For the H80 specimen, which compresses at much lower stresses, the strain rate can be obtained all the way through the deformation

In figure 6.11 the stress-strain curves for the 5 lines in figure 6.9a are plotted. Again, the effect of the localized deformation is seen. Looking for example at Line-2 then, because there is less material to support the stresses, the straining happens at a lower stress than the stresses needed to compress e.g. Line-4 to the same amount of strain. For Line-4, which contains part of the foam specimen away from the centre region, the cell structure is, on average, denser and can thus support larger stresses, which is why the shown difference between the stress-strain behaviour of LIne2 and 4 is seen. Previously it was shown that Line-1 had an average strain rate representative of the target strain rate for the given example. It therefore would be obvious to use Line-1 to generate the stress-strain curve for the foam specimen, but as seen in figure 6.11, using Line-1 will give an initially too low stiffness. This is because when the compression plates make contact with the foam, locally large strains develop in the contact region until proper contact is established.

To generate a proper stress-strain curve representative of the average strain rate by which the specimen is deformed, it has therefore been decided to use a combination of Line-1 and Line-5 as this choice will give: (a) the correct initial stiffness (b) a stress-strain curve for the deformation of the foam specimen all the way up to densification, and (c) a correct representation of the average strain rate by which the specimen has been deformed. In figure 6.12, Line-1 and Line-5 are shown together with the combined line. Here Line-5 has been used up to a deformation of

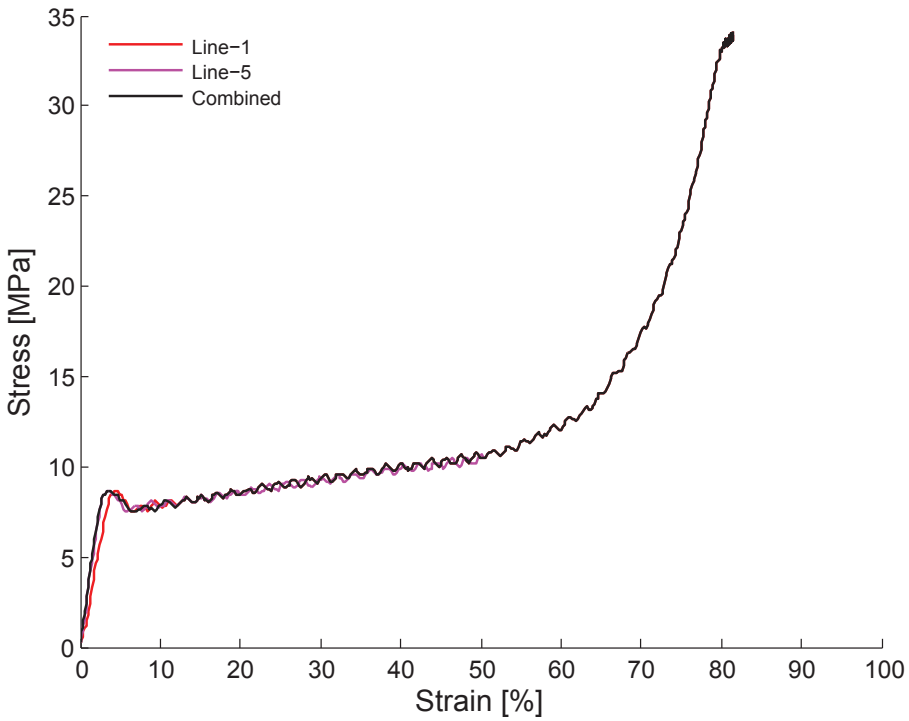

Figure 6.12: Stress-strain curve for the H250 foam example based on the combination of the stress-strain curves measured from Line-1 and 5 in figure 6.9b

20% after which Line-1 takes over. For all the tests performed on H80 and H250, at the strain rates given in tables 6.1 to 6.2 on pages 71–72, this procedure was used to generate proper stress-strain curves for the tested specimens. The *cut-over* strain level, where the curves are combined, are judged manually from test to test.

6.3.2 Stress Strain Relationship

For each repetition, a stress-strain curve was generated using the principle described above. From these stress-strain curves a single average stress-strain curve was then generated by use of interpolation. Figures 6.13 and 6.14 show the obtained average stress strain curves. The shape of the curves shows the characteristic behaviour of a foam under uniaxial compression as described in figure 6.1 on page 68. Both foam types show a local stress peak at the crush strength followed by the stress plateau. For the H80 foam the stress plateau has an almost constant stress until the densification takes over at a strain of approximately 80%. For the H250 foam the stress continuously increases during the crushing regime until the densification takes over, which happens at approximately 70% strain. For both foam types a clear response to the strain rate can be observed. The rate response can be expressed as '*an upward shift of the curves with the slope of the elastic part giving the direction of the shift*'. The elastic stiffness does not seem to be affected by the strain rate, as indicated by the coincident slopes of the initial part of the stress-strain curves. Table 6.6 shows the crush strength for the two foams at the tested strain rates. Comparing the crush stress level of the two foams, the H250 can withstand stresses of approximately five times the level of the H80. Looking at the increase in the crush strength levels with respect to the values at quasi-static strain rate, the same relative increase is seen for the two foams indicating that the rate sensitivity is similar, which makes sense since they are made from the same polymer base.

From the DIAB data sheet (appendix B.6) the nominal and minimum crush strength values for H80 are 1.4MPa and 1.15MPa respectively; and for the H250 foam the data are 7.2MPa and 6.1MPa. Comparing the measured crush strength with the data sheet value, good agreement is found against the nominal data.

6.3.3 Strain Rate Dependency

The observed strain rate response, with the upward shift of the stress-strain curve without a change in the form of the stress-strain curves, indicates that the strain rate response of the foam can be described by scaling a reference stress-strain curve up or down by a scaling parameter, which depends on the applied strain rate relative to the strain rate, which the reference curve

Table 6.6: Measured crush strength of the two foam types

	H80			H250		
Strain Rate	σ_{cr} [MPa]	95% CI	RI[a]	σ_{cr} [MPa]	95% CI	RI[a]
0.001	1.32	0.05	–	6.99	0.25	–
0.01	1.51	0.06	1.14	7.92	0.12	1.13
1	1.71	0 02	1.3	8.84	0.23	1.26
10	1.91	0.1	1.45	9.82	0.20	1.40

[a] Relative increase in crush stress relative to the crush stress at quasi-static strain rate

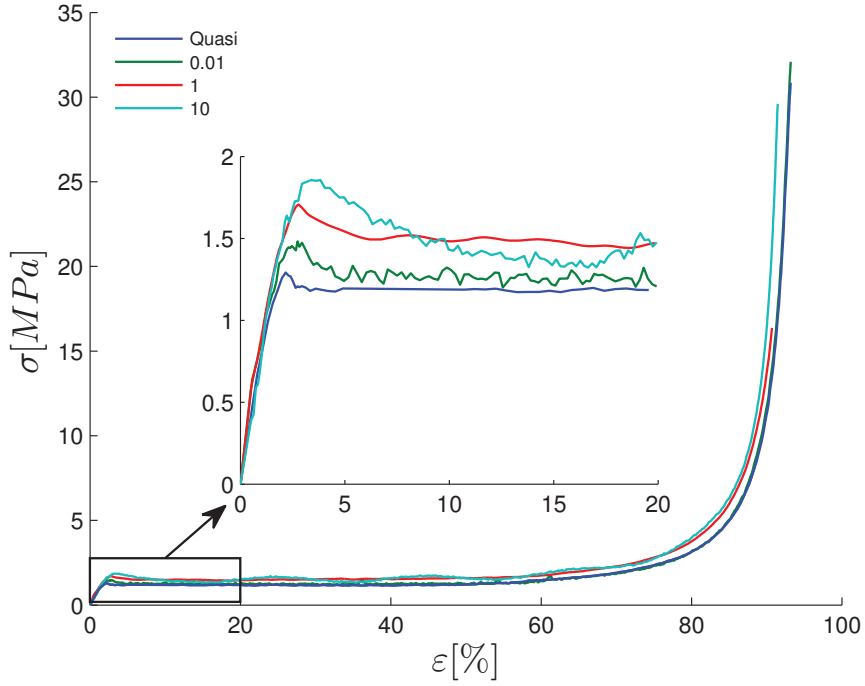

Figure 6.13: Measured stress strain curves for the H80 foam

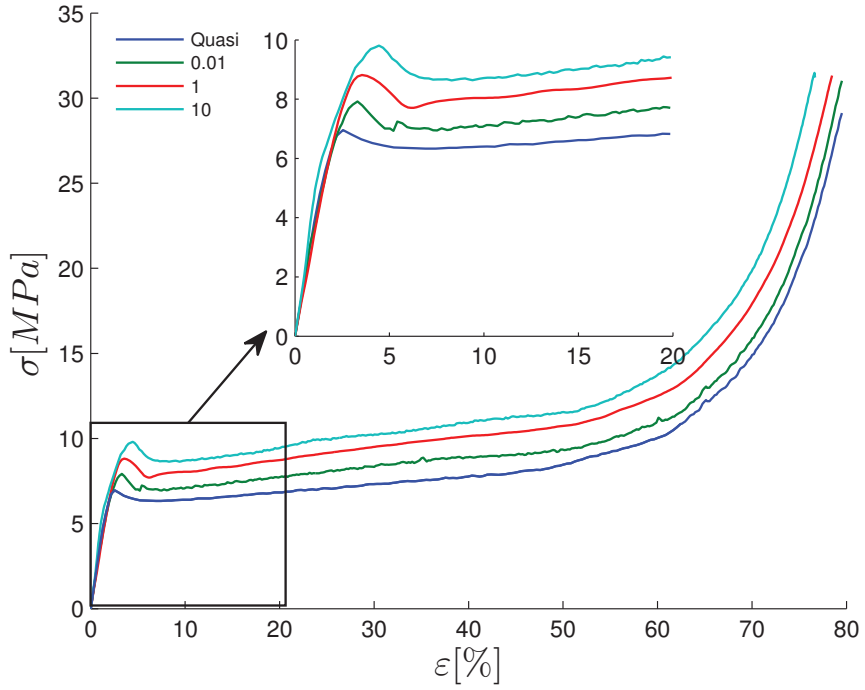

Figure 6.14: Measured stress strain curves for the H250 foam

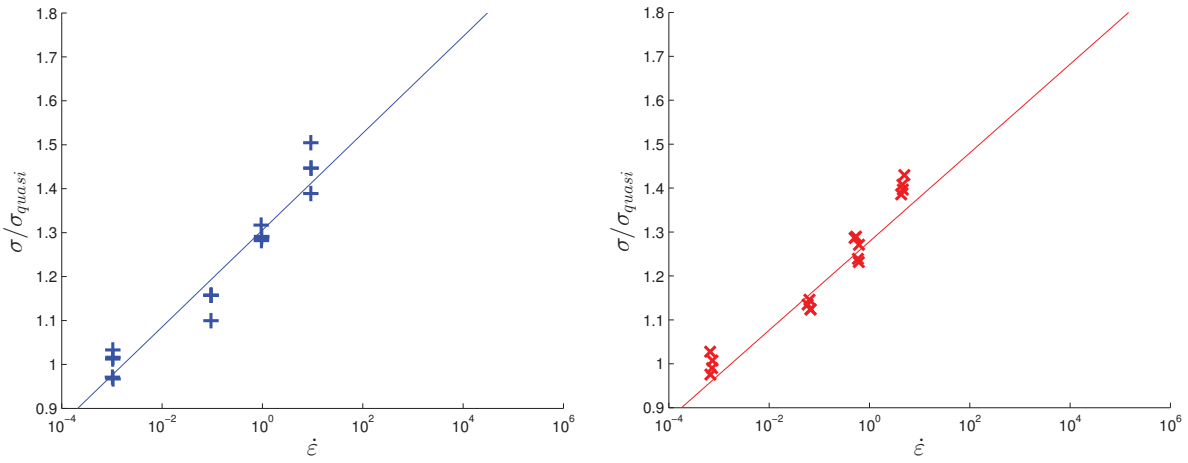

(a) H80 **(b)** H250

Figure 6.15: Relative increase in crush strength as a function of strain rate

is been based on. A suitable candidate for generating a scaling parameter could be the crush strength σ_{cr}. According to [52] the strain rate response of σ_{cr} can be described by a logarithmic relationship of the following form

$$\sigma_{cr} = \sigma_{cr}^{ref}\left(1 - \frac{AT}{T_g}\ln\frac{\dot{\varepsilon}_{ref}}{\dot{\varepsilon}}\right) \tag{6.3}$$

where σ_{cr}^{ref} and $\dot{\varepsilon}_{ref}$ can be taken as the crush strength and strain rate for the reference curve, T and T_g are the temperature of the material and its glass transition temperature and A is a material parameter. In figure 6.15 the measured crush strength for the two foams is plotted as a function of strain rate, with the x-axis set to logarithmic scale. A logarithmic function of the form shown in equation (6.4)

$$\frac{\sigma_{cr}}{\sigma_{cr}^{ref}} = a\ln\frac{\dot{\varepsilon}}{\dot{\varepsilon}_{ref}} + b \tag{6.4}$$

which is a paraphrasing of equation (6.3), was fitted through the data as shown in the figure. In table 6.7 the fitted model parameters are shown together with the *coefficient of determination* R^2, showing a good fit to the proposed model for both data sets. Looking at the b parameter, then for a perfect fit with the proposed model; $b = 1$, which is almost the case for both foam types indicating that for the reference strain rate the model will predict the reference crush strength with good accuracy. The a parameter expresses how sensitive the foam is against rate effects. The higher a the larger a change in crush strength with increasing or decreasing strain

Table 6.7: Fitting parameters for the two foam types, when fitting the relative increase in crush strength to expression (6.4), with R^2 being the coefficient of determination

Foam type	a	b	R^2
H80	0.11	0.98	0.94
H250	0.10	0.98	0.95

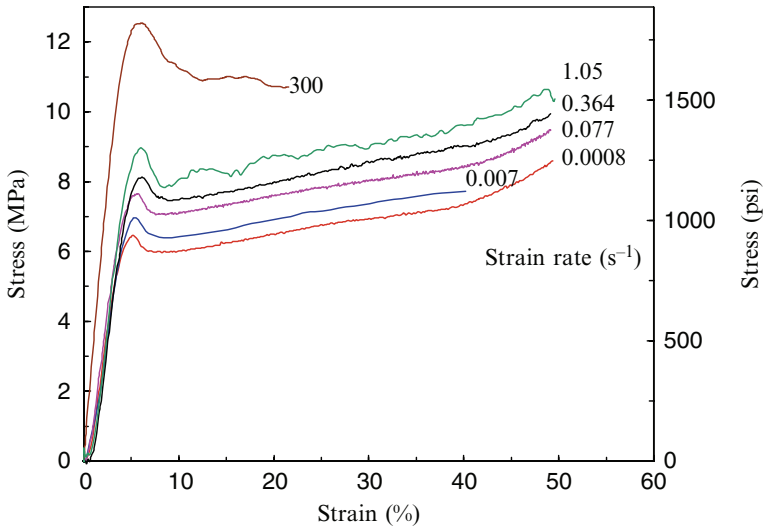

Figure 6.16: Stress-strain curves reported in [59], measured at the indicated strain rates

rate will be seen. From table 6.7 it is observed that the a value is almost equal for the two foams, indicating that their response to rate effects is very similar, which makes sense as the foams are based on the same polymer base and thus should show the same rate behaviour [52]. Because the rate response of the foams corresponds to a vertical parallel shift of a reference curve with known strain rate and σ_{cr}, it is therefore possible, using equation (6.4) and the found parameters for the two foams, to generate stress strain curves at an arbitrary strain rate, where the new curve will have the same shape as the reference curve and a crush strength predicted by (6.4).

In [59] stress-strain curves for Divinycell H250 foam obtained at different strain rates were reported, and are shown in figure 6.16. In figure 6.17a the crush strength of the curves in figure 6.16 at their indicated strain rates have been plotted together with the measured crush strength for the H250 foam. As can be seen good agreement is found between the data in the strain rate regime tested here ($\dot{\varepsilon}_{max} \leq 10$). Following the trend line based on the performed measurements, the point reported in [59] at $\dot{\varepsilon} = 300$ clearly deviates from this fit, and fitting a line through the data from [59] also results in a fit showing a more rate sensitive response than found for the tested H250 foam.

In [59] it is reported that the data for strain rates below $\dot{\varepsilon} = 1$ were generated by uniaxial compression tests, whereas the data for higher strain rates ($\dot{\varepsilon} = 300$) are obtained by use of Split Hopkinson Pressure Bar tests. The data sets in [59] have thus been obtained from two different test set-ups, where different specimen sizes could have been used. This has not been verified since no details regarding specimen sizes are reported in [59], but the use of two different test set-ups alone could give rise to questioning whether such data can be compared. In figure 6.17b a new fit for the data in [59] has been made where the data point at $\dot{\varepsilon} = 300$ has been ignored in the fitting procedure. Here, where only test data obtained from uniaxial compression test were used, a much better correlation between the fitted models for the two data sets is seen, indicating that the data set obtained from the Split Hopkinson Pressure Bar test has affected the measured response of the material, such that it does not conform with the response obtained through uniaxial compression tests.

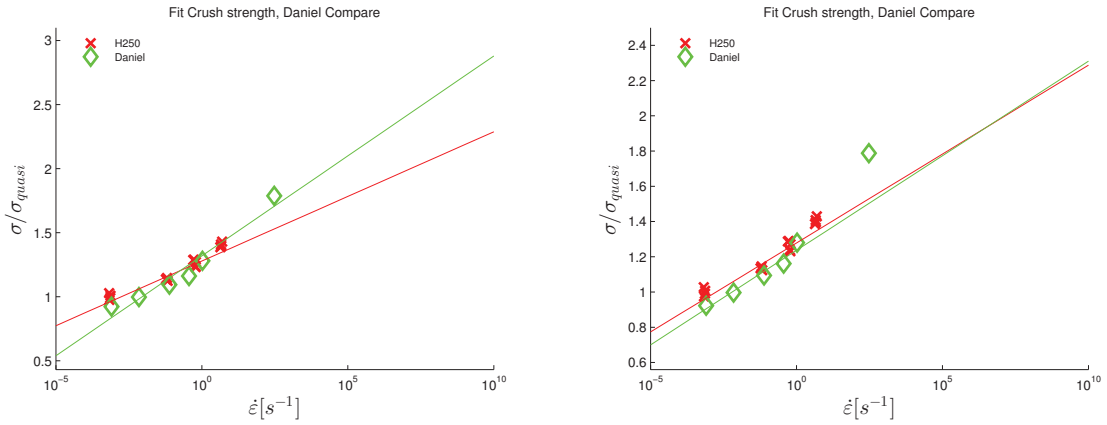

Figure 6.17: Comparison between the measured crush strength of H250 and data obtained taken from [59]

6.4 Summary

Foam types Divinycell H80 and H250 from DIAB were tested in uniaxial compression at different strain rates. Firstly to measure the elastic properties of the foams and to generate stress-strain curves for the foams for use as input in numerical models where the foam is to be modelled; and secondly, to gain knowledge on the rate response of the material and see if the response could be modelled in a simple manner such that rate effect could be included in the numerical modelling of the foam.

The compressive modulus and the Poisons ratios were measured by use of DIC on both specimen types. The found data agreed well with the data in the DIAB data sheets and also with data from the literature. The measurements also showed that the material was transverse isotropic, an observation supported by other studies. In this work only the through thickness and in-plane modulus was measured. For modelling purposes, data for the shear modulus is also needed. Data for this will be obtained from[54].

During the compression tests to measure the foam stress-strain relationship, it was found that the foams did not deform uniformly, but collapse lines developed from which all further straining arose. This collapse line formation could be related to the non-uniform cell structure distribution in the material, which caused a non-uniform density distribution in the material. The collapse line developed in the area of the foam having the lowest density and thus the least amount of material to carry the stresses. The collapse line formations were not alike for the two foam types, which again could be related to the H250 foam, which has a much more pronounced difference in the cell structure through the thickness than was seen for the H80 foam.

The identification of the collapse line deformation meant that considerations about how to establish the stress-strain curves for the foams had to be made. The presence of the collapse lines entailed that the strain development in the foam was non-uniform and that the strain rate therefore was not constant. A choice was made to use an overall average strain for the specimen, as this took into account both the weak and strong parts of the foam, and it also meant that a constant average strain rate could be ascribed to the stress-strain curves.

For both foam types, stress-strain curves were established for the tested strain rates, showing

the characteristic shape of a rigid foam under uniaxial compression. A clear rate response was identified showing a similar rate sensitivity for the two foam types. Plotting the crush strength level for the different strain rates showed that the increase in crush strength could be described by a simple logarithmic relation given in [52]. Since the rate response of the foams was expressed as an upward parallel shift of the stress-strain curves, the used rate law for the crush strength can be used to generate scaling parameters to shift a reference stress-strain curve such that it can express the stress-strain curve at an arbitrary strain rate. A set of scaling parameters for a set of strain rates can thus be made and used in numerical models as a simple way to account for rate effects of the foam.

Chapter 7

Blast Modelling

One of the objectives of this project was to establish a numerical framework for modelling blast loading on laminated panels. From the start it was decided to use LS-DYNA as the numerical solver, and to use the available models in LS-DYNA for modelling the blast load and the laminated structures. As described in chapter 3, two laminate models, *MAT_ORTHOTROPIC_ELASTIC and *MAT_COMPOSITE_DMG_MSC, were selected to represent the monolithic laminates and the skins on the sandwich panels. *MAT_HONEYCOMB was selected to represent the foam core in the sandwich panels. Input data for these models are based on material tests, where the data for the laminates can be found in appendix B and [37], and the data for the foam are based on the measurements in chapter 6 and data from [54, 59].

In LS-DYNA the blast load can be modelled using two approaches as described in chapter 3; the *Emperical* or the *Fully Coupled* approach. Here both approaches have been used in the modelling work. First of all to compare the two approaches, and secondly, to identify if the reflections from the closed sides of the blast box contribute to the impulse transferred to the panel. The application of the *LOAD_BLAST_ENHANCED (LBE) model is straightforward, but the fully coupled approach requires a much more complex model design, because for example both the blast itself and the fluid structure interaction between the blast wave and panel is modelled numerically.

7.1 Design of Numerical Blast Load Model

Several challenges exist in the design of a numerical blast model;

- The explosive charge should, as a minimum, be covered by 6–10 elements over its radius[1]
- The geometrical size of the panels to be modelled is 700 × 700mm including the clamped area, and the depth of the blast box is 300mm
- The element size in the ALE and Lagrangian parts should be of similar size for the FSI coupling to work properly.
- The time for the load transfer to the panel is much shorter than the response time of the panel.

[1]Recommendation received at an LSTC seminar for modelling blast problems in LS-DYNA

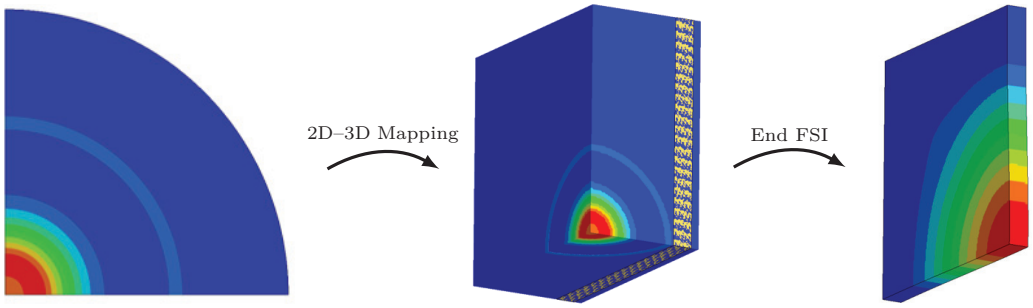

Figure 7.1: Illustration of the 3 step blast model where: (a) illustrates the first model step, a 2D model, where the explosive is detonated and the blast wave is build up; (b) illustrates the step where the pressure from the 2D model is mapped on to a 3D model, representing the blast box, and the interaction between the blast wave and panel is handled through an FSI coupling; and (c) illustrates the last step where, after all impulse has been transferred to the panel, the ALE mesh is removed and the structural analysis is continued

The combination of these effects would for a single model lead to a computationally demanding model consisting of a very large number of elements. To approach the challenge of designing a computationally efficient load model it was therefore split up in three parts, as illustrated in figure 7.1, each of which can be described as follows;

Blast wave generation, illustrated in 7.1a, where a 2D model is used to model the explosive geometry, the detonation of the explosive and the initial generation of the blast wave. Utilizing that the blast waves from a spherical charge spreads spherically in space, the generated pressure can be used to initialize a pressure in a 3D model, by choosing proper axis for rotational symmetry.

Fluid Structure Interaction, illustrated in 7.1b, where the pressure from the 2D model is mapped on to the 3D model mesh, representing the air in the blast box, and the Fluid Structure Interaction between the blast wave and panel is modelled.

Structural response, illustrated in 7.1c, where the *air mesh* has been removed, after checking that no more impulse from the blast load is transferred to the panel, leaving the model with only the panel part, which will continue to respond to the applied loading, resulting in much faster computation than with the FSI coupling active.

The clear advantage of this model design is first of all the time efficiency. By using a 2D model for detonation of the explosive and generation of the blast wave, a model with a very fine numerical mesh can be constructed, resulting in the generation of a sharp pressure front of the blast wave, and which can execute within minutes. Making a similar model in 3D would result in a significantly larger model that would take several hours of calculation time. A second advantage is that the time where the FSI coupling is active is minimized. The FSI coupling is computationally expensive as it requires continuous search algorithms to monitor for fluid structure contact. Finally the removal of the ALE mesh, after load transfer, also reduces run

time since only the Lagrangian structure is kept in the model, which is computationally not as demanding as the ALE parts, due to the advection calculations for those elements. In the following, details of each model part will be given.

7.1.1 Blast Wave Generation

The first step in the numerical load model is to model the explosive charge itself, its detonation and the initial generation of the blast wave. This will be done using the models described in chapter 3. When detonating a perfectly spherically shaped charge, spherical blast waves are generated and spread in space from the detonation point. Because of this, quarter symmetry can be used in the 2D model to model the explosive charge and air, as illustrated in figure 7.2a, where the yellow part is the initial charge and the green area the surrounding air. The symmetrical expansion of the blast wave is also utilized in the next model step, where the modelled 2D pressure is used to initialize the pressure in the air domain of the 3D FSI model, by choosing proper axis for rotational symmetry of the generated blast pressure.

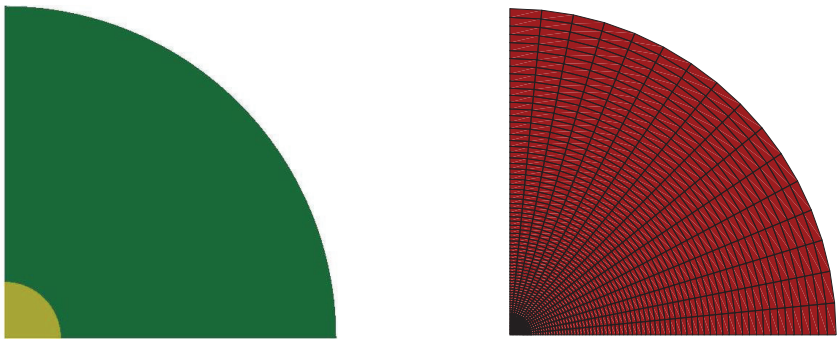

(a) (b)

Figure 7.2: Design of the 2D model where; (a) shows the initial model setup with the yellow part representing the explosive charge and the green is the surrounding air, and (b) shows the mesh structure used in the 2D model

In figure 7.2b the mesh structure used for modelling the blast wave generation is shown. A convergence study was carried out to see how the generated blast pressure developed as function of the number of elements used in the model. The mesh refinement was done by giving the circular arc a finer and finer division, going from 16 and up to 256 (referred to as $Div16$ and $Div256$ in the following, with the other divisions named in the same manner) line elements, resulting in the overall number of elements going from 1216 elements, for $Div16$, to 311296 elements for $Div256$. The study was performed for a 100g TNT charge, where the free air pressure, or incident pressure, was measured at 100mm from the charge centre. Figure 7.3 shows the measured pressure for the five mesh refinements used, measured 100mm from the charge centre, and figure 7.4 shows the corresponding accumulated impulse for each pressure curve. As can be seen the finer mesh used the larger peak pressure measured, which is due to a more clearly defined pressure wave front, with decreasing elements size, which is also shown by the more instantaneous pressure rise observed. Looking at the impulse, a decrease is seen as the element size is decreased. From $Div128$ to $Div256$ the impulse decreases by -1.7% which is an acceptable change, and $Div128$ is taken as the converged mesh size. In figure 7.3 the generated incident pressure for a similar set-up, but with the blast pressure modelled with the

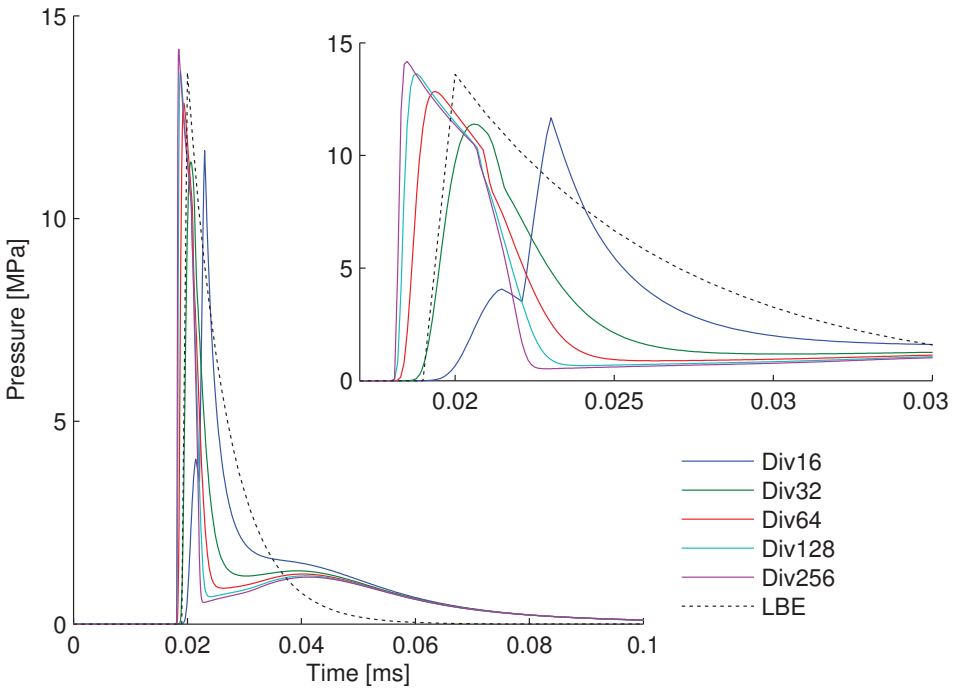

Figure 7.3: Measured pressure for the different mesh refinements of the 2D model, measured 100mm from the charge centre

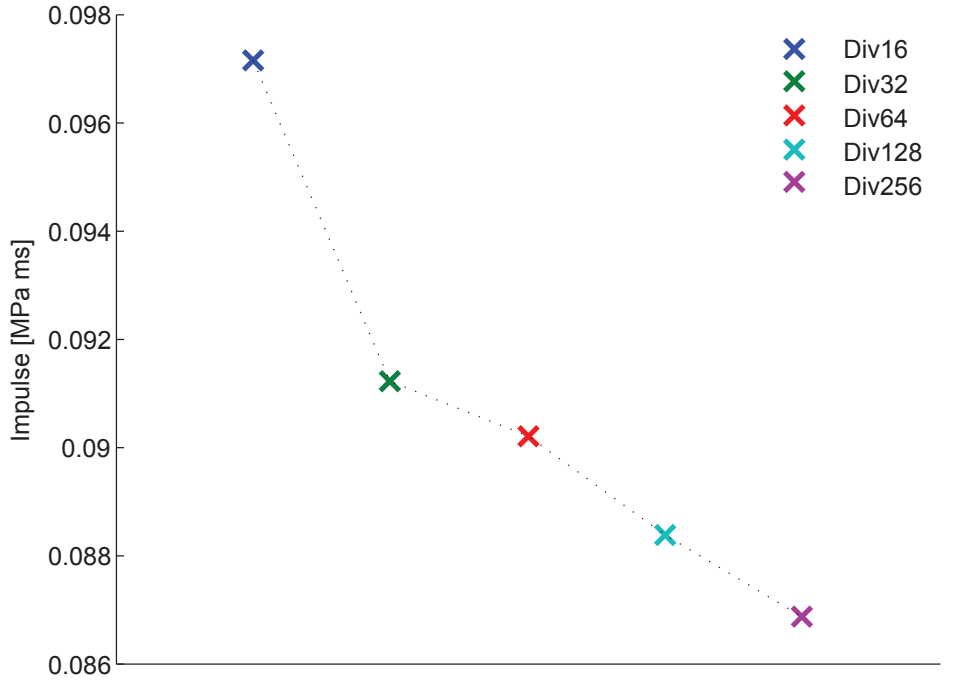

Figure 7.4: Accumulated impulse generated from the pressure curves in figure 7.3

LBE model, is also plotted, showing similar peak pressure as the pressure of *Div*128, supporting the convergence for this set-up. The pressure and impulse shown in figure 7.3 and figure 7.4 have been measured along the horizontal edge of the air domain 100mm from the charge centre. Taking a similar measurement 100mm from the detonation point, on a line inclined by 45°, exactly the same pressure and impulse are obtained showing the perfectly spherical expansion of the blast wave.

Comparing the impulse from the pressure curves of LBE and *Div*128, by looking at the area under their respective curves in figure 7.3, it is clear that the impulse from LBE is significantly higher. Looking closer at the pressure curves for *Div*32 to *Div*256 a characteristic bend is observed at approximately 0.021ms, indicating a shift in the behaviour of the pressure. Figure7.5a shows the pressure wave when it reaches the measuring point and (b) shows the *detonation products* from the decomposed explosive material lagging behind the pressure front. The detonation products should be understood as the fire, smoke etc. that develops from the detonation of the explosive. The peak pressure in figure 7.3 corresponds to the time at which the pressure front passes the marked measuring point, positioned 100mm from the charge centre. The bend observed in the pressure curves coincides with the time where the detonation product front passes the measuring point, indicating that it is a change in material composition that causes the pressure change, and that the domain with the detonation products has a much lower pressure than that in the blast wave front. In [60] similar effects are observed, where it is argued that *LOAD_BLAST_ENHANCED might not be accurate for near field blast cases, where interaction with the detonation products can happen. It has not been confirmed if the effect represents reality since measuring incident pressure will require the establishment of a test set-up suitable for measuring such pressures.

Based on the convergence analysis, the *Div*128 mesh will be used further on to generate pressure initialization maps for the 3D FSI model. The 2D model will then be run for a specific charge size for which a modelled plate response is required. The pressure map files are automatically created by LS-DYNA at the termination of the 2D model, and the files are then used as input in the 3D FSI model.

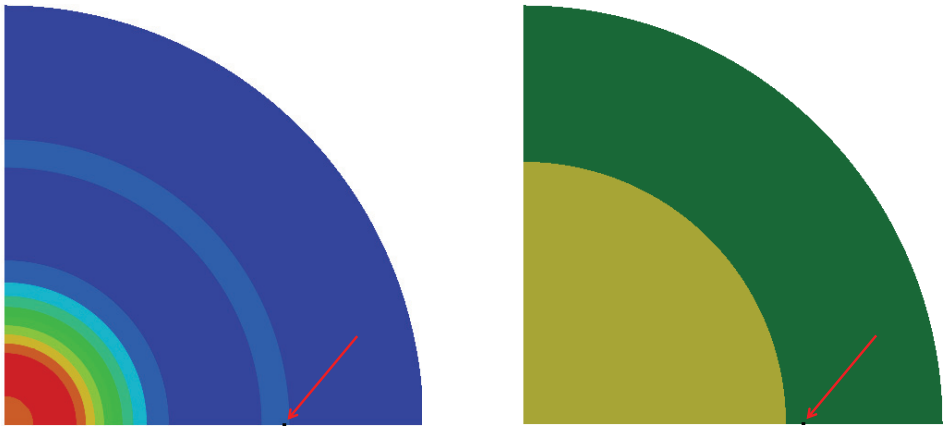

(a) **(b)**

Figure 7.5: In (a) the pressure wave front is shown for the time step when it reaches the pressure measuring point (small black marker in bottom of the figure), and in (b) the expansion of the detonation products is shown at the identical time step

7.1.2 Fluid Structure Interaction

Using the mapping file generated from the 2D model, the pressure in the air domain of the 3D FSI model, representing the air inside the blast box, is initialized as illustrated in figure 7.6. The pressure is then coupled with the panel, through FSI coupling, such that a pressure build-up can take place on the panel surface, which will be the reflected pressure, and make the panel react to the blast load. To get the 2D pressure mapped into the 3D domain the y-axis has been used for rotational symmetry. The 2D model has been run until the pressure wave is just in front of the modelled panel. Depending on the used stand-off distance and size of the explosive charge, the run time for the 2D model needs to be adjusted to make sure that the pressure wave has not passed the location of the panel surface. This reduces the number of calculations needed in the 3D model before the FSI coupling occurs.

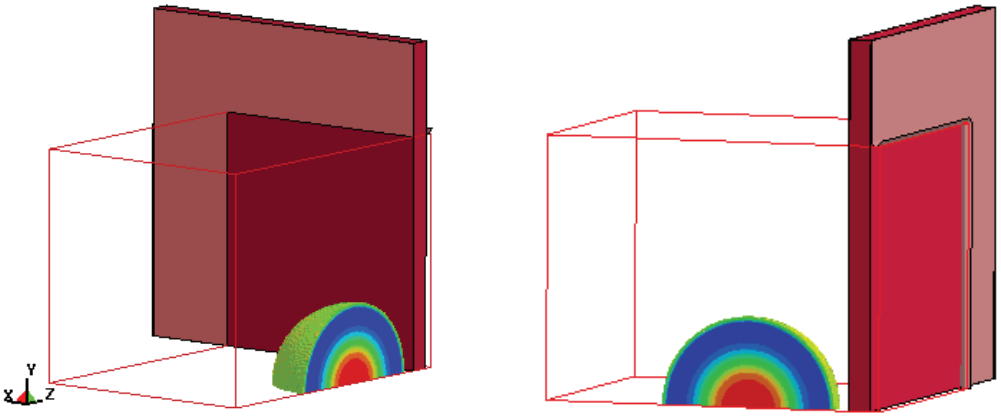

Figure 7.6: Contour plot of the mapped pressure from the 2D model on to the 3D model

Blast Box and Panel Representation

In all model cases the geometrical outline of the 3D model represents the test set-up used in the blast test. To reduce the size of the model, symmetry has been applied on the xz and yz planes cutting the blast box and panel into a quarter of its original size. For the blast wave, symmetry could have been applied on the xy plane also, but this is not supported by the blast box and panel because the panel is only in one end of the model. Imposing eight part symmetry would thus create false reflections that would increase the loading on the panel. The blast box therefore has to be modelled in its full depth. The blast box itself is not physically modelled. Instead the air inside the blast box, bounded by the blast box sides, has been modelled, and is represented by the red lines in figure 7.6. From figure 4.5a on page 34 it can be seen that outflow is only possible through the two openings in the sides and through the back of the blast box. To represent this outflow limitation, boundary conditions has been imposed on the air domain, illustrated in figure 7.7, where the air cannot flow out through the black marked surfaces, representing the top and left side of the blast box. Since outflow is prevented, the pressure will be reflected from these surfaces when impacted. As can be seen from the defined boundaries, a pressure trap can develop at the upper left corner area due to the closed top and left hand top edge. This can create an increased impulse on the panel at this location, an effect which will later be shown in the run models.

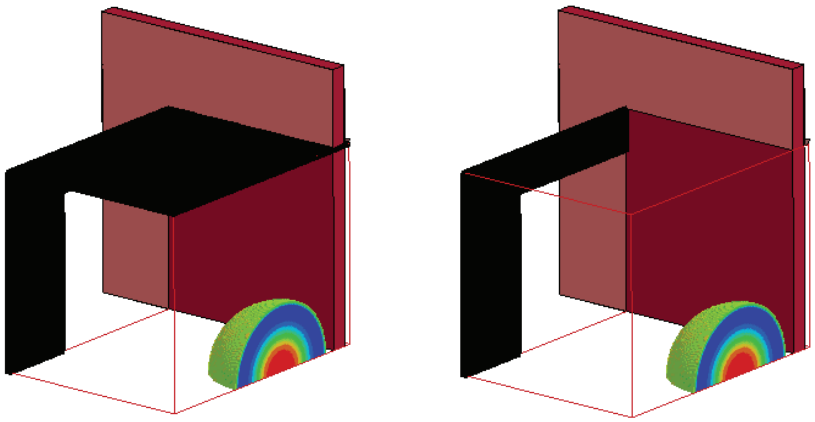

Figure 7.7: Boundary conditions defined for representing the steel edges of the blast box

In all cases the plate has been modelled with the clamped part included, where the frame and box in the clamped area have been represented by rigid shell parts. These have been constrained from any movement. Surface to surface contact conditions have been defined in the clamped region and a dynamic friction is applied with a friction coefficient of 1. Along the outer edge of the panel, the panel has been constrained in all directions. This choice of boundary was made based on the conditions of the panel holes and the panel surface observed during post-test panel inspections as previously described. The clamped area was included in the model, as this was seen to give a more correct behaviour compared to the case where only the part of the panel affected by the blast is modelled, and there imposing constraints on the panel edges. For the test case with 25g@100mm these boundary conditions are believed to represent the actual conditions well. But for the larger blast loads, e.g. 250g@100mm the boundary conditions might not be valid as the damage developed in the at these load conditions might be influenced by the panel boundary conditions. As the model development is progressing the boundary conditions might therefore need to be revised but as a first approach the chosen boundary conditions are found suitable as the mimic the observed experimental behaviour.

2D to 3D Mapping

The mesh of the air domain in the 3D model is made up of cubical shaped elements. The mesh in the 2D and 3D model are thus not of identical shape, which can have an effect when the pressure generated in the spherical 2D mesh is mapped on to the 3D cubical mesh. For three different element sizes, with edge lengths of 4mm, 2mm and 1.5mm, the pressure mapped to the 3D air domain was therefore measured at 100mm from the detonation point at the positions P_1 and P_2 as shown in figure 7.8.

Figure 7.9 shows the pressure measure at P_1 and P_2, and compares it with the pressure from the 2D model at an identical location. For decreasing element sizes the peak pressure is seen to increase and approach the pressure found in the 2D model, but for the pressure measured at P_1 a larger deviation between the 2D and 3D model pressure is seen, compared with the pressure measured at P_2. In figure 7.10 the impulse from the measured pressure is plotted and compared with the impulse from the 2D model. For decreasing element sizes the

impulse is observed to decrease, as seen for the mesh convergence study performed for the 2D

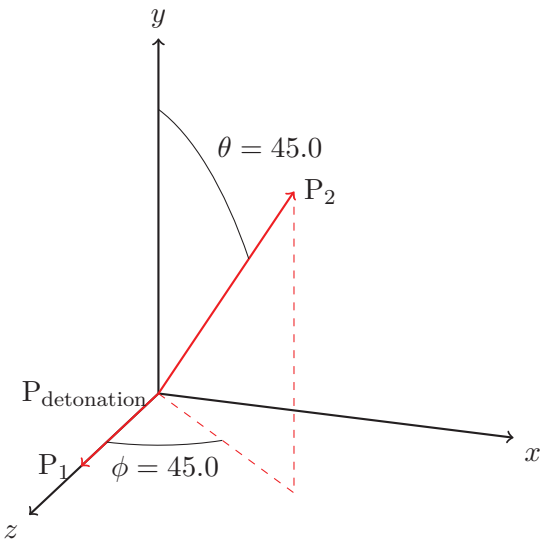

Figure 7.8: Location of pressure measuring points in the 3D model

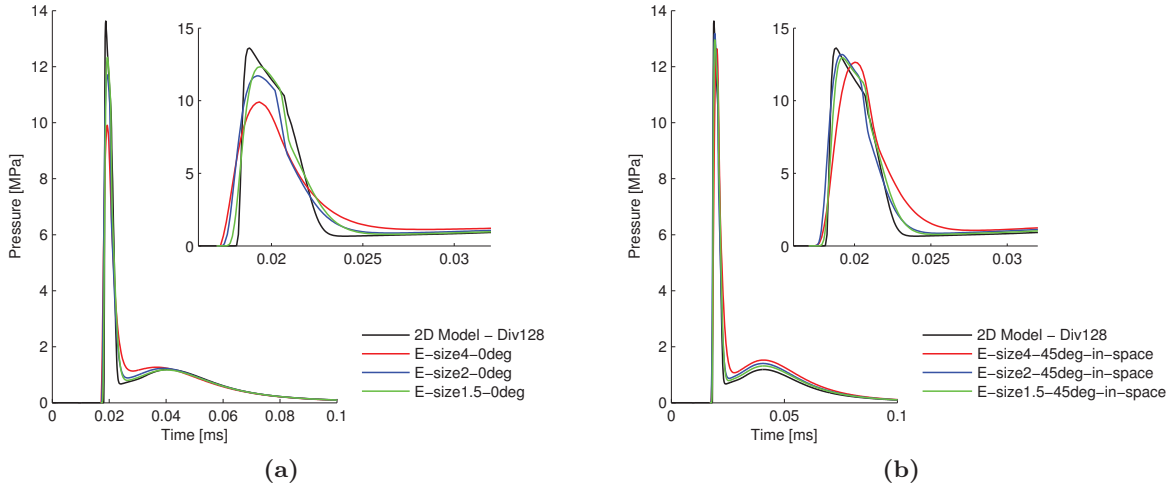

Figure 7.9: Measured pressure in the 3D model for the tested air domain mesh sizes, where (a) shows the pressure at P_1 in figure7.8, and (b) shows the pressure at P_2

model, and approaches the impulse measured in the 2D model. As opposed to the pressure measurements, the impulse at P_1 is in best agreement with the 2D model.

Comparing the pressure at P_1 and P_2 for the 2D and 3D model, with an element size of 1.5mm in the 3D model, there is a 9.5% and 4.5% decrease in pressure, indicating that the mesh in the 3D model is too coarse. Doing the same comparison for the impulse an increase of respectively 0.06% and 7.2% is found, indicating that for P_1, which will be the location for the centre of the panel, the impulse in the 3D model is similar to that of the 2D model. The impulse at P_2 is not at the location of the panel surface, and along this path it will decrease further before it reaches the panel surface. Because the impulse is the controlling property for the panel deflection, that P_1 is point receiving the largest impulse, and that the panel testing

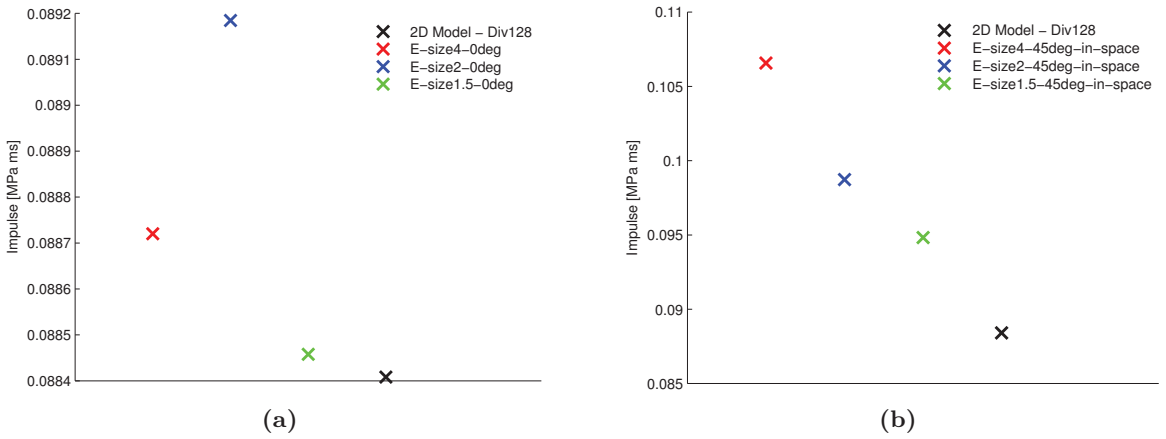

Figure 7.10: Impulse from the measured pressure in figure 7.9, where (a) shows the impulse at P_1 and (b) shows the impulse at P_2

did not indicate damage development due to the peak pressure, the 1.5mm element size was concluded as being acceptable for use as mesh size for the blast box air mesh. With this mesh size the blast box is represented by more than 5.5 million elements. Furthermore, the elements from the panel and the frame parts should be added. Decreasing the element size for the blast box air domain to 1mm, would result in more than 18 million elements for the air volume mesh, resulting in a model which, with the currently available hardware, would be very challenging to run. The choice of the 1.5mm element size should also be seen in this perspective.

FSI Parameter Study

In the current step of the load model, the fluid structure interaction is also included, where the blast wave is coupled to the structural surface. In LS-DYNA the FSI is controlled through the keyword ∗CONSTRAINED_LAGRANGE_IN_SOLID, where a number of parameters can be used to control the coupling conditions. In simple terms it works like a contact coupling between two structures, just with one of the structures being an ALE structure. In the keyword card a master and slave part needs to be defined, where the *slave* must be the Lagrangian part, and the *master* must constitute the ALE part. The master part must cover the entire *region of interaction* with the slave part, meaning that only the part of the Lagrangian structure in contact with the fluid need to be part of the FSI coupling. In table 7.1 the parameters on the ∗CONSTRAINED_LAGRANGE_IN_SOLID card, that can be used to influence the coupling are shown, together with a short description of the parameter. For further details on the parameters see [27].

In addition to the shown parameters, the mesh size on the Lagrangian structure also has an impact on the quality of the FSI coupling. Tthe study was performed to determine what effect changing the values of the parameters in table 7.1, as function of the element size, had on the pressure and impulse received by the panel and on the deflection of the panel. From the study it was found that the panel element size, NQUAD and PFACMM had significant impact on the developed pressure, impulse and panel deflection. The remaining parameters only had little or no effect and for these their default values will be used in the FSI modelling. Using the default value for PFACMM resulted in instantaneous leakage through the Lagrange part.

Table 7.1: Parameters in the *CONSTRAINED_LAGRANGE_IN_SOLID keyword card that can be used to control the FSI coupling conditions

Name	Description
DIREC	Coupling direction, controls if the fluid coupling should be active in normal direction for both tension and compression (1), in compression only (2) or in all directions(3)
FRCMIN	Minimum volume fraction of coupled ALE element before coupling is activated. Default is 0.5
ILEAK	Coupling leakage control; None (0), Weak (1), Strong (2) with 0 as the default value
NQUAD	Number of coupling points distributed over each coupled Lagrangian surface segment. Default is 2
PFAC	Penalty coupling factor for computing the coupling forces. Default is 0.1
PFACMM	Coupling Penalty Stiffness (CPS) factor. Works in conjunction with PFAC. Options are 0–3, which refers to the method by which it is calculated. 0 is the default value. See [27] for further details.
PLEAK	Leakage control penalty factor; $0 <$ PLEAK < 0.2 is recommended

Changing PFACMM to option 3 the CPS factor will be calculated as

$$CPS \propto \text{PFAC} \cdot K_{Lagrangian}$$

where K is the bulk modulus of the Lagrangian part, prevented the instantaneous developed leakage.

Figure 7.11 shows the effect of the element size in the panel on the panel deflection, built up pressure and impulse, for different values of NQUAD. For NQUAD= $[2, 4]$ convergence is seen for an element size of 1.5mm. This matches the element size used in the air domain, as stated earlier, and shows that the best performance of the FSI coupling requires an element size in the Lagrange part of similar or smaller size than that used in the ALE domain. For NQUAD=$[8, 12]$ a sharp increase is seen in the deflection and pressure for elements smaller than 2mm. This is due to instabilities that develop when too many coupling points are defined.

Based on the results of the FSI coupling analysis the parameter values shown in table 7.2 have been chosen as the settings to be used in the FSI modelling, and will thus be used in the models to compare the modelled panel response with that measured from the blast tests.

Table 7.2: Parameters used in the *CONSTRAINED_LAGRANGE_IN_SOLID card for modelling the fluid structure interaction

E_SIZE	DIREC	FRCMIN	ILEAK	NQUAD	PFAC	PFACMM	PLEAK
1.5mm	1	0.5	0	4	0.1	3	0.1

Blast Wave Reflections with FSI

One area where the numerical approach to modelling the blast load is superior compared with using LBE, is the ability to catch reflections from surfaces. As pointed out earlier, the boundary conditions on the air domain representing the blast box have been selected to represent the

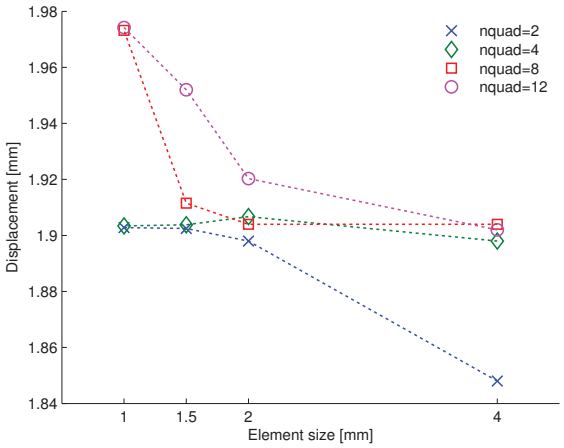

(a)

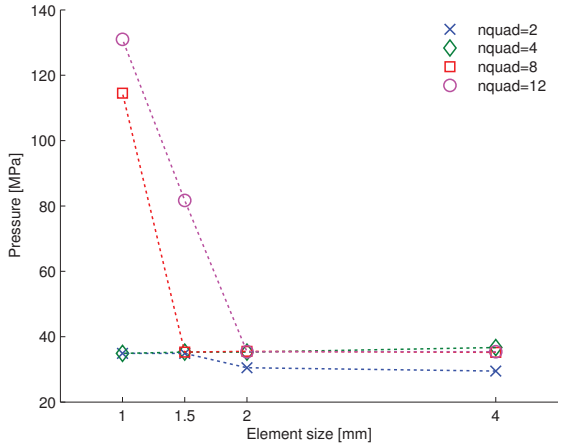

(b)

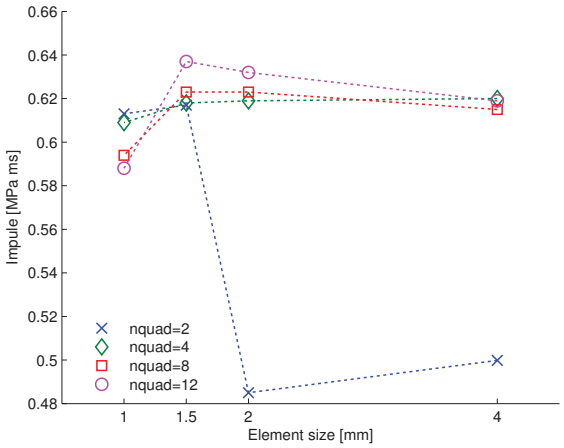

(c)

Figure 7.11: The effect of NQUAD as function of panel element size where; (a) shows the panel centre deflection, (b) shows the pressure on the surface of the panel centre point, and (c) shows the corresponding impulse

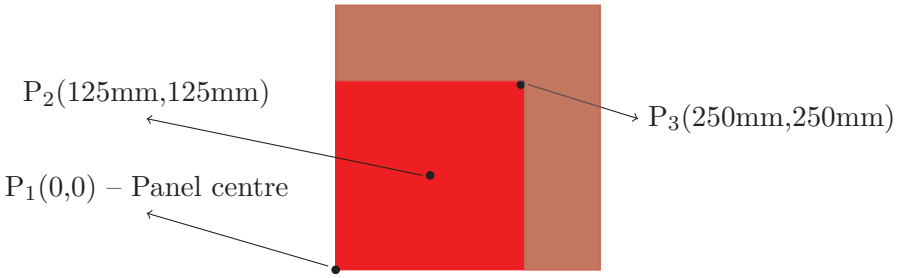

Figure 7.12: Position of pressure measuring points on modelled panel surface

surfaces of the blast box that prevents out flow. To illustrate the effect of reflections, two scenarios have been modelled, where the reflected pressure has been measured on the panel surface at the three locations marked as P_{1-3} in figure 7.12. In the first scenario the boundary conditions on the air domain were applied as shown in figure 7.7 on page 93, and in the second scenario the air domain boundary conditions were removed such that outflow was not prevented.

Figure 7.13 and 7.14 shows the modelled reflected pressure at the three marked locations for the blast box and free out flow configuration respectively. The modelled pressure is based on a blast set-up using a 25g PETN charge with a SOD of 100mm. As can be seen in the case with limited outflow, an increased pressure is measured at P_3, compared with the free outflow scenario. This is due to the pressure trap than develops at this location, as described earlier, which gives rise to a significant impulse contribution at the panel corner area, resulting in an increased panel deflection, as illustrated in figure 7.15, where an approximately 12% increase in the deflection of the panel, compared with the free outflow conditions, is found. Since the pressure at P_1 and P_2 for the two out flow scenarios are the same, the increased panel deflection has to be attributed to the increased pressure build at the corner region.

Using *LOAD_BLAST_ENHANCED, the pressure increase at the corner could not have been captured. This is illustrated in figure 7.16, comparing the pressure at the three marked positions

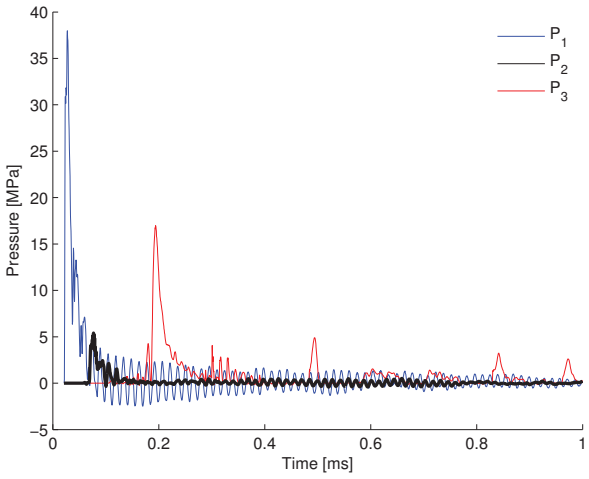

Figure 7.13: Modelled reflected pressure at point 1–3, in figure 7.12, with air domain boundaries defined as in the blast box

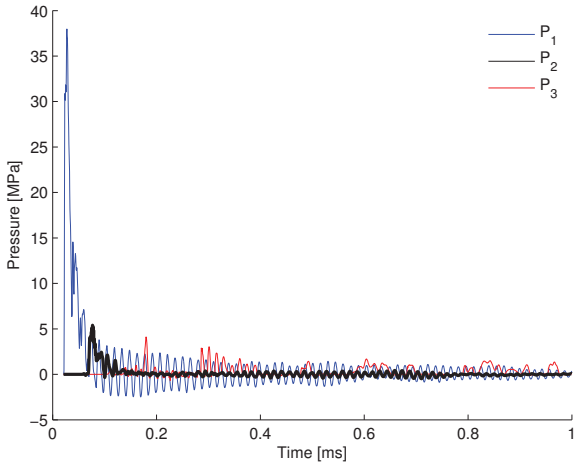

Figure 7.14: Modelled P_{ref} at point 1–3, with air domain boundaries defined for free outflow

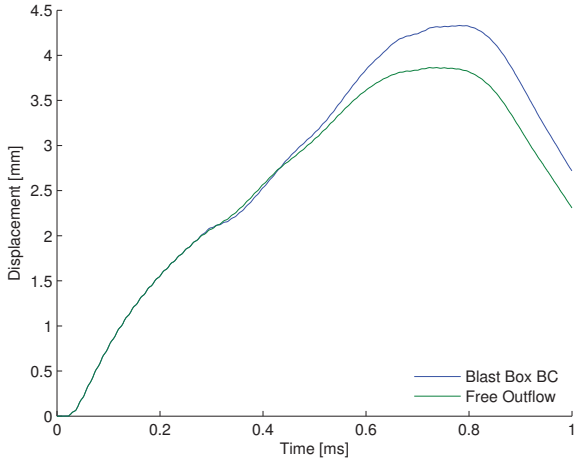

Figure 7.15: Panel centre deflection for P_1 with the two boundary conditions tested

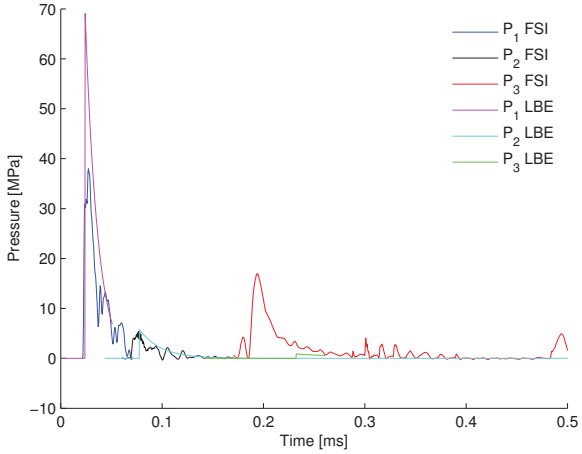

Figure 7.16: Pressure at $P_{1–3}$ modelled with the numerical load model, using blast box boundary conditions, and by use of *LOAD_BLAST_ENHANCED

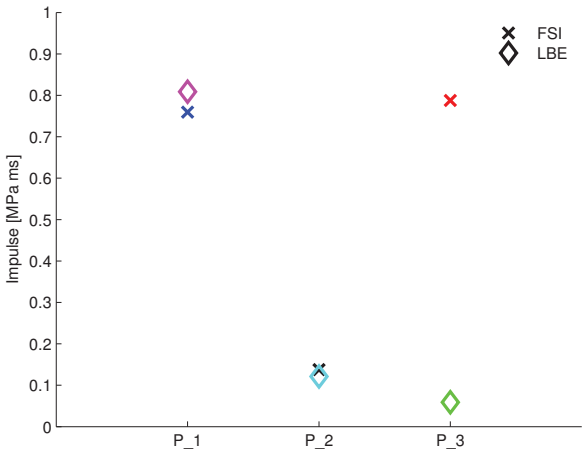

Figure 7.17: Impulse at point 1–3, in figure 7.12, modelled with the numerical load model, using blast box boundary conditions, and by use of ∗LOAD_BLAST_ENHANCED

between the numerical load model and LBE, where it is clear that at P_3 there is almost no pressure by using LBE compared with the numerical approach. Comparing the pressure at P_1, LBE predicts almost twice as high peak reflected pressure. Several factors can be attributed to this difference. First of all, further mesh refinement of the air domain could probably result in an increase in the peak pressure, as this would give a more clearly defined blast wave front. Secondly, as mentioned earlier, LBE might be inaccurate for these near field blast scenarios where the detonation products can affect the generated pressure. Finally, the LBE model is based on TNT, but the numerical model is based on PETN, as this is the explosive used in the experimental tests. There might be a difference in the pressure–time development between the two explosives, as they are based on different chemical compounds. In addition, as described earlier, a conversion factor is applied to the LBE model to account for the difference in the explosive types, which might also influence the developed pressure.

Looking at the impulse at P_1, shown in figure 7.17, the much higher peak reflected pressure in LBE does not contribute to a significantly larger impulse ($\approx 6.5\%$), and since the impulse is the controlling parameter for the deflection, the observed difference in peak reflected pressure can be accepted. Looking at the pressure for P_2 in figure 7.16 the numerical load model and LBE are in good agreement. The pressure here is significantly lower than that of P_1, which very well illustrates the pressure in the blast front dependence of the distance travelled from the detonation point. In the used set-up the distance from the detonation point to P_1 is 100mm, whereas the distance to P_2 is 160mm.

Figure 7.18a shows the panel centre deflection for the two tested outflow boundary conditions, modelled by using the designed numerical blast model, and the panel deflection modelled by the LBE model. As shown, the panel deflection modelled by use of LBE is nearly identical to that obtained by use of the numerical load model with the outflow defined as in the blast box. Since the LBE model did not account for the extra pressure build up at the panel corner, it was expected that the panel deflection modelled with LBE would be closer to that obtained with the numerical model using free outflow conditions, but was found to be approximately 10% larger. But as also shown in figure 7.17 the centre impulse using LBE is approximately 6.5% larger, which can be part of the reason for the deflection seen. In figure 7.18b the impulse at P_1 as function of time for the numerical load model with limited outflow conditions and

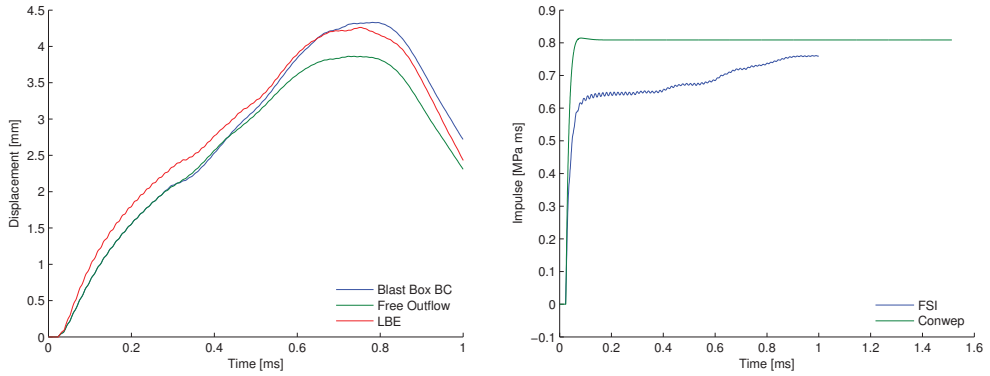

(a) **(b)**

Figure 7.18: Modelled panel response using the numerical load model and LBE where, (a) shows the panel centre deflection, and (b) the panel centre impulse, obtained for the two load model types

the LBE model are shown. As seen the impulse from the LBE model is applied much faster than in the numerical model. Using the LBE model, the panel will therefore receive a higher acceleration which also could contribute to the deflection seen for the LBE model.

With the used FSI coupling settings, fluid leakage through the panel was avoided in the initial contact between fluid and the panel. However, at approximately 0.4ms leakage was observed developing at the centre region of the panel, as illustrated in figure 7.19. Comparing the time and location of the leakage development with the pressure for point P_1–P_3 in figure 7.14 on page 99, the leakage is found to occur after the primary impulse has been delivered, and as it is initiated in the panel centre it will, initially, not influence the FSI coupling at P_3, where the pressure builds up due to reflections. The leakage is thus not believed to have significant impact on the panel response for the modelled case. But for a case where the primary impulse has not been delivered before the leakage occurs it could constitute a problem for the modelled panel response. It has not been possible to prevent the leakage by adjusting the FSI coupling

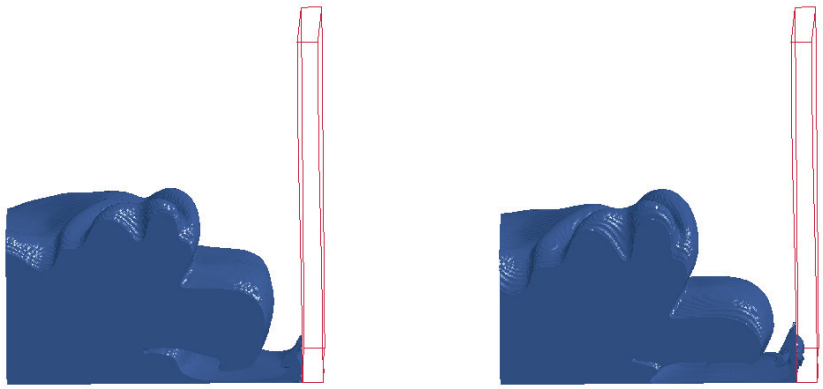

(a) $t = 0.37$ms **(b)** $t = 0.42$ms

Figure 7.19: Observed leakage in the FSI coupling, occurring at approximately 0.4ms

parameters on the *CONSTRAINED_LAGRANGE_IN_SOLID card. An attempt was made to counteract the leakage by changing the DIREC parameter from setting 1 to 3 as this would make the FSI coupling work in all directions instead of only in compression, but without significant change in leakage behaviour. Further mesh refinement of both the air domain mesh and the mesh used for the panel, since the mesh of the two parts should match in size, is therefore believed to be the best way to counteract the observed leakage.

7.1.3 Structural Response

As seen from figure 7.13 on page 98, after approximately 0.5ms the primary impulse has been transferred to the panel. The blast wave pressure has been reduced to ambient pressure and cannot deliver more energy to the panel. A lot of computational power is thus now used just to calculate the circulation of the air and detonation products in the modelled air domain, without affecting the response of the panel further. This leads to the final step in the blast load model, which is a restart of the model, where the air domain and the FSI model have been removed. This is done by terminating the FSI model and instructing LS-DYNA to write a restart file that can be used to initialize a new changed model with new or removed parts. A new model input file is created where the air domain and the FSI model have been removed and LS-DYNA is instructed to use the restart file to initialize the remaining panel part with the deformations, stresses, velocities etc. that have been built up in the panel before the previous model was terminated. When the initialization is ended the calculations are continued until the defined termination time. Figure 7.20 shows the deflection of the panel for the above mentioned blast test set-up. As shown, the deflection of the restarted model continues from where the FSI model ended.

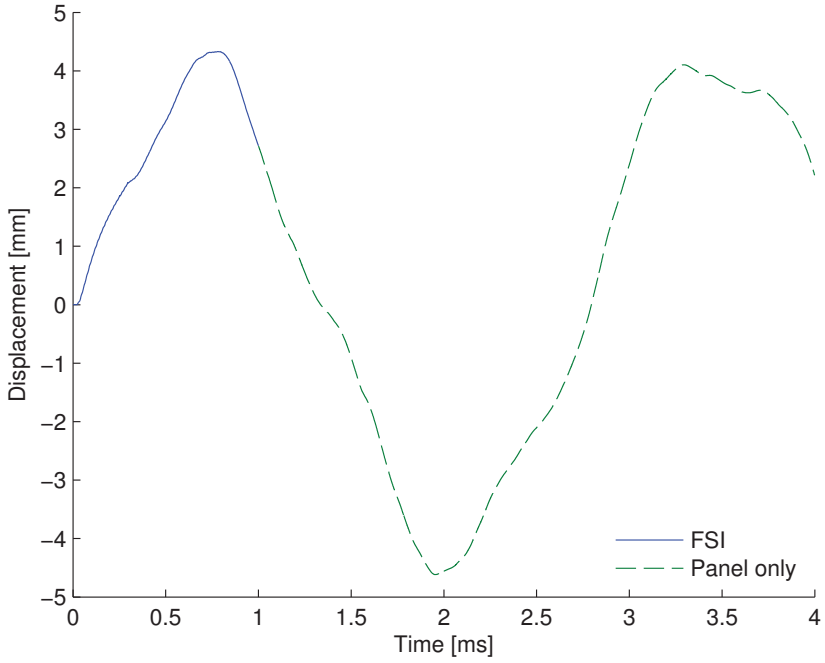

Figure 7.20: Modelled panel centre deflection from step 2 and 3 of the numerical load model, showing the smooth transition between the two model steps

The main reason for performing this restart is to reduce the total run time for the model. The displacement part in figure 7.20 belonging to the FSI model used 18h and 20min to progress the model 1ms forward in time, whereas the part of the deflection belonging to the restarted model, containing only the panel used 52min to progress the model an additional 3ms forward in time. This corresponds to an increase in speed by a factor of approximately 64. Whether the restart step can be performed will depend on the specific model set-up. Modelling a blast in a closed or very confined space will build up a quasi-static pressure, which will last for a long time compared with the actual blast load, and in such case one might be forced to run the FSI modelled step the entire run time.

7.2 Model vs. Experimental Tests

To evaluate the accuracy of the designed blast load model and to evaluate the functionality of the chosen laminate models, the model results and results from the performed blast tests and laminate material tests will be compared. The material input data to describe the monolithic laminates were based on material test data and can be found in appendix B. The rate parameters used in *MAT_COMPOSITE_DMG_MSC has been determined from dynamic material tests performed in [37], where data have been fitted to the rate law used in *MAT_COMPOSITE_DMG_MSC. The material tests on the Eglas/Epoxy laminates showed a clear rate effect on the material strength parameters. Table 7.3 shows the fitted parameters to be used as input in *MAT_COMPOSITE_DMG_MSC to describe the rate effect of the laminate.

As presented in chapter 3 the rate model in *MAT_COMPOSITE_DMG_MSC only takes one input to describe the rate effect of all strength parameters. From table 7.3 it is seen that for the UD material, the tested directions have different rate responses and cannot be described by the same rate parameter C. As shown in the table, only an in-plane tensile test has been performed on the Quarto-axial layup, and the rate parameter C found for this test will be used as the CRATE$_1$ input in the modelling of the laminates. As indicated by the UD test results, this value might not correctly describe the rate effect in for example in-plane or through thickness compression, and will therefore be a source of inaccuracy when comparing the test data with model data. For measuring the moduli, tests were performed using the same layups and directions as shown for the strength parameters in table 7.3. For these the test on the UD laminates showed little or no rate effect. Again this behaviour has been transferred to the quarto-axial layup, and CRATE$_2$–CRATE$_4$ in the input to *MAT_COMPOSITE_DMG_MSC

Table 7.3: Rate parameters to describe the strain rate sensitivity of the Eglas/Epoxy laminates using expression (3.20)

Layup	Property	$\sigma_{fail}(\dot{\varepsilon} = 1)$ [MPa][a]	C [b]
UD	X_{11}^t	1020	0.0773
Quarto	X_{xx}^t	453	0.0598
UD	X_{22}^t	23.5	0.0264
UD	X_{33}^c	44.4	0.0577

[a] Fitted strength at $\dot{\varepsilon} = 1$ based on dynamic material data

[a] Fitted C_n parameter to be in putted in *MAT_COMPOSITE_DMG_MSC and used in (3.20) for determining the rate effect.

Table 7.4: Parameters used for modelling the PETN explosive

ρ [kg/m^3]	$v_{detonation}$ [m/s]	P_{CJ} [GPa]	ω	A [GPa]	B [GPa]	R_1	R_2	E_0 [GPa]
1480	7200	20.5	0.3	373.8	3.647	4.2	1.10	7.00

has been set to zero, indicating no rate effects for the moduli parameters. In the input deck, CRATE$_3$ describes the rate dependence of the shear moduli, which has not been tested for. Here it has been assumed that it also will not show rate dependence as seen for the tested moduli parameters.

The data used in the *MAT_HIGH_EXPLOSIVE_BURN and *EOS_JWL model, for describing the explosive used in the tests, have been taken from [61] and are listed in table 7.4, where $v_{detonation}$ is the detonation velocity , P_{CJ} the Chapman-Jouget pressure and E_0 the detonation energy per unit volume of the explosive material. A, B, R_1, R_2 and ω are model parameters used by the JWL equation of state.

To model the blast load with *LOAD_BLAST_ENHANCED a PETN to TNT conversion factor of 1.08 has been used, based on the data for PETN and calculated from equation (3.13) on page19.

7.2.1 25g Blast on a Monolithic Laminate

A comparison between the measured response of the CRBJ-33 panel tested at 25g, and the modelled panel response from the designed numerical load model, with air domain boundary conditions defined to mimic those present in the real blast box, and by use of *LOAD_BLAST_ENHANCED, has been made. For the blast load modelled by the numerical model, a 2D run was performed to generate the initial blast wave developed by the 25g charge, which then was mapped to the 3D model to take care of the FSI coupling. The FSI model was run for 1ms, after which the primary impulse had been delivered to the plate, and a restart was performed to model the continued panel response. The mesh for the air domain in the 3D model and the FSI coupling parameter settings were as described in section 7.1.2 on page 92. The modelled panel dimensions are the same as in the tests ($700 \times 700 \times 21$mm). The in-plane element size in the panel was 1.5mm, dictated by the air domain mesh size to optimize the FSI coupling, as explained in section 7.1.2. The through thickness element size was set to 1.75mm, resulting in 12 elements through the thickness of the panel. Since the analysis of the response of the tested panel indicated that no failure development could be assumed for the 25g test, and the response thus was purely elastic, the panel was modelled by use of *MAT_ORTHOTROPIC_ELASTIC. The panel was modelled as an orthotropic material, with no individual layers defined. Figure 7.21 shows the comparison between the deflection measured in the test by the DIC system, and the modelled deflection, where FSI refers to the deflection obtained by use of the numerical load model and LBE refers to *LOAD_BLAST_ENHANCED model.

In addition to the models using *MAT_ORTHOTROPIC_ELASTIC to model the laminate, an additional model was constructed using *MAT_COMPOSITE_DMG_MSC to represent the laminate, marked as Mat162 in figure 7.21. For this model, the laminates were represented by 8 individual layers, with nodes merged at the layer interfaces. Each layer is represented by 3 elements through the layer thickness, a recommendation received from the model supplier. The load for this model was applied using LBE.

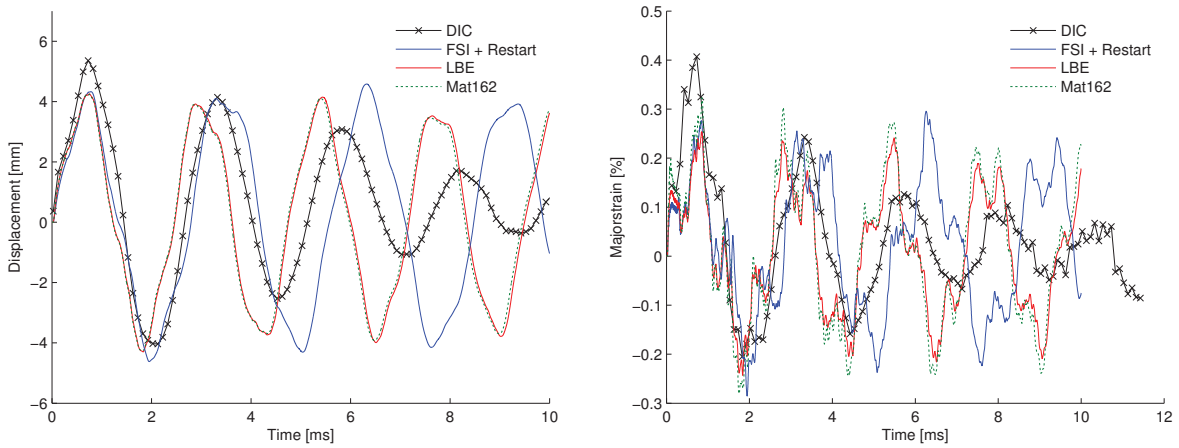

(a) Centre dispalcement **(b)** Centre strain

Figure 7.21: Comparison between the modelled and experimentally measured panel centre deflection and major strain, for a 25g charge load at 100mm stand-off distance

Comparing the modelled peak centre deflection with that measured in the experiments, the model underestimates the deflection. The FSI model shows a peak deflection of 4.33mm whereas the DIC data showed 5.36mm, giving a 19% smaller deflection in the model. Looking at the model using *MAT_COMPOSITE_DMG_MSC as laminate material, exactly the same result as the LBE run is obtained, indicating that the *MAT_COMPOSITE_DMG_MSC model predicts a completely elastic response, and no damage has developed. Up to the first deflection peak the modelled and measured responses show the same curve shape. After passage of the first peak, the FSI model data follow the experimental data better up to the third deflection peak. This might be due to the extra impulse developing at the edges, due to the limited venting in this region. The model data do not predict the damping of the deflection, as seen in the experimental data. The damping in the experimental data is probably due to effects in the clamped region, which are not properly accounted for in the model. This is, however a secondary problem, as the main focus must be to be able to predict the initial response, as this is of most relevance with respect to whether or not the panel can withstand the applied load.

In ARAMIS the major strain is calculated as

$$\varepsilon_{maj} = \frac{\varepsilon_x + \varepsilon_y}{2} + \sqrt{\left(\frac{\varepsilon_x + \varepsilon_y}{2}\right)^2 - \left(\varepsilon_x \cdot \varepsilon_y - \varepsilon_{xy}^2\right)} \tag{7.1}$$

which is a plane strain condition. In the test plane strain does not apply as the blast wave will generate minor compressions in the thickness direction. But since ARAMIS cannot measure the thickness strain, the major strain can only be based on the measured in-plane strain values. The modelled strain, shown in figure 7.21b, has been calculated from (7.1) by taking out the centre element x, y and xy surface strain values. As with the deflection, the model data lie below the DIC data with the FSI data showing a 32% smaller strain. Again the FSI data follow better the DIC data up to the 3 peak, after which the damping in the experimental data reduces the strain compared with the model data. The lower strain found in the model can be a problem in modelling of laminate failure, since the low strain will give lower stresses. Since the failure is based on stress limits, too low stresses could lead to erroneous failure prediction.

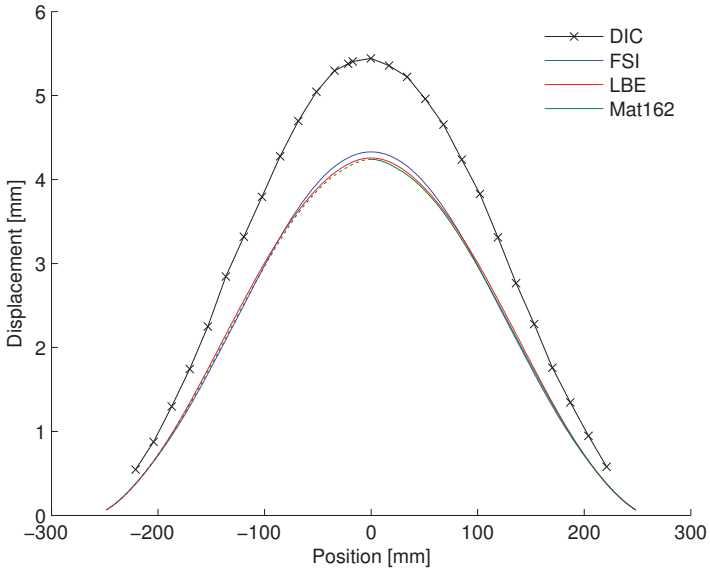

Figure 7.22: Measured and modelled panel deflection along a horizontal section passing through the centre of the panel

Figure 7.22 shows the displacement along a horizontal section through the centre of the panel at the time of the first peak deflection. The shape of the deflection over the cross section of the DIC and model are similar, indicating that the model seems to be offset by a scalar factor. Using the LBE model, the effect of changing the charge mass and stand-off distance was tested. In figure 7.23 the additional model runs using the LBE model have been plotted. One model, where the explosive mass has been scaled up by 50% (LBE×1.5), and a model where

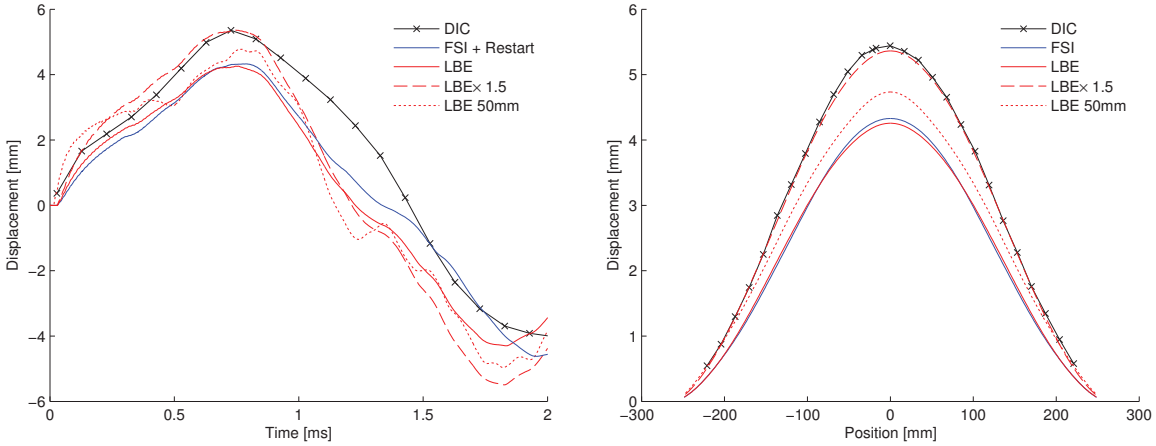

(a) **(b)**

Figure 7.23: Impact on the modelled panel deflection, by increasing the explosive mass with 50% (LBE×1.5), and reducing the standoff distance to from 100mm to 50mm (LBE 50mm)

the SOD has been reduced to 50mm (LBE 50mm). Maintaining the charge size and moving closer to the target do not appear to affect peak panel deflection much, but has an impact of the initial panel response, where a much faster increase in deflection is seen, which must be attributed to the larger reflected peak pressure received by the panel due to the shorter SOD. The explosive mass on the other hand has a large effect on the peak deflection. As seen from figure 7.23a, using a 1.5 PETN to TNT scale factor (corresponding to scale up the charge mass by 50%), the peak deflection of the model and DIC is similar. Compared with the model for the reduced distance, the effect of the increased mass on the initial panel response is minimal, indicating that the increased mass has had a larger effect on the impulse than on the initial peak pressure. This is also expected when looking at the scale laws from section 2.1, showing that the scaled impulse has to be multiplied by $\sqrt[3]{M_{exp}}$ to get the actual impulse. Looking at the sectional deflection in figure 7.23b, the use of an increased conversion factor results in an almost perfect match for DIC and LBE data, supporting the indication that the modelled impulse is too low for the FSI and LBE model in figure 7.21.

The observations made from the comparison between the experimental test data and the model data could indicate that the modelled impulse is too low compared with that developed in the real tests. In LBE the too low impulse can be because the PETN to TNT conversion factor of 1.08 used is not suitable to scale the impulse. As described in chapter 3 on page 13 the conversion factor to be used to obtain the correct peak pressure, might not be the same as the factor to use to obtain the correct impulse. As indicated by the modelling a scale factor of the order 1.5 could be more accurate to scale the impulse. For the FSI load model a scale factor cannot just be applied since the model uses actual explosive material parameters to model the blast, and thus should correctly represent the used explosive type. A problem with this model could be that the mesh or coupling parameters used do not result in the correct impulse on the panel.

One way to confirm that the modelled pressure and impulse are correct would be to compare them with pressure and impulses measured from explosive tests. In corporation with postgraduate student Bjarki Elíasson, as part of his thesis, a test set-up for measuring the reflected blast pressure from a free air explosion was designed, the details of which can be found in appendix E. As can be seen in the appendix, the measurements of the blast pressure could be performed, but the variation in the data was too large to draw valid conclusions regarding the level of the measured pressure, and the measurements were therefore to be found unfit for comparison with model data. It has therefore not been possible to verify if the modelled pressure and impulse represents the actual pressure and impulse from the blast tests.

An important parameter when performing the test-to-model comparison, is experimental variation in the measured data. For the 25g test, only a single test was performed. The comments regarding too low impulse of the models should therefore be taken with some reservations. For the experimental tests performed on CRBJ30-32 a difference of 1.55mm from the lowest to the largest deflection was seen corresponding to a 4.7% difference in peak deflection. Assuming that the same percentage variation is valid for the 25g test, and that the experimentally observed deflection of 5.33mm is the maximum deflection, then the minimum deflection would be 5.09mm. Compared with tests performed at 250g, there are some factors that can indicate that the expected uncertainties for the 25g test is higher. When weighing the explosive used for testing a standard digital kitchen weight is used. For the 25g blast a 1g weighing error will correspond to an 4.2% error on the total amount of the explosive. For the 250g charge the same weighing error would only attribute to a 0.4% error. A weighing error will thus have much larger impact for the 25g test. The detonator contains approximately 1g explosive material. For the 25g charge

test the detonator will therefore add considerably more to the total explosive mass than for the 250g. For the 25g the detonator might therefore add a measurable contribution to the total generated pressure and impulse.

Assuming that the 1.08 PETN to TNT conversion factor used is correct, then from the modelling it was indicated that an 38% increase of the explosive mass, corresponding to 10g, is needed to match the experimental test data. A weighing error of this size is not likely to have happened. However, as indicated, a small weighing error and the contribution of the detonator could explain some of the difference seen. In addition, the exact shape and position of the explosive combined with the panel to panel variation could give further contributions. The mentioned sources of inaccuracy for the experimental data can of course lead to both a decrease and increase in the response, depending on whether for example, if the weighing error is positive or negative. Therefore, before it can be determined if the models are actually measuring correctly on an average level, the experimental variation should be established.

7.2.2 Modelling of a Laminate

From the 250g blast test performed on CRBJ30–32, internal panel failure in the form of delamination was observed. To be able account for this in the modelling of the laminate panels, the used model must be able to account for laminate failure. The *MAT_ORTHOTROPIC_ELASTIC model is therefore not usable for modelling the material, when models of the 250g blast tests are designed. Here the *MAT_COMPOSITE_DMG_MSC has to be used. By using the available material data and rate parameters, a couple of test models of the 250g test were run to determine how well they performed when compared with the experimental measurements. They were found not to compare well and significantly over predicted the amount of failure, indicating that the model does not represent the material properly.

A step back in level of complexity was therefore taken in the modelling of the laminate material to gain a better understanding of how the panels should be modelled. This was done by designing models representing some of the material tests performed on the Eglas/Epoxy laminates, reported in [50]. It was chosen to model the tensile test performed on laminates with an unidirectional (UD) and quarto-axial (QA) layup. Figure 7.24 illustrates the specimen design used in the testing of these two layup configurations, and in table 7.5 the dimensions and fibre layup used for the specimens are shown.

In figure 7.25 the measured stress-strain relationship for the UD and QA specimens at quasi-static strain rate is shown. As can be seen, the UD laminate strength is, as expected, higher than that of the QA laminate. For both laminates non-linearity is shown, most pronounced on the QA laminate showing a non-linear behaviour almost from the beginning of the stress-strain curve. For the UD specimen the non-linearity is most pronounced at the end of the stress-strain curve. For the QA specimen, the non-linearity is likely to be caused by a progressive failure build-up, where the differently oriented layers fail at different levels of strain, giving the observed non-linearity. For the UD laminate all layers build up the same stress and are therefore more

Table 7.5: Specifications for the used specimens in the performed material tests

Specimen dimension[mm]	Gauge length [mm]	Layup
$250 \times 15 \times 2$	100	$[0]_4$
$250 \times 25 \times 4$	100	$[0/-45/90/45/-45/90/45/0]_3$

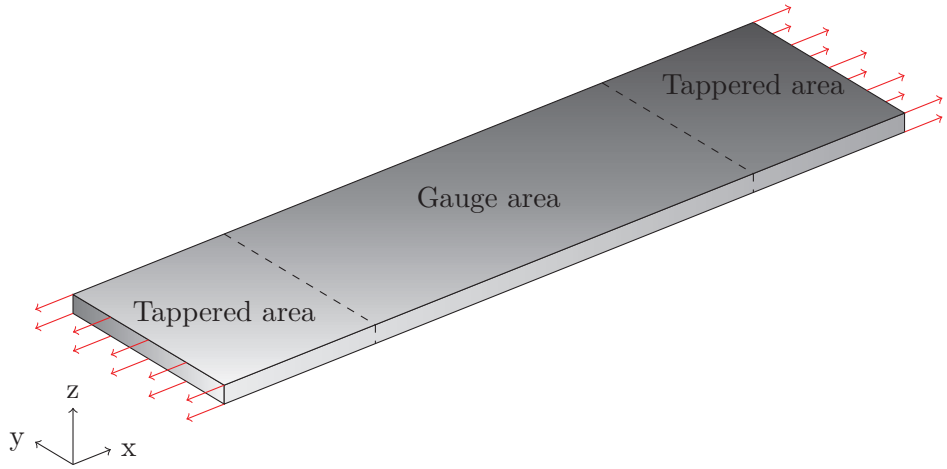

Figure 7.24: Specimen design used in the tensile tests performed on the UD and QA specimens

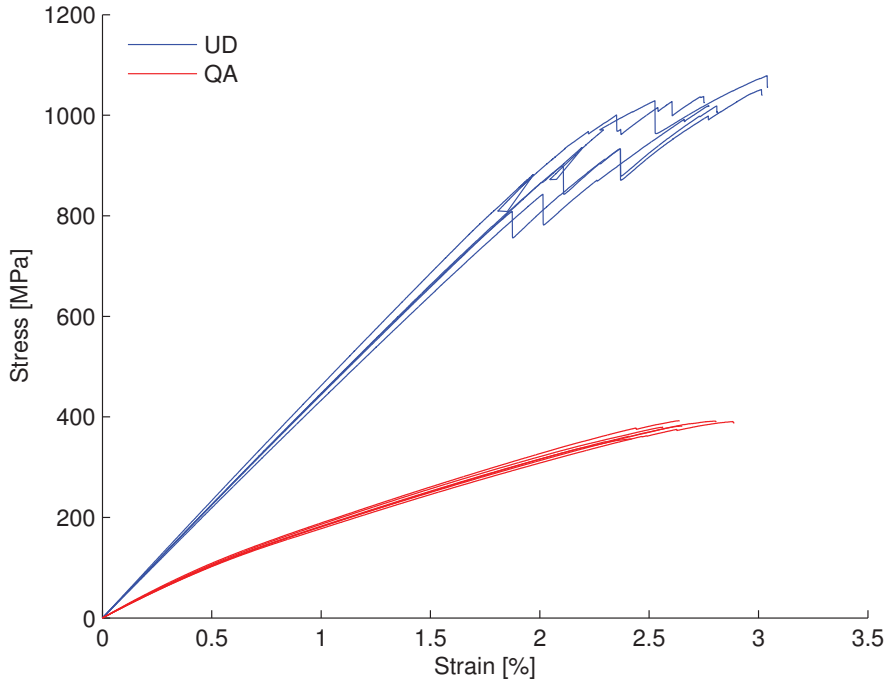

Figure 7.25: Experimentally measured stress–strain relationship for the UD and QA specimens [50]

likely to fail simultaneously, and the non-linearity seen at the end could be due to single fibre failure, caused by imperfections in the material. The bumps seen on the stress-strain curve for the UD laminate are due to slippage in the clamped region or failure of individual fibre layers.

The presence of the non-linear behaviour underlines the need to represent the individual layers in the modelling of the laminate. Since *MAT_COMPOSITE_DMG_MSC is a linear-elastic model, where the stiffness matrix is gradually reduced when failure is initiated, modelling of the laminate as a single layer structure using overall orthotropic values for moduli and strength parameters would result in a linear stress-strain development until failure, and the non-linearity due to the progressive failure of individual laminates would not be seen.

In the following, findings from modelling of the UD and QA material tests will be presented. The test specimens have been represented by modelling only the gauge area part of the specimen, since the exact conditions in the clamped region are unknown, and would complicate the modelling significantly if included. The loading on the specimen has been applied by applying a velocity in the x-direction at one end of the specimen, and restricting movement in the x-direction at the opposite end. Instead of applying the velocity instantaneously, a small initial acceleration was given until the desired velocity was obtained. Applying the velocity instantaneously was found to give an unstable behaviour of the model.

Unidirectional Layup

As seen from table 7.5, the UD specimens were made from 4 fibre layers. In the model of the UD specimen all four layers have been represented. To see how the modelled stress-strain response depended on the model design, 4 different cases were studied where the influence of the number of elements through the thickness of each layer was analysed, together with the effect of *hourglass control*. *MAT_COMPOSITE_DMG_MSC is only formulated for one-point integration. The advantage of this formulation is that it is computationally cheap, but the big disadvantage is that the elements can show zero energy deformation modes, called *Hourglassing modes* [15]. To minimize the hourglass effects, if present, an hourglass control model can be applied, which generally works by adding a small amount of viscous damping or elastic stiffness to the element capable of stopping the hourglass deformation, without affecting the stable global modes too much [15]. The energy dissipated by the hourglass forces, applied to hinder the formation of the hourglass modes, is stored in the MATSUM and GLSTAT output files from LS-DYNA. An indication of an unstable model is if the hourglass energy is larger than 10% of the internal energy in the model.

Table 7.6 shows the settings used for the four runs. The default hourglass model in LS-DYNA

Table 7.6: Specifications for the material test models of the UD specimens

Run number	NE_{layer} [a]	QH [b]
#1	3	0.10
#2	3	0.15
#3	4	0.10
#4	6	0.10

[a] Number of elements through the thickness per layer
[b] Hourglass coefficient

has been used with the hourglass coefficient (QH) set as shown in the table. In the four runs the elements has been designed such that an 1:2 aspect ratio exists between the element dimensions in the thickness to in-plane directions. The stress in the model has been measured by taking the average stress of all the elements at the constrained end. The strain has been calculated from the change in length over the entire specimen length. Due to specimen shape, and that all layers have the same fibre orientation, material and geometrical symmetry exist around the specimen xz-centre-plane. For the UD model, only half of the specimen width is therefore modelled, by defining a symmetry boundary plane along one of the xz edge planes.

Figure 7.26 shows the stress-strain curves achieved from the four model runs. As seen from run #1, #3 and #4 the number of elements through the thickness of each layer has a clear effect, where run #1 and #3 show premature failure. Looking at the energies for the model runs, figure 7.27, it can be seen that for run #1 and #3 a rise in the hourglass energy occurs earlier for these models compared with runs #2 and #4, indicating that too large hourglass effects have developed, leading to the premature failure seen. It is noted that run #3, which has more elements through the layer thickness than run #1, fails before #1 and has become more unstable by adding elements. Increasing the number of elements through the thickness og the layers further stabilizes the model to a level where good agreement between test and model is seen.

Increasing the hourglass coefficient for the design with 3 elements through the layer thickness (#2) is seen to stabilize the model such that good agreement between the test and model is seen. Run #2 shows a slightly smaller peak stress than run #4, 1041MPa compared with 1067MPa respectively, giving a 2.5% difference. Taking the time perspective into consideration, model #2 took 132min to progress the model 2.98ms forward in time, while model #4 took

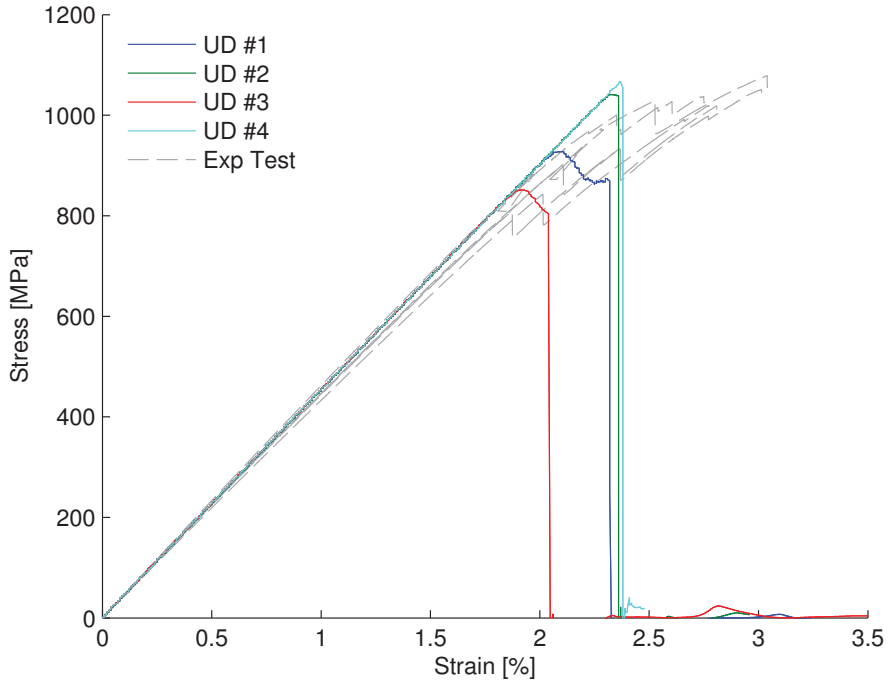

Figure 7.26: Modelled stress-strain relationship for the 4 model settings used to test the modelling of the UD layup

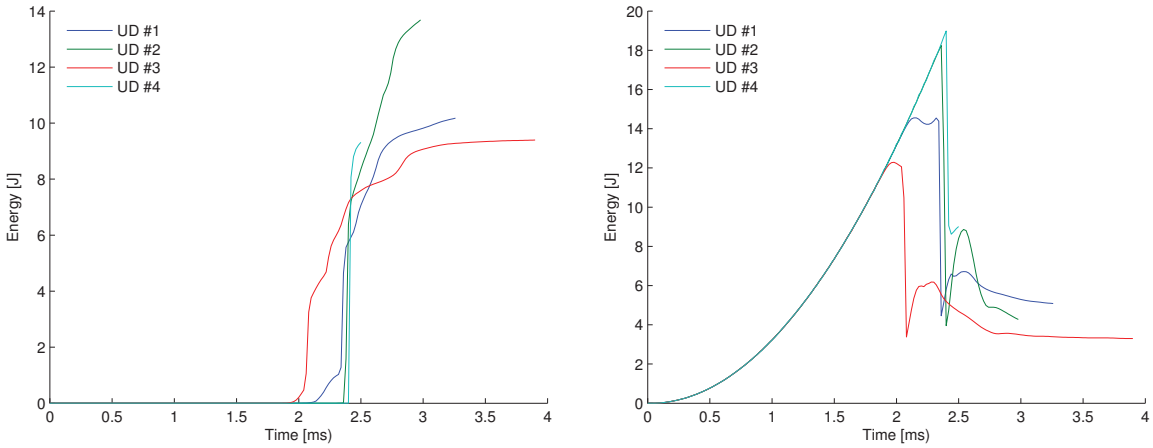

(a) Hourglass energy

(b) Internal energy

Figure 7.27: Energy balance in the modelled laminate during the simulation of the 4 model setting used to test the modelling of the UD layup

1143min to progress to model 2.54ms forward in time, giving a time difference of 759% for a 2.5% improvement in predicted laminate strength. Based on this it is found that model design #2 is best suited for modelling a UD laminate.

Quarto-Axial Layup

Based on the settings found to be most suitable for modelling the UD material test, a model was designed to represent the tensile test performed on the QA specimen type. Before doing this two issues had to be addressed. Firstly, as seen from table 7.5, the QA specimen consists of 3 quarto-axial mats with 8 layers in each mat, giving a total of 24 fibre layers. Modelling all of these layers will result in a model with approximately 9 million elements, using a 1:2 element aspect ratio. A model of this size could not be run with the available computer capacity. Therefore two reduced models, to represent the QA specimen, were designed. In the first model the laminate is represented with a QA mat, and in the second the laminate is represented with two QA mats, giving a total of 8 and 16 layers in the two models, who will be referred to as QA_8 and QA_{16} respectively. Secondly, the symmetry condition used from the UD specimen cannot be used for the QA specimen. As illustrated in figure 7.28, symmetry around a plane going vertically through the centre of the specimen exists for layers with 0° and 90° fibre orientations. But for the 45° material symmetry is not present. When modelling the QA laminate the entire width of the specimen therefore has to be modelled.

Figure 7.29 holds the modelled stress-strain curves for the QA_8 and QA_{16} and shows a poor agreement with the model data. Initially the model and test data compare well, but at approximately 0.2ms a shift in the modelled stress-strain data is observed, after which they start to deviate from the test curve. After the shift, the modelled curve is linear in shape, indicating that the non-linear effect is not captured by the used model design. The modelled curves keep their linear shape until complete failure of the modelled test specimen. The effect of having 16 layers, and thus two 0°layers in the centre of the specimen, is seen to have a strengthening effect on the modelled stress-strain relationship, but also has the effect that the

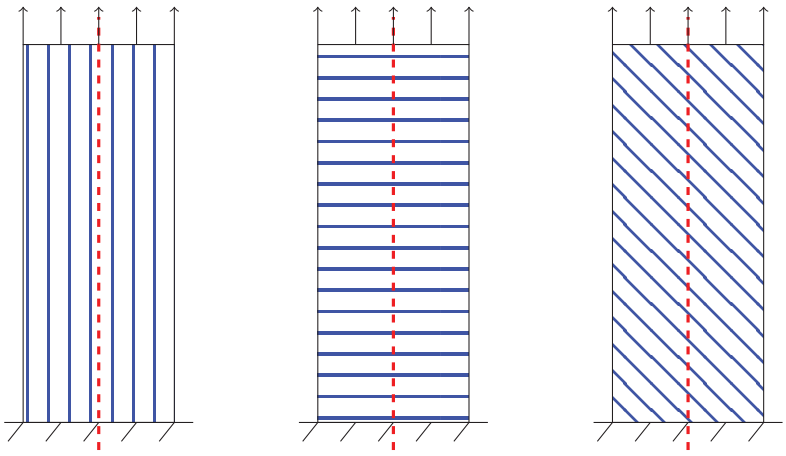

Figure 7.28: Symmetry consideration for a 0°, 90° and 45° fibre layup

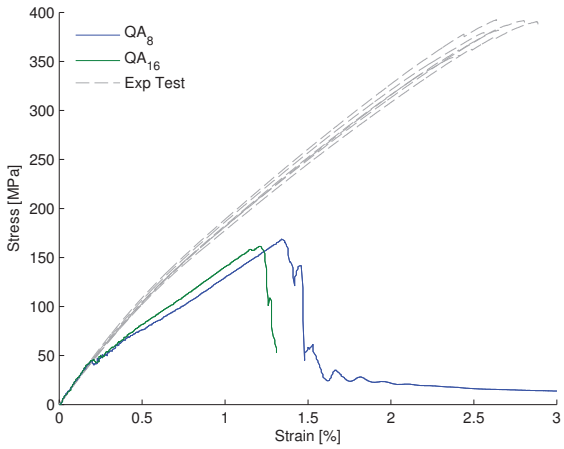

Figure 7.29: Modelled stress-strain relationship for the 2 QA models layouts

specimen fails earlier than that modelled with only 8 layers.

In figure 7.30a the hourglass energy for the two model cases of the QA specimen is shown. Compared with the hourglass energy development of the modelled UD specimen, figure 7.27a, the hourglass energy for the modelled QA specimens builds up almost from the beginning of the model run. Looking closer at the hourglass energy development, it can be seen that the rise in hourglass energy coincides with the time where the shift in stress-strain curve shape is observed in figure 7.29. The shift in the modelled stress-strain relationship is thus due to instabilities that rise due to hourglass energy development.

The early development of hourglass energy, compared with what is seen for the modelled UD specimens, is due to severe element deformation seen at the edge of the specimen, as illustrated in figure 7.31. This deformation generates instabilities at the entire edge area of the specimen leading to the premature failure seen. The reason for this element behaviour is believed to be that the differently oriented layers shares nodes. As the specimens are stretched the individual layers expand/subtract differently, due to the different material orientation in the layers, leading to the observed deformations. In *MAT_COMPOSITE_DMG_MSC delamination failure is included through a failure parameter, and is thus not modelled by modelling the

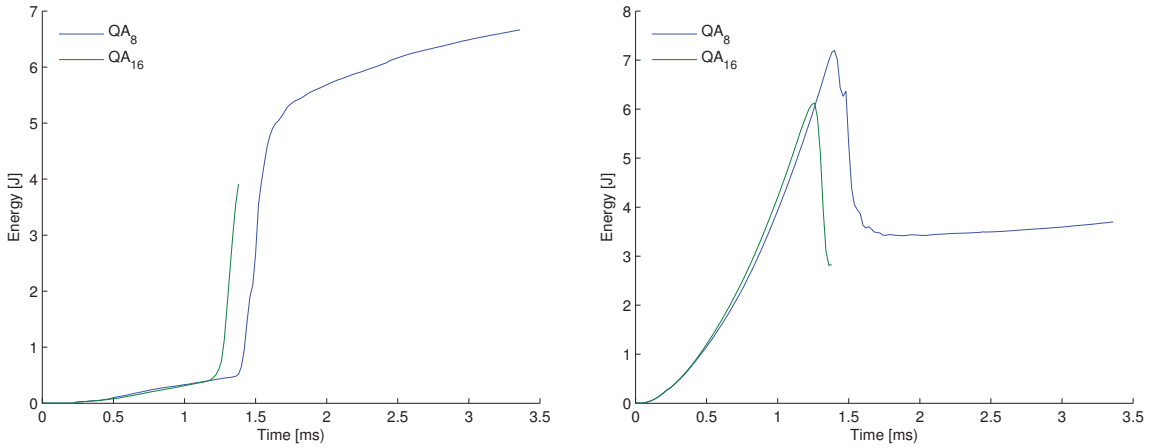

(a) Hourglass energy **(b)** Internal energy

Figure 7.30: Energy balance in the laminate during the modelling of the QA layups

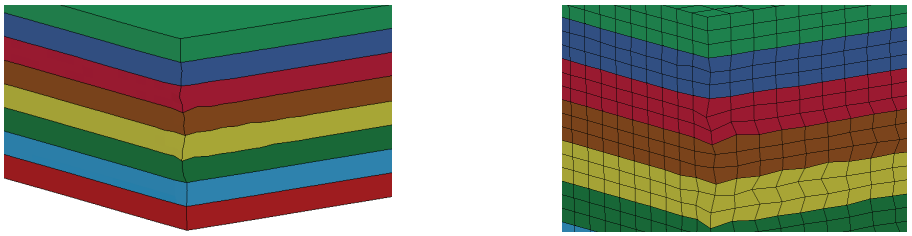

(a) QA_8

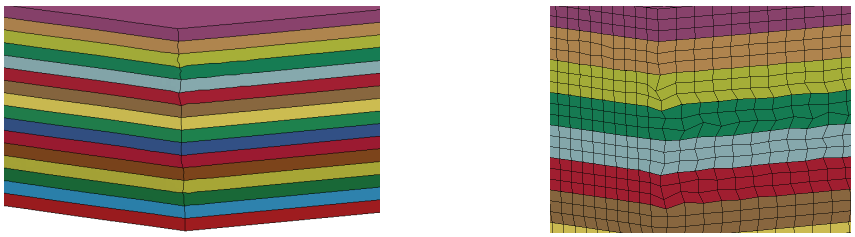

(b) QA_{16}

Figure 7.31: Element deformation at the edge of the specimen modelled with the QA_8 and QA_{16} design

physical interface. But as seen, this leads to odd element deformation due to edge effect, which is known to cause delamination at free edges [62].

Before modelling of laminate panels blast tested at 250g can be carried out, the presented issues regarding modelling of a quarto-axial layup need to be solved. One way to overcome the observed issue with edge effect, namely the merging of the nodes at the layer interfaces needs to be changed, and the actual layer interfaces need to be modelled instead. To model the interfaces, fracture resistance data for the different layer interface orientations, describing the load vs crack opening, is needed. These data can then be used in cohesive models to model the layer interface. In LS-DYNA there are basically two ways to model a cohesive interface. One method

is to model the actual interface by an element layer, where the elements are represented by a cohesive material model with an initial thickness of either zero or a thickness representative of the interface thickness. The other method is to use a contact definition between two interfaces, where the contact model is based on a cohesive law. Using this method a cohesive element layer is not needed which can make this method computationally faster.

7.2.3 250g Blast on a Sandwich Panel

As a final numerical study, modelling of the 250g blast on the sandwich panels with the H250 core type (CRCL-1–3) has been carried out. The CRCL sandwich type was chosen because it has only been possible to obtain all the needed parameter input for *MAT_HONEYCOMB to describe the H250 foam. In addition to the elastic and dynamic properties for the foam, tested for in chapter 6, inputs to the foam model were obtained from [54, 59].

As seen from the results of the blast tests performed on CRCL-1–3, three very different responses with respect to the failure development were found, where CRCL-1 showed no failure, CRCL-2 showed a single core crack and skin-core debonding, and CRCL-3 showed multiple core cracking and skin-core debonding. This constitutes a severe challenge from a modelling point of view, since the same model will not be able to predict these three different responses. The model has therefore been designed with focus on CRCL-1, where no failure was seen. This was chosen for several reasons, one being that it allowed for an evaluation of the obtained foam data when used to describe the core in the sandwich, but the choice was also made as no proper data yet exist to describe a debonding crack in the core-skin interface.

In figure 7.32a the model structure of the sandwich panel is shown. In the production, wooden supports have been placed around the edge of the sandwich, as shown in figure 7.32b, covering the area clamped between the blast box and the frame, to avoid crushing of the foam during the mounting of the frame. These wooden parts has been included in the model, and are represented by a wood material model, (*MAT_WOOD_PINE) available in LS-DYNA , which uses available default properties describing pine wood. To model the skins *MAT_ORTHOTROPIC_ELASTIC has been used, as the blast test performed on CRCL-1 did not show failure in the skin. Along all interfaces of the different model parts, nodes have been merged, such that no debonding can take place, as observed for the tested CRCL-1 panel. The blast load has been applied by use of *LOAD_BLAST_ENHANCED.

From the model run a notable difference in the modelled and tested sandwich response was

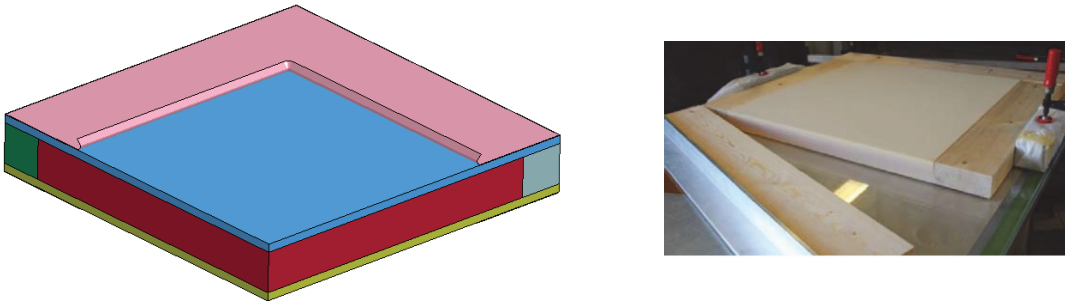

(a) (b)

Figure 7.32: Sandwich model representation, with the wood pieces put in to give support in the clamped region to avoid crushing the sandwich, included in the model

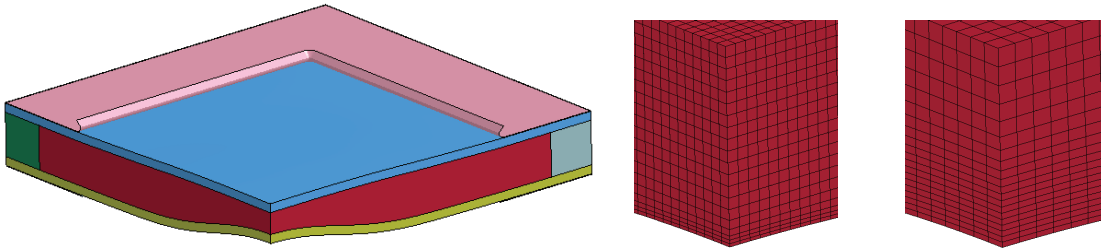

(a) t=0.18ms **(b)** t=0.06 **(c)** t=0.18ms

Figure 7.33: Crushing of the foam core in the model, where it was observed that the foam crushing initiated from the blast impact side of the sandwich (the bottom side of the shown sandwich panel), and then propagated up through the thickness of the modelled foam core, as indicated in (b) and (c)

identified. In contrast to what was seen in the experiments, the foam cores in the modelled sandwich compressed significantly, as indicated in figure7.33a, showing the sandwich model at the time for maximum foam compression. As shown in figure 7.33b and 7.33c the compression is not uniform over the foam cross-section, but is initiated from the side of the sandwich panel impacted by the blast wave, and then travels up through the thickness of the foam. The compression is initiated almost instantaneously after the blast wave impacts the sandwich panel, and thus before the panel has started to deflect.

The observed compression of the foam clearly indicates that one or more interactions are not properly accounted for in the modelled sandwich panel, or that the foam data do not correctly represent the foam core properties. A simple model was set-up to model the performed foam compression test, to determine if they could show the correct stress-strain relationship of the foam, which was found to be the case.

Regarding the foam data, a possible issue could be that the data generated from uni-axial material tests on small foam specimens, are not valid as input for a large foam panel used in the sandwich panels, where the sandwich skins and wood supports impose constraints on the foam. The foam will also experience a multi axial load condition, a load condition not tested for in the material test, and the effect of such load condition on the foam stress-strain behaviour is therefore not known. A study was performed to see how much the foam crush strength σ_{cr} should be increased to avoid the foam compression, showing that the crush strength had to be increased by $8 \times \sigma_{cr}$. Looking at the strain rate experienced by the compressed elements closest to the impact side, strain rates of above 70,000s^{-1} were found. Using the rate law expression (6.4) on page 82 to calculate the dynamic increase expected for the foam crush strength for such strain rates, a factor of 1.8 was found for a strain rate of 72.000s^{-1}, which is much below the needed factor 8. In the material testing the maximum tested strain rate was 10s^{-1}, and it is therefore not certain that extrapolation to such high strain rates is valid. A dynamic increase factor of 8 would require that the material changes behaviour and enters a regime where it becomes significantly more rate dependent than what has been found for the tested strain rate area.

Other factors which might contribute to the observed core compression in the sandwich model could be the improper representation of the skin-core interface, or the used representation of the skin as a non-layered orthrtropic-elastic material. A proper representation of the skins with fibre layers and layer interfaces could be thought to have an impact on the stress wave

impacting the foam, where for example the peak pressure could be attenuated by passage through the laminate layer interfaces, and thus reduce the peak pressure experienced by the foam, hindering the modelled core compression. Before this can be verified the challenges with the representation of the layered laminate needs to be solved.

7.3 Summary

A three step numerical blast load model was set-up using LS-DYNA to model the explosive, detonation of the explosive, the pressure wave expansion, the fluid structure interaction with the blast impacted panel and the response of the panel. The three steps can be described as:

Blast wave generation, using a 2D model to model the explosion and the generation of the blast wave. The use of a 2D model made it possible to use a very fine mesh to generate a well-defined blast wave front. The generated pressure was stored in a mapping file used to initialize the pressure in a 3D model representing the actual blast test set-up

Fluid Structure Interaction, using a 3D model designed to replicate the experimental test set-up. The blast box was represented by modelling the air inside the blast box, where boundary conditions were defined at the edges of the air domain to replicate the outflow constraints imposed by the real blast box. The pressure in the 3D air domain was initialized by reading the 2D pressure mapping file and utilizing rotational symmetry. In this model step FSI coupling with the modelled panel is performed such that the generated blast pressure could be brought into contact with the panel surface.

Structural response, where the air domain from the 3D model has been removed, after checking that no more impulse from the blast load is transferred to the panel, leaving the model with only the panel part, which will continue to respond to the applied loading. This results in a much faster computation time than with the FSI coupling active.

In the 2D model it was observed that the developed pressure was significantly influenced by the detonation products from the explosion, leading to a sudden decrease in pressure. The drop in pressure resulted in a lower incident impulse generated in the numerical load model compared to that obtained when using *LOAD_BLAST_ENHANCED. That the detonation product part of the model has an effect on the generated pressure was supported by [60], but experimental evidence of the observed behaviour has not been produced.

For the 3D part of the load model, studies on the influence of mesh size in the air domain and the panel, and of the FSI parameter settings were performed to optimize the mapping of the pressure in the 3D model and the FSI coupling. Leakage was prevented during the primary load transfer, but at approximately 0.4ms leakage developed in the centre part of the panel. Since the primary load transfer had taken place this was accepted, but in future work measures should be taken to eliminate it since it can have a consequence for modelling other types of blast loading scenarios. Further mesh refinement is seen as the primary measure to prevent the leakage.

The division of the load model into the three parts was primarily done for speed efficiency. Comparing step 2 and 3 of the load model, an increase in computational speed of approximately 64 times was obtained when removing the air domain and FSI coupling. Whether going from step 2 to 3 can take place, will depend on the actual problem in question. Some blast problems,

for example blast in a closed or very confined space, can generate long load transfer times such that step 2 has to be maintained throughout the entire run time.

Compared with the LBE model the clear advantage of the numerical load model approach is that reflections can be taken into consideration. This was shown in the case of modelling a blast on a panel i the blast box, when setting the air domain outflow constraints to mimic the venting conditions in the blast box, where a clear increase in panel deflection was seen compared to modelling a case where no outflow constraints were set. A similar problem cannot be modelled by use of LBE. The clear disadvantage of the numerical approach is the time consumption.

A comparison was performed between the modelled and tested panel response when impacted by a 25g blast load using a SOD of 100mm. The panel response was modelled using both the designed numerical load model and the *LOAD_BLAST_ENHANCED model. For both load models the modelled panel response was found to be smaller than in the test, with the deflection of the panel modelled with the numerical load model being 19% lower than in the experiment. The model results indicated that the modelled impulse was too low compared with the impulse delivered from the explosive in the tests. A study using the LBE model showed that an increase in explosive mass by 50%, leading to a larger impulse delivered to the panel, resulted in an exact match between the model and test results. To verify if the modelled impulse is too low, a test set-up was designed to measure the pressure and impulse from a blast test, but the variation in the measured data was too large for any conclusions to be drawn. An important issue to take into consideration in the model-to-test comparison for the 25g blast is that test data are only available from one test. The experimental variation is therefore not known, which makes it difficult to fairly evaluate how close the model is to match the test data on average. Because the test is from a 25g blast, the result can be sensitive to small deviations in used explosive mass, as it can constitute a relatively large amount of the total charge mass. The detonator itself can also have an effect on the measured response for such small explosive charges.

A number of preliminary models were performed to model blast loading from a 250g on the CRBJ30–32 panel types, resulting in a significant over prediction of deflection and failure of the modelled panels. It was therefore decided to take a step back in level of complexity, and instead model the laminate response obtained from material tests on Eglas/Epoxy laminates such that an evaluation of the performance of *MAT_COMPOSITE_DMG_MSC could be made. Two layups were modelled, a uni-directional and a quarto-axial. For the unidirectional good agreement between model and test data was found when using 3 elements per fibre layer and using the default hourglass model in LS-DYNA with hourglass coefficient QH=0.15. Using the findings from modelling the UD laminates, models of the tested quarto-axial laminates were built. Due to computer power limitations, the QA laminates had to be represented with fewer fibre layers than in the actual tested laminates. Two layups were modelled. One with 8 fibre layers and another with 16 fibre layers using the layer orientations shown in figure 7.5. The modelled stress-strain relationships of the two QA designs were seen to deviate significantly from the test results. The primary reason for the deviation was found to be improper representation of the layer interfaces resulting in odd element deformation leading to model instability. To overcome this problem the layer interfaces need to be represented for example through cohesive zone modelling.

Modelling of a 250g blast on the CRCL sandwich types revealed that the foam cores in the modelled sandwich compressed, a behaviour that is the opposite of that identified in the tested sandwich panels, where no core crushing was seen. It was found that the foam crush strength should be increased by a factor of 8 before the crushing was avoided. Possible reasons for the observed crushing could be that the foam data obtained from uni-axial material testing are

not valid for describing a foam panel under multi-axial loading. Another issue could be that the material data are based on a max strain rate of $10s^{-1}$, and it is therefore not known if the foam rate dependence changes sensitivity for much larger strain rates, which could lead to a larger dynamic increase factor at these strain rates. Finally, the improper representation of the laminate and skin-core interface could also contribute to the observed model behaviour.

Chapter 8

Conclusions and Future Work

Throughout this thesis a presentation has been given of the steps involved in the process of: designing a blast test set-up to conduct small scale blast tests; performing actual blast tests on designed panels; and using LS-DYNA to establish numerical models to predict the dynamic response of panels subjected to blast loading, where the measured panel response from the blast experiments is used as basis of validation for the numerical predictions.

The construction of the blast test facility was necessary for the completion of the project as it laid the foundation for conducting the blast tests and thus allowed the performance of the designed test panels to be evaluated. This work involved the design of the set-up itself, the blast box, the camera rack, and the creation of procedures for carrying out the blast tests. In addition, the work involved introducing the DIC system into the set-up and verifying that usable data could be obtained from blast test measurements. The construction of this facility made up a significant part of the project work. In addition to the construction of the blast test facility the project can be divided in to three additional major work areas;

- Blast testing of the designed laminate and sandwich panels
- Foam testing of the two foam types used as cores in the sandwich panels
- The design of a numerical blast load model in LS-DYNA, and the comparison of model and test data from the blast testing

In the following the overall conclusions from these three work areas are presented.

8.1 Blast Testing

Throughout the performed blast tests, the designed test set-up proved to be highly applicable for performing blast tests and provided data of consistently high quality. With the designed test set-up, blast tests utilizing charge sizes up to 250g were conducted providing usable results for analysis of the panel blast response. In addition to this, it was also shown that the set-up can be used to monitor a panel when tested to rupture. In its current state the test set-up performs best when charge sizes not larger than 250g are used. The main problem with exceeding this charge weight is that the blast box can move during the test, and the larger the charge load the more movement is seen. Successful tests with charges sizes up to 400g were performed, but

when the charge sizes exceeds 250g, the blast box movements become so severe that much work is needed to bring the box back into place. In the worst case, the box needs to be disassembled before repositioning can take place. Some work is thus needed to find a feasible solution to hold the blast box more firmly in place during loading and thereby significantly increase the functionality of the test site.

The DIC set-up has proven to be very usable in analysing the blast response of the tested panels. The ability to analyse the deflection across a section over the panel surface has been particularly useful in comparing the response of the three panel types tested. This kind of analysis would not be easy to perform using for example strain gauges, as that would require many strain gauges mounted on the panel surface. This functionality clearly demonstrates the power of using full field measurement, like DIC, to analyse the response of panels when exposed to blast loading. For the rupture test case, it was seen that the current high-speed cameras have too low a frame rate to provide enough data such that valid analysis of the panel response can be made, before a hole is created. The application of cameras with a higher frame rate could provide better insight into the mechanisms that take place before the rupture occurs, which could improve the understanding of the response of a panel when exposed to a near field blast load and thus lead to a better design of such panels.

During the post-test inspection of the water jet cut panels, it was possible to identify some of the failures that had developed during the blast loading of the panels. For the monolithic laminates the failure development was relatively similar in all tests. The same was not observed for the sandwich panels where especially the CRCL panel type showed a large difference in the extent of failure development. This variation in the level of failure is a significant challenge if modelling of blast loading on such panels is required, since the model always predicts the same behaviour. If no clear failure limit can be predicted from tests it will therefore be difficult to use a model approach to optimize the structure. The large variation in the failure of the sandwich panels also bring out a quandary in evaluating the performance of such panels. It must be determined if the variation is for example, due to inconsistent production quality or due to variations in the material properties of the constituents, to establish whether the variation can be controlled better. If the reasons for the variation of the panel performance cannot be established, then a lower blast limit should be set where a guarantee against failure can be given.

From the post-test inspections of the sandwich panels it was also revealed that no core crushing had taken place for both core types. This indicates that the idea of using a foam core as an energy absorber in a sandwich panel exposed to a blast loading should be rejected. This combined with the large deflection seen, indicates that there is no advantage in using sandwich structure over monolithic laminates for blast protection. This finding might be a consequence of the dimension of, and boundary conditions applied to the tested panels, and therefore only apply to this specific set-up. Other studies has indicated that there are benefits from using sandwich structures and that foam cores can act as an energy absorbers. Care should therefore be taken in concluding that sandwich panels do not offer advantages over monolithic panels based on the results from the limited number of tests carried out in this study.

The performed rupture test showed that the composite panel made from plain weave fibre layers clearly outperformed the panel made from non-woven quarto-axial fabrics. The woven fabric could withstand a charge size 50% larger than the non-woven laminate and still show no sign of being close to rupture. This result indicates that the plain weave fibre layup has attractive properties when it comes to absorbing the energy from a blast load, and their usage should be investigated further.

8.2 Foam Testing

Foam types Divinycell H80 and H250 from DIAB were tested in uniaxial compression at different strain rates. First of all, to measure the elastic properties of the foams and generate stress-strain curves for the foams for use as input in numerical models, and secondly, to gain knowledge of the rate response of the foam material to determine if the rate response could be modelled in a simple manner, such that rate effect could be included in the numerical modelling of the foam.

The compressive modulus and the Poisons ratio was measured by use of DIC on both foam types. The found data agreed well with the data in the DIAB datasheets, and also with data from the literature. The measurements also showed that the material was transverse isotropic, an observation supported by other studies. During the compression tests, to measure the foam stress-strain relationship, it was found that the foams did not deform uniformly. The deformation was seen to take place along collapse lines, developing vertically over the cross section of the foam, from which all further straining arose. This collapse line formation could be related to the non-uniform cell structure distribution in the material, which caused a non-uniform density distribution in the material. The collapse line developed in the area of the foam having the lowest density and thus the least amount of material to carry the stresses. The collapse line formations were not alike for the two foam types, which again could be related back to the cell structure, where the H250 foam had a much more pronounced difference in the cell structure through the thickness than was seen for the H80 foam.

The identification of the deformation taking place along the collapse lines meant that considerations about how to establish the stress-strain curves for the foams had to be made, because the presence of the collapse lines entailed that the strain development in the foam was non-uniform and that the strain rate therefore was not constant. A choice was made to evaluate the strain over the entire specimen height, as this took into account both the weak and strong parts of the foam, and it also meant that a constant average strain rate could be ascribed to the stress-strain curves.

For both foam types, stress-strain curves were established for the tested strain rates, all showing the characteristic shape of a rigid foam under uniaxial compression. A clear rate response was identified, showing a similar rate sensitivity for the two foam types. Plotting the foam crush strength level against strain rate showed that the increase in crush strength could be described by a simple logarithmic relation given in [52]. The rate response of the foams was seen to correspond to an upward parallel shift of the stress-strain curve measured at the lower strain rate, indicating that the stress-strain curves at the higher strain rates could be generated by scaling the initial *reference curve* with a suitable scaling parameter. Such scaling parameters could be generated by using the established rate equation for the crush strength. This was used to generate scaling parameters for a range of strain rate which was used in LS-DYNA to model the rate effect of the foam materials.

8.3 Modelling

A three step numerical blast load model was set-up using LS-DYNA to model the explosive, detonation of the explosive, the pressure wave expansion, the fluid structure interaction with the blast impacted panel and the response of the panel. The model was divided into three steps each taking care of a specific part of the blast loading problem;

Blast wave generation, using a 2D model to model the explosion and the generation of the

blast wave. The use of a 2D model made it possible to use a very fine mesh to generate a well-defined blast wave front. The generated pressure was stored in a mapping file used to initialize the pressure in a 3D model representing the actual blast test set-up

Fluid Structure Interaction, using a 3D model designed to replicate the experimental test set-up. The blast box was represented by modelling the air inside the blast box, where boundary conditions was defined at the edges of the air domain to replicate the outflow constraints imposed by the real blast box. The pressure in the 3D air domain was initialized by reading the 2D pressure mapping file and utilizing rotational symmetry. In this model step FSI coupling with the modelled panel is performed such that the generated blast pressure could be brought into contact with the panel surface.

Structural response, where the air domain from the 3D model has been removed, after checking that no more impulse form the blast load is transferred to the panel, leaving the model with only the panel part, which will continue to respond to the applied loading. This results in a much faster computation time than with the FSI coupling active.

In the 2D model it was observed that the developed pressure was significantly influenced by the detonation products from the explosion, leading to a sudden decrease in pressure. The drop in pressure resulted in a lower incident impulse generated in the numerical load model compared to that obtained when using the *LOAD_BLAST_ENHANCED model. That the detonation product part of the model has an effect on the generated pressure was supported by [60], but experimental evidence of the observed behaviour has not been produced.

For the 3D part of the load model, studies on the influence of mesh size in the air domain and the panel, and of the FSI parameter settings were performed to optimize the mapping of the pressure in the 3D model, and the FSI coupling. Leakage was prevented during the primary load transfer, but at approximately 0.4ms leakage developed in the centre part of the panel. Since the primary load transfer had taken place this was accepted, but in a future work, measures should be taken to eliminate it, since it can have a consequence for modelling other types of blast loading scenarios. Further mesh refinement is seen as the primary measure to prevent the leakage.

The division of the load model into the three parts was primarily done for speed efficiency. Comparing step 2 and 3 of the load model, an increase in computational speed of approximately 64 times was obtained when removing the air domain and FSI coupling. Whether going from step 2 to 3 can take place, will depend on the actual problem in question. Some blast problems, for example blast in a closed or very confined space, can generate long load transfer times such that step 2 has to be maintained through the entire run time. Compared with the LBE model, the clear advantage of the numerical load model approach is that reflections can be taken into consideration. This was shown in the case of modelling blast on a panel in the blast box, where a clear increase in panel deflection was seen compared to modelling a case where no outflow constraints were set on the blast box air domain. A similar problem cannot be modelled by use of LBE. The clear disadvantage of the numerical approach is the time consumption.

The response of the modelled and tested panel from a 25g blast load using a SOD of 100mm were compared. The panel response was modelled using both the designed numerical load model and the *LOAD_BLAST_ENHANCED model. For both load models the modelled panel response was found to be smaller than in the test, with the deflection of the panel modelled with the numerical load model being 19% lower than in the experiment. The model results indicated that the modelled impulse was too low compared with the impulse delivered from the explosive

in the tests. A study using the LBE model showed that an increase in explosive mass by 50%, leading to a larger impulse delivered to the panel, resulted in an exact match between the model and test results. To verify if the modelled impulse is too low a test set-up was designed to measure the pressure and impulse in a blast test, but the variation in the measured data was too large for any conclusions to be drawn. An important issue to take into consideration in the model-to-test comparison for the 25g blast is, that test data were only available from one test. The experimental variation is therefore not known, which makes it difficult to fairly evaluate how close the model is to match the test data on an average level. Because the test is from a 25g blast, the result can be sensitive to small deviations in used explosive mass, as it can constitute a relatively large amount of the total charge mass. The detonator itself can also have an effect on the measured response for such small explosive charges.

A number of preliminary model runs were performed to model blast loading from a 250g on the CRBJ panel types, resulting in a significant over prediction of deflection and failure of the modelled panels. It was therefore decided to take a step back in level of complexity, and instead model the laminate response obtained from tensile tests performed on Eglas/Epoxy laminates such that an evaluation of the performance of the *MAT_COMPOSITE_DMG_MSC material model could be made. Two layups were modelled; uni-directional and quarto-axial. For the unidirectional layup good agreement between model and test data was found, when using 3 elements per fibre layer and using the default hourglass model in LS-DYNA with hourglass coefficient QH=0.15. Using the findings from modelling the UD laminates, models of the tested quarto-axial laminates were built. Due to computer power limitations, the QA laminates had to be represented with fewer fibre layers than in the actual tested laminates. Two layups were modelled. One with 8 fibre layers and one with 16 fibre layers using the layer orientations shown in figure 7.5 on page 108. The modelled stress-strain relationship of the two QA designs was seen to deviate significantly from the material test results. The primary reason for the deviation was found to be improper representation of the layer interfaces resulting in odd element deformation due to edge effects leading to model instability.

Modelling of a 250g blast on the CRCL sandwich types revealed that the foam cores, in the modelled sandwich, compressed, a behaviour which is opposite of that identified in the tested sandwich panels, where no core crushing was seen. It was found that the foam crush strength should be increased by a factor of 8 before the crushing was avoided. Possible reasons for the observed crushing could be that foam data obtained from uni-axial material testing are not valid for describing a foam panel under multi-axial loading. Another issue could be that the material data used for describing the foam are based on a maximum strain rate of $10s^{-1}$, and in the model strain rates over $70{,}000s^{-1}$ were identified. It is therefore not known if the foam rate dependence changes sensitivity for much larger strain rates, which could lead to a larger dynamic increase factor at these strain rates, and thus a much larger crush strength than predicted by the obtained rate model parameters, which are based on the strain rates used in the foam tests. Finally the improper representation of the laminate and skin-core interface could also contribute to the observed model behaviour.

8.4 Recommendation for Future Work

Several issues have been pointed out as possible reasons for some of the inconsistencies seen when comparing test and model data for the response of the blast tested panels. In future work these challenges should be addressed such that better agreement between model and test

data can be generated. The following are suggestions for future work that is believed to help accommodate some of the challenges pointed out:

- To improve the comparison between model and test data for the 25g blast on the CRBJ panels, a series of additional tests at 25g using a SOD of 100mm should be performed such that the variation in the experimental data, for this blast test set-up, can be estimated. Using a comparison between model and test data for a 25g blast is found attractive since the test results indicate that no failure develops in the panel using this loading. The panel can therefore be modelled by an elastic model without having to consider layer interfaces and the agreement between test and model data will mainly be attributed to the applied loading in the test and model, which leads to the next recommendation.

- To further support the validation of the load modelling, work should be done to improve the pressure measurement set-up, such that valid pressure measurements can be performed. It is suggested to set-up a test with a charge size and stand-off distance combination resulting in a scaled distance $Z \approx 2$. Here the duration time will be longer and the peak pressure lower which might make measuring easier. In addition data in the literature can be found for such a set-up and used for comparison to verify the measured data. Such measurement will help disclose if the designed set-up is one of the problems in the large variation seen in the performed pressure measurements. The pressure measurements will also help to quantify the correct value to be used as a PETN to TNT conversion factor in the LBE model.

- To overcome the challenges in modelling the tensile test of the quarto-axial laminates, the design of the modelled laminate should be changed from not modelling the interfaces physically to representing the layer interfaces for example through the use of cohesive zone modelling. This will require establishment of fracture resistance data for the laminate interfaces such that data for the cohesive laws can be generated. This will allow for proper debonding at the tensile test specimen edges when tensioned and hopefully improve the element deformation seen at the model edges.

- To verify if the rate expression for the foam is valid at higher strain rates than tested for in the performed compression test, additional foam compression tests should be performed at higher strain rates in for example a Split Hopkinson Pressure Bar (SHPB) set-up. Before such tests are performed some considerations should be made with respect to specimen design. Normally tests in an SHPB are performed on round specimens, which is a deviation from the shape used in the performed test and thus could be a source of inconsistency between the two data sets. Secondly the specimen height used in the SHPB set-up should be similar to that used in performed tests as the foam microstructure was seen to have an impact on the foam response. This raises a third issue that the microstructure of the foam in any future test should be similar to that in the test already performed as otherwise that could be a source of error.

Bibliography

[1] Andy Wright and Mark French. The response of carbon fibre composites to blast loading via the europa cafv programme. *JOURNAL OF MATERIALS SCIENCE*, 43(20):6619–6629, 2008.

[2] Kumar P. Dharmasena, Haydn N. G. Wadley, Zhenyu Xue, and John W. Hutchinson. Mechanical response of metallic honeycomb sandwich panel structures to high-intensity dynamic loading. *INTERNATIONAL JOURNAL OF IMPACT ENGINEERING*, 35(9):1063–1074, 2008.

[3] Kumar P. Dharmasena, Haydn N. G. Wadley, Keith Williams, Zhenyu Xue, and John W. Hutchinson. Response of metallic pyramidal lattice core sandwich panels to high intensity impulsive loading in air. *INTERNATIONAL JOURNAL OF IMPACT ENGINEERING*, 38(5):275–289, 2011.

[4] S. A. Tekalur, A. Shukla, and K. Shivakumar. Blast resistance of polyurea based layered composite materials. *COMPOSITE STRUCTURES -BARKING THEN OXFORD-*, 84(3):271–281, 2008.

[5] S. L. Lemanski, G. N. Nurick, G. S. Langdon, M. S. Simmons, W. J. Cantwell, and G. K. Schleyer. Understanding the behaviour of fibre metal laminates subjected to localised blast loading. *COMPOSITE STRUCTURES*, 76(1-2):82–87, 2006.

[6] Y. Chi, G. S. Langdon, and G. N. Nurick. The influence of core height and face plate thickness on the response of honeycomb sandwich panels subjected to blast loading. *MATERIALS AND DESIGN -REIGATE-*, 31(4):1887–1899, 2010.

[7] M. D. Theobald, G. S. Langdon, G. N. Nurick, S. Pillay, A. Heyns, and R. P. Merrett. Large inelastic response of unbonded metallic foam and honeycomb core sandwich panels to blast loading. *COMPOSITE STRUCTURES -BARKING THEN OXFORD-*, 92(10):2465–2475, 2010.

[8] GilbertFord Kinney and Kenneth Judson Graham. *Explosive Shocks in Air*. Springer Berlin Heidelberg, second edition, 1985.

[9] Lapoujade V Le Blanc G, Adoum M. External blast load on structures – Emperical approach. In *5th European LS-Dyna Users Conference*, 2005.

[10] Rajan Sriram, UdayK. Vaidya, and Jong-Eun Kim. Blast impact response of aluminum foam sandwich composites. *Journal of Materials Science*, 41(13):4023–4039, 2006.

[11] T. Krauthammer and A. Altenberg. Negative phase blast effects on glass panels. *International Journal of Impact Engineering*, 24(1):1 – 17, 2000.

[12] A. Neuberger, S. Peles, and D. Rittel. Scaling the response of circular plates subjected to large and close-range spherical explosions. part i: Air-blast loading. *International Journal of Impact Engineering*, 34(5):859 – 873, 2007.

[13] U.S. Army Corps of Engineers Protective Design Center. Methodology manual for the single-degree-of-freedom blast effects design spreadsheets (sbeds). Technical report, U.S. Army Corps of Engineers, September 2008. Report No.: PDC TR-06-01 Rev1.

[14] P. S. Bulson. *Explosive loading of engineering structures : A history of research and a review of recent developments*. Taylor & Francis, 1997.

[15] John O. Hallquist. *LS-DYNA®Theory Manual*. Livermore Software Technology Corporation, March 2006.

[16] T. Borvik, A. G. Hanssen, M. Langseth, and L. Olovsson. Response of structures to planar blast loads - a finite element engineering approach. *COMPUTERS and STRUCTURES*, 87(9-10):507–520, 2009.

[17] D. Jiang, Y. Liu, C. Qi, Z.-D. Ma, B. B. Raju, and W. Bryzik. Innovative composite structure design for blast protection. *PAPERS- SOCIETY OF AUTOMOTIVE ENGINEERS NEW YORK*, pages 2007–01–0483, 2007.

[18] R.D. et al. Cook. *Concepts and applications of finite element analysis*. John Wiley & Sons, fourth edition, 2002.

[19] Klaus Weimar. LS-DYNA *User's Guide*. CAD-FEM GmbH & PWS, 1.19 edition, September 2001.

[20] Kevin Williams, Scott McClennan, Robert Durocher, Benoit St-Jean, and Jocelyn Tremblay. Validation of a loading model for simulating blast mine effects in armoured vehicles. In *7th International LS-Dyna Users Conference*, 2002.

[21] Y. Shi D. Bogosian, J. Ferritto. Measuring uncertainty and conservatism in simplified blast models. In *30th Explosive Safety Seminar*, page 26, August 2002.

[22] David W. Hyde. *User's Guide for Microcomputer Programs CONWEP and FUNPRO, Applications of TM 5-885-1 "Fundementals of Protective Design for Conventional Weapons*. US Army Corp of Engineers, April 1988.

[23] Gerald Bulmash Charles N. Kingery. Airblast parameters from tnt spherical air burst and hemispherical surface burst. Technical report, US Army Armament Research and Development Center, April 1984. Technical Report ARBRL-TR-02555.

[24] P. S. Westine, B. L. Morris, P. A. Cox, and E. Z. Polch. Development of computer program for floor plate response from landmine explosions. Technical report, US Army Tank Aotomotive Command, 1985. Technical Report No.: 13045.

[25] Philip Wagner. *SHOCK User's Manual Version 1.0*.

[26] Kenneth A. Bannister Glenn Randers-Pehrson. Airblast loading model for dyna2d and dyna3d. Technical report, Army Research Laborotory, March 1997. Technical Report ARL-TR-1310.

[27] Livermore Software Technology Corporation. *LS-DYNA®Keyword User's Manual – Volume I*, January 2013.

[28] Michael. M Swisdak. Explosion effects and properties. part i. explosion effects in air. Technical Report NSWC/WOL/TR-75-116, Naval Surface Weapons Center, 1975.

[29] N. Aquelet, M. Souli, J. Gabrys, and L. Olovson. A new ale formulation for sloshing analysis. *STRUCTURAL ENGINEERING AND MECHANICS*, 16(4):423–440, 2003.

[30] Mehdi Sotudeh Chafi, Ghodrat Karami, and Mariusz Ziejewski. Numerical analysis of blast-induced wave propagation using fsi and ale multi-material formulations. *INTERNATIONAL JOURNAL OF IMPACT ENGINEERING*, 36(10-11):1269–1275, 2009.

[31] Livermore Software Technology Corporation. *LS-DYNA®Keyword User's Manual – Volume II Material Models*, January 2013.

[32] Feng Zhu, Longmao Zhao, Guoxing Lu, and Emad Gad. A numerical simulation of the blast impact of square metallic sandwich panels. *INTERNATIONAL JOURNAL OF IMPACT ENGINEERING*, 36(5):687–699, 2009.

[33] A. Alia and M. Souli. High explosive simulation using multi-material formulations. *APPLIED THERMAL ENGINEERING*, 26(10):1032–1042, 2006.

[34] Material Science Corporation & University of Delaware Center for Composite Materials. *A Progressive Composite Damage Model for Unidirectional and Woven Fabric Composites*. University of Delaware Center for Composite Materials, 10.1 edition, 2012.

[35] Z. Hashin. Failure criteria for unidirectional fiber composites. *Journal of Applied Mechanics*, 47(2):329–334, June 1980.

[36] A. Matzenmiller, J. Lubliner, and R.L. Taylor. A constitutive model for anisotropic damage in fiber-composites. *Mechanics of Materials*, 20(2):125 – 152, 1995.

[37] Rasmus Eriksen. *High Strain Rate Performance of Composite Mateirals*. PhD thesis, Technical University of Denmark, 2014.

[38] P. L. Reu and T. J. Miller. The application of high-speed digital image correlation. *JOURNAL OF STRAIN ANALYSIS FOR ENGINEERING DESIGN*, 43(8):673–688, 2008.

[39] Mark W. Nansteel and Charles Chih Tsai Chen. Digital image correlation: A measurement tool for the study of explosive effects. *2009 IEEE Conference on Technologies for Homeland Security, HST 2009*, pages 234–241, 2009.

[40] Spranghers K., Kakogiannis D., Ndambi J.M., Lecompte D., and Sol H. Deformation measurements of blast loaded plates using digital image correlation and high-speed photography. *EPJ Web of Conferences*, 6:12006, 2010.

[41] Vikrant Tiwari, Michael A. Sutton, S. R. McNeill, Shaowen Xu, Xiaomin Deng, William L. Fourney, and Damien Bretall. Application of 3d image correlation for full-field transient plate deformation measurements during blast loading. *INTERNATIONAL JOURNAL OF IMPACT ENGINEERING*, 36(6):862–874, 2009.

[42] Michael A. Sutton, Jean-Jos Orteu, and Hubert Schreier. *Image Correlation for Shape, Motion and Deformation Measurements: Basic Concepts,Theory and Applications*. Springer Publishing Company, Incorporated, 1st edition, 2009.

[43] GOM. *ARAMIS User Manual - Software*, 6.1 edition, 2007.

[44] Lars Billeskov Jansen. Resist Report D08A – Manufacturing of thermosetting panels for 1. series. Technical report, Falck Schmidt Defence Systems A/S, 2011. Unpublished project report.

[45] Christen Malte Markussen and Helmuth Toftegaard. Resist Report D34C – Manufacture of sandwich panels for blast box tests. Technical report, Technical University of Denmark, Department of Wind Energy, 2013. Unpublished project report.

[46] G.S. Langdon, D. Karagiozova, C.J. von Klemperer, G.N. Nurick, A. Ozinsky, and E.G. Pickering. The air-blast response of sandwich panels with composite face sheets and polymer foam cores: Experiments and predictions. *International Journal of Impact Engineering*, 54(0):64 – 82, 2013.

[47] G.N. Nurick, G.S. Langdon, Y. Chi, and N. Jacob. Behaviour of sandwich panels subjected to intense air blast – part 1: Experiments. *Composite Structures*, 91(4):433 – 441, 2009.

[48] Robert W. Bielenberg; John D. Reid. Modeling crushable foam for the safer racetrack barrier. In *8th International LS-DYNA Conference*, 2004.

[49] H. Arora, P.A. Hooper, and J.P. Dear. Dynamic response of full-scale sandwich composite structures subject to air-blast loading. *Composites Part A: Applied Science and Manufacturing*, 42(11):1651 – 1662, 2011.

[50] Helmuth Toftegaard. Resist Report D26B & D27B – Low strain rate material characterization of e-glass/epoxy. Technical report, Technical University of Denmark, Department of Wind Energy, June 2012. Unpublished project report.

[51] *DIAB – Guide to core and sandwich*, 1 edition, December 2012. `http://www.diabgroup.com/`.

[52] J.L. Gibson and M.F. Ashby. *Cellular solids – Structure and properties*. Pergamon Press, 1 edition, 1988.

[53] S. Zhang, J. M. Dulieu-Barton, R. K. Fruehmann, and O. T. Thomsen. A methodology for obtaining material properties of polymeric foam at elevated temperatures. *EXPERIMENTAL MECHANICS*, 52(1):3–15, 2012.

[54] I.M. Daniel and J.-M. Cho. Characterization of anisotropic polymeric foam under static and dynamic loading. *Proceedings of the Society for Experimental Mechanics, Inc*, 51(8):1395–1403, 2011.

[55] EE Gdoutos, IM Daniel, and KA Wang. Failure of cellular foams under multiaxial loading. *COMPOSITES PART A-APPLIED SCIENCE AND MANUFACTURING*, 33(2):163–176, 2002.

[56] V. L. Tagarielli, V. S. Deshpande, and N. A. Fleck. The high strain rate response of pvc foams and end-grain balsa wood. *COMPOSITES PART B-ENGINEERING*, 39(1):83–91, 2008.

[57] MC Saha, H. Mahfuz, UK Chakravarty, M. Uddin, ME Kabir, and S. Jeelani. Effect of density, microstructure, and strain rate on compression behavior of polymeric foams. *MATERIALS SCIENCE AND ENGINEERING A-STRUCTURAL MATERIALS PROPERTIES MICROSTRUCTURE AND PROCESSING*, 406(1-2):328–336, 2005.

[58] Dung D. Luong, Dinesh Pinisetty, and Nikhil Gupta. Compressive properties of closed-cell polyvinyl chloride foams at low and high strain rates: Experimental investigation and critical review of state of the art. *COMPOSITES PART B-ENGINEERING*, 44(1):403–416, 2013.

[59] I.M. Daniel. *Dynamic Failure of Materials and Structures*, chapter 7. Springer-Verlag US, 2010. isbn; 1441904468, 9781441904461.

[60] Len Schwer. Air blast - engineering models. Unpublished, October 2011. Course material from LSTC course on Blast Modelling in LS-DYNA, `www.schwer.net`, Len@Schwer.net.

[61] P. C. Crawford B. M. Dobratz. *LLNL Explosives Handbook: Properties of Chemical Explosives and Explosive Simulants*. Lawrence Livemore National Laboratory, January 1985.

[62] R.M. Jones. *Mechanics of composite materials*. Taylor & Francis, 1999.

[63] R.A. Shenoi, A. Groves, and Y.D.S. Rajapakse, editors. *Theory and applications of sandwich structures*. University of Southampton Press, 2005.

Appendices

Appendix A

Re-Design of the Blast Box

During blast testing using the original blast box, it became clear that some issues existed with its design. Damages to the bolts fixating the frame to the box was observed after testing, and one test resulted in the fracture of a number of bolts along one frame edge, leaving the blast box unusable for further test. A re-design of the blast box was therefore necessary.

A.1 Identified Problems with the Original Blast Box

Figure A.1 shows the original design of the blast box. From testing the following problems were identified;

- Improper design of the blast box frame, where rotation of the frame parts lead to damages on the bolts fixating the frame to the box.
- Sliding of the test plates in the clamped region between the frame and blast box, leading to rupture of the plate material between the plate edge and the edges of the bolt holes going through the plate.
- Insufficient strength of the bolts fixating the frame to the box, severely limiting the possibilities for performing tests in the blast box.

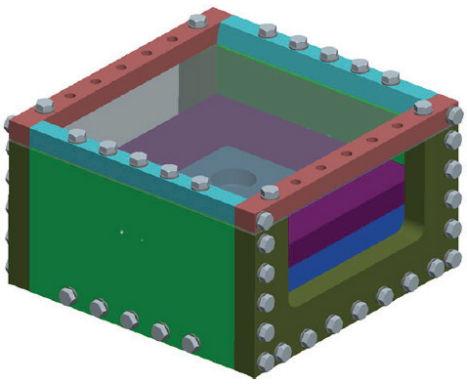

Figure A.1: Design of the original blast box

The most severe of the identified issues was the lack of strength in the frame/box assembly, as it left the box unusable for further test. But the other issues were also detrimental for the functionality of the blast box. The rotation of the frame parts bended the bolts, with the consequence that they had to be changed after a test. But if the bending were to become large enough, the bolts could also start to be dragged out and thereby damaging the threading in the bolt holes, such that the sides of the blast box would have to be repaired or changed. The sliding of the test plate also constituted a problem for the bolts, because the plate was dragged into the side of the bolts, creating indentations in the side of them. In addition the sliding makes it harder to model the response numerically, because the boundary conditions become harder to represent.

A.1.1 Wrong Frame Design

The existing frame consisted of four parts that were assembled by a single bolt in each corner, as illustrated in figure A.1. This made it possible for the two turquoise frame parts to rotate around the axis of the corner bolts. When the plate is deflecting the up-warded bending of the plate will apply a moment to the frame edge, rotating the frame parts, as shown in figure A.2a, leading to the identified deformation of the bolts, see figure A.2b, and indirectly to the damage of their threading, caused by unscrewing the bended bolts from the box, making them unfit for further use.

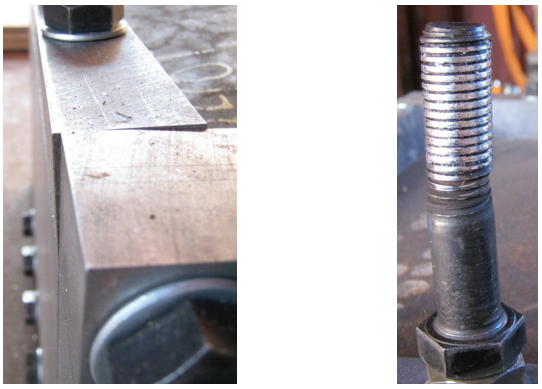

(a) **(b)**

Figure A.2: Damage to bolts due to frame rotation

To solve this problem a redesign of the frame should be made that prevents the observed rotation. This could be done by constructing a solid frame cut out from a large plate, or redesigning the assembly method of the four frame parts.

A.1.2 Sliding of Test Plate in Clamped Area

After testing, it was observed that the holes in the plates, where the bolts go through, were damaged as shown in figure A.3. This indicated that the friction between the frame/box and the target plates was too low to keep the plates in position. When the edges of the holes in the plate are brought into contact with the bolts, large stresses develop, leading to the shown damages. For tests made on composite plates the problem was very severe. There the developed stress between the bolts and plate hole edges got so large that it exceeded the strength of the

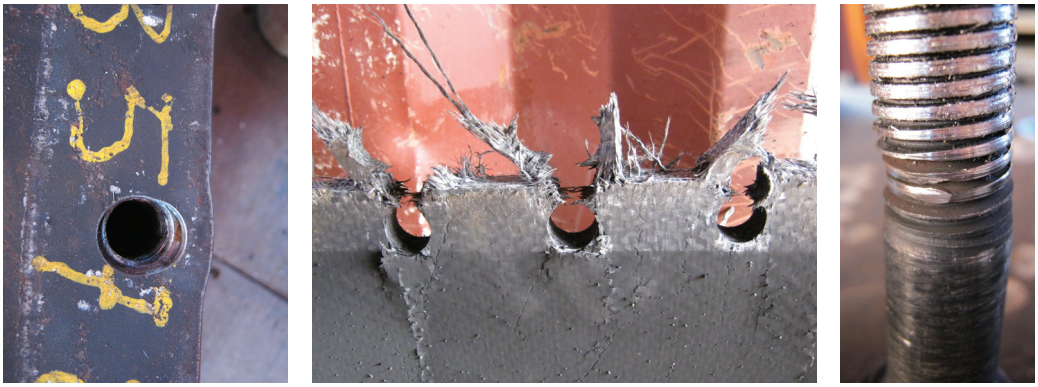

(a) (b) (c)

Figure A.3: Problems with boundary conditions during test

composite material. This resulted in the observed fracture of the material between the hole edges and the plate edge. But also the bolt itself can be damaged by the contact with the plate as seen in A.3c. This will generated a form of shear load in the bolts, which could have been a contributing factor to the observed fracture of the bolts along the frame edge.

The sliding problem is primarily related to the friction between the frame/box and the test plate. Since the friction force is related to the fixating force of the frame and the frictional coefficient μ between the contacting surfaces, this problem could be solved by increasing one or both of these parameters.

A.1.3 Improper Strength of Frame-Box Assembly

In the original blast box, the frame was fastened to the box with 14 M20 8.8 bolts. During a surface detonation test with 250g PETN, fracture of the bolts along one of the frame edges occurred, see figure A.4. The failure was believed to be a combination of the force transferred to the bolts from the upward movement of the test plat, and the damages added to the bolts as described above.

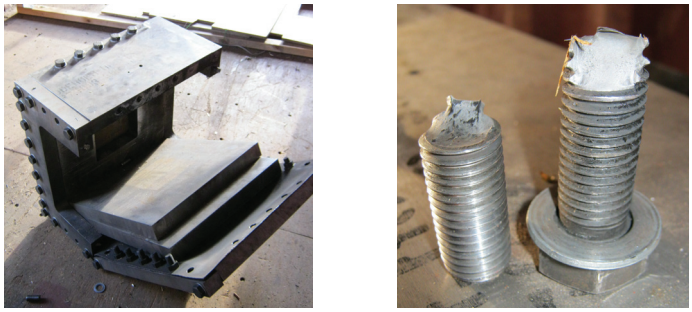

(a) (b)

Figure A.4: Failure of blast box after fracture of bolt along on frame edge

A.2 New Blast Box Design

Based on the identified failure types different solutions have been considered of which the pros and cons have been evaluated. The chosen solutions can be summarised as follows;

- Complete re-design of the frame structure.
- Increased friction in the clamped area by affecting the surface roughness.
- Increased strength of the frame–box assembly by increasing the size and strength of the bolts.

In the following the individual solutions will be described.

A.2.1 New Frame Design

To solve the problem regarding the rotation in the frame structure a new frame structure has been designed, presented in figure A.5

The frame is still made from four parts that are assembled in each corner. This was found better than making the frame as one solid structure, due to cheaper production, but most importantly due to the fact that if one side is damaged it can be replaced. In the new frame design the assembly of the frame parts is made by connecting overlapping slaps using four bolts. To make it possible for the new frame to be positioned on the blast box, the nuts used for tightening the bolts at each corner assembly has been countersunk, as shown in figure A.5b. This new type of assembly will hinder the kind of rotation seen with the previous frame design. The new frame is also constructed in a stronger material than before. The previous frame was constructed from steel S235, whereas the new frame is constructed in Impax Supreme from Uddeholm. The data for the two steels can be seen in table A.1. The Impax Supreme steel is very tough, and should therefore be well suited to withstand the loading from the blast

Table A.1: Comparison of S235 steel and Impax Supreme

	σ_y[MPa]	$\sigma_U TS$[MPa]	ε_{fail}[%]	ρ[kg m^{-3}]
S235	235	360 – 460	26	7850
Impax Supreme	750 – 950	900 – 1100	-	7800

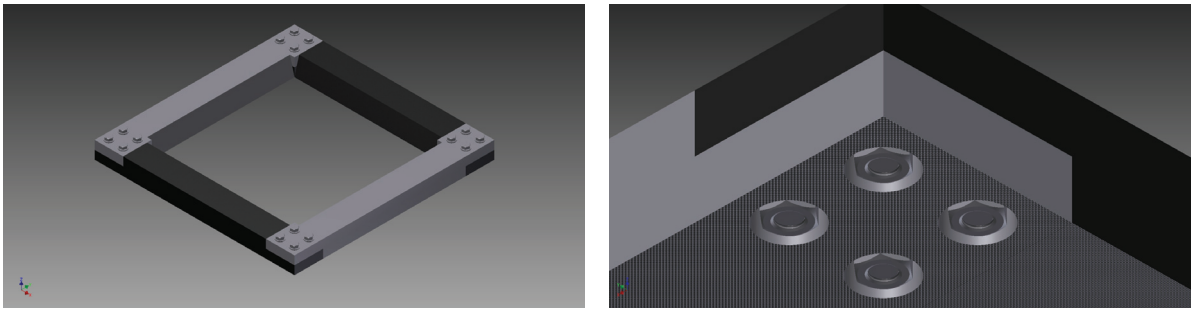

(a) **(b)**

Figure A.5: New frame design

testing. A further improvement of the new frame is that all the interior frame edges has been giving a chamfer of 15° to allow full view from the high speed cameras. The old frame only had the chamfer on two of the edges, resulting in shadows developing on the test plate surface from the non-chamfered frame edges, when monitored by the high speed cameras. This can be detrimental for the DIC analysis, since the shadows will darken that specific area of the images, reducing the available grey-scale level, and thereby making it harder for the correlation algorithm to estimate the movement of the surface pattern, from which the deformation is determined.

Finally the dimensions of the new frame have been increased. The height has been increased from 40 to 60 mm, to give greater bending stiffness to the structure, and the exterior dimension has been increased from 600×600mm to 700×700mm, keeping the interior opening 500×500mm. This has increased the area where the test plates are fixed, from a width of 50 to 100mm. This was done to increase the distance from the edge of the bolt holes in the plate to the edge of the plate. This will give a larger amount of material to support the stress developing if the plates are slid against the bolts, making it more difficult to deform/rupture the plate edge area as seen in figure A.3.

A.2.2 Improved Boundary Conditions

As explained earlier, a problem exists with fixating the plates in the clamped area, which can be regarded as a frictional problem. One way to solve this problem could be to increase the clamping force, by tighten to bolts more. But with the tools available on the test site this is not possible. Instead the problem has been addressed by increasing the surface roughness in the clamping region. This has been done by milling a pyramid shaped pattern into the surfaces of the box and frame that are clamped against the test plate. Each pyramid have a height of 1mm and a bottom area of 2×2mm. The idea behind the pattern is that the small pyramids will generate locally high stresses and are thus able to penetrate into the surface of the test material, such that a higher friction between the box/frame surfaces and the test plate is generated.

A.2.3 Increased Box-Frame Assembly Strength

The observed failure of the bolts in the blast box was, as mentioned above, thought to be due to a combination of the load from the blast pressure and from the damages imparted by the bending of the frame and the contact deformation between test plate and the bolts, due to the sliding of the test plate. The bending and sliding contributions should have been removed or minimized from the redesign of the frame and application of the pyramid pattern in the clamping area. Analysing the load going into the bolts from the blast load and the deflection of the test plate, is not straight forward. First of all because no simple analytical expressions could be found that describe the pressure build-up in a semi confined volume, as that present in the blast box set-up used when failure occurred. An expression for a zero venting volume was found [63], but that was not valid for the explosive mass and box volume combination used. Going to a full numerical analysis was found to be out of the scope for the redesign process, as such a process would take up to much time before a design could be ready.

It was therefore decided to change the bolts holding the frame from M20 8.8 bolts to M30 10.9 bolts, which first and foremost are able to take up more load. The change from M20 to M30, and the redesign of the frame, meant that other parts of the blast box had to be replaced to be able to support the new wider frame and have room for the larger bolts.

A.2.4 New Blast Box Design

Figure A.6 shows a model of the redesigned blast box. Based on the described design changes, the following parts had to be created or replaced with new ones;

- the two solid sides, which were changed from a thickness of 50 to 100mm to give support for the new frame and bolts
- the 4 corner pieces giving frame support in the corners and connects the 100m sides with the reused open sides
- Support plates, to better fixate the target plate along the open sides

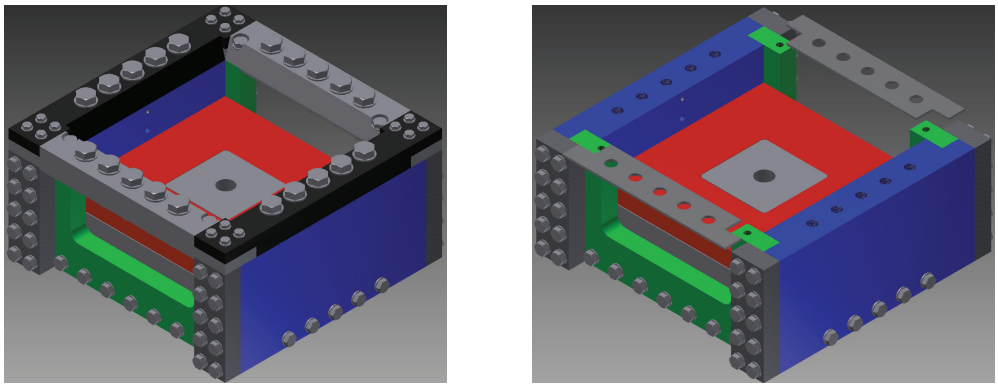

(a) **(b)**

Figure A.6: Redesigned blast box

Appendix **B**

Material Data for Composite and Sandwich Panels

B.1 E-glass Fibre Properties

SAERTEX® GmbH & Co. KG
Brochterbecker Damm 52
D-48369 Saerbeck
phone: ++49/2574/902-0
fax: ++49/2574/902-209
e-mail: info@saertex.com

DATASHEET

STYLE NO.
S32EQ250-00940-01270-464000

DESCRIPTION OF STYLE
QUADRAXIAL-GLASS-FABRIC

CONSTRUCTION	AREAL-WEIGHT [g/m²]	TOLERANCE [+/-%]	MATERIAL	LINEAR DENSITY tex
0°	236	5	E-Glass	600
-45°	234	5	E-Glass	300
90°	236	5	E-Glass	600
+45°	234	5	E-Glass	300
STITCHING:	6	5	PES 76 dtex	

BINDER: Tricot-Warp GAUGES: 5

WIDTH: 1270 mm or in tapes

TOTAL AREAL WEIGHT: 946 g/m² TOTAL TOLERANCE: 5,0 %

23.06.2006 TG

B.2 Epoxy Matrix Properties

Advanced Materials

Structural Composites

HUNTSMAN

MATRIX SYSTEMS FOR INDUSTRIAL COMPOSITES **DATA SHEET**

Hot curing epoxy system based on Araldite® LY 564* / Aradur® 917* / Accelerator 960-1*

Araldite LY 564 is a low-viscosity epoxy resin
Aradur 917 is an anhydride hardener
Accelerator 960-1 is used as an amine accelerator

Applications

Industrial composites (tubes, pipes, profiles)

Properties

Araldite LY 564 with Aradur 917 and Accelerator 960-1 exhibits a low mix viscosity at room temperature in combination with a long pot life. Nevertheless very short cure cycles can be achieved at cure temperatures above 120 °C for an economical production. The system shows good fibre impregnation properties and is easy to process. The cured system has excellent mechanical properties.

Processing

- Filament Winding
- Pultrusion
- Wet lay-up
- Resin Transfer Moulding (RTM)

Key data

Araldite LY 564		
Aspect (visual)	clear liquid	
Colour (Gardner,	1 - 2	
Viscosity at 25 °C (ISO 12058-1))	1200 - 1400	[mPa s]
Density at 25 °C (ISO 1675)	1.1 - 1.2	[g/cm^3]
Flash point	185	[°C]
Aradur 917		
Aspect (visual)	clear liquid	
Colour (Gardner,	≤ 2	
Viscosity at 25 °C (ISO 12058-1)	50 - 100	[mPa s]
Density at 25 °C (ISO 1675)	1.20 - 1.25	[g/cm^3]
Flash point	195	[°C]
Accelerator 960-1		
Aspect (visual)	light yellow liquid	
Colour (Gardner,	≤ 8	
Viscosity at 25 °C (ISO 12058-1)	150 - 300	[mPa s]
Density at 25 °C (ISO 1675)	0.95 - 0.97	[g/cm^3]
Flash point	110 - 120	[°C]
Storage temperature in every case (see expiry date on original container)	2 - 40	[°C]

Storage

Provided that the products described above are stored in a dry place in their original, properly closed containers at the above mentioned storage temperatures they will have the shelf lives indicated on the labels.

Partly emptied containers should be closed immediately after use.

Because Aradur 917 is sensitive to moisture, storage containers should be ventilated with dry air only.

* *In addition to the brand name product denomination may show different appendices , which allows us to differentiate between our production sites: e.g , BD = Germany, US = United States, IN = India, CI = China, etc.. These appendices are in use on packaging, transport and invoicing documents. Generally the same specifications apply for all versions. Please address any additional need for clarification to the appropriate Huntsman contact.*

March 2004 1/1

Hot curing epoxy system based on Araldite LY 564 / Aradur 917/ Accelerator 960-1

Processing data

Mix ratio	*Components*	*Parts by weight*	*Parts by volume*
	Araldite LY 564	100	100
	Aradur 917	98	93
	Accelerator 960-1	3	3.5
Processing recommendations	The hardener and accelerator can be premixed to allow the use of two-component mixing/dosing equipment. The temperature where gelation is being carried out should not be higher than necessary. A high gelation temperature induces shrinkage and generates internal stress within the part.		
Initial mix viscosity	*[°C]*		*[mPa s]*
(Hoeppler, ISO 12058-1B)	at 25		450 - 700
	at 40		100 - 200
Pot life	*[°C]*		
(Tecam, 100 ml, 65 % RH)	at 23	*[h]*	80 - 90
	at 50	*[min]*	210 - 250
Gel time	*[°C]*		*[min]*
(Hot plate)	at 80		30 - 40
	at 100		8 - 13
	at 110		5 - 8
	at 120		3 - 5
	at 130		2 - 4
	at 140		1 - 2
	at 150		0.5 - 1.5
	The values shown are for small amounts of pure resin/hardener mix. In composite structures the gel time can differ significantly from the given values depending on the fibre content and the laminate thickness.		
Typical cure cycles	0.5 - 1 h 130 °C or 4 h 100 °C or 4 h 80 °C + 4 h 120 °C		
	The optimum cure cycle has to be determined case by case depending on the processing and the economic requirements.		

2/2

Hot curing epoxy system based on Araldite LY 564 / Aradur 917/ Accelerator 960-1

Properties of the cured, neat formulation

Glass transition temperature (IEC 1006, DSC, 10 K/min)	*Cure:*			*T_G [°C]*
	4 h 80 °C			88 - 98
	4 h 100 °C			110 - 120
	1 h 130 °C			94 - 102
	4 h 80 °C + 4 h 120°C			122 - 130
	4 h 80 °C + 4 h 140 °C			115 - 123
	4 h 80 °C + 8 h 140 °C			115 - 123
	4 h 80 °C + 4 h 160 °C			112 - 120
Tensile test (ISO 527)		*Cure:*		*4 h 80 °C + 4 h 120 °C*
	Tensile strength	[MPa]		75 - 91
	Elongation at tensile strength	[%]		4 - 5
	Ultimate strength	[MPa]		75 - 91
	Ultimate elongation	[%]		4.5 - 5.5
	Tensile modulus	[MPa]		3100 - 3200
Flexural test (ISO 178)		*Cure:*	*4 h 100 °C*	*4 h 80 °C + 4 h 120 °C*
	Flexural strength	[MPa]	150 - 165	140 - 150
	Elongation at flexural strength	[%]	6 - 7	6 - 7
	Flexural modulus	[MPa]	3250 - 3450	3000 - 3100
Fracture properties Bend notch test (PM 258-0/90)		*Cure:*		*4 h 80 °C + 4 h 120 °C*
	Fracture toughness K_{1C}	[MPa√m]		0.59 - 0.7
	Fracture energy G_{1C}	[J/m^2]		100 - 125
Water absorption (ISO 62)	*Immersion:*	*Cure:*		*4 h 80 °C + 4 h 120 °C*
	1 day H_2O 23 °C	[%]		0.13 - 0.15
	10 days H_2O 23 °C	[%]		0.40 - 0.45
Flexural test (ISO 178)	Laminate comprising 12 layers unidirectional E-glass fabric (425 g/m^2) Fibre volume content: 59 - 64 % Laminate thickness t = 3.0 - 3.3 mm			
		Cure:		*4 h 80 °C + 4 h 120 °C*
	Flexural strength	[MPa]		880 - 980
	Elongation at flexural strength	[%]		2.0 - 2.2
	Flexural modulus	[MPa]		44000 - 46000
Interlaminar shear strength (ASTM D 2344)	Short beam: Laminate comprising 12 layers unidirectional E-glass fabric (425 g/m^2) Fibre volume content: 59 - 64 % Laminate thickness t = 3.0 - 3.3 mm			
		Cure:		*4 h 80 °C + 4 h 120 °C*
	Shear strength	[MPa]		54 - 58

3/3

B.3 Measured Mechanical Properties for UD Eglas/Epoxy laminate

Table B.1: Measured material data for an Eglas/Epoxy UD laminate

Measured property	Symbol	Unit	Average	95%-CI[a]	CLT[b]
Tensile modulus in the 1-direction	E_{11}^t	GPa	45.3	1.3	45.2
Poissons ratio for loading in tension in the 1-direction	ν_{12}	–	0.272	0.013	0.256
Tensile strength in the 1-direction	X_{11}^t	MPa	1041	31	1117
Compressive modulus in the 1-direction	E_{11}^c	GPa	45.89	1.16	45.2
Compressive strength in the 1-direction	X_{11}^c	MPa	801	56	662
Tensile modulus in the 2-direction	E_{22}^t	GPa	12.7	0.8	15.8
Poissons ratio for loading in tension in the 2-direction	ν_{21}	–	0.077	0.008	0.089
Tensile strength in the 2-direction	X_{22}^t	MPa	29	3	65
Compressive modulus in the 2-direction	E_{22}^c	GPa	14.7	0.5	15.8
Compressive strength in the 2-direction	X_{22}^c	MPa	107	1	161
Tensile modulus in the 3-direction	X_{33}^t	MPa	19	3	66.1
Compressive modulus in the 3-direction	E_{33}^c	GPa	16	0.7	15.8
Poissons ratio for loading in tension in the 3-direction	ν_{31}	–	0.096	0.01	0.089
Poissons ratio for loading in tension in the 3-direction	ν_{32}	–	0.040	0.02	0.036
Compressive strength in the 3-direction	X_{33}^c	MPa	186	15	161
Shear modulus in the 12-plane(1× specimen)	G_{12}	GPa	5.19	0.15	5.32
Shear strengths in the 12-plane(1× specimen)	X_{12}	MPa	62.2	0.9	80.6
Shear modulus in the 12-plane(2× specimen)	G_{12}	GPa	5.36	0.11	5.32
Shear strengths in the 12-plane(2× specimen)	X_{12}	MPa	62.0	1.3	80.6
Shear modulus in the 13-plane(1× specimen)	G_{13}	GPa	5.18	0.26	5.32
Shear strengths in the 13-plane(1× specimen)	X_{13}	MPa	58.1	0.8	80.6
Shear modulus in the 23-plane(1× specimen)	G_{23}	GPa	4.34	0.22	5.97
Shear strengths in the 23-plane(1× specimen)	X_{23}	MPa	31.4	3.7	–

[a] Confidence Interval bound
[b] Calculated based on Classic Lamination Theory for a 60 vol-% laminate

B.4 Measured Mechanical properties for Quarto-Axial Eglas/Epoxy Laminate

Table B.2: Measured material data for an Eglas/Epoxu quarto-axial laminate

Measured property	Symbol	Unit	Average	95%-CI[a]	CLT[b]
Tensile modulus	E^t_{xx}	GPa	22.1	0.6	22.8
Poissons ratio	ν_{xy}	–	0.301	0.003	0.308
Tensile strength	X^t_{xx}	MPa	387	8	108
Compressive modulus	E^c_{xx}	GPa	23	1.2	22.8
Compressive strength	X^c_{xx}	MPa	398	18	267
Poissons ratio	ν_{zx}	–	–	–	0.169
Poissons ratio	ν_{zy}	–	–	–	0.169
Shear modulus in the xy-plane(1× specimen)	G_{xy}	GPa	8.0	0.6	8.7
Shear strengths in the xy-plane(1× specimen)	X_{xy}	MPa	224	6	102
Shear modulus in the xy-plane(2× specimen)	G_{xy}	GPa	8.7	0.3	8.7
Shear strengths in the xy-plane(2× specimen)	X_{xy}	MPa	182	9	102
Shear modulus in the xz-plane(1× specimen)	G_{xz}	GPa	–	–	4.66
Shear strengths in the xz-plane(1× specimen)	X_{xz}	MPa	–	–	–
Shear modulus in the yx-plane(1× specimen)	G_{yz}	GPa	–	–	4.66
Shear strengths in the yz-plane(1× specimen)	X_{yz}	MPa	–	–	–

[a] Confidence Interval bound
[b] Calculated based on Classic Lamination Theory for a 56 vol-% laminate

B.5 S-glass/Phenol Laminate Datasheet Properties

Owens Corning Proprietary Data

INNOVATIONS FOR LIVING™

ShieldStrand® S/ Phenolic MAT 162 Input

Version: *1.3*
Updated Date: Jan. 2013

Property	***Unit***	***Input Value***
vf	-	0.62
ρc	*gm/cc*	2.00
E1	*GPa*	29.7
E2	*GPa*	24.8
E3	*GPa*	12.0
v21	-	0.100
v31	-	0.200
v32	-	0.200
G12	*GPa*	4.500
G23	*GPa*	2.900
G31	*GPa*	3.100
X1T	*MPa*	549
X1C	*MPa*	204
X2T	*MPa*	457
X2C	*MPa*	138
X3T	*MPa*	52
SFC	*MPa*	1540
SFS	*MPa*	165
S12	*MPa*	73
S23	*MPa*	49
S31	*MPa*	49
AM1	-	2.00
AM2	-	2.00
AM3	-	0.50
AM4	-	-0.20
PHIC	-	10
SFFC	-	0.30
Crate1	-	0.03
Crate2	-	0.00
Crate3	-	0.03
Crate4	-	0.03
SDELM	-	1.2
OMGMX	-	0.988
E_LIMT	-	5.00
EEXPN	-	5.00
ECRSH	-	0.001
AMODEL	-	2 (PW)

Photo Representation:

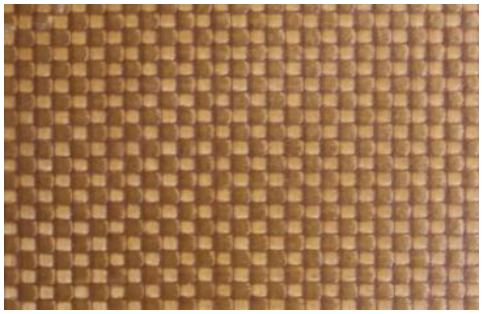

Details:
MIL-DTL-64154B, Class C
Supply Chain Procured Plate
ShieldStrand S - 360 tex Input
24 oz PW Fabric - Phenolic Resin @ 20% RC

Notes:
1) Fabric has a slight increase in fiber count within the Warp (Machine Direction); thus, the value differences in the Transverse and Longitudinal directions. Higher values would generally represent the Warp direction.

2) This data is representative of a Ballistic Grade Laminate. A Structural based laminate (30% RC) may have higher values.

3) Updates will be distributed as necessary and if there is any immediate verification needed, do not hesitate to contact Owens Corning.

Technical Contact: Matthew Berning (513-480-0888)

Owens Corning Proprietary Data

***Data shown for comparative purposes only and is not to be construed as a guaranty or warranty of performance. Absolute performance will vary by resin system and process. Owens Corning believes this to be an accurate representation of our material's performance.

ShieldStrand® S
High-Performance Reinforcements

Grey P. Chapman
Key Account Manager
OCV™ Reinforcements
Phone: 919-518-7855
Email: grey.chapman@owenscorning.com

OCV™ Reinforcements

OWENS CORNING
COMPOSITE MATERIALS, LLC
ONE OWENS CORNING PARKWAY
TOLEDO, OHIO 43659
1.800.GET.PINK™
www.owenscorning.com
www.ocvreinforcements.com

OCV™ Reinforcements

High-Performance Reinforcements

ShieldStrand® S
High-Performance Reinforcements

OWENS CORNING OCV™ Reinforcements

High-Performance Reinforcements

INTRODUCING SHIELDSTRAND® S

OCV™ has developed a new high performance fiber that enables durable lightweight protection.

Delivering Performance

- The ballistic performance has been tested and validated in the supply chain and exceeds the MIL-DTL-64154B (Class A) V50 requirement. Approval is pending.
- ShieldStrand® S provides up to a 50% weight savings versus steel for equivalent FSP protection, increasing vehicle payload and mobility.
- ShieldStrand® S has been tested in combination with a steel or ceramic strike face to provide protection when armor piercing and multi hit capability is required or an overmatched threat exists.
- ShieldStrand® S meets fire, smoke and toxicity requirements.
- ShieldStrand® S solutions provide better durability in high temperature, corrosive and high humidity environments.

Enabling Possibilities

- The strength of ShieldStrand® S provides structure as well as protection, allowing armor to be integrated into the vehicle structure, reducing overall vehicle weight.
- ShieldStrand® S can be molded into large complex-shaped structural parts using proven large scale composite manufacturing technologies.
- ShieldStrand® S composite armor is affordable, at 1/3 the cost of UHMWPE solution, enabling more vehicles to be protected, increasing warfighter survivability.

Readily Available

- ShieldStrand® S reinforcements are produced on a large scale using OCV innovative breakthrough glass fiber technology. Production can support surges common in defense applications.
- ShieldStrand® S composite panels provide an alternative supply chain where pricing is less volatile than aluminum alloys.

COMPARISON OF OCV™ HIGH PERFORMANCE GLASSES

	Test Method	E-Glass	ShieldStrand®	ShieldStrand® S
Pristine Fiber Tensile Strength Gpa (KSI)	ASTM D2101	3.45-3.79 Gpa (500-550 KSI)	4.58 Gpa (664 KSI)	5.11-5.30 Gpa (741-769 KSI)
Impregnated Fiber Tensile Strength Gpa (KSI)	ASTM D2343	1.99-2.48 Gpa (290-360 KSI)	3.17-3.48 Gpa (460-505 KSI)	3.41-3.83 Gpa (495-555 KSI)
Young's Modulus Gpa (MSI)	Sonic Resonance @ 20C	68.9-72.4 Gpa (10-10.5 MSI)	86.9-95.8 Gpa (12.6-13.9 KSI)	88 Gpa (12.7 MSI)
Density g/cc (lb/in^3)	ASTM C693	2.55-2.58 g/cc (0.092-0.093 lb/in^3)	2.55 g/cc (0.0921 lb/in^3)	2.45 g/cc (0.0885 lb/in^3)
Specific Pristine Tensile Strength (m)	Calculated	1.36-1.5 x10^5 m	1.83 x10^5 m	2.01-2.12 x10^5 m
Specific Tensile Modulus (m)	Calculated	2.73-2.85 x10^6 m	3.49x10^6 m	3.67x10^6 m

COMPARISON OF OCV™ SHIELDSTRAND® S TO COMMON ARMOR MATERIALS

	ShieldStrand® S	S-2 Glass®	Steel	Aluminum	Aramid	UHMW Polyethylene
Performance	.30 cal FSP at 2455 fps					
Weight	+	+	--	-	++	+++
Cost	++	+	+++	+++	-	--
Structural Capability	+	+	+++	++	-	--
Part thickness (thin is +)	+	+	+++	++	-	--
Corrosion resistance	++	++	--	-	+	-
Fire, Smoke and Toxicity	+	+	++	++	-	---
Temperature Resistance	++	++	+++	++	+	-

ShieldStrand® S provides a balanced solution.

SHIELDSTRAND® S MEETS CLASS A BALLISTIC PERFORMANCE

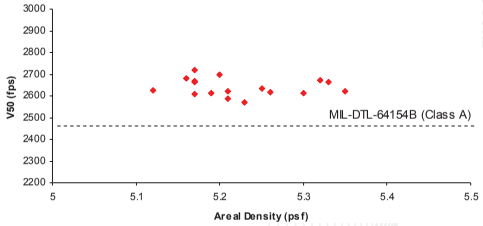

SHIELDSTRAND® ENABLES LIGHTWEIGHT ARMOR

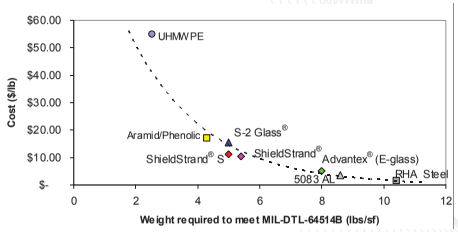

SHIELDSTRAND® S PROVIDES STRUCTURE AS WELL AS PROTECTION

	ASTM Test Method	ShieldStrand® S Phenolic Plate (typical mean property range)
Fiber Volume	D2734	61 - 66%
Resin Weight	D2584	16 - 24%
Water Absorption	D570, D792	< 1.5%
Longitudnal Flexural, Wet Ret.	D790	> 70%
Thickness (in.)		0.470 - 0.530
Ply Thickness (in.)	25 ply	0.019 - 0.020
Areal Density (lb/sf)	25 ply	4.6 - 5.4
Density (lb/ci)	D792	0.072 - 0.074
Hardness (M scale)	D785	> 80
Thermal Transition	D4065	210 - 240
Flammability	UL 94	V0
Time to Ignition @ 50k W/sm	E1354	500 - 600
Total Heat Release (MJ/sm)	E1354	25 - 60
MAHRE (kW/sm)	E1354	20 - 35
FIGRA	E1354	0.10 - 0.20

VARIOUS PRODUCT FORMS ARE AVAILABLE

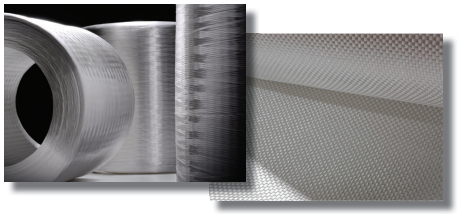

- ShieldStrand® S roving is 360 tex (1377 yds/lbs). The filament diameter is 9 micron.
- Standard 24oz woven roving and custom fabrics are available
- ShieldStrand® S can be processed in low-cost pultrusion, continuous lamination, compression molding of flat plates or infusion of complex shapes

Divinycell® H

Technical Data

The high performance sandwich core

Divinycell H provides excellent mechanical properties to low weight. The unique combination of polyurea and pvc, yields impressive mechanical performance to a low weight. Divinycell H has been widely used and has a proven track record in virtually every application area where sandwich composites are employed including the marine (leisure, military and commercial), land transportation, wind energy, civil engineering/infrastructure and general industrial markets.

Divinycell H is ideal for applications subject to fatigue, slamming or impact loads. Other key features of Divinycell H include consistent high quality, excellent adhesion/peel strength, excellent chemical resistance, low water absorption and good thermal/acoustic insulation. Divinycell H is compatible with virtually all commonly used resin and manufacturing systems.

Product Characteristics

- High temperature resistance
- Low water absorption
- Superior damage tolerance
- Fast and easy to process
- Good chemical resistance
- Excellent fatigue properties
- Low resin uptake
- Wide range of properties
- Provides excellent mechanical properties to a low weight

Mechanical properties Divinycell® H

Property	Test Procedure	Unit		H35	H45	H60	H80	H100	H130	H160	H200	H250
Compressive Strength[1]	ASTM D 1621	MPa	Nominal	0.5	0.6	0.9	1.4	2.0	3.0	3.4	5.4	7.2
			Minimum	0.3	0.5	0.7	1.15	1.65	2.4	2.8	4.5	6.1
Compressive Modulus[1]	ASTM D1621-B-73	MPa	Nominal	40	50	70	90	135	170	200	310	400
			Minimum	29	45	60	80	115	145	175	265	350
Tensile Strength[1]	ASTM D 1623	MPa	Nominal	1.0	1.4	1.8	2.5	3.5	4.8	5.4	7.1	9.2
			Minimum	0.8	1.1	1.5	2.2	2.5	3.5	4.0	6.3	8.0
Tensile Modulus[1]	ASTM D 1623	MPa	Nominal	49	55	75	95	130	175	205	250	320
			Minimum	37	45	57	85	105	135	160	210	260
Shear Strength	ASTM C 273	MPa	Nominal	0.4	0.56	0.76	1.15	1.6	2.2	2.6	3.5	4.5
			Minimum	0.3	0.46	0.63	0.95	1.4	1.9	2.2	3.2	3.9
Shear Modulus	ASTM C 273	MPa	Nominal	12	15	20	27	35	50	60	73	97
			Minimum	9	12	16	23	28	40	50	65	81
Shear Strain	ASTM C 273	%	Nominal	9	12	20	30	40	40	40	45	45
			Minimum	4	8	10	15	25	30	30	35	35
Density	ISO 845	kg/m^3	Nominal	38	48	60	80	100	130	160	200	250

1. Perpendicular to the plane. All values measured at +23°C

Nominal value is an average value of a mechanical property at a nominal density.
Minimum value is a minimum guaranteed mechanical property a material has independently of density.

www.diabgroup.com

Technical Characteristics Divinycell® H

Characteristics[1]	Unit	H35	H45	H60	H80	H100	H130	H160	H200	H250	Test method
Density variation	%	-10% to +20%	± 10	± 10	± 10	± 10	± 10	± 10	± 10	± 10	-
Thermal conductivity[2]	W/(m-K)	0.028	0.028	0.029	0.031	0.033	0.036	0.040	0.044	0.049	EN 12667
Coeff, linear heat expansion	x10^{-6}/°C	40	40	40	40	40	40	40	40	40	ISO 4897
Heat Distortion Temperature	°C	+125	+125	+125	+125	+125	+125	+125	+125	+125	DIN 53424
Continous temp range	°C	-200 to +70	-200 to +70	-200 to +70	-200 to +70	-200 to +70	-200 to +70	-200 to +70	-200 to +70	-200 to +70	-
Max process temp	°C	+90	+90	+90	+90	+110	+110	+110	+110	+110	-
Dissipation factor	-	0.0001	0.0002	0.0003	0.0005	0.0006	0.0009	0.0012	0.0015	0.0019	ASTM D 2520
Dielectric constant	-	1.04	1.05	1.06	1.09	1.11	1.15	1.18	1.23	1.29	ASTM D 2520
Poissons ratio[3]	-	0.4	0.4	0.4	0.4	0.4	0.4	0.4	0.4	0.4	D638-08

1. Typical values
2. Thermal conductivity at +20°C
3. Standard deviation is 0.045

Continuous operating temperature is typically -200°C to +70°C. The foam can be used in sandwich structures, for outdoor exposure, with external skin temperatures up to +85°C. For optimal design of applications used in high operating temperatures in combination with continuous load, please contact DIAB Technical Services for detailed design instructions.

Maximum processing temperature is dependent on time, pressure and process conditions. Therefore users are advised to contact DIAB Technical Services to confirm that Divinycell H is compatible with their particular processing parameters.

Physical characteristics

Format, color		Unit	H35	H45	H60	H80	H100	H130	H160	H200	H250
Plain sheets	Length	mm	2650	2440	2440	2440	2160	1960	1860	1730	1640
	Width	mm	1250	1220	1220	1220	1070	970	915	850	800
GS sheet	Length	mm	1250	1220	1220	1220	1080	980	930	865	-
	Width	mm	883	813	813	813	1070	970	915	850	-
GS sheet	Length	mm	1250	1220	1220	1220	-	-	-	-	-
	Width	mm	1250	1220	1220	1220	-	-	-	-	-
Color			Natural	Natural	Natural	Natural	Natural	Natural	Natural	Natural	Natural

Issued: January 2014 Doc No: H Jan 2014 rev11 SI

DIAB Group
Box 201
SE- 312 22 Laholm, Sweden

Phone: +46 (0)430 163 00
Fax: +46 (0)430 163 96
E-mail: info@se.diabgroup.com

www.diabgroup.com

Appendix C

LS-DYNA Material Model MAT_162

C.1 Manual for MAT_COMPOSIE_DMG_MSC

This appendix holds the description of *MAT_COMPOSITE_DMG_MSC taken from the LS-DYNA material model user manual [31]

***MAT_COMPOSITE_MSC_{*OPTION*}**

Available options include:

<BLANK>

DMG

These are Material Types 161 and 162. These models may be used to model the progressive failure analysis for composite materials consisting of unidirectional and woven fabric layers. The progressive layer failure criteria have been established by adopting the methodology developed by Hashin [1980] with a generalization to include the effect of highly constrained pressure on composite failure. These failure models can be used to effectively simulate fiber failure, matrix damage, and delamination behavior under all conditions - opening, closure, and sliding of failure surfaces. The model with DMG option (material 162) is a generalization of the basic layer failure model of Material 161 by adopting the damage mechanics approach for characterizing the softening behavior after damage initiation. These models require an additional license from Materials Sciences Corporation, which developed and supports these models.

Card 1	1	2	3	4	5	6	7	8
Variable	MID	RO	EA	EB	EC	PRBA	PRCA	PRCB
Type	A8	F	F	F	F	F	F	F

Card 2	1	2	3	4	5	6	7	8
Variable	GAB	GBC	GCA	AOPT	MACF			
Type	F	F	F	F	I			

Card 3	1	2	3	4	5	6	7	8
Variable	XP	YP	ZP	A1	A2	A3		
Type	F	F	F	F	F	F		

Card 4	1	2	3	4	5	6	7	8
Variable	V1	V2	V3	D1	D2	D3	BETA	
Type	F	F	F	F	F	F	F	

Card 5	1	2	3	4	5	6	7	8
Variable	SAT	SAC	SBT	SBC	SCT	SFC	SFS	SAB
Type	F	F	F	F	F	F	F	F

Card 6	1	2	3	4	5	6	7	8
Variable	SBC	SCA	SFFC	AMODEL	PHIC	E_LIMT	S_DELM	
Type	F	F	F	F	F	F	F	

Card 7	1	2	3	4	5	6	7	8
Variable	OMGMX	ECRSH	EEXPN	CERATE1	AM1			
Type	F	F	F	F	F			

Define the following cards if and only if the option DMG is specified

Card 8	1	2	3	4	5	6	7	8
Variable	AM2	AM3	AM4	CERATE2	CERATE3	CERATE4		
Type	F	F	F	F	F	F		

VARIABLE	DESCRIPTION
MID	Material identification. A unique number or label not exceeding 8 characters must be specified.
RO	Mass density
EA	E_a, Young's modulus - longitudinal direction

VARIABLE	DESCRIPTION
EB	E_b, Young's modulus - transverse direction
EC	E_c, Young's modulus - through thickness direction
PRBA	ν_{ba}, Poisson's ratio ba
PRCA	ν_{ca}, Poisson's ratio ca
PRCB	ν_{cb}, Poisson's ratio cb
GAB	G_{ab}, shear modulus ab
GBC	G_{bc}, shear modulus bc
GCA	G_{ca}, shear modulus ca
AOPT	Material axes option, see Figure 2.1: EQ.0.0: locally orthotropic with material axes determined by element nodes as shown in Figure 2.1. Nodes 1, 2, and 4 of an element are identical to the Nodes used for the definition of a coordinate system by *DEFINE_COORDINATE_NODES. EQ.1.0: locally orthotropic with material axes determined by a point in space and the global location of the element center, to define the a-direction. EQ.2.0: globally orthotropic with material axes determined by vectors defined below, as with *DEFINE_COORDINATE_VECTOR. EQ.3.0: locally orthotropic material axes determined by rotating the material axes about the element normal by an angle, BETA, from a line in the plane of the element defined by the cross product of the vector v with the element normal. The plane of a solid element is the midsurface between the inner surface and outer surface defined by the first four nodes and the last four nodes of the connectivity of the element, respectively. EQ.4.0: locally orthotropic in cylindrical coordinate system with the material axes determined by a vector v, and an originating point, p, which define the centerline axis. This option is for solid elements only. LT.0.0: the absolute value of AOPT is a coordinate system ID number (CID on *DEFINE_COORDINATE_NODES, *DEFINE_COORDINATE_SYSTEM or *DEFINE_COORDINATE_VECTOR). Available in R3 version of 971 and later.

VARIABLE	DESCRIPTION
MACF	Material axes change flag: EQ.1: No change, default, EQ.2: switch material axes a and b, EQ.3: switch material axes a and c, EQ.4: switch material axes b and c.
XP YP ZP	Define coordinates of point **p** for AOPT = 1 and 4.
A1 A2 A3	Define components of vector **a** for AOPT = 2.
V1 V2 V3	Define components of vector **v** for AOPT = 3 and 4.
D1 D2 D3	Define components of vector **d** for AOPT = 2.
BETA	Layer in-plane rotational angle in degrees.
SAT	Longitudinal tensile strength
SAC	Longitudinal compressive strength
SBT	Transverse tensile strength
SBC	Transverse compressive strength
SCT	Through thickness tensile strength
SFC	Crush strength
SFS	Fiber mode shear strength
SAB	Matrix mode shear strength, ab plane, see below.
SBC	Matrix mode shear strength, bc plane, see below.
SCA	Matrix mode shear strength, ca plane, see below.
SFFC	Scale factor for residual compressive strength
AMODEL	Material models: EQ.1: Unidirectional layer model EQ.2: Fabric layer model
PHIC	Coulomb friction angle for matrix and delamination failure, <90
E_LIMT	Element eroding axial strain

VARIABLE	DESCRIPTION
S_DELM	Scale factor for delamination criterion
OMGMX	Limit damage parameter for elastic modulus reduction
ECRSH	Limit compressive volume strain for element eroding
EEXPN	Limit tensile volume strain for element eroding
CERATE1	Coefficient for strain rate dependent strength properties
AM1	Coefficient for strain rate softening property for fiber damage in a direction.
AM2	Coefficient for strain rate softening property for fiber damage in b direction.
AM3	Coefficient for strain rate softening property for fiber crush and punch shear damage.
AM4	Coefficient for strain rate softening property for matrix and delamination damage.
CERATE2	Coefficient for strain rate dependent axial moduli.
CERATE3	Coefficient for strain rate dependent shear moduli.
CERATE4	Coefficient for strain rate dependent transverse moduli.

Material Models:

The unidirectional and fabric layer failure criteria and the associated property degradation models for material 161 are described as follows. All the failure criteria are expressed in terms of stress components based on ply level stresses $(\sigma_a, \sigma_b, \sigma_c, \tau_{ab}, \tau_{bc}, \tau_{ca})$ and the associated elastic moduli are $(E_a, E_b, E_c, G_{ab}, G_{bc}, G_{ca})$. Note that for the unidirectional model, a, b and c denote the fiber, in-plane transverse and out-of-plane directions, respectively, while for the fabric model, a, b and c denote the in-plane fill, in-plane warp and out-of-plane directions, respectively.

Unidirectional lamina model

Three criteria are used for fiber failure, one in tension/shear, one in compression and another one in crush under pressure. They are chosen in terms of quadratic stress forms as follows:

Tensile/shear fiber mode:

$$f_1 = \left(\frac{\langle \sigma_a \rangle}{S_{aT}} \right)^2 + \left(\frac{\tau_{ab}^2 + \tau_{ca}^2}{S_{FS}^2} \right) - 1 = 0$$

Compression fiber mode:

$$f_2 = \left(\frac{\langle \sigma_a^{'} \rangle}{S_{aC}} \right)^2 - 1 = 0, \quad \sigma_a^{'} = -\sigma_a + \left\langle -\frac{\sigma_b + \sigma_c}{2} \right\rangle$$

Crush mode:

$$f_3 = \left(\frac{\langle p \rangle}{S_{FC}} \right)^2 - 1 = 0, \quad p = -\frac{\sigma_a + \sigma_b + \sigma_c}{3}$$

where $\langle \ \rangle$ are Macaulay brackets, S_{aT} and S_{aC} are the tensile and compressive strengths in the fiber direction, and S_{FS} and S_{FC} are the layer strengths associated with the fiber shear and crush failure, respectively.

Matrix mode failures must occur without fiber failure, and hence they will be on planes parallel to fibers. For simplicity, only two failure planes are considered: one is perpendicular to the planes of layering and the other one is parallel to them. The matrix failure criteria for the failure plane perpendicular and parallel to the layering planes, respectively, have the forms:

Perpendicular matrix mode:

$$f_4 = \left(\frac{\langle \sigma_b \rangle}{S_{bT}} \right)^2 + \left(\frac{\tau_{bc}}{S_{bc}^{'}} \right)^2 + \left(\frac{\tau_{ab}}{S_{ab}} \right)^2 - 1 = 0$$

Parallel matrix mode (Delamination):

$$f_5 = S^2 \left\{ \left(\frac{\langle \sigma_c \rangle}{S_{bT}} \right)^2 + \left(\frac{\tau_{bc}}{S_{bc}^{''}} \right)^2 + \left(\frac{\tau_{ca}}{S_{ca}} \right)^2 \right\} - 1 = 0$$

where S_{bT} is the transverse tensile strength. Based on the Coulomb-Mohr theory, the shear strengths for the transverse shear failure and the two axial shear failure modes are assumed to be the forms,

$$S_{ab} = S_{ab}^{(0)} + \tan(\varphi) \langle -\sigma_b \rangle$$

$$S_{bc}^{'} = S_{bc}^{(0)} + \tan(\varphi) \langle -\sigma_b \rangle$$

$$S_{ca} = S_{ca}^{(0)} + \tan(\varphi) \langle -\sigma_c \rangle$$

$$S_{bc}^{''} = S_{bc}^{(0)} + \tan(\varphi) \langle -\sigma_c \rangle$$

where φ is a material constant as $\tan(\varphi)$ is similar to the coefficient of friction, and $S_{ab}^{(0)}$, $S_{ca}^{(0)}$ and $S_{bc}^{(0)}$ are the shear strength values of the corresponding tensile modes.

Failure predicted by the criterion of f_4 can be referred to as transverse matrix failure, while the matrix failure predicted by f_5, which is parallel to the layer, can be referred as the delamination mode when it occurs within the elements that are adjacent to the ply interface. Note that a scale factor S is introduced to provide better correlation of delamination area with experiments. The scale factor S can be determined by fitting the analytical prediction to experimental data for the delamination area.

When fiber failure in tension/shear mode is predicted in a layer by f_1, the load carrying capacity of that layer is completely eliminated. All the stress components are reduced to zero instantaneously (100 time steps to avoid numerical instability). For compressive fiber failure, the layer is assumed to carry a residual axial load, while the transverse load carrying capacity is reduced to zero. When the fiber compressive failure mode is reached due to f_2, the axial layer compressive strength stress is assumed to reduce to a residual value S_{RC} $(= SFFC * S_{AC})$. The axial stress is then assumed to remain constant, i.e., $\sigma_a = -S_{RC}$, for continuous compressive loading, while the subsequent unloading curve follows a reduced axial modulus to zero axial stress and strain state. When the fiber crush failure occurs, the material is assumed to behave elastically for compressive pressure, $p > 0$, and to carry no load for tensile pressure, $p < 0$.

When a matrix failure (delamination) in the a-b plane is predicted, the strength values for $S_{ca}^{(0)}$ and $S_{bc}^{(0)}$ are set to zero. This results in reducing the stress components σ_c, τ_{bc} and τ_{ca} to the fractured material strength surface. For tensile mode, $\sigma_c > 0$, these stress components are reduced to zero. For compressive mode, $\sigma_c < 0$, the normal stress σ_c is assumed to deform elastically for the closed matrix crack. Loading on the failure envelop, the shear stresses are assumed to 'slide' on the fractured strength surface (frictional shear stresses) like in an ideal plastic material, while the subsequent unloading shear stress-strain path follows reduced shear moduli to the zero shear stress and strain state for both τ_{bc} and τ_{ca} components.

The post failure behavior for the matrix crack in the a-c plane due to f_4 is modeled in the same fashion as that in the a-b plane as described above. In this case, when failure occurs, $S_{ab}^{(0)}$ and $S_{bc}^{(0)}$ are reduced to zero instantaneously. The post fracture response is then governed by failure criterion of f_5 with $S_{ab}^{(0)} = 0$ and $S_{bc}^{(0)} = 0$. For tensile mode, $\sigma_b > 0$, σ_b, τ_{ab} and τ_{bc} are zero. For compressive mode, $\sigma_b < 0$, σ_b is assumed to be elastic, while τ_{ab} and τ_{bc} 'slide' on the fracture strength surface as in an ideal plastic material, and the unloading path follows reduced shear moduli to the zero shear stress and strain state. It should be noted that τ_{bc} is governed by both the failure functions and should lie within or on each of these two strength surfaces.

Fabric lamina model

The fiber failure criteria of Hashin for a unidirectional layer are generalized to characterize the fiber damage in terms of strain components for a plain weave layer. The fill and warp fiber tensile/shear failure are given by the quadratic interaction between the associated axial and shear stresses, i.e.

$$f_6 = \left(\frac{\langle \sigma_a \rangle}{S_{aT}} \right)^2 + \frac{\left(\tau_{ab}^2 + \tau_{ca}^2 \right)}{S_{aFS}^2} - 1 = 0$$

$$f_7 = \left(\frac{\langle \sigma_b \rangle}{S_{bT}} \right)^2 + \frac{\left(\tau_{ab}^2 + \tau_{bc}^2 \right)}{S_{bFS}^2} - 1 = 0$$

where S_{aT} and S_{bT} are the axial tensile strengths in the fill and warp directions, respectively, and S_{aFS} and S_{bFS} are the layer shear strengths due to fiber shear failure in the fill and warp directions. These failure criteria are applicable when the associated σ_a or σ_b is positive. It is assumed S_{aFS} = SFS, and

$$S_{bFS} = SFS * S_{bT} / S_{aT} .$$

When σ_a or σ_b is compressive, it is assumed that the in-plane compressive failure in both the fill and warp directions are given by the maximum stress criterion, i.e.

$$f_8 = \left[\frac{\langle \sigma_a^{'} \rangle}{S_{aC}} \right]^2 - 1 = 0, \quad \sigma_a^{'} = -\sigma_a + \langle -\sigma_c \rangle$$

$$f_9 = \left[\frac{\langle \sigma_b^{'} \rangle}{S_{bC}} \right]^2 - 1 = 0, \quad \sigma_b^{'} = -\sigma_b + \langle -\sigma_c \rangle$$

where S_{aC} and S_{bC} are the axial compressive strengths in the fill and warp directions, respectively. The crush failure under compressive pressure is

$$f_{10} = \left(\frac{\langle p \rangle}{S_{FC}} \right)^2 - 1 = 0, \quad p = -\frac{\sigma_a + \sigma_b + \sigma_c}{3}$$

A plain weave layer can fail under in-plane shear stress without the occurrence of fiber breakage. This in-plane matrix failure mode is given by

$$f_{11} = \left(\frac{\tau_{ab}}{S_{ab}} \right)^2 - 1 = 0$$

where S_{ab} is the layer shear strength due to matrix shear failure.

Another failure mode, which is due to the quadratic interaction between the thickness stresses, is expected to be mainly a matrix failure. This through the thickness matrix failure criterion is

$$f_{12} = S^2 \left\{ \left(\frac{\langle \sigma_c \rangle}{S_{cT}} \right)^2 + \left(\frac{\tau_{bc}}{S_{bc}} \right)^2 + \left(\frac{\tau_{ca}}{S_{ca}} \right)^2 \right\} - 1 = 0$$

where S_{cT} is the through the thickness tensile strength, and S_{bc}, and S_{ca} are the shear strengths assumed to depend on the compressive normal stress σ_c, i.e.,

$$\begin{Bmatrix} S_{ca} \\ S_{bc} \end{Bmatrix} = \begin{Bmatrix} S_{ca}^{(0)} \\ S_{bc}^{(0)} \end{Bmatrix} + \tan(\varphi)\langle -\sigma_c \rangle$$

When failure predicted by this criterion occurs within elements that are adjacent to the ply interface, the failure plane is expected to be parallel to the layering planes, and, thus, can be referred to as the delamination mode. Note that a scale factor S is introduced to provide better correlation of delamination area with experiments. The scale factor S can be determined by fitting the analytical prediction to experimental data for the delamination area.

Similar to the unidirectional model, when fiber tensile/shear failure is predicted in a layer by f_6 or f_7, the load carrying capacity of that layer in the associated direction is completely eliminated. For compressive fiber failure due to by f_8 or f_9, the layer is assumed to carry a residual axial load in the failed direction, while the load carrying capacity transverse to the failed direction is assumed unchanged. When the compressive axial stress in a layer reaches the compressive axial strength S_{aC} or S_{bC}, the axial layer stress is assumed to be reduced to the residual strength S_{aRC} or S_{bRC} where $S_{aRC} = SFFC * S_{aC}$ and $S_{bRC} = SFFC * S_{bC}$. The axial stress is assumed to remain constant, i.e., $\sigma_a = -S_{aCR}$ or $\sigma_b = -S_{bCR}$, for continuous compressive loading, while the subsequent unloading curve follows a reduced axial modulus. When the fiber crush failure is occurred, the material is assumed to behave elastically for compressive pressure, $p > 0$, and to carry no load for tensile pressure, $p < 0$.

When the in-plane matrix shear failure is predicted by f_{11} the axial load carrying capacity within a failed element is assumed unchanged, while the in-plane shear stress is assumed to be reduced to zero.

For through the thickness matrix (delamination) failure given by equations f_{12}, the in-plane load carrying capacity within the element is assumed to be elastic, while the strength values for the tensile mode, $S_{ca}^{(0)}$ and $S_{bc}^{(0)}$, are set to zero. For tensile mode, $\sigma_c > 0$, the through the thickness stress components are reduced to zero. For compressive mode, $\sigma_c < 0$, σ_c is assumed to be elastic, while τ_{bc} and τ_{ca} 'slide' on the fracture strength surface as in an ideal plastic material, and the unloading path follows reduced shear moduli to the zero shear stress and strain state.

The effect of strain-rate on the layer strength values of the fiber failure modes is modeled by the strain-rate dependent functions for the strength values $\{S_{RT}\}$ as

$$\{S_{RT}\} = \{S_0\}\left(1 + C_{rate1} \ln \frac{\{\dot{\varepsilon}\}}{\dot{\varepsilon}_0}\right)$$

$$\{S_{RT}\} = \begin{Bmatrix} S_{aT} \\ S_{aC} \\ S_{bT} \\ S_{bC} \\ S_{FC} \\ S_{FS} \end{Bmatrix} \text{ and } \{\dot{\bar{\varepsilon}}\} = \begin{Bmatrix} |\dot{\varepsilon}_a| \\ |\dot{\varepsilon}_a| \\ |\dot{\varepsilon}_b| \\ |\dot{\varepsilon}_b| \\ |\dot{\varepsilon}_c| \\ \left(\dot{\varepsilon}_{ca}^2 + \dot{\varepsilon}_{bc}^2\right)^{1/2} \end{Bmatrix}$$

where C_{rate} is the strain-rate constants, and $\{S_0\}$ are the strength values of $\{S_{RT}\}$ at the reference strain-rate $\dot{\varepsilon}_0$.

Damage model

The damage model is a generalization of the layer failure model of Material 161 by adopting the MLT damage mechanics approach, Matzenmiller et al. [1995], for characterizing the softening behavior after damage initiation. Complete model description is given in Yen [2002]. The damage functions, which are expressed in terms of ply level engineering strains, are converted from the above failure criteria of fiber and matrix failure modes by neglecting the Poisson's effect. Elastic moduli reduction is expressed in terms of the associated damage parameters ϖ_i:

$$E_i^{'} = \left(1 - \varpi_i\right) E_i$$

$$\varpi_i = 1 - \exp\left(-r_i^{m_i} / m_i\right) \qquad r_i \geq 0 \quad i = 1,...,6$$

where E_i are the initial elastic moduli, $E_i^{'}$ are the reduced elastic moduli, r_i are the damage thresholds computed from the associated damage functions for fiber damage, matrix damage and delamination, and m_i are material damage parameters, which are currently assumed to be independent of strain-rate. The damage function is formulated to account for the overall nonlinear elastic response of a lamina including the initial 'hardening' and the subsequent softening beyond the ultimate strengths.

In the damage model (material 162), the effect of strain-rate on the nonlinear stress-strain response of a composite layer is modeled by the strain-rate dependent functions for the elastic moduli $\{E_{RT}\}$ as

$$\{E_{RT}\} = \{E_0\}\left(1 + \{C_{rate}\} \ln \frac{\{\dot{\bar{\varepsilon}}\}}{\dot{\varepsilon}_0}\right)$$

$$\{E_{RT}\} = \begin{Bmatrix} E_a \\ E_b \\ E_c \\ G_{ab} \\ G_{bc} \\ G_{ca} \end{Bmatrix}, \{\dot{\bar{\varepsilon}}\} = \begin{Bmatrix} |\dot{\varepsilon}_a| \\ |\dot{\varepsilon}_b| \\ |\dot{\varepsilon}_c| \\ |\dot{\varepsilon}_{ab}| \\ |\dot{\varepsilon}_{bc}| \\ |\dot{\varepsilon}_{ca}| \end{Bmatrix} \text{ and } \{C_{rate}\} = \begin{Bmatrix} C_{rate2} \\ C_{rate2} \\ C_{rate4} \\ C_{rate3} \\ C_{rate3} \\ C_{rate3} \end{Bmatrix}$$

where $\{C_{rate}\}$ are the strain-rate constants. $\{E_0\}$ are the modulus values of $\{E_{RT}\}$ at the reference strain-rate $\dot{\varepsilon}_0$.

Element Erosion:

A failed element is eroded in any of three different ways:

1. If fiber tensile failure in a unidirectional layer is predicted in the element and the axial tensile strain is greater than E_LIMT. For a fabric layer, both in-plane directions are failed and exceed E_LIMT.
2. If compressive relative volume in a failed element is smaller than ECRSH.
3. If tensile relative volume in a failed element is greater than EEXPN.

Damage History Parameters:

Information about the damage history variables for the associated failure modes can be plotted in LS-PrePost. These additional history variables are tabulated below:

History Variable	Description	Value	LS-PrePost History Variable
1. efa(I)	Fiber mode in a		7
2. efb(I)	Fiber mode in b	0-elastic	8
3. efp(I)	Fiber crush mode		9
4. em(I)	Perpendicular matrix mode	≥ 1-failed	10
5. ed(I)	Parallel matrix/ delamination mode		11
6. delm(I)	delamination mode		12

C.2 Failure Mode Coupling for PW Model Type

PW DAMAGE TYPES		FIBER DAMAGE MODES					MATRIX DAMAGE MODES	
PW DAMAGE MODES		MODE 1f j = 7	MODE 2f j = 8	MODE 3f j = 9	MODE 4f j = 10	MODE 5f j = 11	MODE 6f j = 12	MODE 7f j = 13
MO -DU -LI	q_{ij}^{F}							
E_a		1	0	1	0	1	0	0
E_b		0	1	0	1	1	0	0
E_c		0	0	0	0	1	0	1
G_{ab}		1	1	1	1	1	1	0
G_{bc}		0	1	0	1	1	0	1
G_{ca}		1	0	1	0	1	0	1

Figure C.1: Illustration of which failure modes at hat affects the reduction of specific elastic moduli for the version of the model set to model a laminates with a plain weave fibre layup [34]

Appendix D

Classical Central Difference

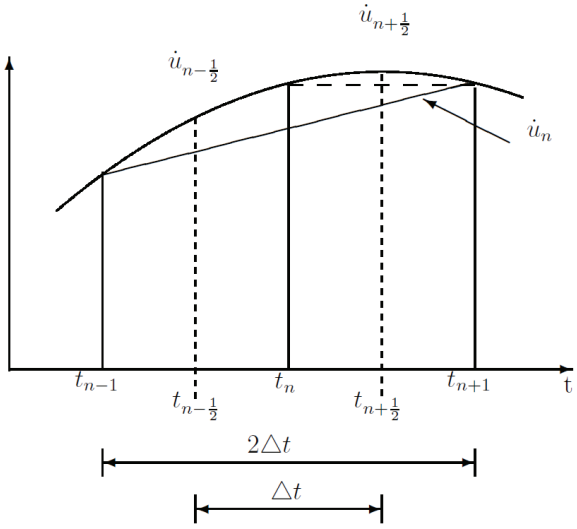

Figure D.1: Discretization used to describe the classical central difference method [19]

For the time step size Δt, the velocity and acceleration at time step n can be approximated by the conventional central difference equations [18, 19];

$$\dot{u}_n = \frac{1}{2\Delta t}\left(u_{n+1} - u_{n-1}\right) \tag{D.1}$$

$$\begin{aligned}\ddot{u}_n &= \frac{1}{\Delta t}\left(\dot{u}_{n+\frac{1}{2}} - \dot{u}_{n-\frac{1}{2}}\right) \\ &= \frac{1}{\Delta t}\left(\frac{u_{n+1} - u_n}{\Delta t} - \frac{u_n - u_{n-1}}{\Delta t}\right) \\ &= \frac{1}{(\Delta t)^2}\left(u_{n+1} - 2u_n + u_{n-1}\right)\end{aligned} \tag{D.2}$$

At time t_n equilibrium is given by;

$$\mathbf{M}\ddot{u}_n + \mathbf{C}\dot{u}_n + \mathbf{K}u_n = \mathbf{P}_n \tag{D.3}$$

Inserting equations (D.1) and (D.2) into (D.3) gives;

$$\left(\mathbf{M} + \frac{1}{2}\Delta t\mathbf{C}\right) u_{n+1} = \Delta t^2 \mathbf{P}_n - \left(\Delta t^2 \mathbf{K} - 2\mathbf{M}\right) u_n - \left(\mathbf{M} - \frac{\Delta t}{2}\mathbf{C}\right) u_{n-1} \tag{D.4}$$

from which the displacement at time step $n+1$ can be found by inverting $\mathbf{M}$ and $\mathbf{C}$ where after the velocity and accelerations can be found. If lumped masses is used $\mathbf{M}$ is diagonal and inversion is trivial. To avoid the solution of simultaneous equations $\mathbf{C}$ also needs to be diagonal or zero. A diagonal $\mathbf{C}$ corresponds to mass proportional damping which will damp lower modes most heavily [18]. It is likely that stiffness-proportional damping is then also desired but then equation (D.4) requires the solution of simultaneous equations. To overcome this problem *Half-Step Central Difference* is preferred and also the method used in LS-DYNA.

In order to start the time integration an initial condition is determined from equations (D.1) and (D.2);

$$u_{-1} = u_0 - \Delta t \dot{u}_0 + \frac{\Delta t^2}{2}\ddot{u}_0 \tag{D.5}$$

Appendix E

Pressure Measurement

In corporation with postgraduate student Bjarki Elíasson, a test set-up for measuring the reflected pressure from an explosive charge was established. The set-up is shown in figure E.1, and consists of a heavy steel plate, with dimensions 700×700×50mm, resting on 4 supporting legs to raise the plate from the ground. In the plate 9 holes for mounting pressure transducers has been made, as illustrated in figure E.2a and (b). The pressure transducer holes were placed in a circular pattern at different distances from the center of the panel. This was done such that pressure measurements at different distance from the detonation point could be performed, and thus measuring how the pressure decays as function of distance from the detonation point. Along the edges of the plate holes has been made, matching the holes in the blast box, such that the pressure plate can be mounted onto the blast box and used for measuring the pressure developing when performing tests in the box.

The explosive is positioned over the center hole, where a pressure transducer always has to be placed. The explosive is hung from a tripod. In the performed tests a single pressure transducer was used, because it was wanted to verify the functionality of the designed set-up, before adding additional pressure transducers to the set-up. A triggering system was designed such that the pressure transducer triggers with the detonation of the explosive.

Figure E.1: Designed test setup used for measuring reflected blast pressure

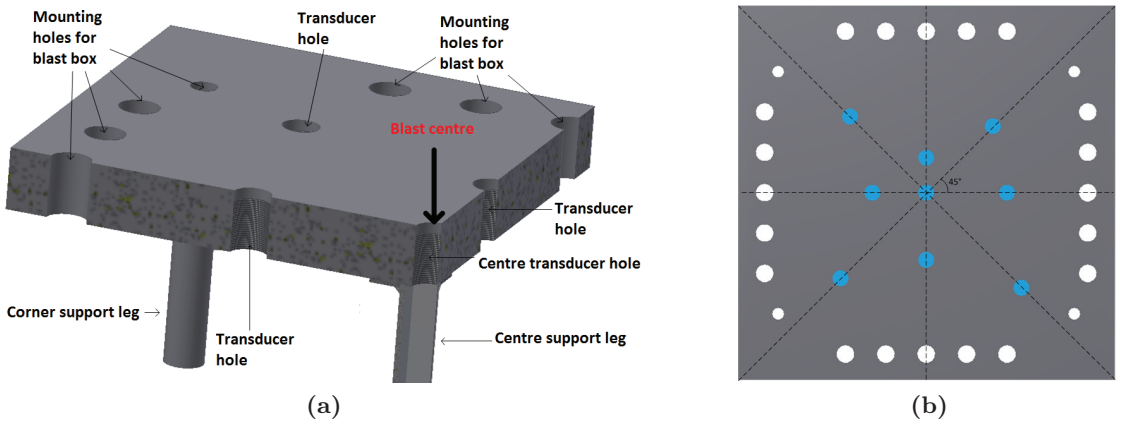

(a) (b)

Figure E.2: Position of holes for mounting pressure transducers

For measuring the pressure a Kistler 217C piezoelectric pressure transducer was used. It is specifically designed to measure high pressures in weapons development and munitions testing. The measurable pressure range is up to 520MPa(75000 psi) with a 2ms rise time. The signal and DC excitation power is emitted through a single coaxial cable. The power can be provided by any industry standard voltage mode IEPE(Integral Electronic Piezo-Electric) power supply/coupler. In appendix E.3 technical data for the pressure transducer can be found.

E.1 Measured Blast Pressure

Four different combinations of charge size and stand-off distance was used for measuring the blast pressure, and for each set-up 3 repetitions were performed;

50g@100mm

50g@150mm

100g@100mm

100g@150mm

Figure E.3 to E.6 shows the measured pressure and impulse, together with modelled pressure and impulse based on the *LOAD_BLAST_ENHANCED model. Looking at the measured pressure, the characteristic shape for the pressure-time development of an explosive is seen, and comparing the duration time from the test with that of the model, a similar level is found. Looking at the impulses, large differences are seen between the individual repetitions, up to 100% in some cases. Comparing the measured and modelled impulse there is a large difference in the agreement with the model, where e.g. 100g@100mm shows relatively good correlation, but 100g@150mm shows poor correlation.

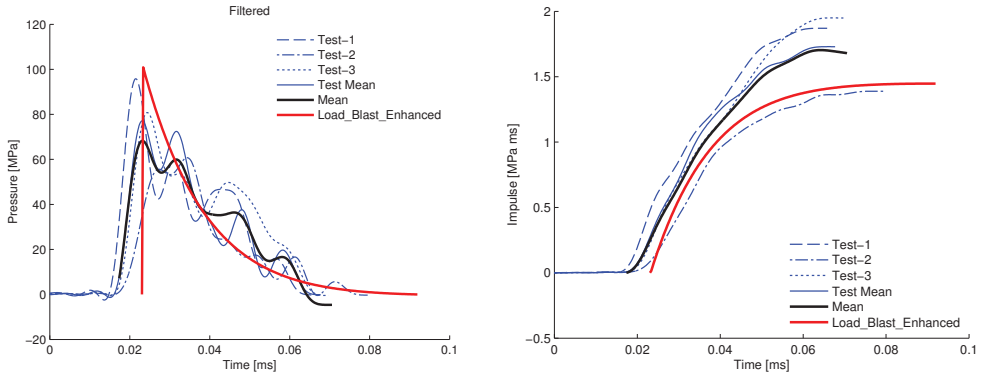

(a) Pressure **(b)** Impulse

Figure E.3: Pressure and impulse measured for 50g@100mm

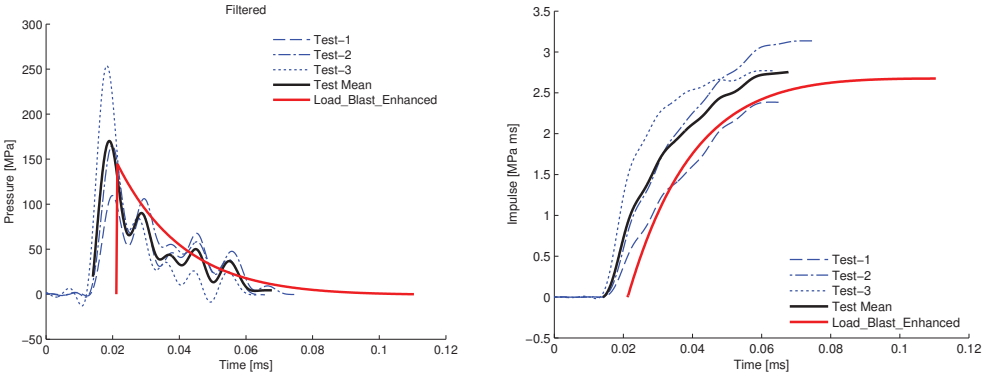

(a) Pressure **(b)** Impulse

Figure E.4: Pressure and impulse measured for 100g@100mm

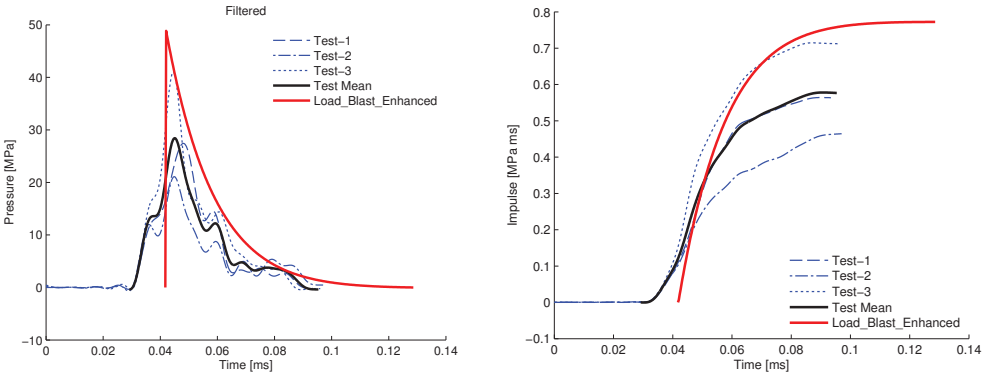

(a) Pressure **(b)** Impulse

Figure E.5: Pressure and impulse measured for 50g@150mm

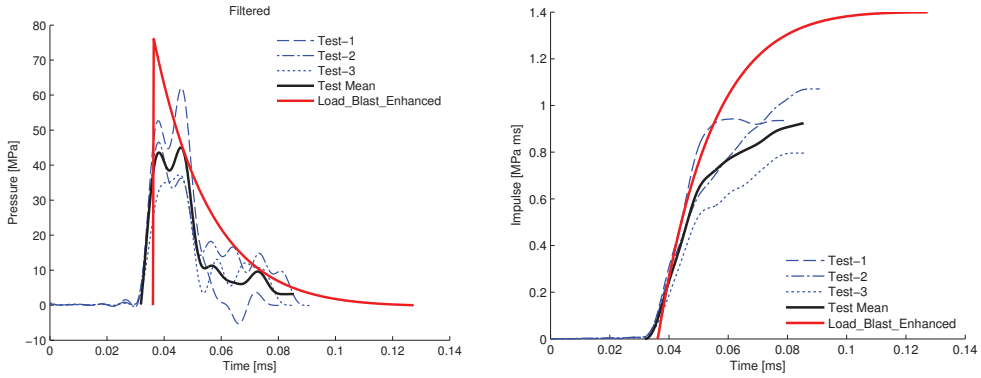

(a) Pressure **(b)** Impulse

Figure E.6: Pressure and impulse measured for 100g@150mm

E.2 Summery of Pressure Measurements

The large inconsistency seen in the measurements is not acceptable and compromises the usage of the data e.g. for comparing with model data. Because the pressure is measured at relatively short distance the deviation in the impulse could be an indication that the impulse is sensitive to the exact shape and position of the explosive charge relative to the pressure transducer. The position of the detonator in the explosive could also be thought to have an effect on the measured response. In the current set-up these properties are not exactly identical from test to test since the explosive is formed in hand, the position of the charge is based on measurements with a ruler, and the detonator is positioned randomly from test to test. More rigorous procedures should be developed such that the variations in the mentioned properties can be reduced from test to test, to minimize the effect of these properties on the measurements. The set-up with the pressure transducers mounted as shown could also be questioned, since ringing in the measured signal was observed in some cases. Also, one pressure transducer lost it functionality after approximately 20 tests had been performed on it, indicating that with the designed set-up the life time of the transducers are limited.

E.3 Kistler 217C Pressure Transducer

Pressure - PAG

KISTLER
measure. analyze. innovate.

Quartz

Type 217C
617C

High Pressure, Ballistics Pressure Sensors

The 217C and 617C sensors are specifically designed to measure high pressures in weapons development and munitions testing.

Both models have a 75,000 psi measuring range but the 217C is a low impedance, voltage mode version while the 617C is a high impedance charge mode type capable of quasi-static measurement.

- Low impedance voltage mode and high impedance, charge mode
- Low thermal transient response
- Excellent accuracy and repeatability
- Less than two microsecond rise time
- Low impedance version conforming to CE

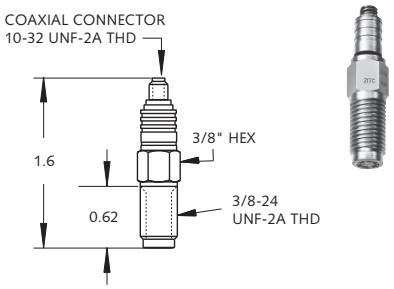

Description

Type 217C and 617C Ballistics Pressure Sensors are intended for measuring high frequency pressure variations found in ammunition acceptance testing, weapon development and closed-bomb powder proof tests. Their fast (2 microsecond) rise time and 75,000 psi measuring range along with excellent accuracy and repeatability make both units well suited for measuring detonation rise time peak pressures and pressure wave forms. Both the 217C and the 617C feature a unique end seal design which assures a positive pressure seal when the correct mounting torque is applied. The units are equipped with heat shields and when used in conjunction with a thermal protector, the affects of flash heat pulses during the pressure measurement are minimized.

Signal and DC excitation power to the 217C is conducted through a single coaxial cable, such as Series 1761 or 1762. Power and signal processing to the sensor can be provided by any one of the series 5100 couplers or by any industry standard voltage mode IEPE (Integral Electronic Piezo-Electric) power supply/coupler.

The charge signal from the 617C sensor is transmitted through a low noise coaxial cable, such as the 1631series, then converted and amplified to a proportional voltage in a multi-range charge amplifier, such as Kistler types 5010.

Technical Data

Type		Units	217C	617C
Pressure Range		psi	75000	75000
Max Pressure		psi	80000	80000
Threshold nom.		psi_{rms}	1	1
Sensitivity nom.	(217C)	mV/psi	0.05	
	(617 C)	pc/psi	–	–0.09
Non-linearity, zero based BFSL		%FSO	±1.5	±1.5
Hysteresis max.		%	1	1
Resonant Frequency nom.		kHz	200	200
Rise Time 10 ... 90%		µsec	2	2
Time Constant @ room temperature nom.		sec	1500	–
Frequency Response		Hz	near DC ... 20000	near DC ... 20000

continued

000-396a-04.03 (K3.217/617)

KISTLER
measure. analyze. innovate.

Technical Data

Type	Units	217C	617C
Temperature Sensitivity Shift	%/°F	–0.025	–0.015
Vibration Sensitivity max.	psi/g	0.06	0.06
Shock (1ms pulse width)	g	5000	5000
Vibration Limit	g	500	500
Temperature Range	°F	–65 ... 250	–65 ... 400
Temperature Range on thread	°F	–65 ... 400	–65 ... 400
Flash Temperature	°F	3000	3000
Capacitance	pF	6	
Output:			
Voltage full scale nom.	V	3.75	–
Current	mA	2	–
Impedance	Ω	<100	–
Bias nom.	VDC	11	–
Source:			
Constant Current nom.	mA	2 ... 20	–
Impedance min.	kΩ	250	–
Voltage	VDC	20 ... 30	–
Ripple max.	mV_{rms}	25	–
Mechanical:			
Case Material	type	maraging steel	maraging steel
Mounting Torque	lbf-ft	13 ... 17	13 ...17
Weight	grams	20	20

1 g = 9.80665 m/s², 1 inch = 25.4 mm, 1 gram = 0.03527 oz, 1 lbf-in = 0.1129 Nm

Application
Ideally suited for accurate and reliable measurement of gun barrel pressures up to 75,000psi under actual repetitive firing conditions. Both models do not require grease or other protective coatings. Life expectancy of about 2000 rounds is typical in most applications.

Mounting
Reliable and accurate pressure measurements require precise machining of the mounting hole. The Operating Instruction Manual for the 217C and 617C provides dimensional detail and machining instruction for installing the sensor in a test structure.

Supplied Accessories

200E24	(1) thermal protector
600A10	(5) seal ring,304 stainless steel 0.010 in thk

Ordering Information

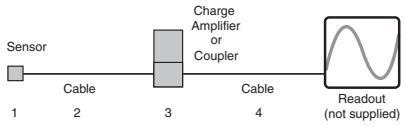

sp = specify cable length in meters

1 - 217C	voltage mode pressure sensor or
617C	charge mode pressure sensor
2 - 1631Asp	charge mode sensor cable,10-32 pos. to BNC pos. or
1761Bsp	voltage mode sensor cable 10-32 pos. to BNC pos.,
3 - 5000	charge amplifier series or
5100	coupler series
4 - 1511sp	output cable, BNC pos. to BNC pos.

000-396a-04.03 (K3.217/617)

List of Tables

List of Figures

DTU Mekanik
Sektion for Faststofmekanik
Danmarks Tekniske Universitet

Nils Koppels Allé, Bygn. 404
2800 Kgs. Lyngby

Tlf.: 4525 4250
Fax: 4593 1475
www.mek.dtu.dk

ISBN: 978-87-7475-388-9

DCAMM
Danish Center for Applied Mathematics and Mechanics

Nils Koppels Allé, Bld. 404
DK-2800 Kgs. Lyngby
Denmark
Phone (+45) 4525 4250
Fax (+45) 4593 1475
www.dcamm.dk
ISSN: 0903-1685